




ADVERTIMENT. L'accés als continguts d'aquesta tesi queda condicionat a l'acceptació de les condicions d'ús establertes per la següent llicència Creative Commons:  <https://creativecommons.org/licenses/?lang=ca>

ADVERTENCIA. El acceso a los contenidos de esta tesis queda condicionado a la aceptación de las condiciones de uso establecidas por la siguiente licencia Creative Commons:  <https://creativecommons.org/licenses/?lang=es>

WARNING. The access to the contents of this doctoral thesis it is limited to the acceptance of the use conditions set by the following Creative Commons license:  <https://creativecommons.org/licenses/?lang=en>



First-Principles Computational Methods for Quantum Materials

Electron Transport, Quantum Interference, Topology, and Superconductivity.

Nils Wittemeier

*Dissertation presented to the Department of Physics at the Autonomous University of Barcelona in partial fulfillment of the requirements for the degree of **Doctor of Philosophy in Physics**.*

Directors: Prof. Dr. Zeila Zanolli
Prof. Dr. Pablo Ordejón Rontomé

Tutor: Prof. Dr. Jordi Sort Viñas

To Aayushi.

Cover design: Spectral function of bulk iron (bcc); interpolated and artistically enhanced.

CERTIFICATE OF SUPERVISION

I hereby certify that the Ph.D. thesis entitled "*First-Principles Computational Methods for Quantum Materials: Electron Transport, Quantum Interference, Topology, and Superconductivity*" submitted to the Department of Physics at Universitat Autònoma de Barcelona for the degree of Doctor of Philosophy in Physics by Nils Wittemeier is the record of research work carried out by him during the period from October 2018 to March 2023 under my guidance and supervision.



Prof. Dr. Zeila Zanolli

*Debye Institute
Chemistry Department
Utrecht University*



Prof. Dr. Pablo Ordejón Rontomé

*Catalan Institute of Nanoscience
and Nanotechnology
Universitat Autònoma de Barcelona*

Abstract

In recent years, the term "quantum materials" has become a powerful unifying concept in science and engineering. These materials manifest quantum effects over large energy and length scales. Quantum materials are at the forefront of the ongoing "second quantum revolution," which promises to bring about paradigm-shifting advances in energy efficiency and beyond. However, with their enormous potential, quantum materials also pose new technical challenges for the scientific community in materials fabrication, characterization, and development of new computational methods. This work addresses some of the most significant problems related to first-principles computational methods for quantum materials (Part II). It uses these methods to gain new insights into low-dimensional quantum materials (Part III).

In particular, implementing the DFT + NEGF formalism based on spinors allow the modeling of charge and spin transport in systems with non-collinear spin and spin-orbit coupling effects (Chapter 6), which is essential for topological materials and spin-orbitronics devices. Furthermore, the development of the Bogolioubov-de-Gennes method and its implementation in the SIESTA software is presented as a semi-empirical tool for modeling superconductors based on first-principles electronic structure calculations (Chapter 7). In addition, postprocessing tools for calculating topological invariants and spin textures complete the code development part of this work (Chapter 8).

Aside from methods development, detailed studies of quantum materials are presented. Interference effects in finite sections of one-dimensional moiré crystals are investigated using a Landauer-Büttiker formalism within the tight-binding approximation (Chapter 9). Wave function interference is visible at the mesoscale: in the strong coupling regime, as a periodic modulation of quantum conductance and emergent localized states; in the localized-insulating regime, as a suppression of interlayer transport and oscillations of the density of states. These effects are linked to changes in the band structure of the ideal carbon nanotubes and are shown to be described by a model of one-dimensional wave interference.

Interactions between topological states in metastable polymorphs of bismuth monolayers (bismuthene) and silicon-based substrates are computed using first-principles methods (Chapter 10). The bismuthene polymorphs bind to silicon carbide (SiC), silicon (Si), and silicon dioxide (SiO₂) substrates. The proximity interaction in these heterostructures significantly affects the electronic structure, e.g., the topological band gap, even when bonding is weak. Van

der Waals interactions and the breaking of the sublattice symmetry are identified as the main factors driving changes in the electronic structure in non-covalently binding heterostructures. The topological character of the bismuthene phases is retained in all monolayer/substrate combinations, except for flat-hexagonal bismuthene on SiC, where covalent bonding drives a topological phase transition. Moreover, this work demonstrates that substrate interaction can strengthen the topological properties of bismuthene polymorphs and make them accessible for experimental investigations and technological applications.

The newly developed methods are applied to various systems to demonstrate possible applications and show the code's validity. In particular, the spinor-based DFT+NEGF method is used to determine the (anisotropic) magnetoresistance in one-dimensional iron chains and a Fe/MgO/Fe tunneling junction ([Chapter 11](#)). The code is also employed to model quantum transport in TMD nanodevices, characterized by strong spin-orbit coupling. Furthermore, the importance of spin-orbit coupling and electron correlation (DFT+U) in carbon nanotubes functionalized with antiferromagnetic molecules are analyzed. Finally, the BdG+DFT method models a conventional superconductor (lead) and an unconventional superconductor (iron selenide). The experimentally observed shape and size of the superconducting gap of both materials are reproduced.

Acknowledgments

As with any Ph.D. thesis, many people have contributed to my Ph.D. thesis: colleagues, friends, mentors, and family have supported me with kind words of encouragement by sharing their wisdom. I will attempt to name the individuals I speak of below.

First and foremost, I would like to thank my supervisors, Zeila Zanolli and Pablo Ordejón, for their belief in me and my work; for trusting me to become a part of their explorations of physics; for their support and feedback. Working with you and learning from you both has been a genuine pleasure. I am ever so grateful.

Throughout my Ph.D. I have had the pleasure of collaborating with many people. I sincerely thank Nick Papior, Matthieu Verstraete, and Mads Brandbyge for sharing their knowledge and experience with me. It has indeed been a pleasure collaborating with you. Special thanks to Miguel Pruneda and Stephan Roche at ICN2, who have repeatedly shared their vast knowledge and experience with me.

I would also like to express my gratitude to all current and former members of the Theory and Simulation group at ICN2, particularly Bogdan, Ramón, Arsalan, Federico, Roberta, Linda, José María, José María, Pol, Jiahui, Vladimir. I am also grateful to everyone in the Condensed Matter Group at Debye Institute at Utrecht University for welcoming me with open arms. Above all, I would like to express my appreciation to Ingmar Swart for his guidance and encouragement and to Daniel, Arnold and Riccardo; working with you has been a pleasure.

My formative academic years would be incomplete without Riccardo Mazzarello, who supervised my work at RWTH Aachen. A big thanks to the people who willingly helped proofread this manuscript: Michael Dick and Praful Aggarwal.

A special thanks and gratitude to my family, my parents, Anke and Ralf, and my sister, Lina, who have always endured me and my oddities. Thank you for everything you have done for me, specifically your love, support, and encouragement. Anke, I owe much to your mathematical brain, Ralf, to your technological expertise, and Lina, to your love and support. And, also, to my in-laws, Mamta and Chander, for your encouragement and kindness.

Lastly, I would like to express my deepest appreciation to Aayushi. Without you, I would not be where I am today. Your love, your trust, and your support have been invaluable to me. Thank you for being with me every step of the way and widening my horizons along the way. Words cannot express my gratitude.

Contents

Abstract	vii
Acknowledgments	ix
Contents	xi
Unit Convention	xv
1 Introduction	1
I Theoretical Background	7
2 Electronic Structure	9
2.1 <i>Introduction: The Many-Body Problem</i>	9
2.2 Born-Oppenheimer Approximation	10
2.3 Hartree-Fock Method	11
2.4 Density Functional Theory Framework	12
2.4.1 Hohenberg-Kohn Theorems	12
2.4.2 Kohn-Sham Scheme	13
2.4.3 Approximating the Exchange-Correlation Energy	15
2.4.4 Spin-Polarized Density Functional Theory	17
2.5 Crystals and Reciprocal Space	18
2.6 Pseudopotentials	19
2.7 Basis Set Expansions of the Kohn-Sham States	21
2.8 The SIESTA Method	23
2.8.1 Basis Sets in SIESTA	23
2.8.2 Electron spin in SIESTA	24
3 Electronic Transport	27
3.1 <i>Introduction: The Transport Problem</i>	27
3.2 Landauer-Büttiker Formalism	29
3.3 Non-Equilibrium Green's Function Formalism	31
3.3.1 Green's Function Transport	31
3.3.2 The DFT+NEGF Method	33
3.3.3 Complex Contour Integration	35
4 Topological Band Theory and the \mathbb{Z}_2 Invariant	37
4.1 <i>Introduction: Topology</i>	37

4.2	The Berry Phase, the Chern Number, and the Quantum Hall Effect	37
4.3	Bulk-Boundary Correspondence	38
4.4	Time-Reversal Invariance, the \mathbb{Z}_2 Invariant and the Quantum Spin Hall Effect	39
5	Superconductivity	41
5.1	<i>Introduction</i> : Beyond Normal Metals	41
5.2	Theories of Superconductivity	42
5.3	Unconventional Superconductivity	43
5.4	The Bogoliubov-de-Gennes Method	44
5.4.1	Mean-Field Approximation of the Many-Body Hamiltonian	45
5.4.2	Bogoliubov Transformation	46
5.4.3	Singlet and Triplet Pairing	47
5.4.4	The BdG+DFT Method	49
II	Methods Development	51
6	Implementing Spinor Transport In TRANSIESTA	53
6.1	Electronic spin in the Non-Equilibrium Green's Function Formalism	53
6.1.1	Calculating the Electrode Surface Self-Energy	55
6.1.2	Calculating the Green's Function	55
6.1.3	Mixing Weights	57
6.1.4	Parallelization and Scaling	57
6.2	Postprocessing	59
6.2.1	Spin Channel Projected Transmission	59
7	Implementing Superconductivity in SIESTA	63
7.1	The BdG Equation for Localized Basis Sets	63
7.2	Solution Methods	64
7.3	Code Structure	65
7.3.1	Updating the Pairing Potential	66
7.3.2	Solving the Eigenvalue Problem	67
7.3.3	Input Options	68
7.4	Tests	69
7.4.1	Bulk lead (Pb)	69
7.4.2	Bulk iron selenide (FeSe)	70
7.4.3	Computational Details	71
8	Tools for Studying Topological Materials	73
8.1	Spin Texture	73
8.1.1	<i>Application</i> : Manipulation of Spin Transport in Graphene/Transition Metal Dichalcogenide Heterobilayers upon Twisting	76
8.2	Interface Z2PACK	77
8.2.1	Numerical Computation of Winding Numbers	78

III Simulations	81
9 Interference Effects in One-Dimensional Moiré Crystals	83
9.1 <i>Introduction: One-Dimensional Moiré Crystals</i>	83
9.2 Basics of Carbon Nanotubes	85
9.3 Methodology	86
9.3.1 First-Principles Calculations	86
9.3.2 Tight-Binding Model	87
9.4 Results and Discussion	89
9.4.1 Strong Coupling Regime	90
9.4.2 Localized Insulating Regime	100
9.4.3 Weak Coupling Regime	102
9.5 Conclusion	104
10 Tuning the Topological Band Gap of Bismuthene	107
10.1 Introduction	107
10.2 Methods	108
10.3 Results and Discussion	110
10.3.1 Free-Standing Bismuthene	110
10.3.2 SiC(0001)	111
10.3.3 SiO ₂ (0001) α -Quartz	114
10.3.4 Si(111)	119
10.4 Conclusion	120
11 Quantum Transport with Spin Orbit Coupling	123
11.1 Monatomic Iron Chain (1D)	123
11.1.1 Magnetic Anisotropy in the Ideal Iron Chain	124
11.1.2 Domain Wall Conductivity	128
11.1.3 Computational Details	131
11.2 Fe-MgO-Fe Hetero Structure (3D)	132
11.2.1 Magneto Resistance of Bulk Iron	132
11.2.2 Magneto Resistance in Fe/MgO/Fe Tunneling Junctions	135
11.2.3 Computation Details	136
11.3 Transition Metal Dichalcogenides (2D)	140
11.3.1 Monolayer MoS ₂ and WS ₂	140
11.3.2 Lateral MoS ₂ -WS ₂ Heterojunction	141
11.3.3 Computational Details	146
11.4 CNT with Magnetic Molecule (1D)	147
11.4.1 Computational Details	153
11.5 Conclusion	153
12 Conclusions and Outlook	155
Bibliography	157

Appendices	189
Appendix List of Publications	191
Appendix List of Figures	193
Appendix List of Tables	197

Unit Convention

Unless units are explicitly stated, this work adopts the Hartree atomic unit convention.

Defining units

Name	Symbol	Value	Alternative Expression
Reduced Planck constant	\hbar	1	$h/2\pi$
Elementary charge	e	1	–
Bohr (radius)	a_0	1	$4\pi\epsilon_0\hbar^2/(m_e e^2)$
Electron mass	m_e	1	–
Hartree (energy)	E_h	1	$\hbar^2/m_e/a_0^2$

Derived units

Unit of	Expression	Value in SI units[NIST18]
Action	\hbar	$1.054\,571\,817 \dots \times 10^{-34}$ J s
Charge	e	$1.602\,176\,634 \times 10^{-19}$ C
Charge density	e/a_0^3	$1.081\,202\,384\,57 \times 10^{12}$ C m ⁻³
Current	eE_h/\hbar	$6.623\,618\,237\,510 \times 10^{-3}$ A
Energy	E_h	$4.359\,744\,722\,2071 \times 10^{-18}$ J
Force	E_h/a_0^2	$8.238\,723\,4983 \times 10^{-8}$ N
Length	a_0	$5.291\,772\,109\,03 \times 10^{-11}$ m
Magnetic dipole moment	$\hbar e/m_e$	$1.854\,802\,015\,66 \times 10^{-2}$ J T ⁻¹
Mass	m_e	$9.109\,383\,7015 \times 10^{-31}$ kg
Momentum	\hbar/a_0	$1.992\,851\,914\,10 \times 10^{-24}$ kg m s ⁻¹
Time	\hbar/E_h	$2.418\,884\,326\,5857 \times 10^{-17}$ s
Velocity	$a_0 E_h/\hbar$	$2.187\,691\,263\,64 \times 10^6$ m s ⁻¹

Over the last decades, the energy consumption of the information and communication sector has increased steadily and is projected to exceed 20% of global energy consumption by 2030 [Jon18]. This makes the development of smaller and more efficient devices for memory storage and information processing a crucial challenge in the pursuit of sustainability. One possible avenue to address this issue is the design of devices that exploit spin degrees of freedom (spintronics). Magnetic phenomena occur on an energy scale that is one order of magnitude smaller than electronic ones, making spintronics devices more efficient [Hir+20; Pue+20; Tra16; ŽFD04]. To date, research in the field of spintronics has led to the discovery of novel devices such as nonvolatile magnetic random access memory or spin-polarised field effect transistors [Ber96; Fer08; Gaj+12; Kat+00; Kaw+12; Khv+13; KW15; Slo96; Wol+10; ŽFD04]. However, neither first-generation (based on spin manipulation via magnetic fields) nor second-generation (based on spin transfer torque) spintronics devices have reached the efficiencies required to help solve the global energy crisis. The ongoing "second quantum revolution" promises to bring about a breakthrough by exploiting quantum physics directly, rather than using it as a mere tool to observe and understand the world around us. Quantum materials, i.e., materials that manifest quantum effects over large energy and length scales, are at the forefront of this development. Developing spintronics devices based on quantum materials may lead to much-needed paradigm-changing advances in energy efficiency and beyond [Giu+20; He+22]. However, with enormous potential, quantum materials also pose new technical challenges to the scientific community regarding material fabrication and characterization, as well as computational methods used to predict and understand the science at play. This thesis addresses some of the most impactful challenges concerning first-principles computational methods for quantum materials and applies these methods to gain novel insights into low-dimensional quantum materials.

What Are Quantum Materials?

The term "Quantum Materials" encompasses many materials, including superconductors, multiferroics, van der Waals heterostructures, moiré crystals, and topological insulators. These materials, which at first glance have little in common, are fundamentally connected by a single thread: they exhibit quantum effects at the macroscopic level.[Giu+20; HK10; Kan13; KM05] Although the physical description of all materials is rooted in quantum mechanics, in most

materials, quantum effects are not observable at the macroscopic scale where classical mechanics can describe their behavior. This is known as Bohr's correspondence principle. However, quantum materials defy this principle and manifest quantum effects at a wide range of energy and length scales. But what sets quantum materials apart from other materials? The answer to this question hinges on two concepts: entanglement and topology.

The concept of invariance is one of the most important in modern theoretical physics. Physical invariants represent the fundamental and unchangeable aspects of any system and allow us to create abstract ideas about physical properties. Without the concept of invariants, we would be left to study any system from scratch, but with invariants, we can generalize the knowledge gained in one system and apply it to groups of materials with specific commonalities. The most prominent examples of invariants include the conservation of energy or (angular) momentum. Wave function topology applies the mathematical concept of topology to identify new invariants at the level of quantum wave functions¹ Topological invariants have produced the understanding that not all states of insulating matter are equivalent to the insulating state of the vacuum. Furthermore, it has brought about the concept of the quantum (spin) Hall effect. Another prominent example of wave function topology is vortices in superconductors and superfluids with quantized flux that remains invariant under smooth changes to the system. These states with different topological invariants are separated from the conventional state by phase transition.

The concept of entanglement has existed since the early days of quantum mechanics. In its most fundamental form, entanglement arises from the Pauli exclusion principle, which demands that the many-body wave function of an electron system must be antisymmetric under particle exchange. Although this condition may appear harmless, its implications are far-reaching. Entanglement creates an inseparable connection between all quantum particles in a system. Even if we can find the quantum mechanical wave function of every component of a quantum system, this does not imply that we know the system's wave function as a whole or vice versa. But not all forms of entanglement originate in the Pauli exclusion. For example, the formation of Cooper pairs in superconductors or the entanglement between spins in complex magnets does not arise from the antisymmetry of the electron wave function alone. Like the wave function topology, these forms of entanglement signify new types of quantum order distinct from conventional matter by a phase transition.

The term Quantum Materials encompasses all materials that exhibit nontrivial wave function topology or unconventional forms of entanglement. Controlled generation and manipulation of the quantum order in these materials by electrical, magnetic, or optical means are key

¹ A more detailed description of topology and topological invariants can be found in [Chapter 4](#).

challenges in the application of quantum materials. For this reason, tunable quantum materials are highly sought after. Possibly the most prototypical example of a tunable quantum material is twisted bilayer graphene (tBLG). In tBLG, the twist angle controls the emerging properties. For special magic angles, tBLG exhibits flat bands [BM11] that host strongly correlated phases, such as a correlated insulator state [Cao+18a; Po+18; Won+20; Zon+20], a superconducting state [Cao+18b; Sai+20; Sha+19; Ste+20; Yan+19], or a *strange metal* state [Cao+20]. In general, two-dimensional moiré crystals are an ideal playground for realizing tunable quantum materials and, as such, have been studied extensively. However, their one-dimensional counterparts have received considerably less attention from the scientific community. As part of this thesis, double-wall carbon nanotubes were studied as examples of one-dimensional tunable quantum materials to understand the role of wave interference and interlayer coupling on the transport properties of one-dimensional moiré crystals.

Using proximity interactions to affect the properties of two-dimensional materials is an alternative approach to creating tunable quantum materials. This effect has been used to enhance the weak spin-orbit coupling and induce the quantum anomalous Hall and quantum spin-Hall effects in graphene [AAU16; CFR18; Gmi+16; Pez+21; Zan+18], topological phases in other topologically trivial 2D materials [Sin+19]. This work presents a detailed study of the effects of proximity interactions on the stability, topology, and band gap of metastable monolayer bismuth phases, which promise to host robust topological phases due to strong intrinsic spin-orbit coupling.

The Role of Spin-Orbit Coupling in Topological Matter

Spin-orbit (SO) coupling is a relativistic effect that originates from the interaction between an electron's spin moment, its orbital moment, and electric fields: An electron moving with momentum (\mathbf{p}) in an electric field (\mathbf{E}) experiences an effective magnetic field ($\mathbf{B}_{\text{eff}} \sim \mathbf{E} \times \mathbf{p}$). This effective field gives rise to a momentum-dependent Zeeman-like energy, the SOC, $H_{\text{SO}} \sim (\mathbf{E} \times \mathbf{p} \cdot \boldsymbol{\sigma})$. In the context of quantum materials, SOC has led to the prediction of topological insulators and superconductors [BHZ06; Giu+20; KM05; QZ11]. But SOC plays a fundamental role far beyond topological matter. It is fundamental in understanding the fine structure of atoms [Woo92]. In solids, the SOC is responsible for coupling the magnetic moments and the underlying crystal structure. It gives rise to magnetic anisotropy [Joh+96], spin relaxation [WJW10], magnetic damping [MR03], anisotropic magnetoresistance [MP75], and the anomalous Hall effect [Nag+10].

New Computational Challenges

Numerical methods are essential for studying any material's physical and chemical properties. However, among the computational methods used today, first-principles methods have a specific place because they do not rely on empirical parameters, which gives them enormous predictive power. To include SOC in first-principles simulations, the Schrödinger equation has to be solved using fully relativistic Hamiltonians and spinor wave functions. During the 1960s, when DFT was first conceptualized, this was difficult to achieve for most systems due to limited computational power. Relativistic effects were approximated as a scalar field, and the Schrödinger equation was solved for spins-up and -down electrons (collinear spin approximation). Today, spinor wave functions have become computationally affordable thanks to improvements in computational power and the efficiency of DFT codes. All state-of-the-art DFT codes include options to perform simulations with SOC.

Although DFT has been widely successful at predicting many material properties, it is not always applicable. In particular, modeling nanodevices under non-equilibrium conditions requires beyond-ground-state DFT methods such as the DFT+NEGF approach. Including the description of SOC in the transport methods is equally important because it drives many spintronics-mechanism like spin-orbit-torques, spin-to-charge conversion, and topological matter in general. Thus far, spinor-based implementations of this framework have only been realized in Gollum [Fer+14], which employs a semi-empirical approach to model non-equilibrium conditions, and some commercial codes with closed source (FHI-AIMS, QuantumATK) [Góm21; Smi+20].

Similarly, methods for modeling superconductors based on first principles require generalizing the DFT framework to the four-component Nambu spinor. In recent years, two types of DFT-based approaches for the simulation of superconductors have emerged: ab initio methods which include the motion of nuclei to calculate the superconducting pairing from the electron-phonon coupling[Lüd+05; Mar+05], and approaches which use a semi-empirical parameter to calculate a self-consistent superconducting pairing based only on electron-electron interactions[OGK88]. However, the computational complexity of fully ab initio methods remains a challenge for systems with more than a few atoms. Semi-empirical approaches to superconductivity, to our knowledge, have only been implemented within the Korringa-Kohn-Rostoker (KKR) method [Csi+18; RB22a; Sau+20].

As part of this work, a spinor-based approach to quantum transport was implemented in the open-source code SIESTA. SIESTA is a mature open-source DFT implementation that exploits strictly localized basis sets and sparse methods to perform highly efficient DFT calculations with thousands of atoms. Until now, TRANSIESTA, the DFT+NEGF extension of SIESTA, used

the collinear spin approximation. With the extension presented here, it is now possible to include fully relativistic effects and simulate non-equilibrium transport in topological materials. The semi-empirical Bogoliubov-de-Gennes method has been implemented in SIESTA (SIESTA-BdG) to leverage the efficiency of SIESTA and make highly accurate calculations of large-scale superconductor structures feasible. The SIESTA-BdG method bridges the gap between large-scale tight-binding and small-scale fully ab initio methods. Furthermore, tools were developed for extracting and visualizing the spin texture and \mathbb{Z}_2 from the SIESTA output to analyze topological material properties. These new methods have been applied to a series of relevant systems to test the correctness of their implementation and highlight their capabilities for understanding the fundamental physical concepts at play.

Thesis Outline

The body of this thesis is organized into three parts. [Part I Theoretical Background](#) introduces and reviews the theoretical frameworks and implementations thereof for quantum mechanical modeling of the electronic structure of solids ([Chapter 2](#)), electron transport ([Chapter 3](#)), topological band theory ([Chapter 4](#)) and superconductivity ([Chapter 5](#)). [Part II Methods Development](#) outlines the development of new methods for modeling specific aspects of Quantum Materials building on top of the state-of-the-art open-source project SIESTA. [Chapter 6](#) describes implementing a spinor-based version of quantum transport, essential to model spin-orbit coupling and simulate transport in topological matter. [Chapter 7](#) details the implementation of the Bogoliubov-de-Gennes method for modeling superconductivity, and [Chapter 8](#) the development of post-processing tool for extracting the spin texture and topological invariants from SIESTA calculations. The new code developments created as part of this work are already publicly available and will become part of the main version of SIESTA in the near future. [Part III Simulations](#) comprises three chapters utilizing the newly developed methods to unravel aspects of quantum materials. [Chapter 9](#) addresses quantum interference and its effect on quantum transport through one-dimensional moiré crystals, exemplified in double-wall carbon nanotubes. [Chapter 10](#) deals with the effects of substrate interactions on the topological insulator phase of bismuth monolayers. Finally, [Chapter 11](#) demonstrates the capabilities of our new quantum transport implementation at the example of magnetic junctions, transition metal dichalcogenides interfaces, and carbon nanotubes functionalized with anti-ferromagnetic molecular magnets.

Part I

Theoretical Background

The quantum many-body problem is the fundamental basis on which solid-state physics rests. Its complexity remains a challenge to theoretical physicists, and analytical solutions are unknown for all but the simplest systems. This chapter briefly outlines the many-body problem itself and the framework of density functional theory as one of the most powerful tools for solving it.

2.1 Introduction: The Many-Body Problem

All matter we encounter in our daily lives is composed of electrons, protons, and neutrons. Protons and neutrons tightly bind to each other, forming atomic nuclei. Negatively charged electrons bind to the positive charge of the nuclei forming the atom. Unlike the very localized nucleus, which has a radius of a few femtometers (1×10^{-15} m) [Jev05], electrons remain much less localized, forming a cloud around the nucleus with (atomic) radii ranging from tens to hundreds of picometers (1×10^{-11} m to 2×10^{-10} m) [Sla64]. In condensed matter, the distance between these atoms is on the order of 1×10^{-10} m. As a result, the electron clouds of neighboring atoms overlap, causing them to interact strongly. Electromagnetic interactions between the electrons and nearby nuclei not only form the bonds that hold solids and molecules together but also determine the electrical, optical, and magnetic properties of all known materials. Therefore, the study of electronic interactions is one of the fundamental issues concerning physicists, chemists, and material scientists trying to understand the materials that make up the world around us and attempting to create new materials tailored to address the technological limitations of naturally occurring ones. At the core of these considerations stands the quantum many-body problem: finding solutions for the time-independent Schrödinger equation for a system of many interacting particles [Sch26a; Sch26b; Sch26c]:

$$\mathbf{H}|\Psi\rangle = E|\Psi\rangle, \quad (2.1)$$

where \mathbf{H} is the Hamiltonian, Ψ is the many-body wave function, and E is the energy of the system. For a state of matter consisting of M nuclei and N electrons, the Hamiltonian is commonly decomposed into six components: the kinetic energy of the electron (T_e) and nuclei (T_n), the electron-electron (U_e) and nuclei-nuclei (U_n) Coulomb repulsion, the electrostatic

interaction between electrons and nuclei (V_{en}) and external potentials (v_{ext}), such as magnetic or electric fields:

$$\begin{aligned}
 \mathbf{H} &= \mathbf{T}_e + \mathbf{T}_n + \mathbf{U}_{ee} + \mathbf{U}_{nn} + \mathbf{V}_{en} + v_{\text{ext}} \\
 &= - \sum_{\alpha=1}^M \frac{1}{2M_\alpha} \nabla_\alpha^2 - \frac{1}{2} \sum_{i=1}^N \nabla_i^2 + \sum_{\alpha=1}^M \sum_{\beta>\alpha}^M \frac{Z_\alpha Z_\beta}{|\mathbf{R}_\alpha - \mathbf{R}_\beta|} \\
 &\quad + \sum_{i=1}^N \sum_{j>i}^N \frac{1}{|\mathbf{r}_i - \mathbf{r}_j|} - \sum_{\alpha=1}^M \sum_{i=1}^N \frac{Z_\alpha}{|\mathbf{R}_\alpha - \mathbf{r}_i|} + v_{\text{ext}}.
 \end{aligned} \tag{2.2}$$

Here, M_α and Z_α are the mass and charge of the nuclei α , and \mathbf{R}_α and \mathbf{r}_i represent the $3M + 3N$ spatial coordinates of the many-body wave function. Finding solutions to this non-linear differential equation in $3M+3N$ dimensions is a complex task. An exact solution can only be obtained for hydrogen-like systems consisting of one electron and one nucleus. It is, therefore, necessary to apply a set of adequate approximations to gain a quantum-mechanical understanding of any system with more than three particles.

The following sections of this chapter discuss approximations and methodologies used to solve the many-body problem, in particular, the density functional theory framework and its application to solid matter. The introduction found here is brief and focused on the aspects most relevant to the work presented in this thesis. A more extensive introduction to electronic structure theory and density functional theory can be found, for example, in R. Martin's "Electronic Structure: Basic Theory and Practical Methods" [Mar04], E. Engel and R. Dreizler's "Density Functional Theory: An Advanced Course" [ED11], or C. Fiolhais, F. Nogueira and M. A. L. Marques' "A Primer in Density Functional Theory" [FNM03].

2.2 Born-Oppenheimer Approximation

Since the mass of an electron is 15 orders of magnitude smaller than that of any nuclei, we assume that the typical relaxation time for electrons is also orders of magnitude smaller. Hence, we can treat the motion of electrons and nuclei effectively as decoupled and search for solutions to the electronic part of the wave function while keeping the nuclei's positions fixed (Born-Oppenheimer approximation [BO27]).

$$\Psi(\mathbf{r}_1, \dots, \mathbf{r}_N, \mathbf{R}_1, \dots, \mathbf{R}_M) = \Phi_e(\mathbf{r}_1, \dots, \mathbf{r}_N) \Phi_n(\mathbf{R}_1, \dots, \mathbf{R}_M) \tag{2.3}$$

$$\mathbf{H}^e |\Phi_e\rangle = E |\Phi_e\rangle \tag{2.4}$$

$$\mathbf{H}^e = -\frac{1}{2} \sum_{i=1}^N \nabla_i^2 + \sum_{i=1}^N \sum_{j>i}^N \frac{1}{|\mathbf{r}_i - \mathbf{r}_j|} + v_{\text{ext}}(\mathbf{r}), \quad (2.5)$$

where the electrostatic potential of the nuclei has been included in the external potential v_{ext} . Although this approximation already significantly reduces the spatial degrees of freedom, the complexity of the problem at hand remains immense.

2.3 Hartree-Fock Method

The Hartree-Fock (HF) method [Foc30; Har28; Sla28; Sla30b; Sla51] was developed as an early attempt to find solutions to this Hamiltonian, based on the assumption that the N -electron wave function Φ could be represented by the Slater determinant of N one-electron wave functions.

$$\Phi^{HF}(\mathbf{r}_1, \mathbf{r}_2, \dots, \mathbf{r}_N) = \frac{1}{\sqrt{N!}} \begin{vmatrix} \phi_1(\mathbf{r}_1) & \phi_2(\mathbf{r}_1) & \cdots & \phi_N(\mathbf{r}_1) \\ \phi_1(\mathbf{r}_2) & \phi_2(\mathbf{r}_2) & \cdots & \phi_N(\mathbf{r}_2) \\ \vdots & \vdots & \ddots & \vdots \\ \phi_1(\mathbf{r}_N) & \phi_2(\mathbf{r}_N) & \cdots & \phi_N(\mathbf{r}_N) \end{vmatrix}. \quad (2.6)$$

The Slater determinant ensures that the wave function satisfies the Pauli principle, i.e., it is antisymmetric under electron exchange. To find the Hartree-Fock ground state wave function, the energy functional $\langle \Phi^{HF} | \mathbf{H}^e | \Phi^{HF} \rangle$ is minimized under the orthonormalizing constraint $\langle \phi_i | \phi_j \rangle = \delta_{ij}$. The constraint minimization problem can be rewritten in terms of Lagrangian multiplier λ_{ij} :

$$\mathcal{L}[\phi_1, \dots, \phi_N] = \langle \Phi^{HF} | \mathbf{H}^e | \Phi^{HF} \rangle - \sum_{i,j=1}^N \lambda_{ij} (\langle \phi_i | \phi_j \rangle - \delta_{ij}). \quad (2.7)$$

Setting the functional derivative to zero yields the Hartree-Fock equations, a set of coupled equations that need to be solved self-consistently:

$$\epsilon_i \phi_i(\mathbf{r}) = \mathbf{h}(\mathbf{r}) \phi_i(\mathbf{r}) + \sum_{\substack{j=1 \\ i \neq j}}^N \int d\mathbf{r}' \frac{|\phi_j^*(\mathbf{r}')|^2}{|\mathbf{r} - \mathbf{r}'|} \phi_i(\mathbf{r}) - \sum_{\substack{j=1 \\ i \neq j}}^N \int d\mathbf{r}' \frac{\phi_j^*(\mathbf{r}') \phi_i^*(\mathbf{r}')}{|\mathbf{r} - \mathbf{r}'|} \phi_i(\mathbf{r}), \quad (2.8)$$

where \mathbf{h} is the one-electron operator $-\frac{1}{2} \nabla_i^2 - \sum_{\alpha=1}^M Z_\alpha / (\mathbf{r} - \mathbf{R}_\alpha)$ and ϵ_i is the energy eigenvalue associated with ϕ_i . The second term on the right-hand side, the Hartree term, represents the electrostatic potential of the electron charge distribution $n(\mathbf{r}) = \sum_j |\phi_j|^2$. The third term arises from the constraint of the Pauli principle and accounts for electron exchanges. While exchange

effects are explicitly included in the Hartree-Fock model, electron-electron correlations are completely neglected by this ansatz, thus limiting the applicability of the Hartree-Fock method.

Since the inception of the Hartree-Fock method, many methods have been developed to incorporate correlation effects [TKV19]. At large there are three types of such extensions *many-body perturbation theory methods*, based on Møller-Plesset [MP34] or Epstein-Nesbet perturbation theory [Eps26; Nes55], *coupled-cluster methods* [Číž66; CK60; Coe58] and *configuration interaction methods* [DS99], like the multi-configuration self-consistent field method [SO96] and the complete active space self-consistent field method [Roo07]. These post-Hartree-Fock methods are widely employed in the area of Quantum Chemistry.

2.4 Density Functional Theory Framework

In contrast to the Hartree-Fock and post-Hartree-Fock methods, the density functional theory framework avoids determining the many-body wave function. Instead, the quantum-mechanical many-body problem is solved in terms of the electronic density. The concept of electronic density as a fundamental quantity that describes the properties of matter can be traced back to the early days of quantum mechanics when Fermi [Fer27; Fer28] and Thomas [Tho27] applied it to the study of isolated atoms (the Thomas-Fermi model). A few years later, Dirac [Dir30] included exchange interactions to improve the description (the Thomas-Fermi-Dirac model) and already stated that the electronic state density fully determines the ground state of an atom. Despite these influential works, the variational principle of the energy on which modern density functional theory hinges was introduced almost 40 years later in the seminal work of Hohenberg and Kohn [HK64].

2.4.1 Hohenberg-Kohn Theorems

The work of Hohenberg and Kohn laid the foundation of modern density functional theory by establishing a one-to-one correspondence between the wave function and the electronic density of the many-body ground state.

► **Theorem 2.1 (Hohenberg-Kohn Theorem 1 [HK64]).** Let $n_0(\mathbf{r})$ be the non-degenerate electronic ground state density of a system consisting of an arbitrary but fixed number of electrons under the influence of an external potential $v_{\text{ext}}(\mathbf{r})$ and mutual Coulomb repulsion. Then the external potential $v_{\text{ext}}(\mathbf{r})$ is a unique functional of $n_0(\mathbf{r})$, apart from a trivial additive constant. ◀

Since a given ground-state density fixes the external potential up to an additive constant, the Hamiltonian is also fixed up to the same additive constant. This, in turn, implies that the

ground- and excited-state wave functions are unique functionals of the ground-state density. Therefore, all the properties of the system are entirely determined by the density of the ground state, and the complexity of the many-body problem has been reduced to finding the density of the ground state with 3 instead of $3N$ spatial degrees of freedom. Furthermore, Hohenberg and Kohn showed:

► **Theorem 2.2 (Hohenberg-Kohn Theorem 2 [HK64]).** There exists a universal functional of the density $F[n(\mathbf{r})]$, independent of $v_{\text{ext}}(\mathbf{r})$, such that the expression $E[n(\mathbf{r})] \equiv \int v_{\text{ext}}(\mathbf{r})n(\mathbf{r}) d^3r + F[n(\mathbf{r})]$ has as its minimum value the correct ground-state energy associated with $v_{\text{ext}}(\mathbf{r})$. ◀

We note that particular emphasis should be placed on the fact that $F[n(\mathbf{r})]$ is independent of $v_{\text{ext}}(\mathbf{r})$, and therefore is universally applicable to any system of interacting electrons in an external potential. Levy later generalized the second Hohenberg-Kohn Theorem to include degenerate ground states [Lev79]. In the case of a degenerate ground-state density, not all observables are functionals of the ground-state density.

2.4.2 Kohn-Sham Scheme

In 1965, W. Kohn and Lu J. Sham proposed another crucial step towards making the quantum mechanical many-body problem computationally accessible [KS65]. They demonstrated that any system of N interacting electrons could be mapped onto an auxiliary system of N non-interaction electrons in an effective local potential $v_S(\mathbf{r})$ with the same ground state density $n_0(\mathbf{r})$. For the non-interacting systems, the density is given by the sum of one-electron densities

$$n_{KS}(\mathbf{r}) = \sum_{i=1}^N |\psi_i^{KS}(\mathbf{r})|^2, \quad (2.9)$$

where ψ_i^{KS} are the eigenstates of the Kohn-Sham Hamiltonian:

$$\epsilon_i \psi_i^{KS}(\mathbf{r}) = \left(-\frac{1}{2}\nabla^2 + v_S(\mathbf{r})\right) \psi_i^{KS}(\mathbf{r}). \quad (2.10)$$

These eigenstates are called Kohn-Sham orbitals. Given that the ground state densities of the non-interacting and interacting systems are assumed to be equal, the energy functionals also have to be the same. The energy functional of the interacting system is the sum of the kinetic energy of the system (\mathbf{T}) and the potential energy of the electrons due to Coulomb interaction (\mathbf{U}) and the external potential $v_{\text{ext}}(\mathbf{r})$:

$$E[n(\mathbf{r})] = \langle \Psi[n(\mathbf{r})] | \mathbf{T} + \mathbf{U} + v_{\text{ext}} | \Psi[n(\mathbf{r})] \rangle$$

$$= T[n(\mathbf{r})] + U[n(\mathbf{r})] + \int v_{\text{ext}}(\mathbf{r})n(\mathbf{r}) d^3r. \quad (2.11)$$

The energy functional of the non-interacting system is the sum of the kinetic energy and the potential energy in the effective potential v_S :

$$E[n(\mathbf{r})] = T_S[n(\mathbf{r})] + \int v_S(\mathbf{r})n(\mathbf{r}) d^3r. \quad (2.12)$$

Equating the two expressions of the energy functional and solving for the effective potential yields

$$v_S(\mathbf{r}) = v_{\text{ext}}(\mathbf{r}) + \frac{\delta}{\delta n} \left(T[n(\mathbf{r})] - T_S[n(\mathbf{r})] + U[n(\mathbf{r})] \right). \quad (2.13)$$

It is important to note that the second term in Equation (2.13) is the difference in the universal part F of the two energy functionals (Theorem 2.2) and, therefore, universal itself. This universal part is commonly rewritten in terms of the Hartree potential v_H and the exchange-correlation potential v_{XC} :

$$v_S(\mathbf{r}) = v_{\text{ext}}(\mathbf{r}) + \underbrace{\frac{\delta E_H[n(\mathbf{r})]}{\delta n}}_{v_H(\mathbf{r})} + \underbrace{\frac{\delta E_{XC}[n(\mathbf{r})]}{\delta n}}_{v_{XC}(\mathbf{r})} \quad (2.14)$$

$$E_H[n(\mathbf{r})] = \frac{1}{2} \iint \frac{n(\mathbf{r})n(\mathbf{r}')}{|\mathbf{r} - \mathbf{r}'|} d^3\mathbf{r} d^3\mathbf{r}' \quad (2.15)$$

$$v_H[n(\mathbf{r})] = \int \frac{n(\mathbf{r}')}{|\mathbf{r} - \mathbf{r}'|} d^3\mathbf{r}' \quad (2.16)$$

$$E_{XC} = T[n(\mathbf{r})] - T_S[n(\mathbf{r})] + U[n(\mathbf{r})] - E_H[n(\mathbf{r})], \quad (2.17)$$

where E_H is the Hartree energy, the potential energy due to the electrostatic interaction of the charge density with itself, and E_{XC} is the exchange-correlation energy, which combines all remaining terms. The exchange-correlation energy (a) accounts for the exchange and correlation contributions to U , (b) corrects for the artificial self-interaction included in the Hartree energy, and (c) corrects for the error in the kinetic energy made by approximating the exact kinetic energy by T_S .

If the exchange-correlation potential was known, the Kohn-Sham equations (Equations (2.9), (2.10) and (2.14)) could be solved iteratively as in the Hartree-Fock method. The advantage of the Kohn-Sham scheme over the Hartree-Fock method lies in the fact that it is, in principle, an exact method and also includes correlation effects. However, it is necessary to approximate the exchange-correlation potential in practice, as the analytical form is unknown.

While the Kohn-Sham approach is the most common DFT approach, it is possible to avoid calculating the wave function entirely. However, the Kohn-Sham approach has advantages over such orbital-free density functional theory (OF-DFT) approaches [LC05; WW13]: OF-DFT suffers from a lack of an accurate kinetic energy functional and is restricted to local pseudopotentials (Section 2.6), which are less transferable than nonlocal pseudopotentials typically used in orbital-dependent DFT.

2.4.3 Approximating the Exchange-Correlation Energy

Many different approximations have been proposed for the exchange-correlation energy, with varying degrees of complexity, universality, and accuracy. The local density approximation (LDA) and the generalized gradient approximation (GGA) are two of the most widely used approximations for the exchange-correlation energy. The LDA assumes that E_{XC} can be locally approximated by the exchange-correlation energy density $\epsilon_{XC}(n(\mathbf{r}))$ of the uniform electron gas with the same density $n(\mathbf{r})$.

$$E_{XC}^{LDA}[n(\mathbf{r})] = \int n(\mathbf{r})\epsilon_{XC}(n(\mathbf{r})) d^3r \quad (2.18)$$

Despite its simplicity, LDA has been remarkably successful in unraveling many aspects of condensed matter [GJL79]. However, LDA is known to yield an incorrect dispersion of the exchange-correlation potential in long-range limit for neutral atoms [TS66] and metal surfaces [LK71], systematically overestimate binding energies, and, in turn, underestimate bond lengths. GGA includes the local density gradient ($\nabla n(\mathbf{r})$) to improve the shortcomings of LDA.

$$E_{XC}^{GGA}[n(\mathbf{r})] = \int f(n(\mathbf{r}), \nabla n(\mathbf{r})) d^3r \quad (2.19)$$

GGA can be used to describe systems with inhomogeneous electronic densities with greater precision, yielding more accurate estimates of bond lengths. However, GGA overcorrects LDA in this regard, overestimates bond lengths, and, in turn, underestimates binding energies. As a result, GGA predicts nonbonding character in van der Waals (vdW) heterostructures such as graphite. LDA functionals often yield estimates of the bonding energies in some vdW systems, which are closer to experimental values, due to partial compensation of the overestimated bonding and the incorrect long-range dispersion. However, this compensation is not systematic. Furthermore, GGA, like LDA, functionals perform poorly in strongly correlated electron systems.

Many corrections and new functionals have been developed to improve the accuracy of the DFT method further:

- **Van der Waals corrections** aim to describe long-range molecular/surface interactions. These semi-empirical corrections are either applied as additional force fields or included in the exchange-correlation energy. Force-field approaches do not affect the electronic structure and only correct the interatomic forces ad-hoc. The most prominent examples of such vdW corrections are the methods developed by Grimme et al. (DFT-D [Gri+10], DFT-D2 [Gri06], DFT-D3 [Gri+10]) and the method of Tkatchenko and Scheffler (TS) [Gri+10]. A comprehensive review of vdW correction included in the exchange-correlation energy can be found in the work of Silvestrelli and Ambrosetti [SA19].
- **meta-GGA functionals** aim to systematically improve the description of the exchange-correlation energy by including second partial derivatives in addition to the gradient. Meta-GGA functionals achieve high accuracy for atoms, molecules, solids, and surfaces simultaneously [Hao+13]. Notable examples of the meta-GGA functional are the M06-L [ZT06] and TPSS [Tao+03] functionals.
- the **Exact Exchange (EXX)** method [LM83] uses the exact Hartree-Fock exchange energy to correct the underestimation of band gaps and to improve the long-range dispersion behavior [Stä+99]. However, the EXX method over-corrects the error in the exchange-correlation energy made by LDA and is unable to describe molecular bonding [Bec93].
- **hybrid functionals** include only a fraction of the exact exchange potential of the Hartree-Fock method to combine the advantages of the classical DFT functionals (LDA/GGA) and the EXX method:

$$E_{XC}^{\text{hybrid}} = \alpha E_X^{\text{HF}} + (1 - \alpha) E_X^{\text{DFT}} + E_C^{\text{DFT}}$$

PBE0 [Bec96] and B3LYP [Bec93] are two of the most prominent examples of hybrid functionals used today.

- **RPA and PT2 functionals** introduce the effect of unoccupied KS orbitals to the correlation energy calculated from second-order perturbation theory (PT2) [Wan+21], or within the random phase approximation (RPA) [JE07]. These approaches are currently the most advanced method available. RPA correlation energy yields a fully ab initio description of vdW interactions and band gaps with an accuracy comparable to the GW approximation [Hed65; NG04].
- **Double-hybrid functionals** are built on top of hybrid functionals and also include a fraction of PT2 or RPA correlation energies to improve accuracy for specific applications:

$$E_{XC}^{\text{hybrid}} = \alpha E_X^{\text{HF}} + (1 - \alpha) E_X^{\text{DFT}} + \beta E_C^{\text{PT2}} + (1 - \beta) E_C^{\text{DFT}}.$$

- **Range-separated functionals:** Numerical convergence of the RPA method is difficult, and its scaling with system size is high [Bru12]. In order to balance the computational cost accuracy range-separated functional interpolate between classic DFT functionals for short interaction ranges and RPA approach for long-range interactions [Bru12].

The number of functionals is enormous, and highly accurate functionals are available for most systems. However, despite considerable efforts, searching for a universally applicable and accurate approximation of the exact exchange-correlation energy remains an open issue.

2.4.4 Spin-Polarized Density Functional Theory

Thus far, electron spin and magnetism have been neglected. The tendency of a material to display magnetic properties is driven by the competition of exchange and kinetic energies. The parallel alignment of electrons results in lower kinetic and higher exchange energies. In an atom where electrons can be considered localized, kinetic energy is the leading contribution and gives rise to the Hunds rules. In solids, electrons tend to be delocalized, reducing their kinetic energy. As a result, the exchange energy becomes dominant, which gives rise to the nonmagnetic character of most solid-state matter. However, solid-state materials with strong electron localization can display magnetism, e.g., elemental metals Fe, Co, Ni, and Cr, where electrons are localized in the d -subshell, rare-earth metals in the f -subshell, and various alloys containing these metals.

The framework of density functional theory was originally extended to spin-polarized systems by Barth and Hedin [BH72] and Pant and Rajagopal [PR72]. In spin density functional theory, the scalar electronic density $n(\mathbf{r})$ becomes a 2×2 matrix $n^{\sigma\sigma'}(\mathbf{r})$, or equivalently, the magnetization density $\mathbf{m}(\mathbf{r})$ is introduced in addition to the electron density. The connection between these three variables is given by

$$\mathbf{n}^{\sigma\sigma'}(\mathbf{r}) = \frac{1}{2} \left(n(\mathbf{r}) \delta^{\sigma\sigma'} + \sum_{\gamma=x,y,z} m_{\gamma} \sigma_{\gamma}^{\sigma\sigma'} \right) \quad (2.20)$$

where σ_{γ} are the Pauli matrices

$$\sigma_x = \begin{pmatrix} 0 & 1 \\ 1 & 0 \end{pmatrix} \quad \sigma_y = \begin{pmatrix} 0 & -i \\ i & 0 \end{pmatrix} \quad \sigma_z = \begin{pmatrix} 1 & 0 \\ 0 & -1 \end{pmatrix}. \quad (2.21)$$

In the simplest case, all spin moments in a system are collinear, and after rotation of the

system, the charge density and the Hamiltonian become diagonal in spin space.

$$A = \left(\begin{array}{c|c} A^\uparrow & 0 \\ \hline 0 & A^\downarrow \end{array} \right) \quad (2.22)$$

where A^σ is the submatrix of the spin channel σ ($\sigma \in \{\uparrow, \downarrow\}$). The Schrödinger equation decouples into separate equations for the majority (\uparrow) and minority (\downarrow) electrons. In this case, the formalism can be applied to the two spin channels independently. Only the exchange-correlation functional depends on both spin components of the electron density and can give rise to magnetic interactions.

In non-collinear spin systems, electron spins are not aligned along a common axis. In this case, the DFT formalism has to be extended from independent spin channels to spinor wave functions. The case of non-collinear spins is essential for fully relativistic DFT calculations, where SO coupling introduces non-zero terms in the off-diagonal spin block of the Hamiltonian.

$$A = \left(\begin{array}{c|c} A^{\uparrow\uparrow} & A^{\uparrow\downarrow} \\ \hline A^{\downarrow\uparrow} & A^{\downarrow\downarrow} \end{array} \right). \quad (2.23)$$

The overlap matrix retains the form in Eq. 2.22.

2.5 Crystals and Reciprocal Space

A crystal is a state of matter in which atoms form a regular pattern, i.e., the atomic positions are periodic in space. The smallest repetitive unit of this structure is the primitive unit cell and may contain an arbitrary number of atoms (at least one). The set of all translations ($\mathbf{T}(\mathbf{R})$) that map a primitive cell to one of its periodic replicas forms a Bravais lattice $\{n_1\mathbf{a}_1 + n_2\mathbf{a}_2 + n_3\mathbf{a}_3 | n_1, n_2, n_3 \in \mathbb{Z}\}$ and encodes the periodicity of the crystal. Vectors \mathbf{a}_i are called lattice vectors. In addition to translational symmetry, a crystal may possess various point-group symmetries (proper and improper rotations). Together with the translations, they form the space group of a crystal, which contains all operations that leave the crystal structure unchanged. All crystals can be classified based on these symmetries and belong to one of the 230 crystallographic space groups.

The importance of crystal symmetries goes far beyond the simple classification of different crystals. The crystal symmetries imply that the electrostatic potential felt by the electrons and, thereby, the Hamiltonian possess the same symmetries. The electronic wave functions in such a periodic Hamiltonian satisfy the Bloch theorem [Blo29].

► **Theorem 2.3 (Bloch theorem).** Let A be a periodic operator, that is, invariant under a set of translations $\mathcal{T} = \{\mathbf{T}(n_1\mathbf{a}_1 + n_2\mathbf{a}_2 + n_3\mathbf{a}_3) | n_1, n_2, n_3 \in \mathbb{Z}\}$, then each eigenfunction Ψ of A can

be chosen so that it satisfies

$$\mathbf{T}(\mathbf{R})\Psi(\mathbf{r}_1, \dots, \mathbf{r}_N) = \Psi(\mathbf{r}_1 + \mathbf{R}, \dots, \mathbf{r}_N + \mathbf{R}) = e^{i\mathbf{k}\cdot\mathbf{R}}\Psi(\mathbf{r}_1, \dots, \mathbf{r}_N) \quad (2.24)$$

for all $\mathbf{T}(\mathbf{R}) \in \mathcal{T}$ and some vector \mathbf{k} . ◀

The choice of \mathbf{k} in Bloch's Theorem is not unique. There exist an infinite number of equivalent vectors that are related to each other by the reciprocal lattice. The reciprocal lattice is spanned by three vectors \mathbf{b}_i that satisfy $\mathbf{a}_i \cdot \mathbf{b}_j = 2\pi\delta_{ij}$. If \mathbf{K} is a reciprocal lattice vector, then $e^{i(\mathbf{k}+\mathbf{K})\cdot\mathbf{R}} = e^{i\mathbf{k}\cdot\mathbf{R}}$. Therefore, the vector \mathbf{k} can always be chosen to lie in the primitive cell of the reciprocal lattice, the first Brillouin zone (BZ).

The Bloch Theorem also applies to the Kohn-Sham states because the effective potential v_S inherits the crystal symmetries from the interacting electron system. Therefore, the Kohn-Sham states $\psi_{i\mathbf{k}}^{KS}$, which are one-electron wave functions, can be decomposed into a lattice periodic part $u_{i\mathbf{k}}$ and a phase.

$$\psi_{i\mathbf{k}}^{KS}(\mathbf{r}) = e^{i\mathbf{k}\mathbf{r}}u_{i\mathbf{k}}(\mathbf{r}). \quad (2.25)$$

Equation (2.10) can be rewritten in terms of the lattice periodic part:

$$\begin{aligned} \epsilon_i(\mathbf{k})u_{i\mathbf{k}}(\mathbf{r}) &= e^{-i\mathbf{k}\mathbf{r}}\mathbf{h}^{KS}(\mathbf{r})e^{i\mathbf{k}\mathbf{r}}u_{i\mathbf{k}}(\mathbf{r}) \\ &= \mathbf{h}_{\mathbf{k}}^{KS}u_{i\mathbf{k}}(\mathbf{r}) \\ &= \left(-\frac{1}{2}(\nabla + i\mathbf{k})^2 + v_S(\mathbf{r})\right)u_{i\mathbf{k}}(\mathbf{r}) \end{aligned} \quad (2.26)$$

Therein lies another key concept used in DFT codes: instead of having to solve the Kohn-Sham equations for an infinite system, it is possible to solve the Kohn-Sham equation within the primitive unit cell of the crystal for any \mathbf{k} . Diagonalization $\mathbf{H}(\mathbf{k})$ yields distinct eigenstates $\psi_{i\mathbf{k}}(\mathbf{r})$ which are a subset of all Kohn-Sham states of the infinite solid. The associated eigenenergies $\epsilon_i(\mathbf{k})$ are known as the crystal band structure. All eigenstates of the infinite solid are recovered in the limit of infinitely dense sampling of \mathbf{k} . Of course, no implementation can achieve an infinite sampling density, but the charge density $n(\mathbf{r}) = \int d\mathbf{k} \sum_i |\psi_{i\mathbf{k}}(\mathbf{r})|^2$ can be approximated with arbitrary accuracy by numerical integration of the first Brillouin zone.

2.6 Pseudopotentials

While some (all-electron) codes directly solve the DFT problem using the techniques discussed here, it is useful to employ pseudopotentials to reduce computational costs further. Pseudopotentials are effective potentials that describe the effect of the nucleus and core electrons felt

by the valence electrons. The idea behind the pseudopotential approximation is that a set of electrons (the core electrons) is closely bound to the nucleus and insensitive to the environment of the atom. Thus, the core electrons act merely as an effective screening of the nuclei potential, and the number of electrons considered in the Kohn-Sham scheme is reduced to the "interacting" valence electrons. The computational benefit of this approach is most significant for heavier atoms with many closed shells, but even for light atoms, it is beneficial because the many computational methods scale cubically with the number of electrons. However, in recent years it has become evident that some material properties cannot be correctly predicted if all closed-shell electrons are treated as core electrons [Zan+07]. Careful consideration of the valence configuration for any pseudopotential is essential to balance accuracy and computational complexity.

Besides reducing the number of electrons, pseudopotentials can help alleviate another computational challenge: The exact solutions to the Kohn-Sham equations for the isolated atom oscillate close to the nucleus, where the wave functions have to be orthogonal to the wave functions of the core electrons. Thus very dense grids are required to represent the wave functions in the core region accurately. By including the effect of the core electrons in the pseudopotential, this orthogonality constraint can be overcome. The atomic potential in the core region can be modified to smooth wave functions for the valence electrons, thereby reducing sampling issues.

Hamann et al. [HSC79] proposed a set of conditions that pseudopotentials should satisfy to improve their transferability:

1. The eigenvalues of all valence electrons are the same for the exact potential and pseudopotential.
2. Outside a chosen core radius (r_c), all valence electrons wave functions are the same for the exact potential and pseudopotential
3. For $r > r_c$ the norm $\int_0^r |\phi(r')|^2 dr'$ of any valence electron wave functions is the same for the exact potential and pseudopotential
4. For $r > r_c$ the logarithmic derivatives $\partial/\partial r_i (\ln \phi(\mathbf{r}))$ of the valence electron wave functions and their first energy derivatives $\partial/\partial \epsilon \partial/\partial r_i (\ln \phi(\mathbf{r}))$ are the same for the exact potential and pseudopotential.

Pseudopotentials that fulfill these conditions are called "norm-conserving." Conditions 1 to 3 ensure that the electrostatic potential of the atom is correctly reproduced outside the core radius, and condition 4 aims to reproduce the scattering properties of the potential well [HSC79].

A balance needs to be struck between accuracy, transferability, and computational cost, which is determined by the smoothness of the potential and the number of valence electrons.

In the simplest form, a pseudopotential can be represented by a local function [HJ78], which must follow $\frac{Z-n_{\text{core}}}{|\mathbf{r}|}$ in the long-range limit. However, the number of degrees of freedom in the local form is limited; for example, condition four can generally not be satisfied in the local form because the derivatives explicitly depend on the angular quantum number l of a given orbital. This shortcoming naturally leads to the formulation of non-local pseudopotentials.

$$V^{PS}(|\mathbf{r}|) = V_{\text{local}}(|\mathbf{r}|) + \sum_{lm} \alpha_l(|\mathbf{r}|) |Y_{l,m}\rangle\langle Y_{l,m}| \quad (2.27)$$

where $|Y_{l,m}\rangle\langle Y_{l,m}|$ are the projectors on the spherical harmonics and α_l are non-local terms (depending on the angular momentum).

2.7 Basis Set Expansions of the Kohn-Sham States

To finally solve the many-body problem, many implementations expand the lattice periodic part of Kohn-Sham orbitals in terms of a set of basis functions ϕ_n .

$$\psi_{i\mathbf{k}}^{KS}(\mathbf{r}) = e^{i\mathbf{k}\cdot\mathbf{r}} \sum_n c_{i\mathbf{k}}^n \phi_n(\mathbf{r}) \quad (2.28)$$

Given that $u_{i\mathbf{k}}$ is periodic by construction, plane waves are a natural choice for the basis expansion in crystals:

$$\psi_{i\mathbf{k}}^{KS}(\mathbf{r}) = e^{i\mathbf{k}\cdot\mathbf{r}} \sum_{\mathbf{K}} c_{i,\mathbf{k}}(\mathbf{K}) e^{i\mathbf{k}\cdot\mathbf{K}}, \quad (2.29)$$

where the sum runs over all reciprocal lattice vectors \mathbf{K} . In practical implementations, the sum is truncated using an energy cutoff: $|\mathbf{k} + \mathbf{K}|^2/2 < E_{\text{cutoff}}$. In the limit of an infinitely large cutoff, this method is exact for a given exchange-correlation potential; i.e., the numerical accuracy can be systematically improved by increasing the cutoff. Another advantage of this method is the orthonormality of the basis set, which simplifies the eigenvalue problem in Equation (2.26).

While plane waves are a natural choice for periodic solids, they are less suited to describe molecules. Localized basis sets are an alternative commonly used in quantum chemistry to model molecules. They are composed of functions centered around discrete points in space, typically around the position of the nuclei. These basis functions are often expressed as the product of a spherical harmonic $Y_{l,m}$ and a radial part $\phi_{n,l}$, and the Kohn-Sham states take the

form:

$$\begin{aligned}\psi_{i,\mathbf{k}}^{KS}(\mathbf{r}) &= e^{i\mathbf{k}\cdot\mathbf{r}} \sum_{\mathbf{R}\alpha} \sum_{n,l,m} c_{i,\mathbf{k}}^{\alpha,n,l,m} \Phi_{\alpha,n,l,m}(\mathbf{r}-\mathbf{R}) \\ &= e^{i\mathbf{k}\cdot\mathbf{r}} \sum_{\mathbf{R}\alpha} \sum_{n,l,m} c_{i,\mathbf{k}}^{\alpha,n,l,m} \phi_{n,l}(|\mathbf{r}-\mathbf{R}_\alpha|-\mathbf{R}) Y_{l,m}(\theta, \phi),\end{aligned}\quad (2.30)$$

where α runs over all atoms in the unit cell and \mathbf{R} over all lattice vectors. The most common localized basis set include Slater-type orbitals [Sla30a] ($\phi_{n,l} \sim r^l e^{-\alpha r}$), Gaussian-type orbitals [Boy50] ($\phi_{n,l}(r) \sim r^l e^{-\alpha r^2}$), and numerical atomic orbitals [AE73]. Unlike Gaussian and Slater-type orbitals, numerical atomic orbitals have no closed analytical form. Instead, they are defined as numerical solutions to the Schrödinger equation for electrons in the (pseudo)potential of the isolated atom.

Localized basis sets are typically non-orthogonal, which turns Equation (2.26) into a generalized eigenvalue problem, whose complexity is higher than the simple eigenvalue problem obtained for plane waves.

$$\sum_{\alpha,n,l,m} H_{\beta,n',l',m';\alpha,n,l,m}(\mathbf{k}) c_{i,\mathbf{k}}^{\alpha,n,l,m} = \epsilon_{i\mathbf{k}} \sum_{\alpha,n,l,m} S_{\beta,n',l',m';\alpha,n,l,m}(\mathbf{k}) c_{i,\mathbf{k}}^{\alpha,n,l,m} \quad (2.31)$$

$$S_{\beta,n',l',m';\alpha,n,l,m}(\mathbf{k}) = \sum_{\mathbf{R}} \langle \Phi_{\beta,n',l',m'}(\mathbf{r}) | \Phi_{\alpha,n,l,m}(\mathbf{r}-\mathbf{R}) \rangle \quad (2.32)$$

$$H_{\beta,n',l',m';\alpha,n,l,m}(\mathbf{k}) = \sum_{\mathbf{R}} \langle \Phi_{\beta,n',l',m'}(\mathbf{r}) | \mathbf{h}_{\mathbf{k}}^{KS} | \Phi_{\alpha,n,l,m}(\mathbf{r}-\mathbf{R}) \rangle \quad (2.33)$$

The atomic character of the basis orbital results in a much better approximation of the ground state of molecules and solids than plane-wave basis sets with the same number of basis functions. The electron configuration of an atom defines a natural (primitive) atomic basis set, e.g., the electron configuration of carbon is $1s^2 2s^2 2p^2$. Disregarding the core-electrons ($n=1$), which may be included in the pseudopotential, the natural basis set includes one $2s$ -orbital ($n=2, l=0$) and three $2p$ -orbitals ($n=2, l=1$). This primitive basis is also referred to as a single- ζ basis set. However, the accuracy achieved with single- ζ basis sets is often not sufficiently high. It is, therefore, necessary to increase the variational degrees of freedom and obtain even better approximations of the charge density by including new basis set orbitals. While plane-wave basis sets can be systematically expanded to any basis set size, expanding a localized basis set is more complicated. Possible ways of increasing a localized basis set while maintaining localization of the basis functions include: adding additional basis functions with modified radial part (multiple- ζ basis sets), adding orbitals with higher angular or primary quantum numbers (e.g., polarization orbitals), or adding basis functions that are not centered on atoms

(floating or ghost orbitals). Floating or ghost orbitals are particularly useful for improving the description of vacuum regions at surfaces or vacancies that might otherwise be poorly represented by the basis set [Gar+09]. It is often sufficient to place single s -orbitals in these regions. Polarization orbitals and multiple- ζ basis sets aim to improve the variational degrees of freedom in the areas already covered by the original basis.

Localized orbitals become particularly attractive when the primitive cell includes large vacuum regions, for example, when simulating surfaces and low-dimensional nanostructures. At fixed energy cut-off, the number of plane waves scales proportionally to the lattice vectors. Therefore, simulating vacuum regions quickly becomes costly. The number of localized basis sets, on the other hand, is independent of the vacuum region and depends only on the number of atoms. Localized orbitals are also well suited for scaling calculations up to thousands of atoms. The shape of the basis orbitals can be optimized to reproduce high-accuracy plane wave results in a small system using far fewer basis functions. This optimized base set can be used in larger systems where the chemical environment is similar. Furthermore, localized basis sets are an ideal basis set modeling quantum transport (Chapter 3).

2.8 The SIESTA Method

SIESTA (Spanish Initiative for Electronic Simulations with Thousands of Atoms) [Gar+20; Sol+02] is a method and computer program to perform electronic structure calculations and ab initio molecular dynamics simulations of molecules and solids. The characteristic feature of SIESTA is the use of a basis set of strictly-localized numerical atomic orbitals. In addition, SIESTA uses the Kohn-Sham approach and supports the use of various exchange-correlation functionals (LDA, GGA, vdW) and norm-conserving pseudopotentials.

2.8.1 Basis Sets in SIESTA

In SIESTA, the basis functions are restricted to a finite sphere with radius r_c , which can be different for each orbital. At first, a single- ζ basis is constructed by solving the Kohn-Sham eigenvalue problem for the isolated atom with an additional confinement potential $V_{\text{conf.}}$, which is flat in the center of the sphere and diverges at r_c^l .

$$\left[-\frac{1}{2r} \frac{d^2}{dr^2} r + \frac{l(l+1)}{2r^2} + V_l^{PP}(r) + V_{\text{conf.}} \right] \phi_l^{1\zeta}(r) = (\epsilon_l + \delta\epsilon_l) \phi_l^{1\zeta}(r) \quad (2.34)$$

$$\phi_l^{1\zeta}(r_c^l) = 0 \quad (2.35)$$

Using a hard-well potential to confine the wave functions leads to discontinuous derivatives at r_c^l [SN89]. Smoother potentials, such as

$$V_{\text{conf.}}(r) = V_0 \frac{\exp\left(-\frac{r_c - r_i}{r - r_i}\right)}{r_c - r}, \quad (2.36)$$

ensure continuous derivatives and reduce problems in calculating forces and stresses [Jun+01]. The added confinement potential leads to an energy shift $\delta\epsilon_l$ in the eigenstates of the free atom concerning the true eigenvalues ϵ_l . Rather than fixing the same confinement radius for each orbital, it is often beneficial to choose a common energy shift is often beneficial.

The single- ζ basis set can then be extended to a double- ζ basis set using different methods. The default method in SIESTA is called the split-valence method: for each orbital $\phi^{1\zeta}(r)$ a modified orbital

$$\phi_l^{2\eta}(r) = \begin{cases} r^l(a_l - b_l r^2) & r \leq r_s^l \\ \phi_l^{1\zeta}(r) & r \geq r_s^l \end{cases}, \quad (2.37)$$

is defined. The split radius r_s^l is optimized so that the norm of $\int_0^{r_s^l} \phi_l^{1\zeta}(r) dr$ corresponds to a specific value (typically 0.15), and a_l and b_l are chosen so that $\phi_l^{2\eta}$ and its first derivative are continuous. The new basis orbital is then given by $\phi_l^{2\zeta}(r) = \phi_l^{1\zeta}(r) - \phi_l^{2\eta}(r)$. This procedure can be repeated with smaller split norms to create a multiple- ζ basis set.

In molecules or solids, the bond formation introduces a deformation of the orbitals. To model this deformation, polarization orbitals can be added to a multiple- ζ basis set to model this deformation. Polarization orbitals are obtained by solving the eigenvalue problem of an isolated atom in a small, uniform electric field. In first-order perturbation theory, selection rules imply that perturbed or polarized orbitals have two components with quantum numbers of angular momentum $l' = l \pm 1, m' = m$. Since orbitals with $l - 1$ are most commonly already included in the basis, only the projection on $l + 1$ needs to be considered and can be added as a new orbital.

The choice of these basis orbitals separates the SIESTA method from other DFT approaches. The atom-like character of the basis orbitals often means that the number of basis functions required is smaller compared to other methods [Ang+02; Art+99; Jun+01]. In addition, strict localization of the orbitals leads to sparse matrices, and sparse methods can be exploited for efficiency.

2.8.2 Electron spin in SIESTA

SIESTA supports four possible spin configurations: unpolarized, polarized, non-collinear, and spin-orbit [CC12]. Unpolarized spin calculations do not consider spin degrees of freedom.

Spin-polarized calculations consider two collinear spin channels for which the Schrödinger equation decouples. However, spins in condensed matter are not always collinear. For example, the ground state of γ -Fe is characterized by a helical spin density wave [SN02], and exchange-frustration in spin glasses or molecular magnets leads to canting of magnetic moments [Yam+00; Yam+01; ZKN17]. In these materials, the Schrödinger equation does not decouple, and it has to be solved using spinor wave functions. Non-collinear and spin-orbit calculations use the spinor wave function to solve the Schrödinger equation for coupled spin channels. Spin-orbit calculations differ from non-collinear calculations in two aspects: (1) They use a fully relativistic Hamiltonian, which includes SO interactions in addition to the Darwin and velocity correction terms. (2) They impose different symmetries on the Hamiltonian or the density matrix: no symmetries in the spin-orbit case and spin box hermiticity ($A^{\sigma,\sigma'} = (A^{\sigma',\sigma})^*$) in the non-collinear case [CC12].

In pursuit of increasing computing power, memory and transistor densities in electronic devices are continuously growing and have already reached the classical-to-quantum crossover point. Therefore, modeling quantum electronic transport is a crucial issue. The quantum mechanical transport problem generally requires descriptions of infinite, nonperiodic structures under non-equilibrium conditions. Ground-state electronic structure methods cannot be applied under these circumstances, and special techniques are required. This chapter introduces the quantum-mechanical transport problem and describes how it can be solved from the first principles of quantum mechanics.

3.1 Introduction: The Transport Problem

Ohm's law describes usual macroscopic electron transport: the current (I) through a wire is proportional to the bias (V_B) applied to it, and the conductance $G = I/V$ is proportional to the cross-section (A), and inversely proportional to the length (L) of a wire.

$$G = \sigma \frac{A}{L}. \quad (3.1)$$

The conductivity σ is an intrinsic material property, i.e., σ is independent of the geometry and dimensions of the wire. However, as electronic devices are scaled to smaller sizes, they enter into a regime where ohmic behavior breaks down, and quantum phenomena become significant. Today's electronic devices are already at the precipice of this limit [Pow08]. To further scale up the computation power at our disposal, every component of our electronic devices needs to be scaled down in size even further. Thus, quantum effects are becoming increasingly more pronounced in electronic devices, and it is essential to develop an understanding of electron transport based on the first principles of quantum mechanics [Dat95].

The simplest case of a quantum transport system is depicted in Figure 3.1 (a): a one-dimensional structure consisting of a device that is connected to two reservoirs by two electrodes (left and right). To describe these systems, an explicit quantum mechanical description of the reservoir is typically neglected because the electrodes tend to be much longer than the coherence length. For this reason, the reservoir is neglected, and electrodes are treated as semi-infinite and effectively act as reservoirs Figure 3.1 (b).

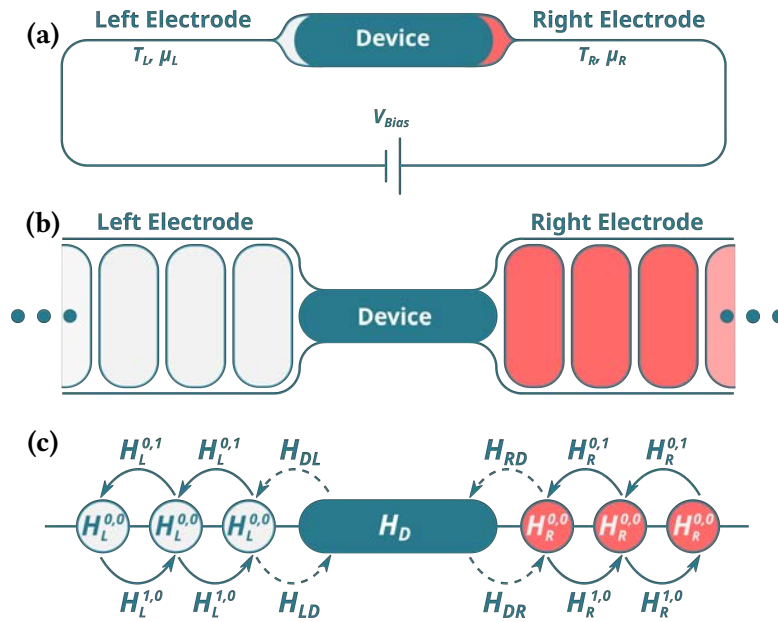


Figure 3.1: Schematic of the quantum mechanical transport problem in one dimension. **(a)** A device connected by two electrodes (left and right) to a battery or two different reservoirs. **(b)** Abstraction of transport setup consisting of the devices and two semi-infinite periodic electrodes. **(c)** Decomposition of the Hamiltonian of the abstracted transport setup. H_D contains all interactions within the device region. H_{LD} and H_{DR} account for the contact between the devices and the electrodes. $H_L^{0,0}$, $H_L^{0,1}$ and $H_L^{1,0}$ describe the interaction within and between the principal layers of the electrodes.

The DFT methods discussed thus far are based on Bloch's theorem and are, therefore, limited to periodic or finite systems and cannot be applied to such a transport setup. Moreover, when modeling electronic transport, it is important to consider non-equilibrium conditions, i.e., different chemical potentials in the two electrodes that make current flow. Under non-equilibrium conditions, the usual relation between eigenenergies and occupations does not hold, and special techniques are required to determine the charge density and other observables.

To solve the transport problem at the atomistic level, it is assumed that the electrodes are screened from the device region; i.e., the presence of the device does not perturb the electronic structure of the electrode. To achieve sufficient screening, it is generally required to include parts of the electrodes inside the device region. Furthermore, the electrodes should be metallic because the low charge carrier density in semiconductors gives rise to macroscopic electrostatic screening lengths. Therefore, modeling semiconductor devices exceeds the scope of atomistic frameworks.

The Hamiltonian \mathcal{H}^2 for such a system can be easily constructed using a basis of strictly localized orbitals (Figure 3.1 (c))

$$\mathcal{H} = \begin{pmatrix} \ddots & \ddots & \ddots & \ddots & \ddots & \ddots & \\ \ddots & H_L^{0,0} & H_L^{0,1} & 0 & 0 & 0 & \ddots \\ \ddots & H_L^{1,0} & H_L^{0,0} & H_{DL} & 0 & 0 & \ddots \\ \ddots & 0 & H_{LD} & H_D & H_{DR} & 0 & \ddots \\ \ddots & 0 & 0 & H_{RD} & H_R^{0,0} & H_R^{0,1} & \ddots \\ \ddots & 0 & 0 & 0 & H_R^{1,0} & H_R^{0,0} & \ddots \\ \ddots & \ddots & \ddots & \ddots & \ddots & \ddots & \ddots \end{pmatrix} \quad (3.2)$$

Here, the electrodes are partitioned into principal layers, interacting only with one previous section and one following section. Starting from a tight-binding or SIESTA Hamiltonian, the principal layers can always be constructed by increasing the size of the primitive cell until the largest interaction range is shorter than the unit cell length. $H_L^{0,0}$, $H_R^{0,0}$ are the Hamiltonian matrices of the principal layers of the left and right electrodes, and H_D the Hamiltonian of the device region. $H_{L/R}^{0,1}$ and $H_{L/R}^{1,0}$ describe the hopping between the principal layers, and $H_{DL/DL}$ and $H_{DR/RD}$ the contact between the electrodes and the device region. If the electrodes are sufficiently screened, the interaction at the contact is limited to the first principal layer.

This chapter reviews two approaches for solving the transport problem described by such a Hamiltonian: the Landauer-Büttiker formalism and the non-equilibrium Green's function (NEGF) formalism [Dat95]. Furthermore, the combination of the DFT method (introduced in Chapter 2) and the NEGF formalism is introduced as a first-principles transport method, and the implementation of this method in TRANSIESTA [Bra+02; Pap+17] is discussed.

A complete review of electronic quantum transport and scattering theory can be found, for example, in Datta's "Electronic Transport in Mesoscopic Systems" [Dat95], or Sakurai and Napolitano's "Modern Quantum Mechanics" [SN21].

3.2 Landauer-Büttiker Formalism

The Landauer-Büttiker formalism, first conceived by Landauer [Lan57; Lan70] and later generalized to multielectrode systems by Büttiker [Büt+85], is one of the most influential frameworks for modeling quantum transport. Its view of the transport problem is simple yet effective: The device region is a scattering potential through which electrons must pass to conduct currents.

² The usage of calligraphic symbols indicates infinite matrices.

The transmission and reflection probabilities associated with pairs of incoming and outgoing wave functions determine the transport properties.

When an incoming wave function from one lead scatters in the potential of the device, the resulting scattering wave function is a superposition of the incoming, outgoing, and reflected parts. Inside the left and right leads, the wave function components asymptotically approach Bloch waves. For an incoming wave from the left electrode, the scattering wave function satisfies

$$\Psi_{scatter}(z) = \begin{cases} u_{vk}^L(z)e^{ikz} + \int dk' \sum_j r_{vk,\mu k'}^L u_{\mu k'}^L(z)e^{-ik'z} & z \rightarrow -\infty \\ \int dk' \sum_j t_{vk,jk'}^{LR} u_{\mu k'}^R(z)e^{ik'z} & z \rightarrow \infty \end{cases}, \quad (3.3)$$

where u is the normalized lattice-periodic parts of the Bloch waves. $|t_{ik,jk'}^{LR}|^2$ is the probability that the i -th eigenstate of the left lead with lattice momentum k is transmitted into the j -th state of the right lead with momentum k' , and $|r_{ik,jk'}^L|^2$ the reflection probability for the same state. Momentum conservation implies that t and r are zero unless $k = k'$. Section 3.3 demonstrates how the scattering matrix can be calculated using Green's function techniques. Finally, the transmission function between the left and right electrodes is given by integrating over the Brillouin zone the sum over all eigenstates of the left and right electrodes with fixed energy:

$$T_{LR}(\epsilon) = \iint dk dk' \sum_{ij} |t_{ik,jk'}^{LR}|^2. \quad (3.4)$$

However, not all states will participate in electronic transport. For a state to contribute to the current flowing through a system, the state has to be (a) occupied on the left-hand side and (b) unoccupied on the right-hand side. The Landauer-Büttiker formalism relates these probabilities and occupations to the current flowing from the left to the right electrode:

$$I_{LR} = \frac{1}{\pi} \int d\epsilon T_{LR}(\epsilon)(f_L(\epsilon) - f_R(\epsilon)). \quad (3.5)$$

After the original formulation by Landauer, Büttiker generalized this approach to multi-electrode systems (Figure 3.2). The currents between any pair of electrodes are expressed in the same form as in the two-terminal device. The sum over all pairs of current originating in α gives the total current through a lead α .

$$I_{\alpha,\beta} = \frac{1}{\pi} \int d\epsilon T_{\alpha,\beta}(\epsilon)f_{\alpha}(\epsilon) - T_{\beta,\alpha}(\epsilon)f_{\beta}(\epsilon) \quad (3.6)$$

$$I_{\alpha} = \sum_{\beta} I_{\alpha,\beta} \quad (3.7)$$

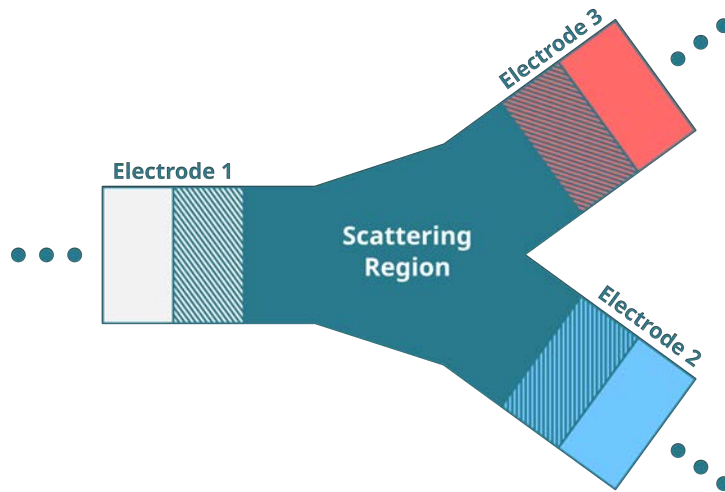


Figure 3.2: Sketch of a setup for 3-electrode transport simulation. The three electrodes are depicted in three different colors (grey, blue, and red). These electrodes extend infinitely in the direction indicated by the dots. The striped regions denote the electrode screening regions, which are used to screen the perturbation of the scattering region. Screening is required to ensure an effective potential similar to the bulk potential of the electrodes at the edge of the scattering region.

An alternative derivation of the Landauer formula that avoids scattering states and gives a more intuitive explanation of its origin can be found in "Introduction to Graphene-Based Nanomaterials" by L.E.F. Foa Torres, S. Roche, and J.-C. Charlier [FRC20].

3.3 Non-Equilibrium Green's Function Formalism

3.3.1 Green's Function Transport

The equilibrium Green's function formalism offers an approach to calculating the charge density of a generic transport system (Figure 3.2) and determining its transmission probabilities using Green's function techniques. In the Green's function formalism, the degrees of freedom of the electrodes are eliminated, and the infinite Hamiltonian of the open system is mapped onto a finite non-hermitian Hamiltonian, which includes the effect of full electrodes as self-energies. Eliminating the electrodes' degrees of freedom is possible because the electrodes are assumed to be bulk-like, i.e., their electronic structure can be determined independently from the presence of the scattering device.

Before considering its extension to multi-terminal devices, it is instructive first to understand how the Green's function formalism works in the two-electrode case. In the Green's function formalism, the transport problem defined by the Hamiltonian \mathcal{H} in Equation (3.2) is rewritten

in terms of the retarded Green's function \mathcal{G}^R .

$$(\epsilon^+ \mathcal{S} - \mathcal{H}) \mathcal{G}^R(\epsilon) = \mathbb{1}, \quad (3.8)$$

where ϵ^+ denotes $\lim_{x \rightarrow 0^+} (\epsilon + i)$. Equation (3.8) can be rewritten in block matrix form:

$$\begin{pmatrix} \epsilon^+ \mathcal{S}_L - \mathcal{H}_L & \epsilon^+ \mathcal{S}_{LD} - \mathcal{H}_{LD} & 0 \\ \epsilon^+ \mathcal{S}_{DL} - \mathcal{H}_{CL} & \epsilon^+ \mathcal{S}_D - \mathbf{H}_D & \epsilon^+ \mathcal{S}_{DR} - \mathcal{H}_{DR} \\ 0 & \epsilon^+ \mathcal{S}_{RD} - \mathcal{H}_{RD} & \epsilon^+ \mathcal{S}_R - \mathcal{H}_R \end{pmatrix} \begin{pmatrix} \mathcal{G}_L & \mathcal{G}_{LD} & \mathcal{G}_{LR} \\ \mathcal{G}_{DL} & \mathbf{G}_D & \mathcal{G}_{DR} \\ \mathcal{G}_{RL} & \mathcal{G}_{RD} & \mathcal{G}_R \end{pmatrix} = \mathbb{1}, \quad (3.9)$$

where the superscript R for the retarded Green's function has been removed. In contrast to the Hamiltonian and the overlap matrix, the blocks \mathcal{G}_{LR} and \mathcal{G}_{RL} of the Green's function do not vanish. They describe the scattering between the two electrodes.

The Green's function formalism approach maps this infinite Hamiltonian onto a finite, effective Hamiltonian

$$\mathbf{H}_{\text{eff}} = \begin{pmatrix} \mathbf{H}_L + \Sigma_L & \mathbf{H}_{LD} & 0 \\ \mathbf{H}_{DL} & \mathbf{H}_D & \mathbf{H}_{DR} \\ 0 & \mathbf{H}_{RD} & \mathbf{H}_R + \Sigma_R \end{pmatrix}, \quad (3.10)$$

which includes the effective interaction with electrodes in the form of surface self-energies. No method is described here to calculate surface self-energies, but various approaches can be found in the works of Allen [All79a; All79b], Chang and Schulman [CS82], Dy et al. [DWS79], Galperin et al. [GTN02], Lee and Joannopoulos [LJ81], Sancho et al. [SSR85], Tomfohr and Sankey [TS02], Umerski [Ume97], and Wu et al. [WCJ94].

The Green's function matrix \mathbf{G} for this effective Hamiltonian can be easily calculated by inversion.³

$$\mathbf{G}(z) = \left(z\mathbf{S} - \mathbf{H} - \Sigma_L(z) - \Sigma_R(z) \right)^{-1} \quad z \in \mathbb{C} \quad (3.11)$$

Finally, the generalized Fisher-Lee relations [Dat95; FL81] or Lippman-Schwinger equation [LS50] can be applied to find the scattering matrix.

$$\mathbf{s}(z) = i\Gamma_L^{1/2}(z)\mathbf{G}(z)\Gamma_R^{1/2}(z), \quad (3.12)$$

³ The subscript D for the device region has been dropped.

which is directly related to the transmission function,

$$T(\epsilon) = \text{Tr}\{\mathbf{s}(\epsilon^+)^\dagger \mathbf{s}(\epsilon^+)\} = \text{Tr}\{\Gamma_L(\epsilon^+) \mathbf{G}(\epsilon^+) \Gamma_R \mathbf{G}^\dagger(\epsilon^+)\}, \quad (3.13)$$

where $\Gamma_{L/R}$ are the broadening matrices of the leads

$$\Gamma_\alpha(z) = i[\Sigma_\alpha(z) - \Sigma_\alpha^\dagger(z)]. \quad (3.14)$$

The Green's function approach to calculating the transmission function can be extended to two- and three-dimensional transport devices. In these cases, it is important to consider reciprocal space sampling, and the procedure described above has to be applied independently for each point in reciprocal space. Finally, the transmission function is obtained by BZ integration:

$$T(\epsilon) = \int_{BZ} d\mathbf{k} \text{Tr}\{\Gamma_{L,\mathbf{k}}(\epsilon^+) \mathbf{G}_{\mathbf{k}}^\dagger(\epsilon^+) \Gamma_{R,\mathbf{k}}(\epsilon^+) \mathbf{G}_{\mathbf{k}}(\epsilon^+)\} \quad (3.15)$$

Similar to the Landauer-Büttiker formalism, the Green's function approach formalism can be applied to devices with an arbitrary number of leads by adding the surface self-energies for each electrode separately.

$$\mathbf{G}_{\mathbf{k}}(z) = \left(z\mathbf{S}_{\mathbf{k}} - \mathbf{H}_{\mathbf{k}} - \sum_{\mathbf{e}} \Sigma_{\mathbf{e},\mathbf{k}}(z) \right)^{-1}. \quad (3.16)$$

The scattering matrix and transmission function for any pair of electrodes \mathbf{e} and \mathbf{e}' are given by

$$\mathbf{s}_{\mathbf{e},\mathbf{e}',\mathbf{k}}(z) = \Gamma_{\mathbf{e},\mathbf{k}}^{1/2}(z) \mathbf{G}_{\mathbf{k}}(z) \Gamma_{\mathbf{e}',\mathbf{k}}^{1/2}(z) \quad (3.17)$$

$$T_{\mathbf{e},\mathbf{e}'}(\epsilon) = \int_{BZ} d\mathbf{k} \text{Tr}\{\mathbf{s}_{\mathbf{e},\mathbf{e}',\mathbf{k}}(\epsilon^+)^\dagger \mathbf{s}_{\mathbf{e},\mathbf{e}',\mathbf{k}}(\epsilon^+)\} \quad (3.18)$$

3.3.2 The DFT+NEGF Method

The techniques discussed above describe quantum transport through open quantum systems. The missing ingredient for a first-principle description of quantum transport is the Hamiltonian of the transport setup. The calculation of the electrode Hamiltonian is straightforward within the DFT framework because it is assumed to be bulk-like. However, the Hamiltonian of the Device and the contact with the electrodes cannot be modeled using DFT. Again, Green's function techniques deliver a solution: the electron density of the open quantum system is

directly related to the lesser Green's function $G_{\mathbf{k}}^<$ [KB62; Kel65]:

$$\rho = \frac{1}{2\pi} \iint_{\text{BZ}} d\mathbf{k} d\epsilon G_{\mathbf{k}}^<(\epsilon) e^{i\mathbf{k}\mathbf{R}}. \quad (3.19)$$

In equilibrium, that is, when the chemical potentials and temperatures of all electrodes are equal, the lesser Green's function is proportional to the imaginary part of the retarded Green's function [Car+72; Kel65]:

$$G_{\mathbf{k}}^<(\epsilon) = -2i \text{Im}\{G_{\mathbf{k}}^R(\epsilon)\} f(\epsilon), \quad (3.20)$$

where $f(\epsilon)$ is the Fermi distribution. Under non-equilibrium conditions, this simple relationship does not hold. Instead, the lesser Green's function can be expressed in terms of the retarded Green's function, and the broadening matrices Γ_{ϵ} [Bra+02; Dat95; HJ96; Roc07]:

$$G_{\mathbf{k}}^<(\epsilon) = \sum_{\epsilon} \mathcal{A}_{\epsilon,\mathbf{k}}(z) f_{\epsilon}(\epsilon) e^{i\mathbf{k}\mathbf{R}} \quad (3.21)$$

$$\mathcal{A}_{\epsilon,\mathbf{k}}(z) = G_{\mathbf{k}}(z) \Gamma_{\epsilon,\mathbf{k}}(z) G_{\mathbf{k}}^{\dagger}(z), \quad (3.22)$$

where $\mathcal{A}_{\epsilon,\mathbf{k}}(z)$ denotes the spectral function of electrode ϵ , respectively. The occupation in the electrode is given by the Fermi distribution (f_{ϵ}) with corresponding chemical potential (μ_{ϵ}) and temperature (T_{ϵ}). Lastly, ρ is the non-equilibrium density matrix of the scattering region.

This allows the NEGF formalism to be combined with the DFT method to find self-consistent solutions for the density matrix. Starting from an initial guess for the density in the scattering region, the Kohn-Sham Hamiltonian in the scattering region is constructed. Using Equation (3.19), the density matrix corresponding to this Hamiltonian is calculated. If the initial and final density matrices coincide within a given threshold, the calculation has converged; otherwise, the density matrices are mixed to create a new initial density matrix, and the procedure is repeated until convergence is achieved. A schematic of this procedure is shown in Figure 3.3.

Thus far, the electrodes have been assumed to be in equilibrium. However, the NEGF formalism also holds when the chemical potentials or the temperatures in the electrodes are different. The non-equilibrium electron density and the non-equilibrium Hamiltonian can be predicted from first principles. Using this technique, electronic transport can be modeled beyond the linear approximation of the Landauer-Büttiker formalism.

$$I_{\epsilon,\epsilon'} = \frac{1}{2\pi} \int d\epsilon \left[f_{\epsilon}(\epsilon) - f'_{\epsilon}(\epsilon) \right] T_{\epsilon,\epsilon'}(\epsilon), \quad (3.23)$$

where $T_{\epsilon,\epsilon'}$ is implicitly dependent on the chemical potential and temperature of all electrodes.

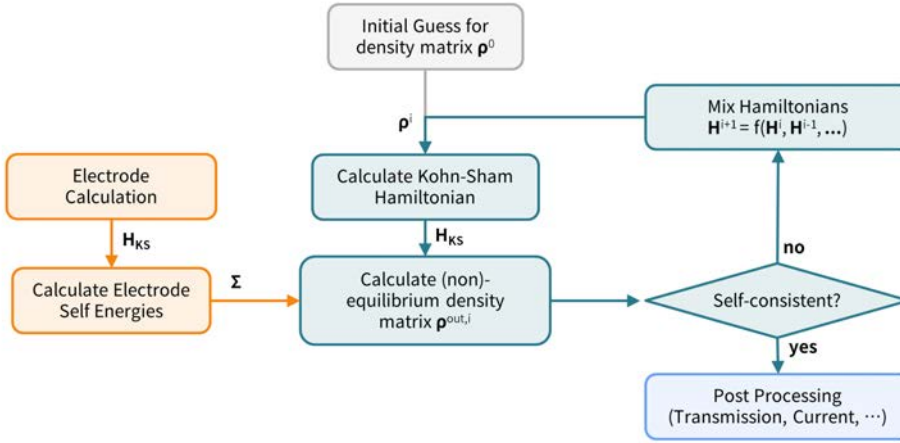


Figure 3.3: Schematic of the DFT+NEGF. The central self-consistent cycle is shown in dark green. The initial guess for the density matrix (grey) and the electrode self-energy (orange) is only calculated once. After self-consistency is achieved, the converged density matrix and Hamiltonian can be post-processed to extract the transmission functions, current or other quantities of the open system.

The DFT+NEGF approach [Bra+02; Roc07; TGW01b] has been implemented in a large number of codes: GECM [Pal+02], G-FLEUR [WIB02], SMEAGOL [Roc+05], TURBOMOLE [Woh+07], GDFTB [Pec+08], OPENMX [ONK10], GPAW [CTJ12], GOLLUM [Fer+14], AITRANSS [Góm21] and has been used successfully in a wide range of systems [CCS99; JI99; TGW01a]. One such implementation is TranSIESTA [Bra+02; Pap+17], which is based on the SIESTA method for simulations of density functional theory. Although there are real-space NEGF formalisms, the SIESTA method is an ideal starting point for the implementation of the DFT+NEGF approach. The strictly localized basis sets used in SIESTA make it easy to define the local Hamiltonians and local Green's functions considered thus far.

3.3.3 Complex Contour Integration

The Green's function in Equation (3.16) is analytical on the whole complex plane except for its poles along the real axis. These poles make the integration over energies in Equation (3.19) numerically challenging. However, the integral can be simplified under equilibrium conditions ($f_{\mathbf{k}}(\epsilon) = f(\epsilon)$ for all \mathbf{k}):

$$\rho = \frac{i}{2\pi} \iint_{\text{BZ}} d\mathbf{k} d\epsilon \left[G_{\mathbf{k}}(z) - G_{\mathbf{k}}^{\dagger}(z) \right] f(\epsilon), \quad (3.24)$$

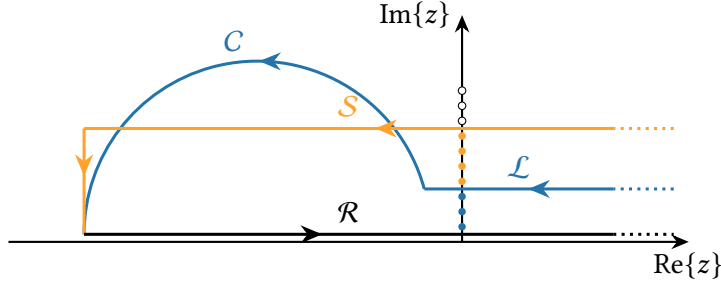


Figure 3.4: Example of two closed, complex contours for the integral in Equation (3.24). The circle contour is composed of three parts: \mathcal{R} parallel the real axis with a small, positive imaginary part, \mathcal{L} parallel the real axis with a large complex part, \mathcal{C} a circular part connecting to \mathcal{L} in the upper-left quadrant of the complex plane and to \mathcal{R} far below the Fermi level. The square contour consists of three straight line segments. Poles of the Fermi function z_ν along the imaginary axis are indicated by dots.

In this form, it becomes clear that the integrand is analytical and that the integral along the real axis can be replaced using the residual theorem.

$$\oint d\epsilon \left[G_{\mathbf{k}}(z) - G_{\mathbf{k}}^\dagger(z) \right] f(\epsilon) = -2\pi i k_B T \sum_{z_\nu} \left[G_{\mathbf{k}}(z_\nu) - G_{\mathbf{k}}^\dagger(z_\nu) \right] \quad (3.25)$$

In the non-equilibrium cases, i.e., when there are differences in the temperatures or chemical potentials of the electrodes, the integrand in Equation (3.19) is generally not analytical. In this case, the residue theorem can only be applied to a part of the integrand. The non-equilibrium integral can be rewritten as

$$\rho = \rho_e^{\text{eq}} + \sum_{e' \neq e} \Delta_{e,e'} \quad (3.26)$$

$$\rho_e^{\text{eq}} = \frac{i}{2\pi} \iint_{\text{BZ}} dk d\epsilon \left[G_{\mathbf{k}}(z) - G_{\mathbf{k}}^\dagger(z) \right] f_e(\epsilon) \quad (3.27)$$

$$\Delta_{e,e'} = \frac{i}{2\pi} \iint_{\text{BZ}} dk d\epsilon \mathcal{A}_{e,\mathbf{k}}(z) \left[f_{e'}(\epsilon) - f_e(\epsilon) \right]. \quad (3.28)$$

In this form, the equilibrium part of the density matrix (Equation (3.27)) can still be calculated using the residual theorem, and the non-equilibrium part (Equation (3.28)) only requires integration along the real axis. The two occupation functions are equal outside the bias window from $\min(\mu_e)$ to $\max(\mu_e)$. Therefore, the integral along the real axis can be limited to this window, which makes this recast form of Equation (3.19) very suitable for numerical integration.

4

Topological Band Theory and the \mathbb{Z}_2 Invariant

4.1 *Introduction: Topology*

Topology is a branch of mathematics concerned with properties of geometric objects that are invariants under smooth deformations. This concept is most easily exemplified in closed two-dimensional surfaces embedded in three-dimensional space: By smoothly deforming a sphere, you can create a variety of shapes, such as a disk or a bowl; by smoothly deforming a doughnut, you can create a tube or a coffee mug. However, the smooth deformation of a sphere never yields a doughnut or vice versa. The sphere and the doughnut can be distinguished by the number of holes in the object (0 for the sphere and 1 for the doughnut). Since integers are discrete and cannot change smoothly, surfaces with different numbers of holes must be topologically distinct. On the other hand, surfaces with the same number of holes can be transformed into one another and are topologically equivalent. This intuitive concept is formalized in the Gauss-Bonnet theorem [Bon48; GSA70], which states that the integral of the Gaussian curvature over a closed smooth surface is an integer multiple of 2π .

In the following sections, we will show how the mathematical concept of topology can be applied to the band structure of semiconductors and address the physical implications of band topology. The discussion will be based on the band theory of solids, which is only valid in the picture of noninteracting electrons, e.g., Kohn-Sham or tight-binding picture. However, in reality, electrons interact, and the concept of a band structure cannot be invoked. It can be shown that the concepts discussed in the following apply to systems of interacting electrons, nevertheless. Such explanations for the applicability of band topology in interacting electron systems can, for example, be found in "Topological Band Theory and the \mathbb{Z}_2 Invariant" by Kane [Kan13] and "Berry Phases in Electronic Structure Theory" by Vanderbilt [Van18].

4.2 **The Berry Phase, the Chern Number, and the Quantum Hall Effect**

The band structure of a solid is defined by the Bloch Hamiltonian $H(\mathbf{k})$ or equivalently the set of eigenvalues $\epsilon_v(\mathbf{k})$ and eigenvectors $|u(\mathbf{k})\rangle$. The set of occupied eigenstates in a gapped system defines a subspace in the Hilbert space of all wave functions. This can be viewed as an

analogy to the closed surface embedded in a higher dimensional space. Topological band theory aims to identify which subspaces are equivalent under smooth deformation of the underlying Hamiltonian.

The central concept in band topology is the Berry phase. It is defined as the integral over a closed loop C in reciprocal space:

$$\gamma_C = \oint_C \mathbf{d}\mathbf{k} \mathbf{A} = -i \oint_C \mathbf{d}\mathbf{k} \langle u(\mathbf{k}) | \nabla_{\mathbf{k}} | u(\mathbf{k}) \rangle, \quad (4.1)$$

where $|u(\mathbf{k})\rangle$ is a Bloch state and $\mathbf{A} = -i\langle u(\mathbf{k}) | \nabla_{\mathbf{k}} | u(\mathbf{k}) \rangle$ is called Berry connection. The Berry phase is the phase difference acquired by the Bloch state along the curve C during a cyclic adiabatic process. Unlike the Berry connection, the Berry phase is invariant under gauge transformation of the Bloch states $|u(\mathbf{k})\rangle \rightarrow e^{i\phi(\mathbf{k})} |u(\mathbf{k})\rangle$. Using Stokes' theorem, the Berry phase can be rewritten as a surface integral

$$\gamma_C = \int_S \mathbf{d}^2\mathbf{k} \mathcal{F}, \quad (4.2)$$

where \mathcal{F} is the Berry curvature

$$\mathcal{F} = \nabla \times \mathbf{A}. \quad (4.3)$$

While the Gaussian curvature describes the change in the tangent space on a surface, the Berry curvature describes the change in the Hilbert space of the occupied states [Kan13; Van18]. Similarly to the Gaussian curvature, the integral of the Berry curvature over a closed two-dimensional space is quantized [Tho+82]:

$$n = \frac{1}{2\pi} \int_{\text{BZ}} \mathbf{d}^2\mathbf{k} \mathcal{F} \quad (4.4)$$

This invariant is called the Chern number or the TKNN invariant. It is directly related to the integer quantum Hall effect [WK78]: in conventional states of matter, the Chern number is zero, and in quantum Hall states, it is nonzero. The Chern number equals the integer n in the observed Hall conductance $G_{xy} = ne^2/h$.

4.3 Bulk-Boundary Correspondence

Gapless edge states emerge at the boundary between the integer quantum Hall state and the vacuum [Hal82]. In contrast to conventional edge states, these edge states are chiral, i.e., they

move only in one direction along the edge. Furthermore, the absence of counter-propagating edge states implies that electrons moving through these states cannot backscatter and are insensitive to disorder. In this way, the chirality of the edge states is the origin of perfectly quantized electronic conductance in the quantum Hall effect. Such chiral edge states are closely related to the bulk quantum Hall state's topology by the bulk-boundary correspondence: while the number of edge states can change during smooth deformation of the Hamiltonian near the surface, the difference between the number of left-handed and right-handed edge states is invariant and always equal to the Chern number [Kan13].

4.4 Time-Reversal Invariance, the \mathbb{Z}_2 Invariant and the Quantum Spin Hall Effect

The quantum Hall conductivity, and therefore the Chern number C , is odd under the operation of time-reversal ($\mathcal{T}C\mathcal{T}^{-1} = -C$). On the other hand, the Chern number of a time-reversal symmetric system has to be time-reversal invariant ($\mathcal{T}C\mathcal{T}^{-1} = C$) like any observable. This implies that the Chern number can only be nonzero if the time-reversal symmetry is broken through an external magnetic field or the magnetic order in the crystal. However, not all time-reversal-symmetric semiconductors are topologically equivalent. The topological invariant distinguishing these states is the \mathbb{Z}_2 invariant.

To understand the origin of the \mathbb{Z}_2 invariant it is essential to recall Kramers' theorem [Kra30], which states that the eigenstates of a time-reversal-symmetric Hamiltonian occur in pairs ($|\phi_i^I\rangle$, $|\phi_i^II\rangle$) with the same eigenenergy. The two states are related to each other by the time reversal

$$|\phi_i^II\rangle = \mathcal{T}|\phi_i^I\rangle.$$

These pairs of states are called Kramers pairs and naturally give rise to a partition of the Hilbert space of occupied states \mathcal{H} into two subspaces linked by time-reversal symmetry:

$$\mathcal{H} = \mathcal{H}^I \cup \underbrace{\left\{ \mathcal{T}|\phi_i^I\rangle \mid |\phi_i^I\rangle \in \mathcal{H}^I \right\}}_{\mathcal{H}^{II}}. \quad (4.5)$$

The Chern number for the entire system is given by the sum of the Chern numbers of the two subspaces $C = C^I + C^{II}$. Since the Chern number of the whole system is zero, the Chern numbers associated with the two subspaces must be opposites $C^I = -C^{II}$. It should be noted

that this partition is not unique: instead of assigning

$$|\phi_i^I\rangle \rightarrow \mathcal{H}^I \quad \text{and} \quad \mathcal{T}|\phi_i^I\rangle \rightarrow \mathcal{H}^{II} \quad (4.6)$$

it is possible to assign

$$\mathcal{T}|\phi_i^I\rangle \rightarrow \mathcal{H}^I \quad \text{and} \quad \mathcal{T}^2|\phi_i^I\rangle = -|\phi_i^I\rangle \rightarrow \mathcal{H}^{II}. \quad (4.7)$$

In other words, the two states forming a Kramers pair can simultaneously swap subspaces. Since the subspace formed by any Kramers pair is time-reversal invariant, the two individual states have to carry opposite Chern numbers c_i^I and $c_i^{II} = -c_i^I$. As a result, the Chern numbers of the two subspaces for two different partitions can only differ by multiples of two.

$$C^I \rightarrow C^I - c_i^I + c_i^{II} = C^I - 2c_i^I \quad (4.8)$$

$$C^{II} \rightarrow C^{II} - c_i^{II} + c_i^I = C^{II} + 2c_i^I \quad (4.9)$$

Therefore, the two Chern numbers $C^{I/II}$ are always odd or even, regardless of which partition is chosen. This is formalized in the definition of the \mathbb{Z}_2 invariant:

$$\mathbb{Z}_2 = (C^I - C^{II}) / 2 \pmod{2}. \quad (4.10)$$

Two-dimensional materials with $\mathbb{Z}_2 = 1$ are called topological insulators.

Topologically protected edge states emerge at the interface between a topological insulator and a vacuum. Due to time-reversal symmetry, the edge state appears in Kramer pairs. Like in the integer Hall effect, the number of edge states itself is not a topological invariant, but the number of Kramers pairs of edge modes modulo 2 is ($N_K = \mathbb{Z}_2 \pmod{2}$).

In three-dimensional systems, a single invariant is not enough to characterize the topology of the ground state wave function. Instead, a set of four invariants $[v; (v_x, v_y, v_z)]$ can be used. These indices are defined in terms of the \mathbb{Z}_2 invariants of two-dimensional cross-sections of the reciprocal cell. Each cut is obtained by fixing one component of the k -vector. The four indices are defined as

$$v = \Delta(k_i = 0) + \Delta(k_i = 0.5) \pmod{2}, \quad (4.11)$$

$$v_i = \Delta(k_i = 0), \quad (4.12)$$

where k_i is in reduced coordinates. A material is called a weak topological insulator if any of the v_i is nonzero and a strong insulator if v is nonzero.

The first observation of vanishing resistivity baffled the physics community and sparked a tremendous amount of academic work on the phenomenon of superconductivity. One of the crowning achievements of this time is the Bardeen, Cooper, and Schrieffer (BCS) theory, a comprehensive microscopic description capable of explaining many superconducting phenomena. However, a growing number of superconductors defy the BCS theory today. This chapter outlines different theories of superconductivity and introduces the semi-empirical Bogoliubov-de-Gennes method for simulating superconductivity within the DFT framework.

5.1 Introduction: Beyond Normal Metals

Both metals and insulators possess a finite resistivity, which limits the number of electrons conducted through the material. Resistivity varies between $10^{-8} \Omega\text{m}$ for most metals and more than $10^9 \Omega\text{m}$ for many insulators. In normal metals, inelastic scattering processes limit the mobility of electrons and give rise to finite resistivity. With a decrease in temperature, the number of occupied phonon modes is reduced, and the resistivity of a perfect metal asymptotically approaches zero. However, the crystal structure of real materials is imperfect, and impurities, vacancies, and lattice distortions lead to non-vanishing resistivity. However, in 1911 Onnes discovered that the resistivity of pure mercury below a critical temperature of $T_C = 4.154 \text{ K}$ dropped to zero [Onn11]. This hallmark discovery was the first observation of superconductivity. Since then, many other superconductors have been discovered, first in other pure metals (aluminum, lead, niobium) and later in alloys. The number of known superconducting materials has increased steadily since then. Finding superconductors that can operate close to room temperature is the primary objective of much of this research.

In addition to a vanishing resistivity below the critical temperature, one observes a few other characteristic properties:

1. **Meissner–Ochsenfeld effect:** *Up to a critical magnetic field strength B_C superconductors completely expel magnetic fields from their interior.* This effect was first demonstrated by Meissner and Ochsenfeld [MO33]. Once the magnetic field strength exceeds B_C , either the superconducting phase disappears completely and the magnetic field penetrates the

sample like any other metal (Type-I superconductors), or the magnetic field starts to penetrate the superconductor in isolated points called vortices leaving the superconductivity intact (Type-II superconductors). In Type-II superconductors, a second, larger critical magnetic field strength exists at which the superconducting phase breaks down, and the sample returns to the normal metallic state.

2. **London moment:** *A rotating superconductor generates a magnetic field whose axis is perfectly aligned with the rotation axis.* This effect was first predicted by Becker et al. [BHS33] for a superconductor being set into motion. Becker et al. explained that electrons near the superconductor's surface, which lag behind rotation, generate this magnetic moment of the rotating superconductors [BHS33]. Later, London also predicted that this magnetic moment would arise when an already rotating sample is cooled from the normal state below the critical temperature [Lon50]. In the normal state, electrons do not exhibit such a lag, and no magnetic moment is measured. However, as Hildebrandt [Hil64] showed, the predicted magnetic field sets in at the critical temperature proving London's prediction that the initial state of the probe does not affect the final state.
3. **Josephson effect** [Jos62; Jos74]: *In a junction consisting of two weakly coupled superconductors, a superconducting current can flow between the superconductors without external electromagnetic fields (DC Josephson effect).* A junction with weak coupling can be achieved by inserting a normal metal or insulator between two superconductors or by creating a constriction in the superconducting material. If the superconducting current is increased above a critical current, for example, by applying a bias V , a superconducting current starts to oscillate with the Josephson frequency $\nu = 2e/h V$ (AC Josephson effect).

This chapter briefly reviews different theories of superconductivity and outlines the Bogoliubov-de Gennes (BdG) [Bog58; BTŠ58; De 18] method. The last section demonstrates how the BdG method can be combined with the DFT to create a semi-empirical framework for simulating superconductivity based on the first-principles electronic structure. A comprehensive review of the theories of superconductivity can be found in Bang and Stewart [BS17], Hirschfeld [Hir16], Schmalian [Sch10], and Sharma [Sha21].

5.2 Theories of Superconductivity

The first phenomenological theory of superconductors was proposed by London and London [LL35] and treated electrons as free particles within a metal. Their theory extended the Maxwell equations by two new equations for superconductors. The London-London theory

was able to explain the Meissner effect and infinite conductivity. However, the quantitative agreement of the predicted penetration depths for magnetic fields with experiments was poor.

A few years later, Ginzburg and Landau [GL50] drew an analogy between the superconducting and second-order ferromagnetic phase transitions. They introduced a superconducting order parameter called the superconducting wave function. The Ginzburg–Landau theory predicts a parameter that distinguishes Type-I and Type-II superconductors and arrives at the key equations of the London–London theory as a special case. Even though the Josephson effect had not been discovered in 1950, it can still be predicted in the framework of the Ginzburg–Landau theory [Sha21].

Ginzburg–Landau only described superconductors near the phase transition ($(T - T_C) \ll T_C$), which limited its applicability deep inside the superconducting phase. The first microscopic theory of superconductivity valid for all temperatures between $T = 0$ and $T = T_C$ was formulated by Bardeen, Cooper, and Schrieffer (BCS) in their influential article "Theory of Superconductivity" [BCS57]. The BCS theory was based on Fröhlich's ideas that electron-phonon processes are responsible for superconductivity [Frö50]. The BCS theory proposes that interactions between electrons and virtual phonons lead to an effective, attractive potential for electrons, in which pairs of electrons form bosonic quasiparticles (Cooper pairs). In superconductors, these quasiparticles condense into a ground state. The Ginzburg–Landau theory can be derived from BCS theory as a limiting case near the critical temperature T_C [Gor59].

5.3 Unconventional Superconductivity

BCS theory has been instrumental in understanding many superconductors. However, some superconductors exhibit behaviors that are not consistent with BCS theory. These not-BCS-like superconductors are called unconventional superconductors. The first unconventional superconductor, CeCu_2Si_2 , was discovered in 1979 by Steglich et al. [Ste+79], followed shortly after that by the discovery of unconventional organic superconductors in 1980 by Jérôme et al. [Jér+80]. Since then, many other unconventional superconductors have been discovered, which can be grouped into five categories (except for Sr_2RuO_4): heavy fermion, cuprate, iron-based, non-centrosymmetric, and organic superconductors [Ste17].

While Schrodi et al. [SOA21] argue that unconventional superconductivity is a purely electronic effect, Hirsch and Marsiglio [HM89] proposed a theory based on hole-pairing rather than electron-pairing. This theory of hole-superconductivity explains the Meissner effect in unconventional superconductors and predicts a Spin-Meissner effect [Hir08], which has not been observed yet. Furthermore, hole-superconductivity has been used to understand high-temperature superconductivity in electron-doped cuprates [AFG10; DG07; Li+19]. How-

ever, understanding the origins of unconventional superconductivity remains one of the most important and controversial issues in the field.

5.4 The Bogoliubov-de-Gennes Method

In recent years, fully ab initio methods for superconductivity have been proposed by Lüders et al. [Lüd+05], Marques et al. [Mar+05], and Sanna et al. [San+18] and [Pav+17, Chapter 16]. These methods go beyond the Born-Oppenheimer approximation and include the nuclei in the DFT framework. Such ab initio methods can explain conventional phonon-mediated superconductivity. However, a different approach is required to model unconventional superconductors.

The BdG method is based on a Hartree-Fock-like mean-field approximation of the many-body Hamiltonian. It assumes that well-defined quasiparticles (Bogoliubons) exist in superconductors. This assumption allows for the one-particle local density of states (LDOS) of a system to be easily calculated. Furthermore, the one-particle LDOS can be directly linked to low-temperature STM experiments probing excitation spectra near interfaces, surfaces, or vortices. Herein lies one of the strengths of the BdG method. Furthermore, the BdG method goes beyond BCS theory and can describe multiband effects and treat inhomogeneous superconductors and interfaces between superconductors and non-superconductors [Zhu16]. Another advantage of the BdG method is its applicability to unconventional superconductors. The BdG method uses a semi-empirical parameter to describe the pairing responsible for the emergence of the superconducting states. This phenomenological parameter does not impose any assumption about the underlying pairing mechanism, which means that the framework of the BdG method can be applied to unconventional superconductors [Gyo+98; Tem+96].

Note that the BdG formalism technically only describes the weak-coupling regime, where the pairing interaction is limited to a small range around the Fermi level. However, it also yields qualitative results in some cases of systems with strong coupling [Bee97].

The following section follows the derivation of the BdG equation in Zhu [Zhu16]. However, the assumption that the pairing potential only couples particles with opposite spins is avoided here to derive the BdG equation in its most general form. In Section 5.4.3, the former case is discussed as the special case of singlet pairing.

5.4.1 Mean-Field Approximation of the Many-Body Hamiltonian

In second quantization, the quantum many-body Hamiltonian with a two-particle potential V_{eff} reads

$$\begin{aligned} \mathbf{H} = & \int d\mathbf{r} \psi_{\sigma}^{\dagger}(\mathbf{r}) h_{\sigma\sigma'}(\mathbf{r}) \psi_{\sigma'}(\mathbf{r}) \\ & - \frac{1}{2} \iint d\mathbf{r} d\mathbf{r}' \psi_{\sigma}^{\dagger}(\mathbf{r}) \psi_{\sigma'}^{\dagger}(\mathbf{r}') V_{\text{eff}}(\mathbf{r}, \mathbf{r}') \psi_{\sigma'}(\mathbf{r}') \psi_{\sigma}(\mathbf{r}). \end{aligned} \quad (5.1)$$

where $\psi_{\sigma}^{\dagger}(\mathbf{r})$ and $\psi_{\sigma}(\mathbf{r})$ are the creation and annihilation operators of an electron with spin σ at position \mathbf{r} . $h_{\sigma\sigma'}$ is a single particle Hamiltonian. The potential V_{eff} is assumed to be positive, making the two-particle interaction attractive, and is symmetric under particle exchange $V_{\text{eff}}(\mathbf{r}', \mathbf{r}) = V_{\text{eff}}(\mathbf{r}, \mathbf{r}') = V_{\text{eff}}(\mathbf{r} - \mathbf{r}')$. Equation (5.1) and all the following equations use the Einstein summation convention. The BCS Hamiltonian has the same form and can be understood as a special case of Equation (5.1). Therefore, the following derivation applies to BCS theory and any other type of pairing mechanism based on two-particle interaction.

A mean-field approximation⁴ of this Hamiltonian yields

$$\begin{aligned} \mathbf{H}_{\text{MF}} = & \int d\mathbf{r} \psi_{\sigma}^{\dagger}(\mathbf{r}) h_{\sigma\sigma'}(\mathbf{r}) \psi_{\sigma'}(\mathbf{r}) \\ & + \frac{1}{2} \iint d\mathbf{r} d\mathbf{r}' (\Delta_{\sigma\sigma'}(\mathbf{r}, \mathbf{r}') \psi_{\sigma}^{\dagger}(\mathbf{r}) \psi_{\sigma'}^{\dagger}(\mathbf{r}') + \text{H.c.}) \\ & + \frac{1}{2} \iint d\mathbf{r} d\mathbf{r}' |\Delta_{\sigma\sigma'}(\mathbf{r}, \mathbf{r}')|^2 / V_{\text{eff}}(\mathbf{r}, \mathbf{r}'). \end{aligned} \quad (5.2)$$

The pairing potential $\Delta_{\sigma\sigma'}$ is given by

$$\begin{aligned} \Delta_{\sigma\sigma'}(\mathbf{r}, \mathbf{r}') &= -V_{\text{eff}}(\mathbf{r} - \mathbf{r}') \langle \psi_{\sigma'}(\mathbf{r}') \psi_{\sigma}(\mathbf{r}) \rangle \\ &= V_{\text{eff}}(\mathbf{r}' - \mathbf{r}) \langle \psi_{\sigma}(\mathbf{r}) \psi_{\sigma'}(\mathbf{r}') \rangle = -\Delta_{\sigma'\sigma}(\mathbf{r}', \mathbf{r}) \end{aligned} \quad (5.3)$$

$$\Delta_{\sigma\sigma'}(\mathbf{r}, \mathbf{r}')^* = -V_{\text{eff}}(\mathbf{r} - \mathbf{r}') \langle \psi_{\sigma}^{\dagger}(\mathbf{r}) \psi_{\sigma'}^{\dagger}(\mathbf{r}') \rangle = (\Delta^{\dagger})_{\sigma'\sigma}(\mathbf{r}', \mathbf{r}) \quad (5.4)$$

The statistical averages $\chi_{\sigma\sigma'} = \langle \psi_{\sigma}(\mathbf{r}) \psi_{\sigma'}(\mathbf{r}') \rangle$ are order parameters of the superconducting state. In the normal state, they vanish. However, in the superconducting state, the terms remain finite. $\chi_{\sigma\sigma'}$ is called the anomalous density in analogy to the normal density $n_{\sigma\sigma'} = \langle \psi_{\sigma}^{\dagger}(\mathbf{r}) \psi_{\sigma'}(\mathbf{r}') \rangle$

⁴ The two operators $\psi_{\sigma'} \psi_{\sigma}$ and $\psi_{\sigma}^{\dagger} \psi_{\sigma'}^{\dagger}$ are expressed as a small deviation ($\delta = \psi_{\sigma'} \psi_{\sigma} - \langle \psi_{\sigma'} \psi_{\sigma} \rangle$) from their expectation value and quadratic terms in δ are neglected:

$$\begin{aligned} \psi_{\sigma}^{\dagger} \psi_{\sigma'}^{\dagger} \psi_{\sigma'} \psi_{\sigma} &= (\langle \psi_{\sigma}^{\dagger} \psi_{\sigma'}^{\dagger} \rangle + \delta^{\dagger})(\langle \psi_{\sigma'} \psi_{\sigma} \rangle + \delta) \approx \langle \psi_{\sigma}^{\dagger} \psi_{\sigma'}^{\dagger} \rangle \langle \psi_{\sigma'} \psi_{\sigma} \rangle + \langle \psi_{\sigma}^{\dagger} \psi_{\sigma'}^{\dagger} \rangle \delta + \delta^{\dagger} \langle \psi_{\sigma'} \psi_{\sigma} \rangle \\ &\approx \langle \psi_{\sigma}^{\dagger} \psi_{\sigma'}^{\dagger} \rangle \psi_{\sigma'} \psi_{\sigma} + \psi_{\sigma}^{\dagger} \psi_{\sigma'}^{\dagger} \langle \psi_{\sigma'} \psi_{\sigma} \rangle - \langle \psi_{\sigma}^{\dagger} \psi_{\sigma'}^{\dagger} \rangle \langle \psi_{\sigma'} \psi_{\sigma} \rangle \end{aligned}$$

This mean-field Hamiltonian does not conserve the particle number. Applying \mathbf{H}_{MF} to a state with N particles yields a superposition of states with $N - 2$, N , and $N + 2$ particles. This property of the Hamiltonian is a signature of spontaneous breaking of the $U(1)$ symmetry in the superconducting state [Zhu16]. Of course, the observable number of particles in the system is fixed; that is, the statistical average of the particle number operator $\langle \mathcal{N} \rangle$ of the superconducting ground states is equal to the expectation value of the normal state.

Using the anti-commutation relations

$$\{\psi_\sigma(\mathbf{r}), \psi_{\sigma'}^\dagger(\mathbf{r}')\} = \delta(\mathbf{r} - \mathbf{r}')\delta_{\sigma\sigma'} \quad (5.5)$$

$$\{\psi_\sigma(\mathbf{r}), \psi_{\sigma'}(\mathbf{r}')\} = \{\psi_\sigma^\dagger(\mathbf{r}), \psi_{\sigma'}^\dagger(\mathbf{r}')\} = 0 \quad (5.6)$$

and the identities

$$[A, BC] = \{A, B\}C - B\{A, C\} \quad (5.7)$$

$$[A^\dagger, B] = -[A, B^\dagger]^\dagger \quad (5.8)$$

the commutator relations for the field operators and the Hamiltonian can be obtained.

$$[\psi_\sigma(\mathbf{r}), \mathbf{H}_{\text{MF}}] = -h_{\sigma\sigma'}(\mathbf{r})\psi_{\sigma'}(\mathbf{r}) + \int d\mathbf{r}' \Delta_{\sigma\sigma'}(\mathbf{r}, \mathbf{r}')\psi_{\sigma'}^\dagger(\mathbf{r}') \quad (5.9)$$

$$[\psi_\sigma^\dagger(\mathbf{r}), \mathbf{H}_{\text{MF}}] = -h_{\sigma\sigma'}^*(\mathbf{r})\psi_\sigma^\dagger(\mathbf{r}) - \int d\mathbf{r}' \Delta_{\sigma\sigma'}^*(\mathbf{r}, \mathbf{r}')\psi_{\sigma'}(\mathbf{r}') \quad (5.10)$$

5.4.2 Bogliubov Transformation

To derive the BdG Hamiltonian, the field operators are expanded in terms of orthogonal quasi-particle operators $\gamma_{\tilde{n}}$ and $\gamma_{\tilde{n}}^\dagger$, which create and destroy Bogoliubons. In contrast to Cooper pairs, Bogoliubons are fermionic particles. Bogoliubons diagonalize the mean-filed Hamiltonian⁵

$$\psi_\sigma(\mathbf{r}) = \sum_{\tilde{n}}' (u_{\sigma}^{\tilde{n}}(\mathbf{r})\gamma_{\tilde{n}} + v_{\sigma}^{\tilde{n}*}(\mathbf{r})\gamma_{\tilde{n}}^\dagger) \quad (5.11)$$

where ' indicates that sum of \tilde{n} only runs over the states with positive excitation energy.

$$\mathbf{H}_{\text{MF}} = E_0 + E_{\tilde{n}}\gamma_{\tilde{n}}^\dagger\gamma_{\tilde{n}} \quad (5.12)$$

$$\{\gamma_{\tilde{n}}, \gamma_{\tilde{m}}^\dagger\} = \delta_{\tilde{n}\tilde{m}} \quad (5.13)$$

⁵ Many authors use the definition of $\psi_\sigma(\mathbf{r}) = (u_{\sigma}^{\tilde{n}}(\mathbf{r})\gamma_{\tilde{n}} + \sigma v_{\sigma}^{\tilde{n}*}(\mathbf{r})\gamma_{\tilde{n}}^\dagger)$ for the Bogoliubon operators instead. However, the spin-dependent prefactor can be absorbed into v , simplifying the following equations.

$$\{\gamma_{\tilde{n}}, \gamma_{\tilde{m}}\} = \{\gamma_{\tilde{n}}^\dagger, \gamma_{\tilde{m}}^\dagger\} = 0. \quad (5.14)$$

Inserting this transformation into Equation (5.9) and comparing the coefficients in front of $\gamma_{\tilde{n}}$ (or, since the quasiparticle operators are orthogonal, taking the anticommutator with $\gamma_{\tilde{n}}$) produces the BdG eigenvalue problem.

$$E_{\tilde{n}} \begin{pmatrix} u_{\uparrow}^{\tilde{n}}(\mathbf{r}) \\ u_{\downarrow}^{\tilde{n}}(\mathbf{r}) \\ v_{\uparrow}^{\tilde{n}}(\mathbf{r}) \\ v_{\downarrow}^{\tilde{n}}(\mathbf{r}) \end{pmatrix} = \int d\mathbf{r}' \mathbf{H}_{\text{BdG}}(\mathbf{r}, \mathbf{r}') \begin{pmatrix} u_{\uparrow}^{\tilde{n}}(\mathbf{r}') \\ u_{\downarrow}^{\tilde{n}}(\mathbf{r}') \\ v_{\uparrow}^{\tilde{n}}(\mathbf{r}') \\ v_{\downarrow}^{\tilde{n}}(\mathbf{r}') \end{pmatrix} \quad (5.15)$$

$$\mathbf{H}_{\text{BdG}}(\mathbf{r}, \mathbf{r}') = \begin{pmatrix} h_{\uparrow\uparrow}(\mathbf{r}')\delta(\mathbf{r}-\mathbf{r}') & h_{\uparrow\downarrow}(\mathbf{r}')\delta(\mathbf{r}-\mathbf{r}') & \Delta_{\uparrow\uparrow}(\mathbf{r}, \mathbf{r}') & \Delta_{\uparrow\downarrow}(\mathbf{r}, \mathbf{r}') \\ h_{\downarrow\uparrow}(\mathbf{r}')\delta(\mathbf{r}-\mathbf{r}') & h_{\downarrow\downarrow}(\mathbf{r}')\delta(\mathbf{r}-\mathbf{r}') & \Delta_{\downarrow\uparrow}(\mathbf{r}, \mathbf{r}') & \Delta_{\downarrow\downarrow}(\mathbf{r}, \mathbf{r}') \\ -\Delta_{\uparrow\uparrow}^*(\mathbf{r}, \mathbf{r}') & -\Delta_{\uparrow\downarrow}^*(\mathbf{r}, \mathbf{r}') & -h_{\uparrow\uparrow}^*(\mathbf{r}')\delta(\mathbf{r}-\mathbf{r}') & -h_{\uparrow\downarrow}^*(\mathbf{r}')\delta(\mathbf{r}-\mathbf{r}') \\ -\Delta_{\downarrow\uparrow}^*(\mathbf{r}, \mathbf{r}') & -\Delta_{\downarrow\downarrow}^*(\mathbf{r}, \mathbf{r}') & -h_{\downarrow\uparrow}^*(\mathbf{r}')\delta(\mathbf{r}-\mathbf{r}') & -h_{\downarrow\downarrow}^*(\mathbf{r}')\delta(\mathbf{r}-\mathbf{r}') \end{pmatrix} \quad (5.16)$$

5.4.3 Singlet and Triplet Pairing

In BCS theory, the single-particle Hamiltonian $h_{\sigma\sigma'}$ is diagonal in spin space, and the pairing potential is symmetric in the two spatial coordinates.

$$\Delta_{\sigma\sigma'}(\mathbf{r}, \mathbf{r}') = \Delta_{\sigma\sigma'}(\mathbf{r}', \mathbf{r}) = -\Delta_{\sigma'\sigma}(\mathbf{r}, \mathbf{r}') \quad (5.17)$$

$$\Delta(\mathbf{r}, \mathbf{r}') \equiv \Delta_{\uparrow\downarrow}(\mathbf{r}, \mathbf{r}') = \frac{1}{2} V_{\text{eff}}(\mathbf{r} - \mathbf{r}') \left(\langle \psi_{\uparrow}(\mathbf{r}) \psi_{\downarrow}(\mathbf{r}') \rangle + \langle \psi_{\uparrow}(\mathbf{r}') \psi_{\downarrow}(\mathbf{r}) \rangle \right) \quad (5.18)$$

$$\Delta_{\uparrow\uparrow}(\mathbf{r}, \mathbf{r}') = \Delta_{\downarrow\downarrow}(\mathbf{r}, \mathbf{r}') = 0 \quad (5.19)$$

As a result of these symmetries, the mean-field Hamiltonian simplifies to

$$\begin{aligned} \mathbf{H}_{\text{BCS}} &= \int d\mathbf{r} \psi_{\sigma}^\dagger(\mathbf{r}) h_{\sigma\sigma'}(\mathbf{r}) \psi_{\sigma'}(\mathbf{r}) \\ &+ \frac{1}{2} \iint d\mathbf{r} d\mathbf{r}' \Delta(\mathbf{r}, \mathbf{r}') \left(\psi_{\uparrow}^\dagger(\mathbf{r}) \psi_{\downarrow}^\dagger(\mathbf{r}') - \psi_{\downarrow}^\dagger(\mathbf{r}) \psi_{\uparrow}^\dagger(\mathbf{r}') \right) + \text{H.c.} \\ &+ E_{\text{const}}. \end{aligned} \quad (5.20)$$

The second term on the right-hand side contains the creation and annihilation operators for spin-less, bosonic particles (Cooper pairs). This type of pairing is also called singlet-pairing because the corresponding particles are spin-less.

As a result of these symmetries, the BdG eigenvalue problem splits into two decoupled

eigenvalue problems

$$E_{\tilde{n}} \begin{pmatrix} u_{\uparrow}^{\tilde{n}}(\mathbf{r}) \\ v_{\downarrow}^{\tilde{n}}(\mathbf{r}) \end{pmatrix} = \int d\mathbf{r}' \begin{pmatrix} h_{\uparrow\uparrow}(\mathbf{r}')\delta(\mathbf{r}-\mathbf{r}') & \Delta_{\uparrow\downarrow}(\mathbf{r}, \mathbf{r}') \\ -\Delta_{\uparrow\downarrow}^*(\mathbf{r}, \mathbf{r}') & -h_{\downarrow\downarrow}^*(\mathbf{r}')\delta(\mathbf{r}-\mathbf{r}') \end{pmatrix} \begin{pmatrix} u_{\uparrow}^{\tilde{n}}(\mathbf{r}') \\ v_{\downarrow}^{\tilde{n}}(\mathbf{r}') \end{pmatrix} \quad (5.21)$$

$$E_{\tilde{n}} \begin{pmatrix} u_{\downarrow}^{\tilde{n}}(\mathbf{r}) \\ v_{\uparrow}^{\tilde{n}}(\mathbf{r}) \end{pmatrix} = \int d\mathbf{r}' \begin{pmatrix} h_{\downarrow\downarrow}(\mathbf{r}')\delta(\mathbf{r}-\mathbf{r}') & \Delta_{\downarrow\uparrow}(\mathbf{r}, \mathbf{r}') \\ -\Delta_{\downarrow\uparrow}^*(\mathbf{r}, \mathbf{r}') & -h_{\uparrow\uparrow}^*(\mathbf{r}')\delta(\mathbf{r}-\mathbf{r}') \end{pmatrix} \begin{pmatrix} u_{\downarrow}^{\tilde{n}}(\mathbf{r}') \\ v_{\uparrow}^{\tilde{n}}(\mathbf{r}') \end{pmatrix}. \quad (5.22)$$

Taking the complex conjugate of Equation (5.22) reveals that the two eigenvalues problems are equivalent. The eigenvalues and eigenvectors occur in pairs.

$$E_{\tilde{n}1} = -E_{\tilde{n}2} \quad u_{\uparrow}^{\tilde{n}1}(\mathbf{r}) = -v_{\downarrow}^{\tilde{n}2}(\mathbf{r})^* \quad v_{\uparrow}^{\tilde{n}1}(\mathbf{r}) = -u_{\downarrow}^{\tilde{n}2}(\mathbf{r})^* \quad (5.23)$$

This symmetry of the spectrum and the amplitudes u and v demonstrates the particle-hole symmetry of the BCS Hamiltonian.

However, in some unconventional superconductors, supercurrents are spin-polarized. Using only singlet contributions the superconducting quasiparticles are spin-less and it is necessary to consider the remaining terms Equation (5.2) to explain this phenomenon. These terms correspond to the creation and annihilation of spin-triplet states. It is convenient to rewrite the Pairing potential and the anomalous density in terms of singlet and triplet components:

$$\Xi^S(\mathbf{r}, \mathbf{r}') = \frac{\Xi_{\uparrow\downarrow}(\mathbf{r}, \mathbf{r}') - \Xi_{\downarrow\uparrow}(\mathbf{r}, \mathbf{r}')}{2} \quad \Xi^{T_x}(\mathbf{r}, \mathbf{r}') = \frac{\Xi_{\downarrow\downarrow}(\mathbf{r}, \mathbf{r}') - \Xi_{\uparrow\uparrow}(\mathbf{r}, \mathbf{r}')}{2} \quad (5.24)$$

$$\Xi^{T_y}(\mathbf{r}, \mathbf{r}') = \frac{\Xi_{\downarrow\downarrow}(\mathbf{r}, \mathbf{r}') + \Xi_{\uparrow\uparrow}(\mathbf{r}, \mathbf{r}')}{2i} \quad \Xi^{T_z}(\mathbf{r}, \mathbf{r}') = \frac{\Xi_{\uparrow\downarrow}(\mathbf{r}, \mathbf{r}') + \Xi_{\downarrow\uparrow}(\mathbf{r}, \mathbf{r}')}{2} \quad (5.25)$$

where $\Xi_{\sigma\sigma'}(\mathbf{r}, \mathbf{r}')$ can be $\chi_{\sigma\sigma'}(\mathbf{r}, \mathbf{r}')$, $\Delta_{\sigma\sigma'}(\mathbf{r}, \mathbf{r}')$, or $\Psi_{\sigma\sigma'}(\mathbf{r}, \mathbf{r}') = \Psi_{\sigma}(\mathbf{r})\Psi_{\sigma'}(\mathbf{r}')$. While the singlet component is symmetric in space the three triplet components are anti-symmetric in space. An in-depth analysis of crystal, magnetic, and time-reversal symmetries can help identify which of these four components can contribute to a given system.

Finally, the mean-field Hamiltonian can be rewritten in terms of singlet and triplet components:

$$\begin{aligned} H_{\text{MF}} &= \int d\mathbf{r} \psi_{\sigma}^{\dagger}(\mathbf{r}) h_{\sigma\sigma'}(\mathbf{r}) \psi_{\sigma'}(\mathbf{r}) \\ &+ \frac{1}{2} \iint d\mathbf{r} d\mathbf{r}' \Delta^S(\mathbf{r}, \mathbf{r}') \Psi^{S\dagger}(\mathbf{r}, \mathbf{r}') + \text{H.c.} \\ &+ \sum_{\nu=x,y,z} \frac{1}{2} \iint d\mathbf{r} d\mathbf{r}' \Delta^{T_{\nu}}(\mathbf{r}, \mathbf{r}') \Psi^{T_{\nu}\dagger}(\mathbf{r}, \mathbf{r}') + \text{H.c.} \\ &+ E_{\text{const}}. \end{aligned} \quad (5.26)$$

The same decomposition can of course be applied to the BdG Hamiltonian as well.

5.4.4 The BdG+DFT Method

Similar to how the magnetic density was used to expand the DFT framework to spin-polarized systems, Kohn et al. [KGO89] and Oliveira et al. [OGK88] used the anomalous density to extend the DFT framework to superconductors. The Kohn-Sham Hamiltonian for superconductors has the form of Equation (5.16).

$$H^{\text{KS+BdG}} = \begin{pmatrix} h_{\uparrow\uparrow}^{\text{KS}} & h_{\uparrow\downarrow}^{\text{KS}} & \Delta_{\uparrow\uparrow} & \Delta_{\uparrow\downarrow} \\ h_{\downarrow\uparrow}^{\text{KS}} & h_{\downarrow\downarrow}^{\text{KS}} & \Delta_{\downarrow\uparrow} & \Delta_{\downarrow\downarrow} \\ -\Delta_{\uparrow\uparrow}^* & -\Delta_{\uparrow\downarrow}^* & -h_{\uparrow\uparrow}^{\text{KS}*} & -h_{\uparrow\downarrow}^{\text{KS}*} \\ -\Delta_{\downarrow\uparrow}^* & -\Delta_{\downarrow\downarrow}^* & -h_{\downarrow\uparrow}^{\text{KS}*} & -h_{\downarrow\downarrow}^{\text{KS}*} \end{pmatrix} \quad (5.27)$$

$$h_{\sigma\sigma'}^{\text{KS}}(\mathbf{r}, \mathbf{r}'; [\mathbf{n}, \chi]) = -\nabla^2 + V_{\sigma\sigma'}^{\text{eff}}(\mathbf{r}, \mathbf{r}'; [\mathbf{n}, \chi]) \quad (5.28)$$

$$V_{\sigma\sigma'}^{\text{eff}}(\mathbf{r}; [\mathbf{n}, \chi]) = V_{\sigma\sigma'}^{\text{ext}}(\mathbf{r}) + \int d\mathbf{r}' \frac{n^{\uparrow\uparrow}(\mathbf{r}') + n^{\downarrow\downarrow}(\mathbf{r}')}{|\mathbf{r} - \mathbf{r}'|} \delta_{\sigma\sigma'} + \frac{\delta E_{xc}(\mathbf{r}, \mathbf{r}'; [\mathbf{n}, \chi])}{\delta n_{\sigma\sigma'}} \quad (5.29)$$

$$\Delta_{\sigma\sigma'}(\mathbf{r}, \mathbf{r}'; [\mathbf{n}, \chi]) = \Delta_{\sigma\sigma'}^{\text{ext}}(\mathbf{r}) - \frac{\delta E_{xc}(\mathbf{r}, \mathbf{r}'; [\mathbf{n}, \chi])}{\delta \chi_{\sigma\sigma'}} \quad (5.30)$$

This approach is an exact theory for describing superconductors. However, like in the case of normal-state DFT, the issue lies in the unknown exchange-correlation potential. To make the formalism useful, Kohn et al. [KGO89] suggested rewriting the exchange energy as

$$E_{xc}(\mathbf{r}, \mathbf{r}'; [\mathbf{n}, \chi]) = E_{xc}^0(\mathbf{r}; \mathbf{n}) - \iiint d\mathbf{r}' d\mathbf{x}' \chi_{\sigma\sigma'}^*(\mathbf{r}, \mathbf{r}') \Lambda_{\sigma\sigma'}(\mathbf{r}, \mathbf{r}', \mathbf{x}, \mathbf{x}'; [\mathbf{n}, \chi]) \chi_{\sigma\sigma'}(\mathbf{x}, \mathbf{x}') \quad (5.31)$$

where $E_{xc}^0(\mathbf{r}; \mathbf{n})$ is the exchange-correlation potential in the normal state, for which any of the approximations discussed above can be used. The kernel $\Lambda_{\sigma\sigma'}$ could be calculated based on a specific coupling mechanism to obtain an ab initio method for superconductivity [Lüd+05; Mar+05; San+18]. Alternatively, the kernel can be treated as a phenomenological parameter. A commonly used form of the kernel was proposed by Oliveira et al. [OGK88] and Suvasini and Gyorffy [SG92]: (a) the kernel is non-zero only inside a well potential around atomic sites and

vanishes everywhere else

$$\Lambda_{\sigma\sigma'}(\mathbf{r}, \mathbf{r}', \mathbf{x}, \mathbf{x}'; [\mathbf{n}, \chi]) = \begin{cases} \Lambda^i([\mathbf{n}, \chi])\delta(\mathbf{r} - \mathbf{r}')\delta(\mathbf{r} - \mathbf{x})\delta(\mathbf{r} - \mathbf{x}'), \\ \text{if } \mathbf{r}, \mathbf{r}', \mathbf{x}, \text{ and } \mathbf{x}' \text{ are inside the potential wells at site } i \\ 0, \quad \text{otherwise} \end{cases} \quad (5.32)$$

and (b) Λ^i is not an explicit functional of \mathbf{n} and χ , and only depends on the atomic site.

Now, the functional derivative can be evaluated analytically, and the resulting pairing potential is given by

$$\Delta_{\sigma\sigma'}(\mathbf{r}, \mathbf{r}'; [\mathbf{n}, \chi]) = \Delta_{\sigma\sigma'}^{\text{ext}}(\mathbf{r}, \mathbf{r}') - \Lambda(\mathbf{r}, \mathbf{r}')\chi(\mathbf{r}, \mathbf{r}'). \quad (5.33)$$

Although the first part of this approximation is unproblematic for superconductors with short coherence lengths [STG93], the second part makes the BdG+DFT approach semiphenomenological and undermines the predictive aspect of DFT. However, it is exactly the phenomenological parameter that makes the modeling of unconventional superconductors feasible. Once the underlying mechanisms for unconventional superconductivity have been unveiled, the corresponding kernel can replace the phenomenological approximation.

Part II

Methods Development

In this chapter, we present how we implemented support for a non-collinear spin and fully relativistic calculations in TRANSIESTA and the postprocessing code TBTRANS. This version of TRANSIESTA (TBTRANS) can be found online at <https://gitlab.com/nils.wittemeier/siesta/-/tree/ts-soc> (<https://gitlab.com/nils.wittemeier/siesta/-/tree/tbtrans-soc-new>). A publication of the work presented in this chapter and the applications of the new code described in Chapter 11 is currently in preparation.

6.1 Electronic spin in the Non-Equilibrium Green's Function Formalism

Just like the DFT formalism, the NEGF formalism can be extended to include electronic spin. In the case of collinear spins, Green's function, spectral functions, and non-equilibrium density factorize into independent quantities for each spin channel:

$$\mathbf{G}_{\mathbf{k}}^R(z) \rightarrow \left\{ \mathbf{G}_{\mathbf{k}}^{R\uparrow}(z), \mathbf{G}_{\mathbf{k}}^{R\downarrow}(z) \right\} \quad (6.1)$$

$$\mathcal{A}_{\mathbf{e},\mathbf{k}}(z) \rightarrow \left\{ \mathcal{A}_{\mathbf{e},\mathbf{k}}^{\uparrow}(z), \mathcal{A}_{\mathbf{e},\mathbf{k}}^{\downarrow}(z) \right\} \quad (6.2)$$

$$\boldsymbol{\rho}_{\mathbf{k}}(z) \rightarrow \left\{ \boldsymbol{\rho}_{\mathbf{k}}^{\uparrow}(z), \boldsymbol{\rho}_{\mathbf{k}}^{\downarrow}(z) \right\} \quad (6.3)$$

The total transmission and the total current are given by the sum of the two spin components.

$$\begin{aligned} T_{\mathbf{e},\mathbf{e}'}(\epsilon) &= T_{\mathbf{e},\mathbf{e}'}^{\uparrow}(\epsilon) + T_{\mathbf{e},\mathbf{e}'}^{\downarrow}(\epsilon) \\ &= \sum_{\sigma} \int_{BZ} dk \operatorname{Tr} \left\{ \Gamma_{\mathbf{e},\mathbf{k}}^{\sigma}(z) G_{\mathbf{k}}^{\sigma\dagger}(z) \Gamma_{\mathbf{e}',\mathbf{k}}^{\sigma}(z) G_{\mathbf{k}}^{\sigma}(z) \right\} \end{aligned} \quad (6.4)$$

$$I_{\mathbf{e},\mathbf{e}'} = I_{\mathbf{e},\mathbf{e}'}^{\uparrow} + I_{\mathbf{e},\mathbf{e}'}^{\downarrow} = \frac{1}{2\pi} \int d\epsilon \left[f_{\mathbf{e}}(\epsilon) - f_{\mathbf{e}'}(\epsilon) \right] T_{\mathbf{e},\mathbf{e}'}^{\sigma}(\epsilon). \quad (6.5)$$

In the non-collinear case, the two spin channels are not independent and the whole formalism

has to be extended to a full description with spinor matrices:

$$\mathbf{G}_k^R(z) \rightarrow \begin{pmatrix} \mathbf{G}_k^{R\uparrow\uparrow}(z) & \mathbf{G}_k^{R\uparrow\downarrow}(z) \\ \mathbf{G}_k^{R\downarrow\uparrow}(z) & \mathbf{G}_k^{R\downarrow\downarrow}(z) \end{pmatrix} \quad (6.6)$$

$$\mathcal{A}_{e,k}(z) \rightarrow \begin{pmatrix} \mathcal{A}_{e,k}^{\uparrow\uparrow}(z) & \mathcal{A}_{e,k}^{\uparrow\downarrow}(z) \\ \mathcal{A}_{e,k}^{\downarrow\uparrow}(z) & \mathcal{A}_{e,k}^{\downarrow\downarrow}(z) \end{pmatrix} \quad (6.7)$$

$$\boldsymbol{\rho}_k(z) \rightarrow \begin{pmatrix} \boldsymbol{\rho}_k^{\uparrow\uparrow}(z) & \boldsymbol{\rho}_k^{\uparrow\downarrow}(z) \\ \boldsymbol{\rho}_k^{\downarrow\uparrow}(z) & \boldsymbol{\rho}_k^{\downarrow\downarrow}(z) \end{pmatrix} \quad (6.8)$$

$$T_{e,e'}(\epsilon) = \sum_{\substack{\sigma_1\sigma_2 \\ \sigma_3\sigma_4}} \int_{BZ} dk \text{Tr} \left\{ \Gamma_{e,k}^{\sigma_1\sigma_2}(z) G_k^{\dagger\sigma_2\sigma_3}(z) \Gamma_{e',k}^{\sigma_3\sigma_4}(z) G_k^{\sigma_4\sigma_1}(z) \right\}. \quad (6.9)$$

So far TRANSIESTA has been able to perform NEGF+DFT calculations with collinear spin calculations, and we have extended the implementation now to support simulations with non-collinear spins and spin-orbit coupling as well.

For our new implementation, we have added a set of new modules to the SIESTA code base. These modules are labeled with the `_spinor` postfix to indicate that they specifically address the spinor implementation.

Every TRANSIESTA calculation follows the following steps:

1. For every energy point z in a given contour and every k point:
 - a) Calculate the electrode surface self-energy: `m_ts_electrode_spinor`
 - b) Calculate the Green's function and determine the contribution to the density matrix from current k and energy point: `m_ts_fullg_spinor`, `m_ts_fullk_spinor`, `m_ts_trig_spinor`, `m_ts_trik_spinor`
 - c) If non-equilibrium conditions, weigh the different contributions to density matrix: `m_ts_weight_spinor`
2. Update the SIESTA density matrix: `m_ts_dm_update`
3. Check convergence and mix density matrix for next iteration: *no code change required*
4. Repeat

After convergence of the self-consistency cycle TBTRANS can be used to extract the transmission, currents, density-of-states, and various other quantities. To have the same analysis tools available for spinor calculations, we have also extended the capabilities of TBTRANS.

6.1.1 Calculating the Electrode Surface Self-Energy

To calculate the electrode surface self-energy, we use the Sancho-Sancho-Rubio (SSR) algorithm, an iterative scheme for calculation of surface self-energies by Sancho et al. [SSR85]. This algorithm requires us to construct the Hamiltonian and overlap matrices for the principal layer and the corresponding interlayer matrices.

$$\mathbf{H}_{0,0}^e(\mathbf{k}) = \sum_{\mathbf{R}_\perp} \mathbf{H}_{0,0}^e(\mathbf{R}_\perp) e^{i\mathbf{k}\mathbf{R}_\perp} \quad \mathbf{S}_{0,0}^e(\mathbf{k}) = \sum_{\mathbf{R}_\perp} \mathbf{S}_{0,0}^e(\mathbf{R}_\perp) e^{i\mathbf{k}\mathbf{R}_\perp} \quad (6.10)$$

$$\mathbf{H}_{0,1}^e(\mathbf{k}) = \sum_{\mathbf{R}_\perp} \mathbf{H}_{0,1}^e(\mathbf{R}_\perp) e^{i\mathbf{k}\mathbf{R}_\perp} \quad \mathbf{S}_{0,1}^e(\mathbf{k}) = \sum_{\mathbf{R}_\perp} \mathbf{S}_{0,1}^e(\mathbf{R}_\perp) e^{i\mathbf{k}\mathbf{R}_\perp}, \quad (6.11)$$

where the sum runs over all lattice vectors perpendicular to the semi-infinite direction of the electrode \mathbf{e} . At this stage, we convert the Hamiltonian matrix of the electrodes from their usual sparse matrix format (Table 6.1) to the dense matrix format in Equation (2.23). A dummy code for the conversion between the sparse matrix and the dense matrix for a specific \mathbf{k} -point can be found in Listing 1. After determining the \mathbf{k} -point matrices, we reuse the existing implementation of the SSR algorithm, which is agnostic to the difference of spin and orbitals indices. Therefore, it can be reused completely.

By default, the surface self-energies for all energies and all \mathbf{k} -points are calculated during the initialization of SIESTA, written to a file and later read when needed. Alternatively, the self-energies can be calculated *on demand*. The latter option significantly reduces the amount of disk space used by TRANSIESTA. However, calculating the self-energies only *on demand*, means that the same calculation must be repeated at every step of the iterative procedure.

6.1.2 Calculating the Green's Function

To calculate the Green's function, we first set up its inverse $z\mathbf{S}_k - \mathbf{H}_k - \sum_{\mathbf{e}} \Sigma_{\mathbf{e},k}(z)$. For unpolarized and collinear spin calculations TRANSIESTA supports three inversion methods: full matrix inversion using (Sca)LAPACK [And+99; Bla+97], block-tridiagonal (BTD) inversion method [Pap+17], and MUMPS [Ame+01; Ame+19]. For spinor calculations, we have only implemented support for full matrix inversion using (Sca)LAPACK and the BTD method because the BTD method is by far the most efficient [Pap+17] and the simplicity of the full inversion method makes it ideal as a reference.

We convert the Hamiltonian and overlap matrices of the device region for a given \mathbf{k} -point using a similar procedure used to set up the \mathbf{k} -point matrices for the SSR algorithm. For the full inversion method, we set up the inverse Green's function as a dense matrix and for the block-tridiagonal inversion method as a sparse matrix. In either case, the matrix is structured

	Unpolarized	Collinear	non-collinear	Spin-orbit
H(:,1)	Re{H}	Re{H ^{↑↑} }	Re{H ^{↑↑} }	Re{H ^{↑↑} }
H(:,2)	–	Re{H ^{↓↓} }	Re{H ^{↓↓} }	Re{H ^{↓↓} }
H(:,3)	–	–	Re{H ^{↑↓} }	Re{H ^{↑↓} }
H(:,4)	–	–	–Im{H ^{↑↓} }	–Im{H ^{↑↓} }
H(:,5)	–	–	–	Im{H ^{↑↑} }
H(:,6)	–	–	–	Im{H ^{↓↓} }
H(:,7)	–	–	–	Re{H ^{↓↑} }
H(:,8)	–	–	–	Im{H ^{↓↑} }

Table 6.1: Sparse matrix format for the Hamiltonian and density matrix in SIESTA. The first dimension corresponds to orbital indices (μ, ν, \mathbf{R}) with non-zero matrix elements, and the second dimension to real and imaginary parts of the different spin components. The negative sign in front of the $\uparrow\downarrow$ component is motivated by the σ_y Pauli matrix.

```

1  do ind = 0 ... N_nonzero
2      ! Convert i to orbital indices and the corresponding lattice vector
3      mu, nu, R_vec = convert_indices(ind)
4      kphase = exp(cmplx(0._dp, -dot_product(k_vec, R_vec), dp))
5      Sk(mu,nu) = complex(S(nd), 0._dp, dp) * kphase
6
7      if ( spin%none == .true. ) ! spin-unpolarized
8          Hk(mu,nu) = complex(H(ind,1), 0._dp, dp) * kphase
9      else if ( spin%Col == .true. ) ! collinear spin
10         ! > ispin : spin index currently being addressed
11         Hk(mu,nu) = complex(H(ind,ispin), 0._dp, dp) * kphase
12     else if ( spin%NCol == .true. ) ! non collinear spin
13         Hk(1,mu,1,nu) = complex(H(ind,1), 0._dp, dp) * kphase ! H↑↑μν
14         Hk(1,mu,2,nu) = complex(H(ind,3), -H(ind,4), dp) * kphase ! H↑↓μν
15         Hk(1,mu,2,nu) = complex(H(ind,3), H(ind,4), dp) * kphase ! H↓↑μν
16         Hk(2,mu,2,nu) = complex(H(ind,2), 0._dp, dp) * kphase ! H↓↓μν
17     else ! spin-orbit
18         Hk(1,mu,1,nu) = complex(H(ind,1), H(ind,5), dp) * kphase ! H↑↑μν
19         Hk(1,mu,2,nu) = complex(H(ind,3), -H(ind,4), dp) * kphase ! H↑↓μν
20         Hk(1,mu,2,nu) = complex(H(ind,7), H(ind,8), dp) * kphase ! H↓↑μν
21         Hk(2,mu,2,nu) = complex(H(ind,2), H(ind,6), dp) * kphase ! H↓↓μν
22     end if
23 end do

```

Listing 1: Dummy code for conversion between sparse matrix format of SIESTA and dense k-point matrices

as

$$A = \left(\begin{array}{cc|cc} A_{1,1}^{\uparrow\uparrow} & A_{1,1}^{\uparrow\downarrow} & A_{1,2}^{\uparrow\uparrow} & \cdots \\ A_{1,1}^{\downarrow\uparrow} & A_{1,1}^{\downarrow\downarrow} & A_{1,2}^{\downarrow\uparrow} & \cdots \\ \hline A_{2,1}^{\uparrow\uparrow} & A_{2,1}^{\uparrow\downarrow} & A_{2,2}^{\uparrow\uparrow} & \cdots \\ \vdots & \vdots & \vdots & \ddots \end{array} \right) \quad (6.12)$$

to keep the matrix bandwidth as small as possible and increase the efficiency of the matrix inversion method. Subsequently, we add the self-energy to set up the inverse Green's function (Listing 2).

6.1.3 Mixing Weights

The choices of the electrode ϵ in Eq. 3.26 are all equivalent, making the choice of any electrode as a reference electrode arbitrary. To reduce numerical errors and avoid this arbitrariness, TRANSIESTA weights the non-equilibrium density matrices calculated for each ϵ :

$$\rho = \sum_{\epsilon} w_{\epsilon} \left(\rho_{\epsilon}^{\text{eq}} + \sum_{\epsilon' \neq \epsilon} \Delta_{\epsilon, \epsilon'} \right) \quad (6.13)$$

$$\theta_{\epsilon} = \sum_{\epsilon' \neq \epsilon} \text{Var}[\Delta_{\epsilon, \epsilon'}] \quad (6.14)$$

$$w_{\epsilon} = \prod_{\epsilon' \neq \epsilon} \theta_{\epsilon'} / \sum_{\epsilon'} \prod_{\epsilon'' \neq \epsilon'} \theta_{\epsilon''}. \quad (6.15)$$

For the spinor implementation of TRANSIESTA, we only use the real part of the sum of the diagonal elements of the spin box of $\Delta_{\epsilon, \epsilon'}$ when calculating the weights w_{ϵ} . We omit the spin-box off-diagonal elements following the same rationale as in Ref. [Bra+02] because the off-diagonal terms do not affect the charge density.

6.1.4 Parallelization and Scaling

The newly implemented routine use the same to hybrid parallelization as the existing routines: each MPI task handles a distinct set of energy points, and OpenMP threading is used to speed up parallelized matrix operations. In Figure 6.1, we show the scaling with the number of MPI tasks and OMP threads for a test system comprising 816 atoms (11088 orbitals) and a complex contour containing 256 energy points. The tests were performed using the BTM method (20 blocks; 200 to 720 orbitals each) with bias on a single node composed of 2 sockets holding 128 AMD Rome 7H12 CPUs each. The calculations scale close to perfectly up to 128 MPI tasks and 8 OMP threads. For a larger number of OMP threads the performance scales sub-linear, but

```

1  ! (1) Full matrix inversion method
2  ! =====
3  do ind = 0 ... N_nonzero
4      iu, ju = convert_index(ind)    ! Convert ind to orbital indices
5      GFinv(1, ju, 1, iu) = Z * Sk(ju,iu) - Hk(1, ju, 1, iu)
6      GFinv(2, ju, 1, iu) =                - Hk(2, ju, 1, iu)
7      GFinv(1, ju, 2, iu) =                - Hk(1, ju, 2, iu)
8      GFinv(2, ju, 2, iu) = Z * Sk(ju,iu) - Hk(2, ju, 2, iu)
9  end do
10 do iElectrode in 1, nElectrodes
11     off = Electrodes(iElec)%offset ! Position of first electrode orbital in device
12     do jElec, iElec = 1, Electrodes(iElec)%orbitals()
13         do ii,jj = 1, 2
14             Gfinv(ii, off+iElec, jj, off+jElec) = El%Sigma(ii iElec, jj jElec)
15         end do
16     end do
17 end do
18
19 ! (2) BTD matrix inversion method
20 ! =====
21 do ind = 0 ... N_nonzero
22     iu, ju = convert_index(ind)    ! Convert ind to orbital indices
23     ! idx_BTD : map from indices i,j onto element in block-tridiagonal matrix
24     GFinv(idx_BTD(2*iu-1, 2*ju-1)) = Z*Sk(ind) - Hk(1, ju, 1, iu)
25     GFinv(idx_BTD(2*iu, 2*ju-1)) =                - Hk(2, ju, 1, iu)
26     GFinv(idx_BTD(2*iu-1, 2*ju )) =                - Hk(1, ju, 2, iu)
27     GFinv(idx_BTD(2*iu, 2*ju )) = Z*Sk(ind) - Hk(2, ju, 2, iu)
28 end do
29 do iElectrode in 1, nElectrodes
30     off = Electrodes(iElec)%offset ! Position of first electrode orbital in device
31     do jElec, iElec = 1, Electrodes(iElec)%orbitals()
32         i = 2*iElec - 1
33         j = 2*jElec - 1
34         do ii,jj = 1, 2
35             Gfinv(idx_BTD(i+ii, j+jj)) = El%Sigma(ii, iElec, jj, jElec)
36         end do
37     end do
38 end do

```

Listing 2: Dummy code for setting up the inverse Green's function

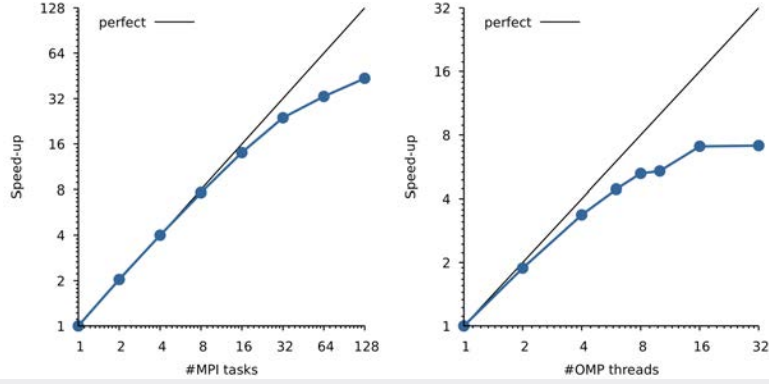


Figure 6.1: Performance characterization of TRANSIESTA using a Fe/MgO/Fe tunneling junction with 816 atoms (11088 orbitals)

remains good up to 16 threads. The reported OMP performance characteristics show slightly better scaling with the number of OMP threads than previously reported [Pap+17]. Improved scaling results from the larger block sizes in the BTD matrix due to the spin blocks.

6.2 Postprocessing

6.2.1 Spin Channel Projected Transmission

There are several approaches to analyze transport properties by calculating the local density of states, transmission eigenchannels [PB07], bond-currents [Sol+10] or molecular state projection transmission [Pap+17]. With these methods, it is possible to gain insight into which states or regions contribute to the transmission. Similarly, it might be desirable to decompose the transmission into contributions of different spin channels and transitions between them. In the collinear spin case, this decomposition arises naturally since all operators are diagonal in spin space. In the non-collinear case, the spin-up and spin-down transmission can be recovered discarding the off-diagonal spin terms of the scattering matrix $\mathbf{s}^{\uparrow\downarrow}$ and $\mathbf{s}^{\downarrow\uparrow}$. We can then calculate the transmission probability between states with the same spin σ .

$$T_{e,e'}^{\sigma\sigma}(z) = \int_{\text{BZ}} d\mathbf{k} \text{Tr} \left\{ \mathbf{s}_{e,e',\mathbf{k}}^{\sigma\sigma} \mathbf{s}_{e,e',\mathbf{k}}^{\sigma\sigma\dagger} \right\} \quad (6.16)$$

In addition to the spin-up and spin-down transmission, we might also find a non-zero probability for transmission between states with opposite spins

$$T_{e,e'}^{\sigma\sigma'}(z) = \int_{\text{BZ}} d\mathbf{k} \text{Tr} \left\{ \mathbf{s}_{e,e',\mathbf{k}}^{\sigma\sigma'} \mathbf{s}_{e,e',\mathbf{k}}^{\sigma'\sigma\dagger} \right\} \quad (6.17)$$

Such spin-flip transitions are possible because the Green's function matrix couples the different spin channels. The total transmission can be recovered as the sum of spin-up and spin-down and spin-flip transmissions.

$$T_{e,e'}^{\text{total}} = T_{e,e'}^{\uparrow\uparrow} + T_{e,e'}^{\uparrow\downarrow} + T_{e,e'}^{\downarrow\uparrow} + T_{e,e'}^{\downarrow\downarrow} \quad (6.18)$$

More generally, we might be interested in the transmission probability between states with spin (up or down) along an axis \vec{n} in electrode e and along axis \vec{m} in electrode e' . We can easily generalize the spin-projected transmission function to the case of arbitrary polarization axes

$$T_{e,e'}^{\sigma\vec{n},\sigma'\vec{m}}(z) = \int_{\text{BZ}} d\mathbf{k} \text{Tr} \left\{ \langle \sigma\vec{n} | s_{e,e',\mathbf{k}}^\dagger | \sigma'\vec{m} \rangle \langle \sigma'\vec{m} | s_{e,e',\mathbf{k}} | \sigma\vec{n} \rangle \right\} \quad (6.19)$$

where $|\sigma\vec{n}\rangle$ is the eigenstate of the spin operator oriented along \vec{n} with eigenvalues σ , that is, $\sigma|\sigma\vec{n}\rangle = (\sum_{i=x,y,z} n_i \hat{\sigma}_i) |\sigma\vec{n}\rangle$.

Instead of implementing Equation (6.19) directly and constructing the scattering matrices, we define the spin projected broadening matrix and the spin projected spectral density matrix.

$$\Gamma_{e,\mathbf{k}}(z)^{\sigma\vec{n}} = \Gamma_{e,\mathbf{k}}(z)^{\frac{1}{2}} |\sigma\vec{n}\rangle \langle \sigma\vec{n}| \Gamma_{e,\mathbf{k}}(z)^{\frac{1}{2}} \quad (6.20)$$

$$\mathcal{A}_{e,\mathbf{k}}(z)^{\sigma\vec{n}} = \mathbf{G}_{\mathbf{k}}(z) \Gamma_{e,\mathbf{k}}(z)^{\sigma\vec{n}} \mathbf{G}_{\mathbf{k}}^\dagger(z) \quad (6.21)$$

We can then rewrite the spin projected transmission as

$$T_{e,e'}^{\sigma\vec{n},\sigma'\vec{m}}(z) = \int_{\text{BZ}} d\mathbf{k} \text{Tr} \left\{ \Gamma_{e,\mathbf{k}}(z)^{\sigma\vec{n}} \mathcal{A}_{e',\mathbf{k}}(z)^{\sigma'\vec{m}} \right\} \quad (6.22)$$

To calculate the spin-projected broadening matrices $\Gamma^{\sigma\vec{n}}$, we (1) diagonalize Γ to obtain the eigenvalues d_i and the eigenvectors matrix v ($v_j^\dagger \Gamma v_i = d_i \delta_{ij}$), (2) construct the matrix square root of Γ ($\Gamma_{ij}^{1/2} = \sum_k (v_k)_i \sqrt{d_k} (v_k)_j^*$), and (3) calculate the triple matrix product $\Gamma^{1/2} |\sigma\vec{n}\rangle \langle \sigma\vec{n}| \Gamma^{1/2}$.

We also explored an alternative approach to calculating the spin-channel projected transmission, following the same strategy employed to define the molecular state projection transmission [Tod02]. Instead of projecting the broadening matrices Γ_e onto molecular eigenstates, we project them onto different spin channels. In this light, we can define the transmission between a spin channel \vec{n} in electrode e and a spin channel \vec{m} in electrode e' as

$$T_{e,e'}^{\sigma\vec{n},\sigma'\vec{m}}(z) = \int_{\text{BZ}} d\mathbf{k} \text{Tr} \left\{ \langle \sigma\vec{n} | \Gamma_{e,\mathbf{k}}(z) | \sigma\vec{n} \rangle \langle \sigma\vec{n} | \mathbf{G}_{\mathbf{k}}(z) | \sigma'\vec{m} \rangle \right. \\ \left. \langle \sigma'\vec{m} | \Gamma_{e',\mathbf{k}}(z) | \sigma'\vec{m} \rangle \langle \sigma'\vec{m} | \mathbf{G}_{\mathbf{k}}^\dagger(z) | \sigma\vec{n} \rangle \right\}. \quad (6.23)$$

If the spins in both electrodes are collinear and aligned with the projection axes \vec{n} and \vec{m} , then the projector and the broadening matrix commute, and both approaches are equivalent. However, if the electrode states at a given energy are not collinear, the resulting transmission is incorrect. In [Chapter 11](#), we will see an example of this. Therefore, the latter approach is generally not applicable in fully relativistic calculations. It can find applications in calculations where both electrodes are perfectly collinear and non-collinear effects occur only in the scattering region. Directly projecting the broadening matrix is less computationally demanding than the first approach because it avoids diagonalizing the broadening matrix. However, in most cases the number of electrode orbitals is small compared to the scattering device and in these cases diagonalizing the broadening matrix will not affect the computing time significantly. For these reasons, we have enabled the scattering matrix approach as the default way of calculating spin channel projected transmissions.

In this chapter, we present how we implemented the BdG+DFT method in SIESTA. The initial implementation of the method was performed by Gabor Csire in the group of Prof. Pablo Ordejón at ICN2, Barcelona. The completion, parallelization, and improvement of this implementation is an ongoing collaborative effort with the group of Prof. Zeila Zanolli at the University of Utrecht. The development version of SIESTA with support for BdG calculations can be found online at <https://gitlab.com/nils.wittemeier/bdg-siesta/-/tree/bdg-future>. A publication of the work presented in this chapter and its applications to a selected test systems is currently in preparation.

7.1 The BdG Equation for Localized Basis Sets

In order to implement the BdG method in SIESTA, we need to rewrite the BdG equation (Equation (5.16)) in terms of the localized basis sets. Since we will use periodic boundary conditions, we first expand the Bogoliubon amplitudes $u_{\sigma}^{\tilde{n}}$ and $v_{\sigma}^{\tilde{n}}$ in terms of Bloch waves

$$u_{\sigma}^{\tilde{n}}(\mathbf{r}) = u_{\sigma}^{nk}(\mathbf{r})e^{i\mathbf{k}\mathbf{r}} \quad v_{\sigma}^{\tilde{n}}(\mathbf{r}) = v_{\sigma}^{nk}(\mathbf{r})e^{i\mathbf{k}\mathbf{r}} \quad (7.1)$$

and then expand the Bloch wave in terms of a localized basis set ϕ_{ν} .

$$u_{nk}^{\sigma}(\mathbf{r}) = \sum_{\mathbf{R}\nu} u_{nk}^{\nu\sigma} \phi_{\nu}(\mathbf{r} - \mathbf{R}) \quad (7.2)$$

$$v_{nk}^{\sigma}(\mathbf{r}) = \sum_{\mathbf{R}\nu} v_{nk}^{\nu\sigma} \phi_{\nu}(\mathbf{r} - \mathbf{R}) \quad (7.3)$$

where the sum runs through all lattice vectors \mathbf{R} and all orbitals ν within the unit cell.

To obtain the BdG equation for localized basis sets, we insert these identities in Equation (5.16), multiply the equation from the left with $\phi_{\mu}^*(\mathbf{r})e^{-i\mathbf{k}\mathbf{r}}$ and integrate over \mathbf{r} . Furthermore, we assume that the pairing potential $\Delta(\mathbf{r}, \mathbf{r}')$ and the anomalous density $\chi(\mathbf{r}, \mathbf{r}')$ are local, that is, $\Delta(\mathbf{r}, \mathbf{r}') = \Delta(\mathbf{r})\delta(\mathbf{r}, \mathbf{r}')$ and $\chi(\mathbf{r}, \mathbf{r}') = \chi(\mathbf{r})\delta(\mathbf{r}, \mathbf{r}')$. The assumption of locality drastically

simplifies the calculations and is therefore widely applied [Csi+18; Csi17; RB22a; RB22b; STG93].

$$E_{nk} \underbrace{\sum_{\mathbf{R}} e^{i\mathbf{k}\mathbf{R}} \mathbf{S}_{\mu\nu}(\mathbf{R})}_{\mathbf{S}_{\mu\nu}(\mathbf{k})} \begin{pmatrix} u_{v\uparrow}^{nk} \\ u_{v\downarrow}^{nk} \\ v_{v\uparrow}^{nk} \\ v_{v\downarrow}^{nk} \end{pmatrix} = \sum_{\mathbf{R}} e^{i\mathbf{k}\mathbf{R}} \underbrace{\mathbf{H}_{\mu\nu}^{\text{BdG}}(\mathbf{R})}_{\mathbf{H}_{\mu\nu}^{\text{BdG}}(\mathbf{k})} \begin{pmatrix} u_{v\uparrow}^{nk} \\ u_{v\downarrow}^{nk} \\ v_{v\uparrow}^{nk} \\ v_{v\downarrow}^{nk} \end{pmatrix} \quad (7.4)$$

where

$$\mathbf{S}_{\mu\nu}(\mathbf{R}) = \int d\mathbf{r} \phi_{\mu}(\mathbf{r}) \phi_{\nu}(\mathbf{r} - \mathbf{R}) \mathbb{1}_4 = s_{\mu\nu}(\mathbf{R}) \begin{pmatrix} 1 & 0 & 0 & 0 \\ 0 & 1 & 0 & 0 \\ 0 & 0 & 1 & 0 \\ 0 & 0 & 0 & 1 \end{pmatrix} \quad (7.5)$$

$$\begin{aligned} \mathbf{H}_{\mu\nu}^{\text{BdG}}(\mathbf{R}) &= \int d\mathbf{r} \phi_{\mu}(\mathbf{r}) \mathbf{H}_{\text{BdG}}(\mathbf{r}) \phi_{\nu}(\mathbf{r} - \mathbf{R}) \\ &= \begin{pmatrix} h_{\mu\uparrow\nu\uparrow}(\mathbf{R}) & h_{\mu\uparrow\nu\downarrow}(\mathbf{R}) & \Delta_{\mu\uparrow\nu\uparrow}(\mathbf{R}) & \Delta_{\mu\uparrow\nu\downarrow}(\mathbf{R}) \\ h_{\mu\downarrow\nu\uparrow}(\mathbf{R}) & h_{\mu\downarrow\nu\downarrow}(\mathbf{R}) & \Delta_{\mu\downarrow\nu\uparrow}(\mathbf{R}) & \Delta_{\mu\downarrow\nu\downarrow}(\mathbf{R}) \\ -\Delta_{\mu\uparrow\nu\uparrow}^*(\mathbf{R}) & -\Delta_{\mu\uparrow\nu\downarrow}^*(\mathbf{R}) & -h_{\mu\uparrow\nu\uparrow}^*(\mathbf{R}) & -h_{\mu\uparrow\nu\downarrow}^*(\mathbf{R}) \\ -\Delta_{\mu\downarrow\nu\uparrow}^*(\mathbf{R}) & -\Delta_{\mu\downarrow\nu\downarrow}^*(\mathbf{R}) & -h_{\mu\downarrow\nu\uparrow}^*(\mathbf{R}) & -h_{\mu\downarrow\nu\downarrow}^*(\mathbf{R}) \end{pmatrix} \end{aligned} \quad (7.6)$$

$$h_{\mu\sigma\nu\sigma'}(\mathbf{R}) = \int d\mathbf{r} \phi_{\mu}(\mathbf{r}) h_{\sigma\sigma'}(\mathbf{r}) \phi_{\nu}(\mathbf{r} - \mathbf{R}) \quad (7.7)$$

$$\Delta_{\mu\sigma\nu\sigma'}(\mathbf{R}) = \int d\mathbf{r} \phi_{\mu}(\mathbf{r}) \Delta_{\sigma\sigma'}(\mathbf{r}) \phi_{\nu}(\mathbf{r} - \mathbf{R}). \quad (7.8)$$

7.2 Solution Methods

BdG calculations are always performed on top of fully relativistic calculations and can currently not be performed on top of collinear spin or spin-unpolarized calculations. We implemented three different solution methods for BdG calculations, which treat self-consistency at different levels:

1. **One-shot** method: Performs a normal state DFT calculation to find self-consistent h and n . After convergence, we switch from a normal spinor calculation to a Nambu spinor calculation to calculate bands, density-of-states, and other quantities in the analysis phase of SIESTA. At this stage, the pairing potential is used exactly as specified in the input file. This method has significantly lower computational cost compared to the *fixed- Δ* and *fixed- Λ* methods (see below), which have two times more wave functions and two

times more coefficients per wave function. However, the assumption behind the *one-shot* method is that the perturbations of h and n are negligible. This may be true for very small pairing potentials Δ . In general, it is well suited to test the effects of different choices of Δ , but users are advised to double-check the results obtained with this method with one of the more advanced methods.

2. **Fixed- Δ** method: Performs a calculation with Nambu spinors⁶. At every step of the self-consistent cycle, the normal part (h) of the BdG Hamiltonian and the normal density n are updated. The pairing Δ is kept constant throughout the calculation. The Fermi level is shifted to zero at the beginning of the calculation and is not updated. This means that *fixed- Δ* does not take into account particle conservation. Technically, the Fermi level could be updated to keep the number of the particles $N_{\text{elec}} = \text{Tr}\{n\mathbf{S}\}$ fixed. However, the pairing potential Δ is typically a small perturbation, and the change in the number of particles is multiple orders of magnitude lower than the total number of particles.
3. **Fixed- Λ** method: Performs a calculation with Nambu spinors, and updates h , n , Δ , and χ at every step using $\Delta(\mathbf{r}, \mathbf{r}') = \Lambda(\mathbf{r}, \mathbf{r}')\chi(\mathbf{r}, \mathbf{r}')$. This method is an implementation of the full, self-consistent BdG method, excluding particle conservation. Just like the *fixed- Δ* method, this method pins the Fermi level to 0 eV and does not update it.

7.3 Code Structure

Most routines specific to BdG calculations have been isolated in a new module (`m_bdg`). This module contains routines for

1. Parsing BdG-specific input flags; *called only once, during initialization.*
2. Documenting all BdG-specific options in the output file, including options not changed in the input file; *used only once, during initialization.*
3. Setting up the initial guess of Δ ; *used only once during the preparation of the first SCF step.*
4. Calculate and print anomalous charges

$$\chi_{\text{eff}}^{\alpha} = \text{tr}\{\mathbf{S}\chi_{\text{out}}^{\alpha}\}$$

⁶ The Nambu spinor is extension of the Dirac spinor. It describes a four-component (particle-hole + half-integer spin) wave function.

and effective pairing amplitudes.

$$\Lambda_{\text{eff}}^{\alpha} = \text{tr}\{\mathbf{S}\Delta_{\text{in}}^{\alpha}\} / \chi_{\text{eff}}^{\alpha}$$

for the singlet, and three triplet channels ($\alpha \in \{\text{S}, \text{T}_x, \text{T}_y, \text{T}_z\}$) at every SCF step for monitoring purposes.

5. Clean-up of BdG-specific data; used during general clean-up, immediately before the code exits.

During the initialization of SIESTA sparse arrays are allocated to store Δ and the anomalous density χ for the current and the previous SCF step in the same format as all quantities of the normal state. In the *fixed- Λ* method additional memory is allocated to store Λ as a grid quantity.

7.3.1 Updating the Pairing Potential

In order to update the pairing potential Δ in the local pairing approximation (Equation (5.33)), we need to extract χ from u and v at every SCF step. In contrast to the Hamiltonian, we define the matrix elements of χ with respect to the dual basis $\tilde{\phi}^{\mu}$.

$$\tilde{\phi}^{\mu}(\mathbf{r}) = \sum_{\mathbf{R}} (\mathbf{S}^{-1})^{\mu\nu}(\mathbf{R}) \phi_{\nu}(\mathbf{r} - \mathbf{R}) \quad (7.9)$$

$$\int d\mathbf{r} \tilde{\phi}^{\mu}(\mathbf{r}) \phi_{\nu}(\mathbf{r} - \mathbf{R}) = \delta_{\nu}^{\mu} \delta(\mathbf{R}) \quad (7.10)$$

First, we rewrite the anomalous density in terms of the Bogoliubon amplitudes u and v and expand them in the basis of localized orbitals.

$$\begin{aligned} \chi^{\sigma\sigma'}(\mathbf{r}, \mathbf{r}') &= \langle \Psi^{\sigma}(\mathbf{r}) \Psi^{\sigma'}(\mathbf{r}') \rangle \\ &= \phi_{\nu}(\mathbf{r}) \sum_n \left(u_{nk}^{\nu\sigma} v_{nk}^{\mu\sigma'*} f(-E^{nk}) v_{nk}^{\nu\sigma*} u_{nk}^{\mu\sigma'} f(E^{nk}) \right) \phi_{\mu}(\mathbf{r}') \end{aligned} \quad (7.11)$$

where we used Equation (5.14) and the statistical averages $\langle \gamma^{\tilde{n}} \gamma^{\tilde{m}} \rangle = 0$ and $\langle \gamma^{\tilde{n}\dagger} \gamma^{\tilde{m}} \rangle = \delta^{\tilde{n}\tilde{m}} f(E^{\tilde{n}})$. Finally, we obtain the matrix elements

$$\begin{aligned} \chi^{\mu\sigma\nu\sigma'} &= \iint d\mathbf{r} d\mathbf{r}' \tilde{\phi}_{\mu}(\mathbf{r}) \chi(\mathbf{r}, \mathbf{r}') \tilde{\phi}_{\nu}^*(\mathbf{r}') \\ &= \sum_n u_{nk}^{\mu\sigma} v_{nk}^{\nu\sigma'*} f(-E^{nk}) + v_{nk}^{\mu\sigma*} u_{nk}^{\nu\sigma'} f(E^{nk}). \end{aligned} \quad (7.12)$$

This shows how defining the anomalous density matrix with respect to the dual basis makes it easy to calculate $\chi^{\mu\sigma\nu\sigma'}$ directly from u and v . Using the matrix elements with respect to the direct basis would require a triple matrix product $\chi_{\mu\sigma\nu\sigma'} = S_{\mu\alpha}\chi^{\alpha\sigma\beta\sigma'}S_{\beta\nu}$ and calculation $\chi(\mathbf{r}, \mathbf{r}')$. More importantly, this definition makes it possible to convert the matrix $\chi^{\mu\sigma\nu\sigma'}$ to χ in real space.

$$\chi(\mathbf{r}, \mathbf{r}') = \phi_\nu(\mathbf{r})\chi^{\mu\sigma\nu\sigma'}\phi_\mu(\mathbf{r}') \quad (7.13)$$

Doing the same transformation starting from $\chi_{\mu\nu}$, would require calculating the inverse of the overlap matrix, which cannot be done exactly for periodic crystals, and is the resulting matrix would no longer be sparse. In SIESTA the electron density matrix is defined equivalently to avoid similar issues when calculating the electrostatic and exchange-correlation terms of the Hamiltonian from the real-space charge density. Thus, our treatment of the anomalous density matrix is consistent with the existing code base. In BdG calculations, we write the electron density matrix as

$$n^{\mu\sigma\nu\sigma'} = \sum_n u_{nk}^{\mu\sigma*} u_{nk}^{\nu\sigma'} f(E^{nk}) + v_{nk}^{\mu\sigma} v_{nk}^{\nu\sigma'*} f(-E^{nk}). \quad (7.14)$$

We remind ourselves that n only runs over states with positive excitation energy, and therefore the contribution of the second term vanishes at zero temperature. Furthermore, with the vanishing pairing potential $\Delta = 0$, the amplitudes satisfy $v^{\mu\sigma} = u^{\mu\sigma*}$ and we again arrive at the usual expression for the electron density matrix.

$$n^{\mu\sigma\nu\sigma'} = \sum_n u_{nk}^{\mu\sigma*} u_{nk}^{\nu\sigma'} f(E^{nk}) \quad (7.15)$$

Equation (7.12) and Equation (7.14) are implemented in `diagbk` and `diagbkp`. We have implemented the transformation between $\chi^{\mu\nu}$ and $\chi(\mathbf{r}, \mathbf{r}')$ in `chiofd`, the real-space product $\lambda(\mathbf{r}, \mathbf{r}')\chi(\mathbf{r}, \mathbf{r})$ and the calculation of the matrix elements $\Delta_{\mu\nu}$ in `dhbgdscf`.

7.3.2 Solving the Eigenvalue Problem

The energy scale of the superconducting gap is typically significantly smaller than the electronic and spin energy scales. Describing materials at these small energy scales requires very dense grids in reciprocal space and very small electronic temperatures. Additionally, the matrix dimension are a factor of two larger compared to normal spinor calculations and a factor of four larger compared to spin-unpolarized calculations. Due to the cubic scaling of matrix

diagonalization with the matrix size and the necessity of dense grids, BdG+DFT calculation are computationally demanding and efficient parallelization strategies are indispensable. We introduce two new routines to solve the eigenvalue problem and construct the new normal and anomalous density for calculations with Nambu spinors (`diagbk`, which is parallelized over orbitals and `diagbkp`, which is parallelized over k points). These routines are structured in the same way as the diagonalization routines for normal spinor or non-spinor calculations: for every k point $H(k)$ and $S(k)$ are calculated by Fourier transforming the sparse real-space matrices $H(R)$ and $S(R)$. Then the corresponding eigenvalues and occupation levels are calculated. On the basis of the occupations, the minimal number of eigenvectors required to construct the normal and anomalous density is determined. Finally, the eigenvectors are calculated and the normal and anomalous density is constructed. In SIESTA, the sparse matrices like $H(R)$ are distributed over MPI tasks. To perform the calculation in parallel over multiple k points, we gather the distributed parts of the sparse matrices on each MPI task at the beginning of the diagonalization routine. At the end of the routine, we need to sum the contribution to n and χ calculated by each MPI task and again distribute the final matrices. Similarly to `diagbk` and `diagbkp`, we implement two more routines that solve the eigenvalue problem and subsequently calculate the projected density of states (PDOS) (`pdosbk` and `pdosbkp`).

7.3.3 Input Options

For BdG calculations, we introduce a set of new input flags and options. So far, SIESTA has recognized four different spin configurations: *unpolarized* (no spins), *collinear* spins, *non-collinear* spins, and *spin-orbit* (fully relativistic calculations). Now, we introduce a new option *Nambu*, which enables BdG+DFT calculations.

To specify the initial pairing potential, we added new input blocks that allow users to specify whether to use singlet or triplet pairing, its strength, and its complex phase. With these blocks, Δ can be specified on an orbital-by-orbital basis, including options to select the ranges of orbitals in a single line. In the case of triplet pairing, the values for each spin channel can be defined separately. This input format allows for maximum flexibility and a combination of multiple pairing options to create any imaginable electron-hole pairing. In the same format, the pairing amplitude Λ can be specified orbital-by-orbital for each pairing channel.

The user can specify convergence criteria can for the Δ and χ , in addition to the usual criteria. At every SCF, the code will check whether the maximum change in all matrix elements is below the threshold if the convergence check is activated.

7.4 Tests

In order to verify the validity of our implementation we study two test systems: bulk lead (Pb) and bulk iron selenide (FeSe).

7.4.1 Bulk lead (Pb)

Bulk Pb is a conventional s-wave superconductor where the pairing potential arises from electron-phonon interactions [Hei+10; Sir+16; Skl+12]. The superconducting gap of lead is U-shaped, that is, the density of states inside superconducting gap is flat. It rises sharply at the edge of the gap [Lyk+71]. The size of the superconducting gap has been measured between 4.6 and 5 meV depending on the crystal orientation [BM69; Lyk+71].

Based on this knowledge, we use a singlet-pairing potential with a strength of 2.5 meV (half of the gap size) to model the superconducting state of Pb. We assume that this potential is uniform and isotropic, i.e., in matrix form the pairing potential can be written as

$$\Delta_{\mu\nu}(\mathbf{R}) = 2.5 \text{ meV} \begin{pmatrix} 0 & s_{\mu\nu}(\mathbf{R}) \\ -s_{\mu\nu}(\mathbf{R}) & 0 \end{pmatrix} \quad (7.16)$$

and perform a *one-shot* calculation to obtain the density of states for the superconducting phase of Pb. The resulting superconducting gap has a U-shape and is approximately 2 meV wide (Figure 7.1 (a)). The coherence peaks at the edge of the gap are sharp and the density of states forms a small plateau right next to these peaks. All of these aspects are consistent with previous

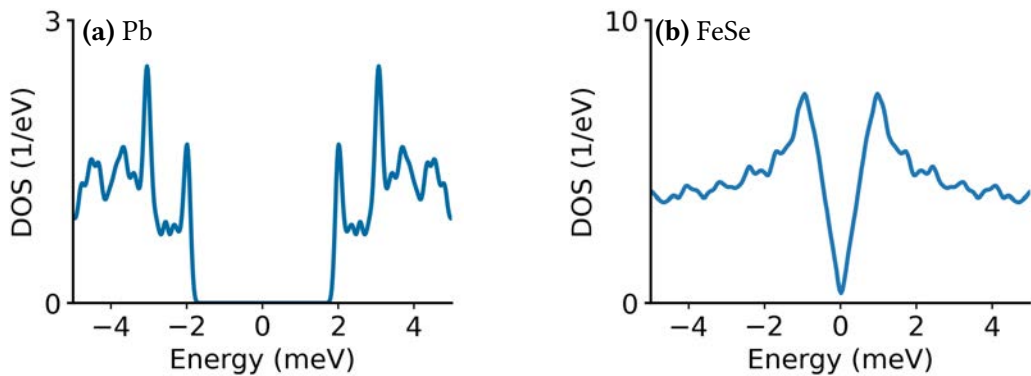


Figure 7.1: Density of states of bulk a conventional (lead, panel (a)) and an unconventional (iron selenide, panel (b)) superconductor calculated with the BdG+DFT method assuming isotropic pairing ($\Delta = 2.5$ meV and 3 meV, respectively). The simulations reproduce the size and shape of experimentally observed superconducting gap [Lyk+71] and [Kas+14], respectively.

measurements [Lyk+71]. The superconducting gap is 0.5 meV smaller than the experimentally observed gap, which indicates the limits of using a phenomenological parameter Δ .

7.4.2 Bulk iron selenide (FeSe)

The origin and character of FeSe and other high-temperature iron-based superconductors remain unclear. However, research thus far suggests that FeSe is unconventional, d-wave superconductor [Bae+15; Mas+16; PG10] driven by pairing interaction in $3d_{xz}$ and $3d_{yz}$ orbitals of iron [Zha+15]. Unlike Pb, the superconducting gap of FeSe is V-shaped and approximately 5 meV wide [Kas+14]. Again, we use a uniform isotropic pairing potential to model the superconducting state in FeSe. Despite this simple guess, the correct shape of the superconducting gap emerges from our calculations (Figure 7.1 (b)). This suggests that orbital symmetries and the electronic structure near the Fermi level are sufficient to explain the V-shape of the superconducting gap.

We limit the pairing interaction to specific orbitals to analyze further the role of different orbitals in opening the superconducting gap. Among the Fe(3d) orbitals, we observe that a pairing potential applied to the d_{xz} and d_{yz} orbitals opens a V-shaped gap (Figure 7.2). The

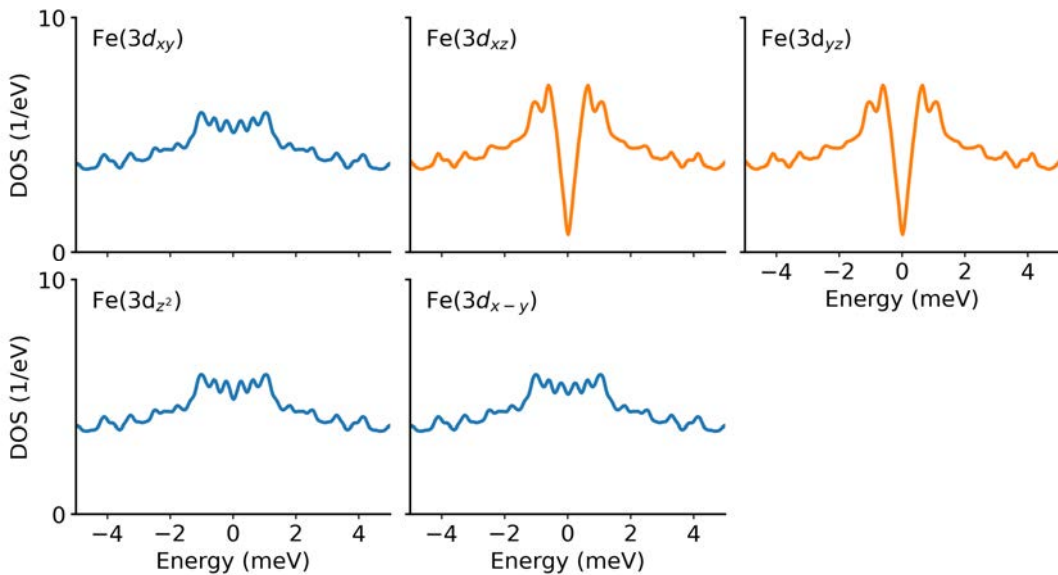


Figure 7.2: Density of states of iron selenide for different pairing potentials calculated with the BdG+DFT method. Each subplot shows the density of states a pairing potential limited to a different Fe-d orbital ($\Delta_{d_v} = 3$ meV). The superconducting gap only emerges if the pairing potential is applied to the d_{xz} or d_{yz} orbitals.

superconducting gap is smaller than the one obtained with isotropic pairing because the pairing interaction is limited to a subset of all orbitals, reducing the pairing potential's average strength. No superconducting gap emerges if the pairing interaction is restricted to any of the other Fe($3d$) orbitals. Similarly, no gap is observed if the pairing potential is restricted to any other shell or Se orbitals. This is consistent with previous analysis of the superconducting state in FeSe, which suggested that the electron and hole pockets formed by d_{xz} and d_{yz} bands are responsible for the superconducting state [Zha+15].

7.4.3 Computational Details

For the lead simulation, we solve the KS-equations using an electronic temperature of 0.1 meV, a $24 \times 24 \times 24$ grid, and a mesh cut-off of 500 Ry. For the simulation of FeSe, we employ an electronic temperature of 0.5 meV, a $29 \times 29 \times 29$ grid for the sampling of reciprocal space, and a mesh cut-off of 1300 Ry. In both cases, the simulations are performed with PBE [PBE96] functional and norm-conserving pseudopotentials from the Pseudo-Dojo database [van+18]. The density of states is sampled on much denser grids in order to obtain sufficient resolution at the meV scale: $120 \times 120 \times 120$ k points for lead and $480 \times 480 \times 120$ k points for iron selenide.

Experimental evidence suggests that FeSe does not possess long-range magnetic order. Even at low temperatures (4 K), spin fluctuations are significant [Wan+16]. These fluctuations occur primarily between two magnetic phases: Néel (or checkerboard) and staggered dimer. Due to the periodic boundary conditions, simulating such a nematic phase would require very large supercells. Instead, we only report results for the Néel magnetic structure with the smaller unit cell. In this magnetic structure, the magnetic moments of neighboring iron atoms are antiparallel.

The simulations presented here were performed with the *one-shot* method, which is already sufficient to obtain qualitatively correct results for the superconducting gap of Pb and FeSe. Using the *fixed- Δ* method for FeSe, we observe no qualitative changes in the density of states and therefore refrain from showcasing them here. A comparison to the *fixed- Λ* method is impossible because we are still finalizing this implementation at the time of writing. A detailed comparison between the different solution methods will be included in our future publication of this method.

8

Tools for Studying Topological Materials

We have designed a set of scripts to calculate and visualize the spin texture of different materials based on `SISL`, a library of tight binding and DFT interfaces, and created an interface between `SISL` and `Z2PACK`, a Python library capable of calculating \mathbb{Z}_2 invariants. We have published these scripts online at <https://github.com/juijan/TopoToolsSiesta>.

Alongside these scripts, we are hosting a set of tutorials developed for the "Advanced school on Quantum Transport using SIESTA", which explain the key concepts behind these calculations and how to perform them.

8.1 Spin Texture

We have created a script (`SpinTexture.py`) to calculate the spin texture of materials from the SIESTA output using the Python library `SISL` as a back-end. Our script provides an interface for users to specify a path in the \mathbf{k} -space and point to the output files. The script then automatically reads the converged SIESTA Hamiltonian and can calculate the spin texture. Currently, users can either manually provide a list of \mathbf{k} points or use one of the following methods to generate a path: circular path (requires center, radius, and number of points or spacing), Monkhorst-Pack grid (requires the number of points in each direction and potentially a shift), linear path (requires a set of edge points to be connected linearly and the number of points along the path). The script uses `SISL` to retrieve the Hamiltonian and the overlap matrix from SIESTA output files and calculate the eigenvalues $\epsilon^{\nu}(\mathbf{k})$ and the spin moments \mathbf{s}^{ν} of each eigenstate.

$$s_{\alpha}^{\nu}(\mathbf{k}) = \langle \phi^{\nu}(\mathbf{k}) | \sigma_{\alpha} \otimes \mathbf{S}(\mathbf{k}) | \phi^{\nu}(\mathbf{k}) \rangle, \quad (8.1)$$

where $\phi^{\nu}(\mathbf{k})$ is the ν -th eigenstate with lattice momentum \mathbf{k} , and $\sigma_{\alpha} \otimes \mathbf{S}(\mathbf{k})$ denotes the Kronecker product of the Pauli matrix σ_{α} and the overlap matrix $\mathbf{S}(\mathbf{k})$. The results are saved in an easily parsable format with one block per band, each containing one line per \mathbf{k} -point (Listing 3). In addition, we have developed a second script (`PlotSpinTexture.py`) to visualize the output of the first script, which can display the magnitude of the spin moments either as a color scale in a typical band structure plot (Figure 8.1), or as arrows in a plane in the \mathbf{k} space (Figure 8.2). Our file format is also compatible with other visualization software such as `GNUPLOT` [Wil+13].

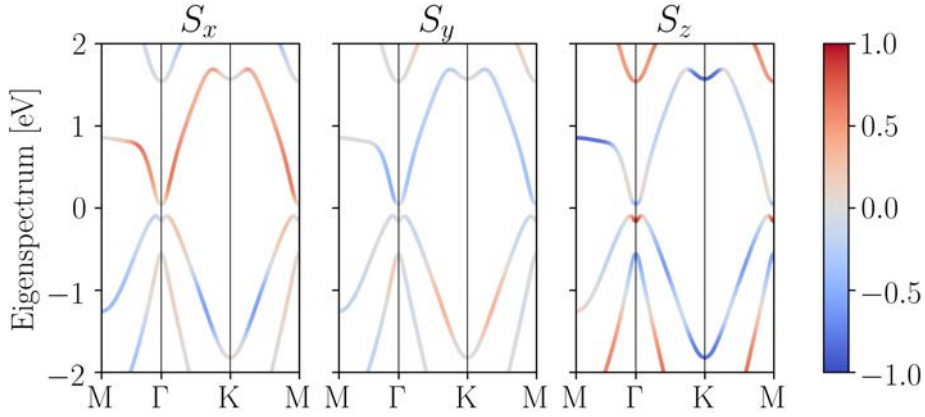


Figure 8.1: Spin texture of a Bi(111) monolayer, the x , y , and z components of the spin texture are indicated by the red-to-blue color scale. Red color represents a state with a magnetic moment of $+\mu_B$, and blue a state with $-\mu_B$. AT the high-symmetry points K and Γ , the spin moments of the highest occupied and lowest unoccupied bands are aligned with the z . Around the K point, the spin moments of the lowest unoccupied are parallel to the lattice plane. Overall the structure exhibits a non-collinear spin texture, which varies particularly rapidly around the avoided crossing at the Γ point.

We also implemented an option to find a closed path on which the energy is constant. This method starts from a circular path and optimizes the distance r_i of each point on the path to the center independently by minimizing the function:

$$f(r_i) = \min \left\{ E^v(r\hat{\mathbf{k}}_i + \mathbf{k}_{\text{center}}) - E^{\text{const}} \right\}, \quad (8.2)$$

where $\hat{\mathbf{k}}_i$ is the normalized vector pointing from the center of the path to the i -th point along the path. For this minimization procedure, it is necessary to specify E^{const} and an interval $[r_{\min}, r_{\max}]$ for the distances from the center. The interval has to be large enough that the constant energy path lies between the two circles defined by the interval. However, if the interval is too large and multiple bands are in the energy window $E(\mathbf{k}(r_{\min}))$ and $E(\mathbf{k}(r_{\max}))$, then the minimization problem may not have a unique solution. Therefore, it is essential to carefully choose r_{\min} and r_{\max} . An example of a spin texture of few-layer Bi_2Se_3 calculated along two constant energy paths obtained by this process is shown in Figure 8.2. These results compare well to ARPES measurements of surface states of Bi_2Se_3 [Che+09]. They reproduce a circular shape with a chiral spin texture close to the charge neutrality point and a star-like shape at higher energies.

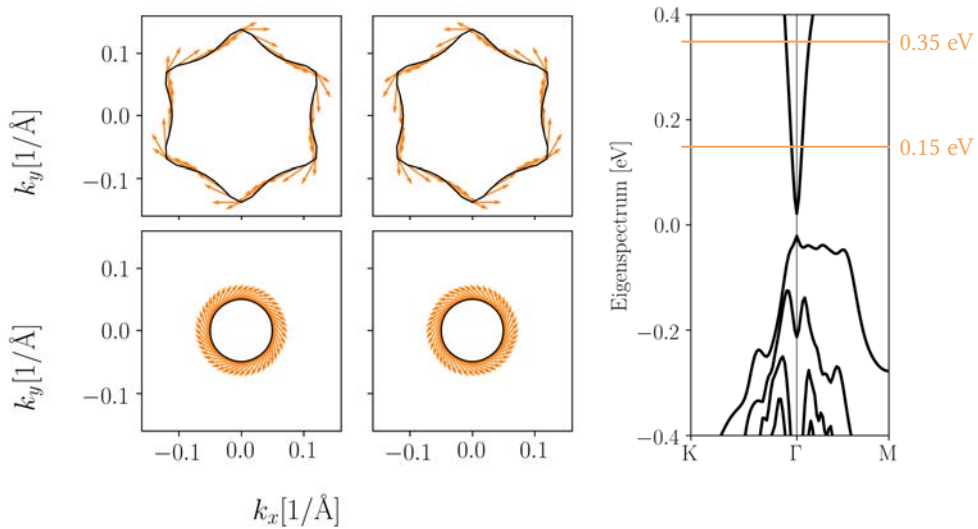


Figure 8.2: In-plane spin texture of 3-quintuple-layer Bi_2Se_3 along two constant energy paths (top: 0.35 eV; bottom: 0.15 eV). For reference, the band structure along the $K - \Gamma - M$ direction is shown on the right side. The two Kramer's pairs (left/right) have opposite spins at every point along the path. The shape of the paths and the direction of the spin moments reproduce ARPES measurements of surface states in Bi_2Se_3 [Che+09].

```

1  # // ***** HEADER ***** //
2  #   nk, nbnds = <<Number of k points>>, <<Number of bands>>
3  #
4  # Ticks and labels
5  #   tick 1: << Pos of edge point 1 along path >>, << Label of edge point 1 >>
6  #   ...
7  #   tick n: << Pos of edge point n along path >>, << Label of edge point n >>
8  # // ***** BODY ***** //
9  lk( 1) [kx( 1) ky( 1) kz( 1)] e( 1,1) s_x( 1,1) s_y( 1,1) s_z( 1,1)
10 lk( 2) [kx( 2) ky( 2) kz( 2)] e( 2,1) s_x( 2,1) s_y( 2,1) s_z( 2,1)
11 ...
12 lk(nk) [kx(nk) ky(nk) kz(nk)] e(nk,1) s_x(nk,1) s_y(nk,1) s_z(nk,1)
13
14 lk( 1) [kx( 1) ky( 1) kz( 1)] e( 1,2) s_x( 1,2) s_y( 1,2) s_z( 1,2)
15 ...
16 lk(nk) [kx(nk) ky(nk) kz(nk)] e(nk,nbnds) s_x(nk,nbnds) s_y(nk,nbnds) s_z(nk,nbnds)

```

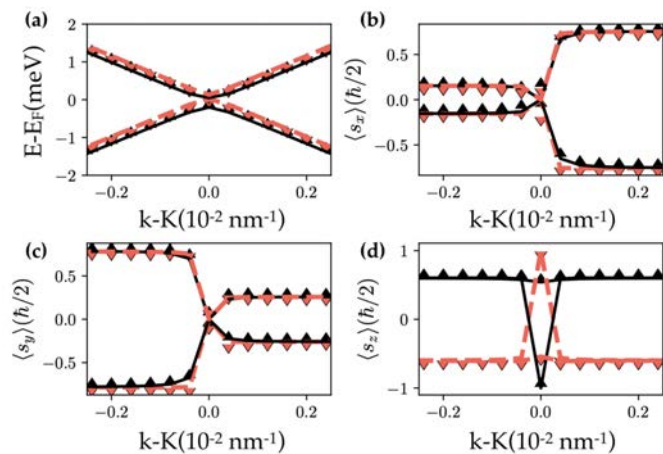
Listing 3: Output file format of our spin texture tool. If the user has specified a path defined by multiple edge points, the file contains the positions of all points along the path $lk(i)$ in units of $1/\text{\AA}$. In all other cases, the first three columns of the file contain the x , y , and z coordinates of k points in units of $1/\text{\AA}$. Energies e are specified in eV and are the unit less expectation value of the spin-momentum operators for the corresponding eigenstate.

8.1.1 Application: Manipulation of Spin Transport in Graphene/Transition Metal Dichalcogenide Heterobilayers upon Twisting

We have also employed our spin texture tool to calculate the spin texture of twisted graphene/transition metal dichalcogenide (TMD) bilayers [Pez+21]. Graphene possesses large carrier mobility and long spin relaxation lengths, making it a great candidate for application in spintronics [Fer+15; Hal19; Roc+15; Sie+21]. However, its weak intrinsic spin-orbit coupling is detrimental for electronic control of spins [Fer+15; GN07; Roc+15]. Enhancing the SOC of graphene via proximity interaction with another 2D material with strong SOC is a possible solution to this problem. A prime example for this are graphene/transition-metal dichalcogenides (TMDs) heterostructures [AAU16; AAU18; Avs+14; CFR18; Dav+19; Gmi+16]. Some experimental studies suggest that the strength of the induced SOC can be as high as 10 meV [Wak+18; Wak+19; Wan+15], while first principles calculation predict spin-orbitcoupling parameters between 0.1 meV and 1 meV [AAU16; AAU18; Avs+14; CFR18; Dav+19; Gmi+16; LK19]. This discrepancy could be the result moiré physics, which could induces modulation of the SOC depending on the the strain and rotational alignment of the two materials [AAU18; Dav+19; LK19].

We performed large-scale DFT simulations of graphene/TMD heterostructure with various rotational alignments and different strains. We used our new tool to extract the band structure from the first principles wavefunction (Figure 8.3). Our collaborators used this data to fit a spin-orbit coupling Hamiltonian model for graphene based on the model proposed by Kochan et al. [KIF17]. From this model, it was possible to extract the strength of different spin-orbit coupling and the dependence on the twist angle and applied strain published in [Pez+21].

Figure 8.3: Electronic band structure around one of the Dirac points (a) and spin texture components (b-d) computed from DFT (symbols) and model Hamiltonian (lines) for graphene/MoTe₂ twisted by 15°. Red and black colors identify spin-up and down, respectively. Spin textures in momentum space are computed along the same path as the band structure. © IOP Publishing. Reproduced with permission. All rights reserved.



Using the spin texture in addition to the band structure was essential in order to unravel the contribution of different SOC mechanisms (intrinsic, valley Zeeman, Rashba).

Our work demonstrated that the spin-orbit coupling strength in graphene/TMD heterostructure depends strongly on the twist angle and the strain but does not explain the experimentally observed giant enhancement of SOC. Rashba-type SOC was found to be particularly sensitive to strain and twist angle. Furthermore, it was discovered that specific combinations of twist angles and TMDs induce a topological phase in graphene.

8.2 Interface Z2PACK

Topological invariants are calculated in Z2Pack [Gre+17] using Hybrid Wannier Charge Centers (HWCC), which are defined in terms of Hybrid Wannier Functions (HWF). The difference between HWFs and Wannier functions is that the former are localized only in one direction (for instance, x) and delocalized in the others. In 2D, a Hybrid Wannier function can be written as:

$$|n, l_x, k_y\rangle = \frac{1}{2\pi} \int dk_x e^{ik_x l_x a_x} |\psi_{k_x, k_y}^n\rangle \quad (8.3)$$

where n is the band index, l_x is an integer, and a_x is the lattice constant along the direction where the wave function is localized (x). The charge center of an HWF is defined as the average position of the function along x . The hybrid Wannier charge centers are defined modulo the lattice constant as:

$$\bar{x}_n(k_y) = \langle n, 0, k_y | \hat{x} | n, 0, k_y \rangle \pmod{a_x} \quad (8.4)$$

One can think of an HWCC as the charge center of a Wannier function in a 1D system coupled to an external parameter k_y . In this interpretation, the sum of all HWCCs is directly linked to the 1D hybrid electronic polarization (equation 19 in [Gre+17])

$$\mathbf{P}_e^h(k_y) = e \sum_n \bar{x}_n(k_y) \quad (8.5)$$

Although individual HWCCs are not gauge invariant, the sum of all HWCCs and $\mathbf{P}_e^h(k_y)$ are gauge invariant.

Since HWCCs are defined modulo the lattice constant a_x , we can think of $\bar{x}(k_y)$ as a point on the unit circle for any given k_y . As k_y goes from 0 to $2\pi/a_y$ the HWCCs and electronic polarization (\mathbf{P}_e^h) describe the trajectories on a cylinder (Figure 8.4). These trajectories can loop around the cylinder axis an arbitrary number of times. Given that $\bar{x}(0) = \bar{x}(2\pi)$, the number

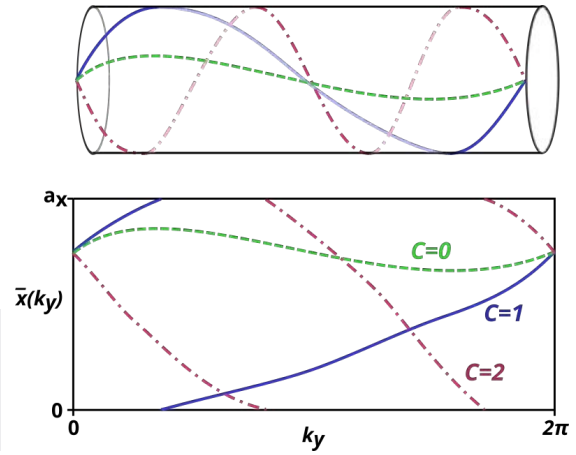


Figure 8.4: Sketch of the three different trajectories of an HWCC as a function of k_y on a rolled (top) and unrolled (bottom) cylinder.

of loops is a well-defined integer, the winding number. The winding number of \mathbf{P}_e^h is equal to the Chern number of the system [Van18]. Therefore, the Chern number of any system can be calculated as the sum of the winding numbers of all HWCCs corresponding to occupied states.

8.2.1 Numerical Computation of Winding Numbers

In order to determine the winding number, we can unroll the cylinder and determine the winding number by counting the number of times the trajectory jumps from one side to the other (Figure 8.4). For example, if the trajectory jumps from $\bar{x} = a_x$ to $\bar{x} = 0$, the winding number increases by one. Instead, the winding number decreases by one for a jump in the opposite direction. To determine \mathbb{Z}_2 , which is defined modulo 2, we can neglect the direction of the jump and count the number of times the trajectory crosses $\bar{x} = 0$. In fact, it is possible to choose any line $f(k_y)$ (green line in Figure 8.5) and count the number of intersections between this line and the trajectories, as long as the line connects the two ends of the cylinder (Figure 8.5). Furthermore, the HWCC trajectories of a Kramer pair (i, j) on each half of the cylinder are related by:

$$\bar{x}_j\left(\frac{\pi}{a_y} + k_y\right) = \bar{x}_i\left(\frac{\pi}{a_y} - k_y\right) \pmod{a_x}. \quad (8.6)$$

due to time-reversal symmetry. Therefore, counting the intersection on one half of the cylinder is sufficient.

Our discussion thus far has focused on continuous trajectories. However, unless we are dealing with a model in which the dependence on k_x and k_y can be expressed analytically, wave functions and HWCCs must be calculated on discrete meshes. In particular, the discretization in k_y can be a numerical challenge: When we calculate the HWCCs for a finite set of k_y , we probe the trajectories on lines (grid lines) parallel to \bar{x} . To correctly determine the winding number,

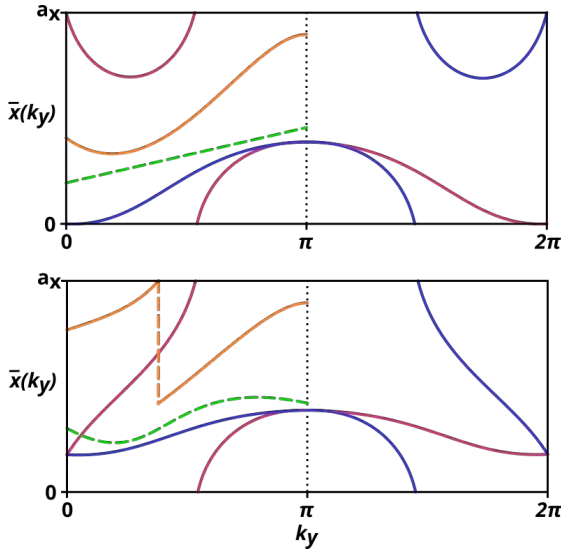


Figure 8.5: Sketch of possible evolutions of HWCCs (red and blue lines) for a system with two occupied bands and time-reversal symmetry. The invariant can be calculated via the number of crossings of the trajectory with the arbitrary line (dashed green) or the line formed by the center of the largest gap (orange). In the top panel, neither line intersects with the trajectories: $\mathbb{Z}_2=0$. In the bottom panel, both lines intersect one time with the trajectories: $\mathbb{Z}_2=1$.

we must determine which points on neighboring grid lines are connected. This requires a sufficiently dense k_y sampling. In principle, increasing the mesh until the connectivity is evident from a visual inspection is possible [RK11]. However, HWCCs typically cluster at some points along k_y . If this clustering occurs near an intersection with $f(k_y)$, a dense grid is required, which can be computationally challenging and difficult to automatize. A different approach, the Vanderbilt method, proposed by A. Soluyanov and D. Vanderbilt [SV11], addresses this issue and offers a systematic way to calculate winding numbers:

1. Evaluate the distances between pairs of neighboring HWCCs at every k_y
2. Find the pair with the largest distance
3. Define the function $g(k_y)$ as the middle point of this distance (orange line in Figure 8.5).
4. Count the number of HWCCs this function $g(k_y)$ crosses from one mesh point to the next

This method is implemented in Z2pack.

So far, Z2Pack was able to perform calculations of \mathbb{Z}_2 using the Vanderbilt method from Wannier coefficients and tight-binding models with orthogonal basis sets. We have now extended Z2Pack to work with non-orthogonal basis sets as well. This involves an extension of the existing interface for tight-binding models, which accepts an overlap in addition to the Hamiltonian. Within this interface, Z2pack now performs a Löwdin transformation of the

Hamiltonian at every k-point to switch to an orthogonal basis set before diagonalization.

$$\tilde{\mathbf{H}}_{\mathbf{k}} = \mathbf{S}_{\mathbf{k}}^{-1/2} \mathbf{H}_{\mathbf{k}} \mathbf{S}_{\mathbf{k}}^{-1/2} \quad (8.7)$$

In [Chapter 10](#), we have used this interface to calculate the topological invariants of two bismuth monolayer phases in free-standing form and supported by a substrate [[WOZ22](#)]. Our new interface correctly reproduces previously published results for the topological invariants of the free-standing monolayers and one of the heterostructures (f-hex@SiC).

Part III

Simulations

Double-wall carbon nanotubes (DWNTs) are prime examples of one-dimensional moiré crystals, which exhibit three distinct coupling regimes: strong coupling, localized insulating, and weak coupling. Here, first-principle methods, a tight-binding model and the Landauer-Büttiker formalism are employed to explain interlayer transport in telescopic DWNTs with finite overlap and interference effects. In the weak coupling regime, the electronic structure of the DWNTs is a superposition of that of the individual tubes, and interlayer transport is suppressed. In the strong coupling regime, interference effects are observable at the mesoscale as a periodic modulation of quantum conductance and emergent localized states. In the localized-insulating regime, similar interference effects cause suppression of interlayer transport and oscillations of the density of states. The results presented here could be used for the design of quantum electronic devices, e.g., nano-electronic switches. The content of this chapter was published in January 2022 in Carbon [Wit+22].

9.1 Introduction: One-Dimensional Moiré Crystals

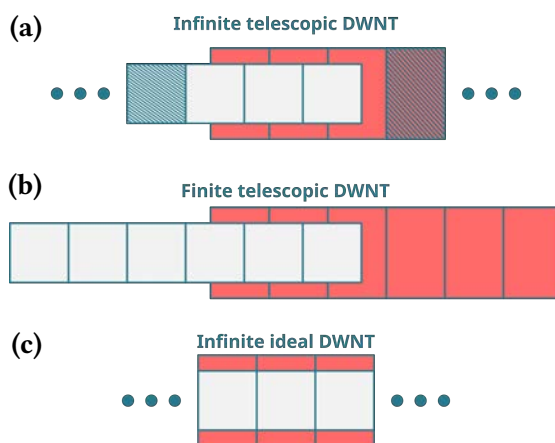
Double-wall carbon nanotubes (DWNTs) are the one-dimensional counterparts of twisted bilayer graphene (tBLG) and a prime example of a one-dimensional moiré system. In tBLG, the effective interlayer interaction is determined by a single parameter, the chiral angle. In contrast, in a DWNT the interlayer interaction depends on two parameters: the angle between the two sheets, like in tBLG, and the difference between the two radii. The difference in radii introduces an effect comparable to that of uniaxial strain applied to one layer of twisted bilayer graphene. Although two-dimensional moiré crystals have been extensively studied, their one-dimensional counterparts are less well understood. Existing studies have addressed ideal, infinite nanotubes [Bon+16; KMS15; Zha+20] and commensurate telescopic nanotubes [GBL04; KC02; TC06; TSH05; UA05; Yan+06].

Recently, Koshino et al. [KMS15] studied the interlayer interaction in ideal infinite DWNTs using a continuum model and proposed a classification of double-wall carbon nanotubes into three groups depending on the nature of the interlayer interaction: *localized insulating* nanotubes, in which dispersionless, flat bands emerge due to electron localization in an effective potential with very long periodicity, *strongly coupled* nanotubes, in which the interlayer interaction strongly perturbs the electronic structure of the individual tubes, and *weakly coupled* nanotubes,

in which the interlayer interaction is negligible, and the electronic structure of the DWNTs is the superposition of the individual tubes. In *strongly coupled* nanotubes, the interlayer interaction can even affect metallicity. As a result, DWNTs composed of two semiconducting tubes may exhibit a finite density of states at the Fermi level and a band gap may open up in DWNTs composed of two metallic nanotubes. The existence of this strong coupling regime has been experimentally confirmed by Zhao et al. [Zha+20] in multi-wall carbon nanotubes (MWNTs). However, the relationship between the measurements and the continuum model for ideal infinite DWNTs is not trivial, and the agreement between measurement and model is only qualitative. In the experiment, the inner tubes are inaccessible, and electrical contacts can only be placed on the outer tube. In addition, the measured nanotubes have finite lengths, and it is not clear whether the coupling regimes predicted by Koshino et al. apply to finite-length tubes or in which limit they are recovered. In finite SWNTs, strong confinement effects occur [RSA99; Rub+99], which could affect DWNTs as well. Answering these basic questions is essential to gain a deeper understanding of carbon nanotubes and making it feasible to incorporate CNTs into future nanoelectronic devices [Nak+20].

In this chapter, we present our answers to these questions achieved by studying the interlayer transport properties of telescopic double-wall carbon nanotubes (tDWNTs). TDWNTs are composed of two concentric nanotubes with finite overlaps that extend infinitely in opposite directions (Figure 9.1 (a)). We unveil how the length of the overlap region affects the electronic structure and the interlayer transport. Our study goes beyond existing works by taking into account the three coupling regimes predicted by Koshino et al. and considering commensurate and incommensurate tDWNT.

Figure 9.1: Schematic of three different types of DWNT geometries: (a) an infinite telescopic DWNT, consisting of two semi-infinite SWNTs with a finite overlap, (b) a finite telescopic DWNT consisting of two finite SWNTs with finite overlap, and (c) infinite, ideal DWNTs consisting of two infinite DWNTs with infinite overlap. Infinite, ideal DWNTs are only periodic along the tube axis if the two layers are commensurate. A periodic approximation of incommensurate DWNTs can be obtained by applying small amounts of strain on both tubes and choosing an appropriate number of repetitions for each tube.



9.2 Basics of Carbon Nanotubes

Carbon is one of the most versatile elements known to humankind. Despite missing only two electrons to a noble state configuration, carbon can form up to four bonds with neighboring atoms. This becomes possible through rehybridization between the $2s$ and $2p$ valence shells, which form new orbitals sp^3 , sp^2 , sp . Each type of hybridized orbitals gives rise to different shape and directionality: sp^3 hybridization is found in methane and diamonds, sp^2 hybridization in graphite and its derivatives, and sp hybridization in linear molecules like acetylene. The different bond formations also give rise to drastically different physical properties and are the basis of Carbon's versatility.

Carbon nanotubes (CNTs), a carbon-based nanostructure made up of one or more cylinders that surround one another, have raised broad fundamental and technological interests since their discovery in 1991 by Iijima [Iij91]. Each layer of a CNTs is a rolled-up sheet of graphene [Nov04] and has a diameter on the nanoscale. Single-walled carbon nanotubes (SWNTs) are fully characterized by the chiral vector $C_h = n \mathbf{a}_1 + m \mathbf{a}_2 \equiv (n, m)$ along which the nanotubes are rolled (Figure 9.2). In the first approximation, the electronic structure can be inferred from that of graphene by considering that rolling-up sheets of graphene introduce periodic boundary conditions along the chiral vector. The periodic boundary conditions quantize the allowed wave vectors perpendicular to the tube axis, and the CNT electronic structure is given by parallel cuts through the BZ of graphene. This zone-folding approximation predicted that CNTs with $n \equiv m \pmod{3}$ are metallic and CNTs with $n - m \equiv \pm 1 \pmod{3}$ are semiconducting. The band gap of semiconducting CNTs is inversely proportional to the tube diameter. In CNTs metallic nanotubes, the Dirac point of graphene is preserved, which makes these tubes metallic. However, curvature effects induce a secondary tiny band gap in all nanotubes with

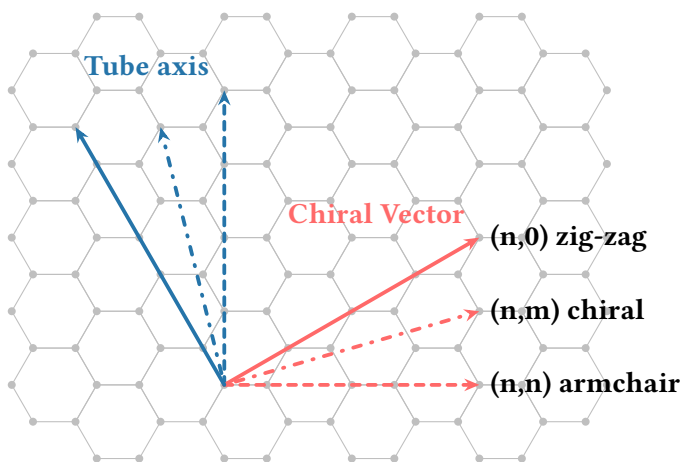


Figure 9.2: Schematic of three chiral vectors and corresponding carbon nanotube axes.

$n \neq m$, which scales inversely with the square of the diameter of the tube. As a result, only the armchair nanotubes ($n = m$) are truly metallic. While the electronic structure of SWNTs can be understood well using such a simple picture, double-wall carbon nanotubes (DWNTs) are far more complex.

9.3 Methodology

9.3.1 First-Principles Calculations

We performed DFT simulations of ideal, infinite CNTs using the SIESTA [Gar+20; Sol+02] DFT implementation and modeled telescopic double-wall carbon nanotubes using the NEGF-code TRANSIESTA [Bra+02; Pap+17]. We extracted transmission functions and the density of states from the converged Hamiltonians using the TBTRANS postprocessing tool [Pap+17]. We employed the LDA exchange-correlation functional as parametrized J. P. Perdew and Y. Wang [PBE96], which has proven to be well suited for carbon-based nanostructure [RS09]. In conjunction with LDA, we used norm-conserving Vanderbilt (ONCV) scalar-relativistic pseudopotentials [Ham13; van+18] with $2s$ and $2p$ valence electrons. We expanded the Kohn-Sham states in a custom double- ζ basis set (Listing 4), which includes two sets of $2s$ and $2p$ orbitals and an additional single set of $3p$ orbitals. The first sets of $2s$ and $2p$ orbital have a cut-off radius larger than the default to ensure that interlayer interactions are modeled correctly. Comparison between SIESTA and QUANTUMESPRESSO (plane-waves) calculations revealed that basis sets

```

1 # Atomic Label, number l-shells, ionic charge
2 C      3      -0.0671
3 # ===== Carbon 2s =====
4 # n, l, Nzeta, soft conf. pot., V_0[Ry], r_i[Bohr]
5 n=2  0  2      E      37.7993  5.9570
6      7.35211218440568  4.86544155511571 # cut-off radii [Bohr]
7 # ===== Carbon 2p =====
8 n=2  1  2      E      37.1931  3.4222
9      7.67179628290414  3.04785080450208 # cut-off radii [Bohr]
10 # ===== Carbon 3d =====
11 n=3  2  1      E      47.1819  0.0109
12      5.12166197009186      # cut-off radius [Bohr]
```

Listing 4: Custom basis set for carbon including two sets of $2s$ and $2p$ atomic orbitals and a single set of $3d$ orbitals to increase variational degrees of freedom. The first sets of $2s$ and $2p$ orbitals are long-range ($> 3.8 \text{ \AA}$ [$7.3 a_0$]) to accurately describe the interlayer interaction in carbon-based nanostructures.

with short cut-off radii fail to account for the interlayer interactions accurately [Gar+09; RLO05]. The Brillouin zone was sampled using a Γ -centered one-dimensional grid of 78 equidistant k -points for the pristine armchair nanotubes and was scaled inversely with the length of the unit cell for longer CNTs.

9.3.2 Tight-Binding Model

To reduce computational complexity, reach the mesoscale regime (up to 100 nm), and make simulations of hundreds of configurations for individual tDWNTs possible, we employ a custom tight-binding (TB) model fitted against *ab initio* calculations. Our TB model is a non-orthogonal tight-binding Hamiltonian with a single $2p$ atomic orbital per carbon site based on the models of Bonnet et al. [Bon+16], Reich et al. [Rei+02], and Trambly de Laissardière et al. [TMM10]. We assume that p orbitals on each carbon atom are perpendicular to the local surface of the cylinder (Figure 9.3). Using the normal vectors $\hat{\mathbf{n}}^i$ we can write the orbital at side i as a linear combination of three p orbitals centered on this site: $|i\rangle = \sum_{v=x,y,z} \hat{\mathbf{n}}_v^i |p_v(\mathbf{R}^i)\rangle$. Using a Slater-Koster parameterization, the hopping and overlap terms between neighboring p orbitals can be described as a linear combination of $pp\pi$ and $pp\sigma$ interactions.

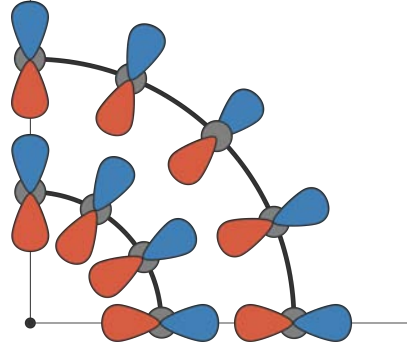


Figure 9.3: Schematic of p orbitals in a double-wall carbon nanotube, each perpendicular to the tube surface.

$$\langle i|\mathbf{H}|j\rangle = \sum_{v,\mu=x,y,z} \hat{\mathbf{n}}_v^i \hat{\mathbf{n}}_\mu^j \left\{ H_{pp\sigma}(d^{ij}) \hat{\mathbf{R}}_v^{ij} \hat{\mathbf{R}}_\mu^{ij} + H_{pp\pi}(d^{ij}) (\delta_{v\mu} - \hat{\mathbf{R}}_v^{ij} \hat{\mathbf{R}}_\mu^{ij}) \right\} \quad (9.1)$$

$$\langle i|\mathbf{S}|j\rangle = \sum_{v,\mu=x,y,z} \hat{\mathbf{n}}_v^i \hat{\mathbf{n}}_\mu^j \left\{ S_{pp\sigma}(d^{ij}) \hat{\mathbf{R}}_v^{ij} \hat{\mathbf{R}}_\mu^{ij} + S_{pp\pi}(d^{ij}) (\delta_{v\mu} - \hat{\mathbf{R}}_v^{ij} \hat{\mathbf{R}}_\mu^{ij}) \right\} \quad (9.2)$$

where $d^{ij} = |\mathbf{R}^i - \mathbf{R}^j|$ is the distance between two atomic sites and $\hat{\mathbf{R}}^{ij} = (\mathbf{R}^i - \mathbf{R}^j)/d^{ij}$ is the normalized vector that points from one site to the other. The $pp\pi$ -terms account for hopping between p orbitals orthogonal to $\hat{\mathbf{R}}^{ij}$. The $pp\sigma$ -terms describe hopping between p orbitals parallel to $\hat{\mathbf{R}}^{ij}$ and are required to describe the curvature dependence of the electronic structure.

We split the tight-binding parameters into intra-layer interactions, in which we describe constant parameters up to third-nearest neighbors. The interlayer interaction is modeled using an exponentially decaying term that is cut off at a distance of 5 Å. In total, this model consists

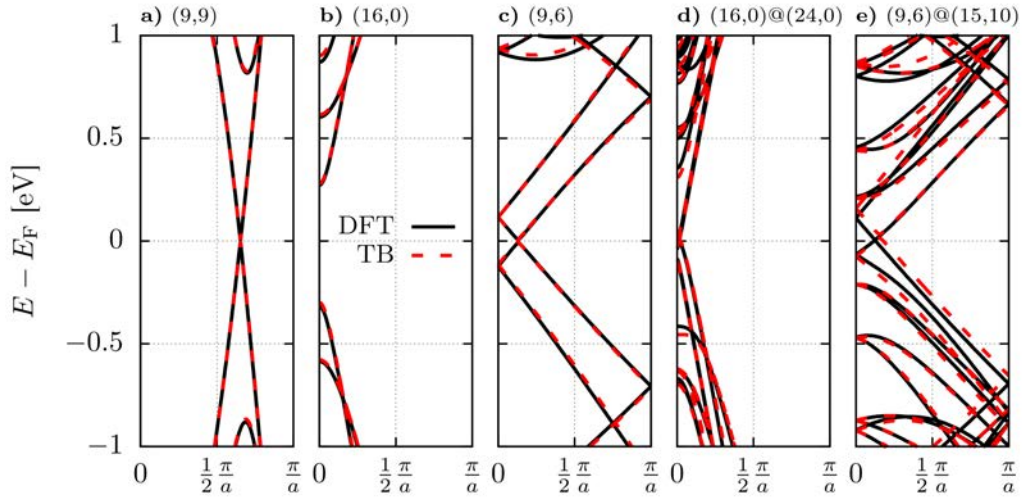


Figure 9.4: Comparison of tight-binding band structures to first-principle simulations for a selection of SWNTs and commensurate DWNTs.

of 21 parameters: on-site energy $E_p = \langle \mathbf{R}_i | \mathbf{H} | \mathbf{R}_i \rangle$ (1), intralayer Hamiltonian (6) and overlap (6), and interlayer Hamiltonian (4) and overlap (4):

$$H_\alpha(d_{ij}) = \begin{cases} H_\alpha^{1nn} & \text{if } i \text{ and } j \text{ are first nearest neighbors} \\ H_\alpha^{2nn} & \text{if } i \text{ and } j \text{ are second nearest neighbors} \\ H_\alpha^{3nn} & \text{if } i \text{ and } j \text{ are third nearest neighbors} \\ H_\alpha^{\text{inter}} e^{(d-a_0)/g_\alpha} & \text{if } i \text{ and } j \text{ in different layers \& } |d_{ij}| < 5 \text{ \AA} \\ 0 & \text{otherwise} \end{cases} \quad (9.3)$$

$$S_\alpha(d_{ij}) = \begin{cases} S_\alpha^{1nn} & \text{if } i \text{ and } j \text{ are first nearest neighbors} \\ S_\alpha^{2nn} & \text{if } i \text{ and } j \text{ are second nearest neighbors} \\ S_\alpha^{3nn} & \text{if } i \text{ and } j \text{ are third nearest neighbors} \\ S_\alpha^{\text{inter}} e^{(d-a_0)/h_\alpha} & \text{if } i \text{ and } j \text{ in different layers \& } |d_{ij}| < 5 \text{ \AA} \\ 0 & \text{otherwise} \end{cases}, \quad (9.4)$$

where $a_0 = 3.35 \text{ \AA}$ is the interlayer spacing of bulk graphite and $\alpha \in \{pp\sigma/pp\pi\}$.

We optimize the parameters to reproduce the *ab initio* band structure of graphene, three small diameter SWNTs, and two DWNTs (Figure 9.4). Fitting to graphene ensures the correct limiting behavior for very large diameter nanotubes and fixes the *pp* π parameters of the intra-layer

Onsite		Intra-Layer			Inter-Layer		
		$pp\sigma$		$pp\pi$	$pp\sigma$		$pp\pi$
E_p [eV]	-2.04	H^{1nn} [eV]	3.93	-2.81	H^{inter} [eV]	0.505	0.709
		S^{1nn}	0.573	0.301	S^{inter}	0.003	0.062
		H^{2nn} [eV]	1.17	-0.679	g [Å]	0.408	0.387
		S^{2nn}	0.018	0.047	h [Å]	1.12	0.620
		H^{3nn} [eV]	1.11	-0.298			
		S^{3nn}	0.074	0.040			

Table 9.1: Optimized tight-binding parameters.

interaction. Small diameter nanotubes, in which curvature effects are strongest, should be used to optimize the $pp\sigma$ terms. However, in nanotubes with radii below 4 Å, rehybridization becomes relevant, which can not be described in our model. Therefore we use three SWNTs with radii between 5.2 Å and 6.2 Å ((9,9), (16,0), and (9,6)) to fix the intra-layer $pp\sigma$ terms. Lastly, we fix the eight parameters of the interlayer interaction using one achiral DWNT, (16,0)@(24,0), and a chiral one, (9,6)@(15,10). In each case, we minimize the absolute difference between the TB and *ab initio* band structure around the Fermi level (from -0.3 eV to 0.3 eV). Table 9.1 summarizes the optimized parameters. In this way, our TB model retains the accuracy of the DFT calculations in the transport-relevant energy window.

9.4 Results and Discussion

We simulate the open quantum system of an infinite telescopic nanotube consisting of two concentric nanotubes with a finite overlap region of length L (Figure 9.5). This transport setup allows us to probe the interlayer interaction directly and is expected to primarily depend on the coupling regimes, assuming they are present in the finite overlap. We start our analysis in the strong coupling regime, discussing the interlayer conductance and its modulation with changing overlap length L . Then we move on to the localized-insulating regime, where we discuss the emergence of localized states in the open system with increasing size of the overlap region. Last, we demonstrate that inter-layer transport is suppressed in the weak coupling regime. In total, we present results for ten different SWNT combinations with all possible combinations of chiralities, commensurabilities, and coupling regimes and with different interlayer spacings (Table 9.2).

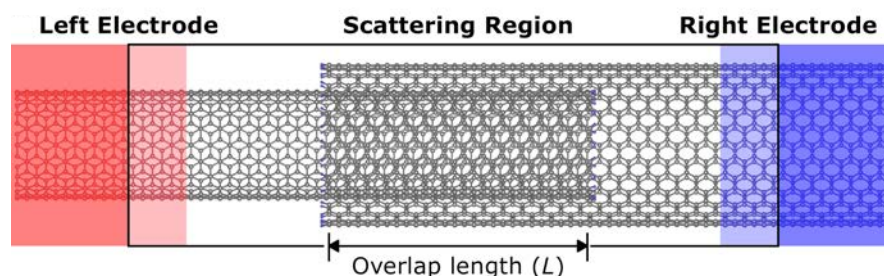


Figure 9.5: Transport set-up: The scattering region consists of two overlapping nanotubes. It encompasses the whole overlap region, a section of the individual tubes required to screen the electrode (light red/blue), and one principle layer of each electrode. The electrodes (red/blue) extend in opposite semi-infinite directions.

A few introductory remarks before discussing the results for individual nanotubes are in order:

1. The edges of the nanotubes in the overlap region do not influence transport properties significantly. Rochefort et al. [RSA99] and Rubio et al. [Rub+99] demonstrated that edge effects are negligible for nanotubes longer than 5 nm to 10 nm and can safely be neglected for our semi-infinite leads.
2. The electron transmission through the scattering device can not exceed the number of electrode channels. If one electrode has n available channels at a given energy and the other $m > n$, then the total transmission is at maximum n . Of course, scattering in the overlap region can always reduce the total transmission below n . For semiconducting tubes, this implies that electron transmission requires the gating of the nanotubes to shift the chemical potential into the valence or conduction bands of both tubes. Alternatively, sufficiently large temperatures could partly populate (depopulate) the conduction (valence) bands and lead to finite transmissions.
3. While the exact crystal structure and some details of the electronic structure can depend on the rotational alignment of the two nanotubes, the moiré lattice vector and, thus, the coupling regime is unaffected by relative rotations.

9.4.1 Strong Coupling Regime

The strong coupling regime encompasses all pairs of nanotubes for which the chiral vectors are nearly parallel, and their difference points along the armchair direction (n, n) . Naturally,

Nanotube	Type	Coupling regime	Commens.	Chirality	Spacing	Main results
(10,10)@(15,15)	(M@M)	Strong coupling	yes	(A@A)	3.39 Å	<ul style="list-style-type: none"> · Tuneable conductance · Localized states
(18,15)@(23,20)	(M@M)	Strong coupling	no	(C@C)	3.48 Å	<ul style="list-style-type: none"> · Tuneable conductance
(27,3)@(36,3)	(M@M)	Localized insulating	no	(C@C)	3.51 Å	<ul style="list-style-type: none"> · Flat bands · Quantization of energy levels
(27,3)@(35,3)	(M@SC)	Localized insulating	no	(C@C)	3.12 Å	<ul style="list-style-type: none"> · Flat bands · Conductance suppressed
(45,18)@(54,18)	(M@SC)	Localized insulating	no	(C@C)	3.40 Å	<ul style="list-style-type: none"> · Conductance suppressed
(399,336)@(408,336)	(M@M)	Localized insulating	no	(C@C)	3.14 Å	<ul style="list-style-type: none"> · Flat bands · Conductance suppressed
(9,0)@(18,0)	(M@M)	Weak coupling	yes	(A@A)	3.52 Å	<ul style="list-style-type: none"> · Tunable conductance
(18,0)@(27,0)	(M@M)	Weak coupling	yes	(A@A)	3.52 Å	<ul style="list-style-type: none"> · Conductance suppressed
(9,0)@(10,10)	(M@M)	Weak coupling	no	(A@A)	3.25 Å	<ul style="list-style-type: none"> · Conductance suppressed
(39,0)@(36,18)	(M@M)	Weak coupling	no	(A@C)	3.37 Å	<ul style="list-style-type: none"> · Conductance suppressed

Table 9.2: Summary of key characteristics of all DWNTs studied in this work. All possible combinations of coupling regimes, chirality, and commensurability are represented. Short-hand notations: Type (M=Metallic, SC=Semiconducting), Chirality (A=Achiral, C=Chiral)

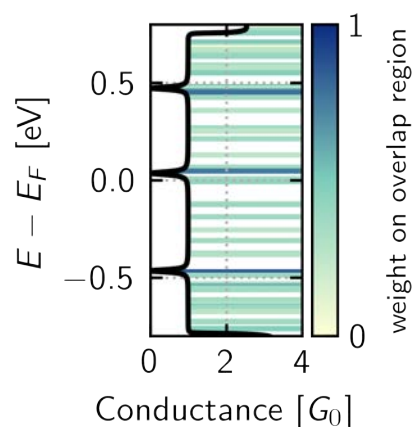
DWNTs composed of two armchair SWNTs (armchair@armchair) fulfill these conditions exactly. Since parallelity of the two chiral vectors is not strictly required, chiral nanotubes $(n,m)@(n+d,m+d)$ can also fall into the strong coupling regime if n and m are sufficiently large. In the following section, we discuss the interlayer transport properties of two strong-coupling tDWNTs with different chirality and commensurability: $(10,10)@(15,15)$ and $(18,15)@(23,20)$.

Achiral and Commensurate: $(10,10)@(15,15)$

For the telescopic DWNT $(10,10)@(15,15)$ with an overlap length of $L = 34.08 \text{ \AA}$, we observe a conductance which is $1G_0$ for most energies near the Fermi level and a series of narrow dips at which the conductance drops to zero (Figure 9.6). For other overlap lengths, the height of the plateaus and the position and width of the dips vary. We will first analyze the special case of $L = 34.08 \text{ \AA}$, before explaining the modulation of the transmission with changing overlap length.

Similar dips have previously been observed in defective and functionalized CNTs [Zan+11; ZC09; ZC10; ZC12]. Here, in the absence of such impurities, the dips have to arise from the interlayer interaction in the finite overlap region. To better understand this effect, it is helpful to consider an isolated, finite $(10,10)@(15,15)$ tDWNT with the same overlap length (Figure 9.1). We start from the scattering region, extend the size of the electrode sections in the scattering region, and place the new CNT system in a large box surrounded by a vacuum. We then determine the energy levels and the wave function for this finite-length approximation of the infinite tDWNT using our TB model. In Figure 9.6, the horizontal lines visualize the position of the tight-binding energy levels of the isolated, finite $(10,10)@(15,15)$ tDWNT with 44 \AA extra electrodes regions on each. Each line is colored according to the weight of the corresponding wave function in the overlap region. We see that each dip corresponds to one

Figure 9.6: TB electron transmission between two semi-infinite SWNTs $((10,10)$ and $(15,15))$ through a finite overlap region with a length of 34.08 \AA . The horizontal lines indicate energy levels of an isolated, finite tDWNT obtained by extending the electrodes in the scattering region by an additional 44 \AA on each side by. The yellow-to-blue scale for horizontal lines indicates the weight of corresponding wave functions in the overlap region. Each dip in conductance coincides (approximately) with one or several localized eigenstates.



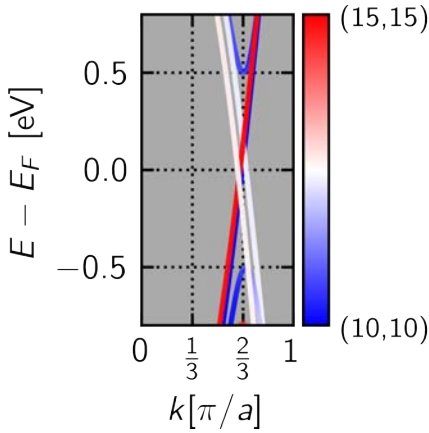


Figure 9.7: Projected TB bandstructure of an ideal (10,10)@(15,15) DWNT (*strongly coupled*). Blue-to-White-to-Red color scale indicates the weight of the wave function on the inner (10,10) and outer (15,15) nanotube. The bands with negative Fermi-velocity (white) are hybridized between the nanotubes, and bands with positive Fermi-velocity (red/blue) are localized on individual SWNTs.

or more eigenstates, which are localized in the overlap region. Depending on the exact size of the included electrode regions, the agreement between the eigenenergies and dip energies varies slightly, but the correspondence remains. In the picture of scattering waves, we can now understand why the conductance curve features multiple dips: rather than simply propagating through the system, wave functions with matching energies scatter with the localized states and are reflected into the same electrode; in-scattering waves with different energies are agnostic to the localized state and can propagate unhindered.

There is another aspect of the calculated conductance that requires explanation: the conductance is limited to $1G_0$. Armchair SWNTs are metallic and their conduction in the linear range around the Dirac point is given by $G = 2G_0$ [CBR07; Dub+09]. Similarly, an ideal infinite armchair@armchair DWNT possesses four channels near the Fermi level (Figure 9.7), and the total conductance of such an ideal DWNT is given by $4G_0$. However, as discussed above, the conductivity in asymmetric transport devices of a telescopic nanotube is limited by the electrode conductivity and, therefore, at most $2G_0$. We can understand this phenomenon by examining the projection of wave functions of the ideal (10,10)@(15,15) DWNT onto the two layers (Figure 9.7). The two linear bands with negative Fermi velocity (negative slope) are perfectly hybridized between the two nanotubes, and the two bands with positive Fermi velocity (positive slope) are fully localized on a single layer of the DWNT. This causes the in-scattering states with positive Fermi velocity to be scattered back into the electrode because these states are insensitive to the interlayer interaction. On the other hand, an in-scattering state with negative Fermi velocity hybridized in the overlap region and can be transmitted seamlessly.

We have performed the same calculations using SIESTA, and the resulting first-principle projected band structure, conductance curve, and the localization of eigenstate in the finite tDWNT agree very well with our tight-binding simulations. Visualization of first-principle

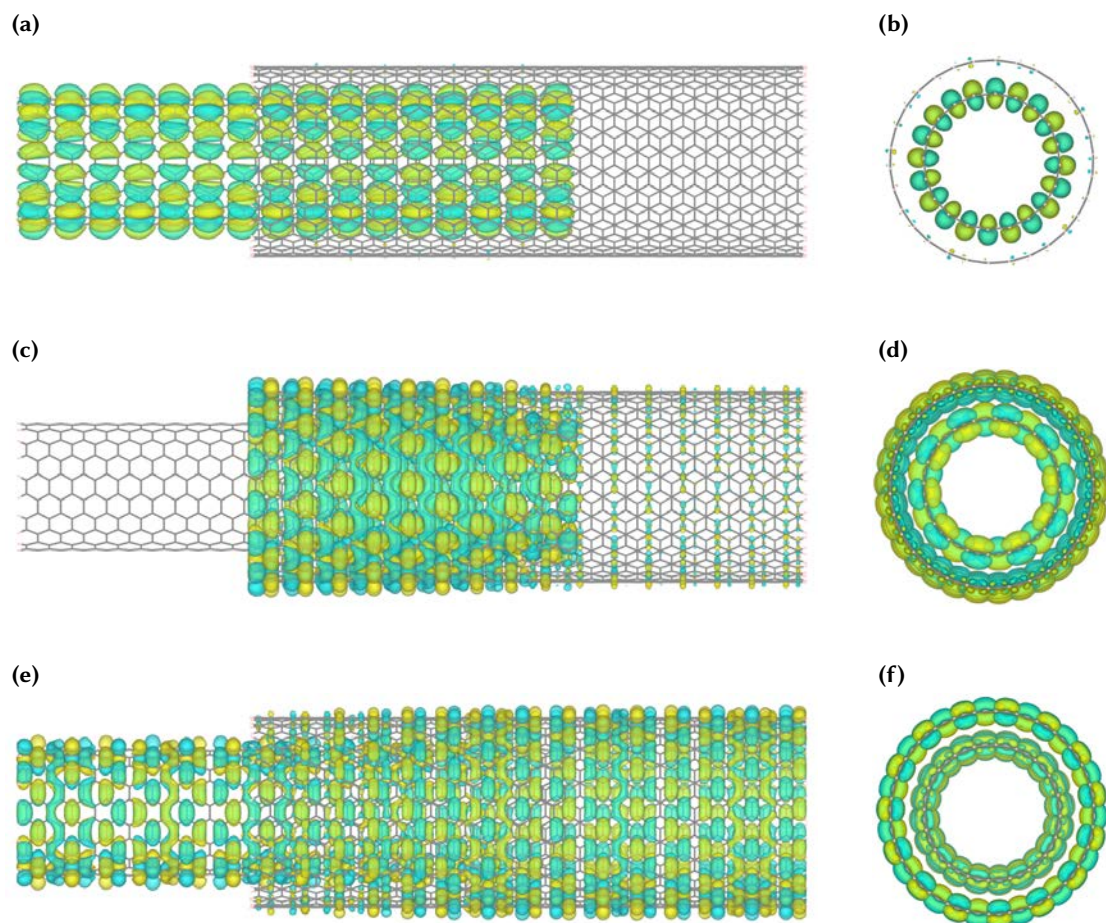


Figure 9.8: DFT wave functions of a telescopic (10,10)@(15,15) DWNT (*strongly coupled*) with an overlap length of 34.08Å: **(a, b)** $E = E_F + 0.005$ eV localized on the inner (10,10) nanotube, **(c, d)** $E = E_F + 0.100$ eV localized in the overlap region, and **(e, f)** $E = E_F + 0.373$ eV delocalized and evenly distributed on both tubes

wave functions beautifully demonstrates the existence of states localized on the inner tube or the overlap region and fully hybridized states (Figure 9.8). The states localized in the overlap region at this overlap length are cone-shaped: the wave function weight on the atoms at the tube terminations is the highest, and they decay towards the electrode regions.

Until now, we have considered only a single overlap length ($L = 34.08 \text{ \AA}$). Our tight-binding model allows us to perform similar calculations for hundreds of configurations of the same DWNT. Scanning a wide range of overlap lengths from 17 \AA to 194 \AA reveals that the number, position, and width of the dips are sensitive to the overlap length (Figure 9.9 (a)). The height of the conductance plateaus in the energy window around the Fermi level oscillates with a periodicity of roughly 100 \AA . It is the largest ($1G_0$) around $L \approx 50 \text{ \AA}$ and $L \approx 150 \text{ \AA}$ and zero around $L \approx 100 \text{ \AA}$ and $L \approx 200 \text{ \AA}$. Similarly, the width of the dips oscillates. Around $L \approx 50 \text{ \AA}$ and $L \approx 150 \text{ \AA}$ the dips in the transmission become very narrow and barely visible; for larger and smaller overlap lengths, the dips become wider until the conduction is completely suppressed around $L \approx 100 \text{ \AA}$ and $L \approx 200 \text{ \AA}$.

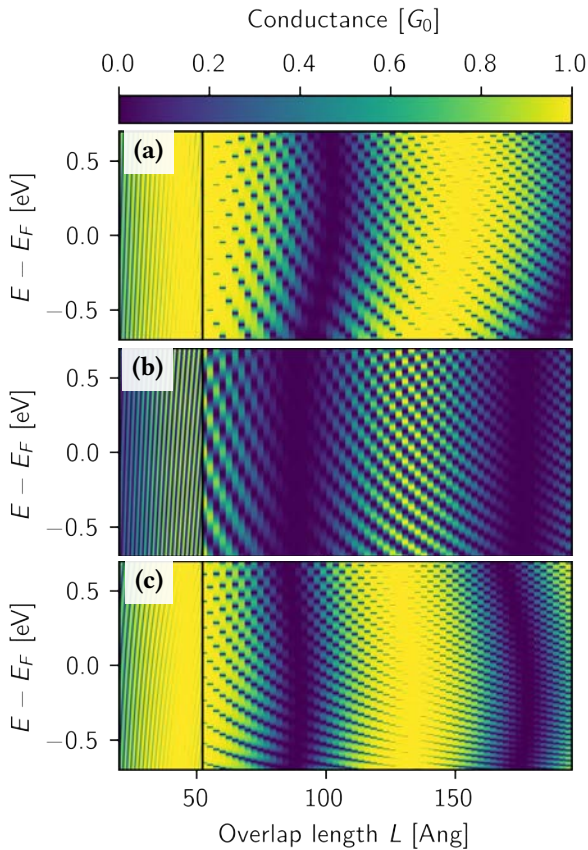


Figure 9.9: TB electron transmission from a (10,10) SWNT into a (15,15) SWNT through a finite overlap region at different overlap lengths calculated with **(a)** LB+TB formalism, and **(b)** our 1D-wave model (Equation (9.5)) with linear band dispersion, and **(c)** our 1D-wave model using band dispersion from the ideal, infinite DWNT. The overlap length L is sampled with a high density ($1/(40 \cdot 2.459 \text{ \AA})$) below 50 \AA and lower density above ($1/2.459 \text{ \AA}$). The 1D-wave model reproduces both trends in LB transmission: the energy-independent modulation of the transmission with overlap length on a long spatial period and the secondary modulation of the transmission dependent on energy and overlap.

The reduction of the maximum conduction to $1 G_0$ as well as the oscillation with overlap length was predicted by Tamura et al. [TSH05] for the (10,10)@(15,15) tDWNT. We have now shown that localized states cause the dips in the conductance and further show that the modulation of the transmission can be observed in a wide range of energy and overlap lengths.

Wave Interference Model

The origin of the localized states and the modulation of the transmission can be explained using a simple one-dimensional wave interference model (Figure 9.10). We assume that the dispersion of the SWNT and DWNT bands is linear $E(k) = \pm v_F(k - k_F)$, and the Fermi wave vector k_F and velocity v_F are the same for both SWNTs and the non-hybridized bands of the DWNT. The hybridized bands are split, and therefore the Fermi vectors of the two bands are not the same. Assuming that the splitting of the bands with negative v_F in the DWNT is considered symmetric around the Fermi wave vector, we can write the dispersion relations as $E^\pm = -v_F(k - k_F \mp \delta k_F)$.

An in-scattering electron wave with energy E can have one of two wave vectors $k^0(E) = \pm E/v_F + k_F$. To pass from one tube into the other, the in-scattering electron wave needs to couple to the hybridized DWNT states with the same energy. So, we can neglect the states with positive Fermi velocity and consider only the wave with $k^0(E) = -E/v_F + k_F$. Once this wave

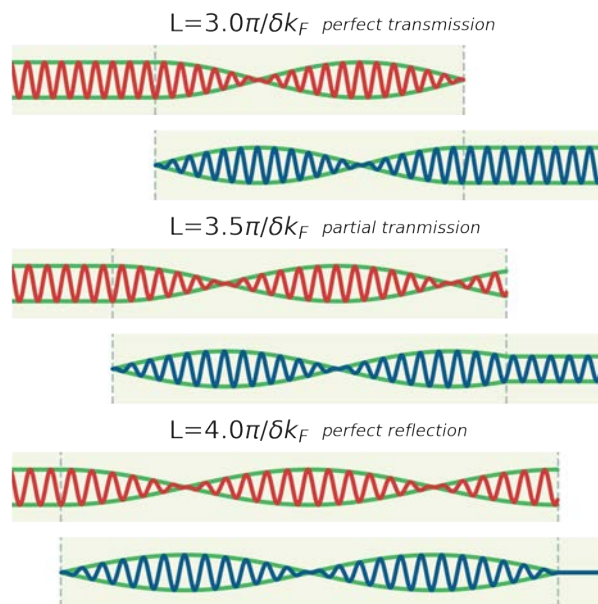


Figure 9.10: Schematic of one-dimensional scattering waves in the quantum box of the overlap region between two semi-infinite nanotubes.

enters the overlap region and hybridizes, it propagates as a superposition of the two waves with $k^\pm(E) = k^0(E) \pm \delta k_F/2$. We rewrite the superposition as the product of a fast, primary wave function and a slower envelope function. The primary component propagates with the average wave vector $\bar{k} = (k^+ + k^-)/2 = k^0(E)$, which is the same as the initial wave vector. The envelope wave vector is given by the difference $\delta k_F/2$ and is much shorter. The envelope modulates the incoming wave and describes how the weight oscillates between the two tubes. The incoming electron wave is reflected if the weight of the wave function is completely on the initial tube at the end of the overlap region (Figure 9.10 bottom). This condition is satisfied whenever the overlap length is commensurate with the envelope wave vector $\delta k_F L/2 = n\pi$. On the other hand, if the overlap length fits an extra quarter of the enveloping wave $\delta k_F L/2 = (n + 1/2)\pi$, then the wave function can pass through the overlap region without backscattering (Figure 9.10 top). For all intermediate overlap lengths, the incoming wave is partially reflected, thus reducing the conductance without fully blocking it.

Of course, the fast wave function component can also become commensurate with the overlap length ($k(E)L = n\pi$). The corresponding incoming wave can form a standing wave in the quantum box of the overlap region and is not transmitted through the systems. At every overlap length, this condition is satisfied for a set of energies $E = -v_F(n\pi/L + k_F)$. This explains the origin of the localized states.

We combine both of these effects, the energy-independent global oscillation of the transmission with L and the E and L -dependent position of the dips, to create a simple model for the transmission function T :

$$T(E, L) = \sin\left(L \frac{\delta k_F}{2}\right)^2 \cdot \sin\left(L\left(k_F - \frac{E}{v_F}\right)\right)^2 \quad (9.5)$$

$$T\left(E, \frac{2\pi n}{\delta k_F}\right) = 0$$

$$T\left(-v_F\left(\frac{\pi n}{L} + k_F\right), L\right) = 0$$

This simple expression can also be obtained by simplifying the model of Kim and Chang [KC02] assuming the linear dispersion relationship.

From the band structure of the ideal infinite (10,10)@(15,15) DWNT we obtain $\delta k_F \approx 0.715 \text{ \AA}^{-1}$, and $k_F = 2\pi/3/a$. Using these two parameters, this simple model shows good agreement with the TB conductance over the full range of energies and overlaps (Figure 9.9 (b)). The corresponding periodicity of the global oscillations predicted by our model is 89 Å, while the periodicity observed in the TB transmission is only slightly higher (100 Å). The model also reproduces the E and L -dependent positions of the smaller dips observed in the

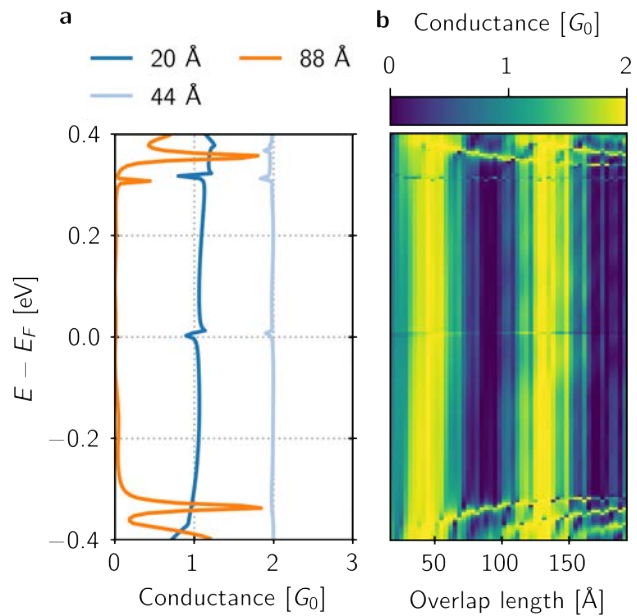
transmission. The sine functions make the dips smoother compared to the Landauer-Büttiker (LB) calculation, but the general trends are accurately reproduced. The curvature of regions without transmission (dark blue in Figure 9.9) can be recovered when the linear bands are replaced by the dispersion of the TB band of the infinite ideal DWNT (Figure 9.9 (c)).

Chiral, Incommensurate: (18,15)@(23,20)

For the telescopic DWNT (18,15)@(23,20), we find a similar oscillatory behavior of the transmission as a function of the overlap length with a period of 90 Å (Figure 9.11). However, there are a few key differences compared to the armchair@armchair tDWNT. The maximum conductance near the Fermi level is $2 G_0$ rather than $1 G_0$, and we do not observe suppression of conductivity at multiple overlap-dependent energies.

Although (18,15)@(23,20) is an incommensurate DWNT, we can use a periodic approximation to calculate its band structure. For this purpose, we create a supercell consisting of 4 and 3 repetitions of (18,15) and (23,20), respectively, and strain both tubes by $\pm 1\%$. Near the Fermi level, the band structure of this periodic approximation consists of many fully hybridized bands (Figure 9.12). This hybridization of the linear bands allows electrons to flow through the overlap region and thus yields a maximum conductivity of $2 G_0$. The overlap-independent dips and peaks at 0 eV and ± 0.31 eV are the results of small gaps in the eigenspectrum of the DWNT.

Figure 9.11: TB electron transmission from (18,15) into (23,20) (*strongly coupled*) (a) for three selected overlap length L showcasing "perfect" ($L = 44$ Å), partially blocked ($L = 20$ Å), and blocked transmission ($L = 88$ Å). (b) For a wide range of overlap lengths. The transmission oscillates as a function of L . At 0 eV and ± 0.31 eV sharp features occur irrespective of L .



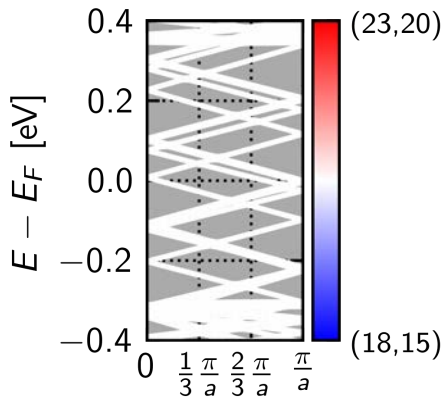


Figure 9.12: Band structure of a periodic approximation of the incommensurate (18,15)@(23,20) (*strongly coupled*), projected on each tube. Periodicity is imposed by building a commensurate supercell consisting of 4 and 3 repetitions of (18,15) and (23,20), respectively, and straining the tubes by $\pm 1\%$. The bands of (18,15)@(23,20) are fully hybridized between the tubes.

These features do not appear in Figure 9.12 but can be seen in the band structure calculated with a continuum model of Koshino et al. [KMS15], which does not artificially impose periodicity.

The chiral nanotubes (n,m) possess far fewer symmetries compared to achiral tubes. Therefore, chiral nanotubes can only have nodes at a few specific points along the tube circumference and cannot form localized states in the overlap region. This key difference between chiral and achiral nanotubes can be demonstrated by visualizing DFT wave functions (Figure 9.13).

From the band structure reported by Koshino et al. [KMS15] we can also extract the splitting of the Fermi wave vectors $\delta k_F \approx 0.065 \text{ \AA}^{-1}$. In our 1D wave interference model, this corresponds to an envelope wave function with a period of 96 Å, again a good approximation of the actual period observed in the calculated transmission function (90 Å). We note that the oscillations of the transmission will occur in all combinations of strong coupling, metallic@metallic tDWNTs, and depend only on the splitting of Fermi wave vectors induced by the interlayer interaction.

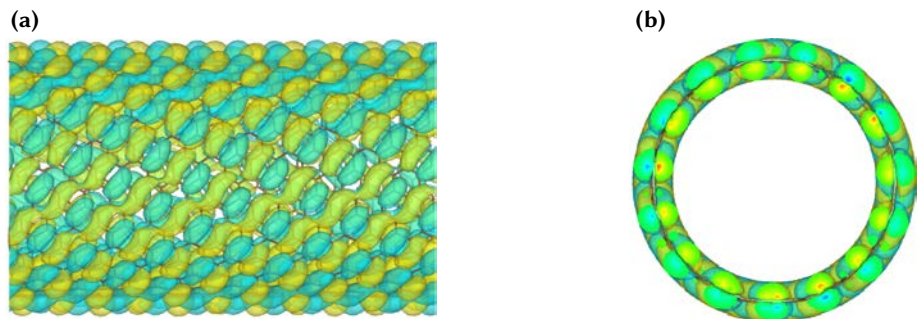


Figure 9.13: DFT wave function ($E = E_F - 0.5 \text{ eV}$) of a chiral nanotube: (18,15). The nodes of the wave function are not aligned along the circumference of the tubes, as is the case in achiral nanotubes.

9.4.2 Localized Insulating Regime

The localized insulating regime is achieved when the chiral vectors of the inner and outer tubes are nearly parallel and their difference points along the zig-zag direction. We consider two representatives of this family, $(27,3)@(36,3)$ and $(27,3)@(35,3)$, which are metallic-metallic (M@M) and metallic-semiconducting (M@SC), respectively. Interference effects are observable as peaks in the $(27,3)@(35,3)$ DOS in Figure 9.15. The small (3.12 Å) interlayer spacing enhances the coupling and suppresses the increase in DOS near the onset of the outer tube parabolic bands (gray area in Figure 9.15 and Figure 9.14). This effect can already be observed in short DWNT segments ($L < 81$ Å) and is not exclusive to the infinite tubes of Ref. [KMS15]. In $(27,3)@(36,3)$, instead, the interference is weaker due to the larger interlayer spacing (3.51 Å), and the onset of the parabolic bands is visible at ± 0.3 eV (Figure 9.16). A series of peaks are observed in the DOS of both cases (Figure 9.15 and Figure 9.16). This is consistent with the flat bands predicted by Koshino et al., who attribute them to the localization of electrons in an effective potential with a long spatial period (≈ 1200 Å for these two cases). However,

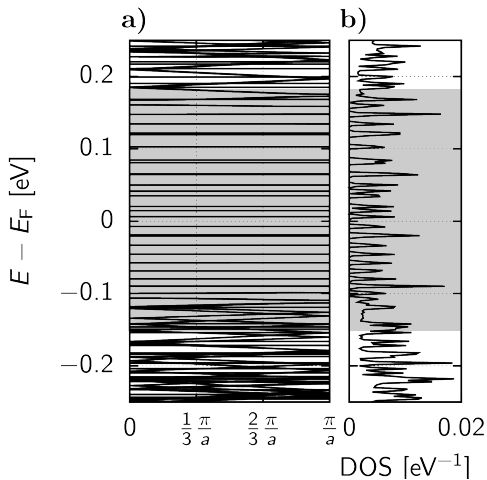


Figure 9.14: Band structure (a) and density of states (b) of a periodic equivalent of the incommensurate $(27, 3)@(35,3)$ (localized insulating). Periodicity is imposed by building a unit cell consisting of 23 and 6 repetitions of $(27,3)$ and $(35,3)$, respectively, and straining the tubes by $\pm 0.07\%$. The bands near the Fermi level are all flat. Significant dispersion only occurs more than 1 eV away from the Fermi level.

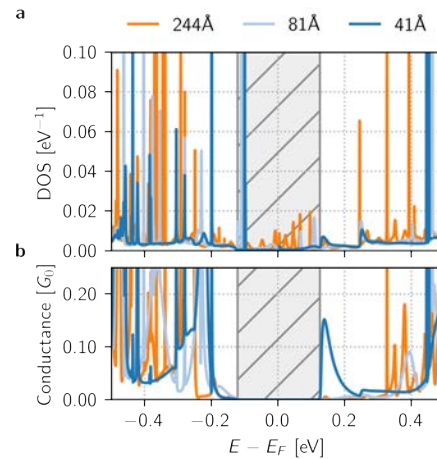


Figure 9.15: Density of states in the scattering region (a) and electron transmission (b) from $(27,3)$ into $(35,3)$ for different overlap lengths (localized insulating). Interference between the tubes results in sharp spikes and flat bands (Figure 9.14), which are more pronounced with increasing overlap length. The transport gap of the outer tube is highlighted in striped gray.

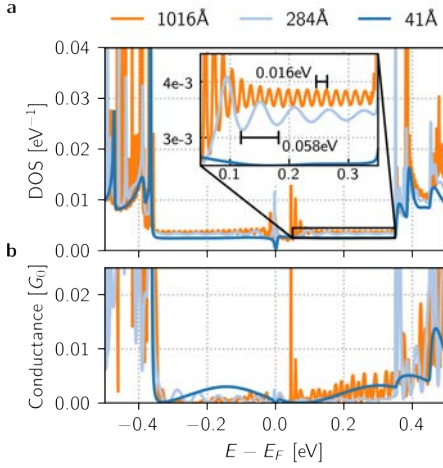


Figure 9.16: Density of states in the scattering region (a) and electron transmission (b) from (27,3) into (36,3) for different overlap lengths (*localized insulating*). Interference between the tubes results in sharp spikes and flat bands at E_F and at the edge of the quasi-insulating gap, which is more pronounced with increasing overlap length.

L [Å]	δE_{DOS} [eV]	δE [eV]
1016	0.016	0.017
528	0.031	0.033
284	0.058	0.062

Table 9.3: Oscillation periods in DOS of a (27,3)@(36,3) tDWNT in the energy ranges -0.35 eV to -0.05 eV and 0.1 eV to 0.35 eV for three different overlap length extracted from TB+LB calculations (δE_{DOS}) and calculated using Equation (9.6) (δE).

our simulations indicate that localized states already emerge in much shorter tube segments ($L \approx 244$ Å) and could be experimentally observable even without requiring long, pristine DWNT samples. While some of the localized states emerge at these short overlap lengths, the peak density in the DOS increases with overlap length and is significantly lower than predicted by Koshino. This shows that the minima of effective potential that cause localization emerge successively with increasing overlap. The full set of localized states will be observable only if the overlap length is larger than the period of the effective potential.

We observe additional oscillations of lower magnitude in the DOS of (27,3)@(36,3) DWNT, which can not be attributed to flat bands. These oscillations occur in the energy ranges between -0.35 eV to -0.05 eV and 0.1 eV to 0.35 eV and are a result of the finite overlap length that causes quantization of the wave vectors of states in the finite overlap region. Analogous to the discussion in the strong coupling regime, we assume linear dispersion of the low-energy bands and determine the energy spacing of states commensurate with the overlap length:

$$\delta E = v_F \frac{\pi}{L} \approx 5.6 \text{ eV } \text{Å} \frac{\pi}{L}, \quad (9.6)$$

which matches the observed periods in the DOS (δE_{DOS}) quite well (Table 9.3).

Given the small size of these oscillations, it will likely be challenging to observe them experimentally. These oscillations are not predicted by Koshino, since they are caused by the finite length of the overlap. This quantization effect is absent in the (27,3)@(35,3) DWNT because its outer tube is semiconducting and, therefore, only one set of linear bands is present. The interlayer conductance is heavily suppressed in both localized insulating DWNTs considered here. The interlayer transmission becomes significant only outside the energy range from -0.35 eV to 0.35 eV, where non-linear bands are present. Different examples of localized-insulating tDWNT (metallic@metallic) with shorter interlayer spacing (dR) can be found in Figure 9.17 ($dR = 3.4 \text{ \AA}$).

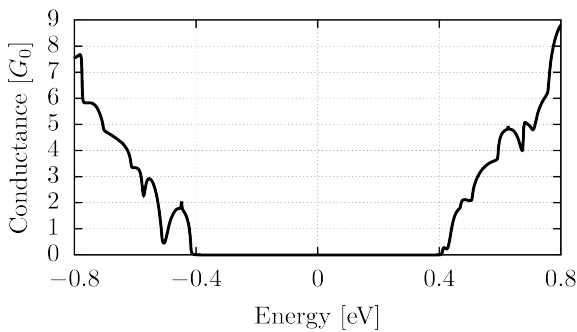


Figure 9.17: Density of states from a semi-infinite (45,18) into a semi-infinite (54,18) for an overlap length of 44 Å. The interlayer transmission is suppressed near the Fermi level, showing that the interlayer conduction is low in localized insulating DWNTs.

9.4.3 Weak Coupling Regime

The weak coupling regime consists of all other nanotubes, that is, all nanotubes for which the difference of the chiral vectors points neither along the armchair nor the zigzag direction, for which the two chiral vectors are not nearly parallel, and all DWNTs composed of two zigzag nanotubes (zig-zag@zig-zag). This regime encompasses the largest fraction of all carbon nanotubes, and for most carbon nanotubes in this regime, the interlayer transmission is completely suppressed. DWNTs composed of two zigzag nanotubes are an exception to this rule. Similarly to armchair@armchair DWNTs, rotational symmetry plays an important role in zigzag@zigzag DWNTs [KC02] and can lead to significant interlayer conductivity. If we restrict ourselves to a realistic interlayer spacing of 2.8 Å to 4.0 Å only one nanotube has the required symmetries: (9,0)@(18,0). Figure 9.18 (a) showcase the transmission function of (9,0)@(18,0) tDWNT: conductivity ranges from zero to $2G_0$ and varies with energy and overlap length. For all energies, there is an overlap length where the conductivity is not zero, except for a small energy window around the Fermi level (-0.04 eV to 0.04 eV), where the conductance is always suppressed. This energy window corresponds to the curvature-induced gap of (9,9) SWNT ($E_g = 0.08 \text{ eV}$ [KE01]), in which no electrode level is available for transport. Other

zigzag@zigzag DWNTs without three-fold rotation symmetry with the same interlayer spacing do not show interlayer conductivity, for example (18,0)@(27,0) (Figure 9.18 (b)). Similarly, the conductivity between layers is reduced for incommensurate achiral nanotubes with a zigzag layer and an armchair layer (Figure 9.18 (c)) and incommensurate chiral DWNTs (Figure 9.18 (d)).

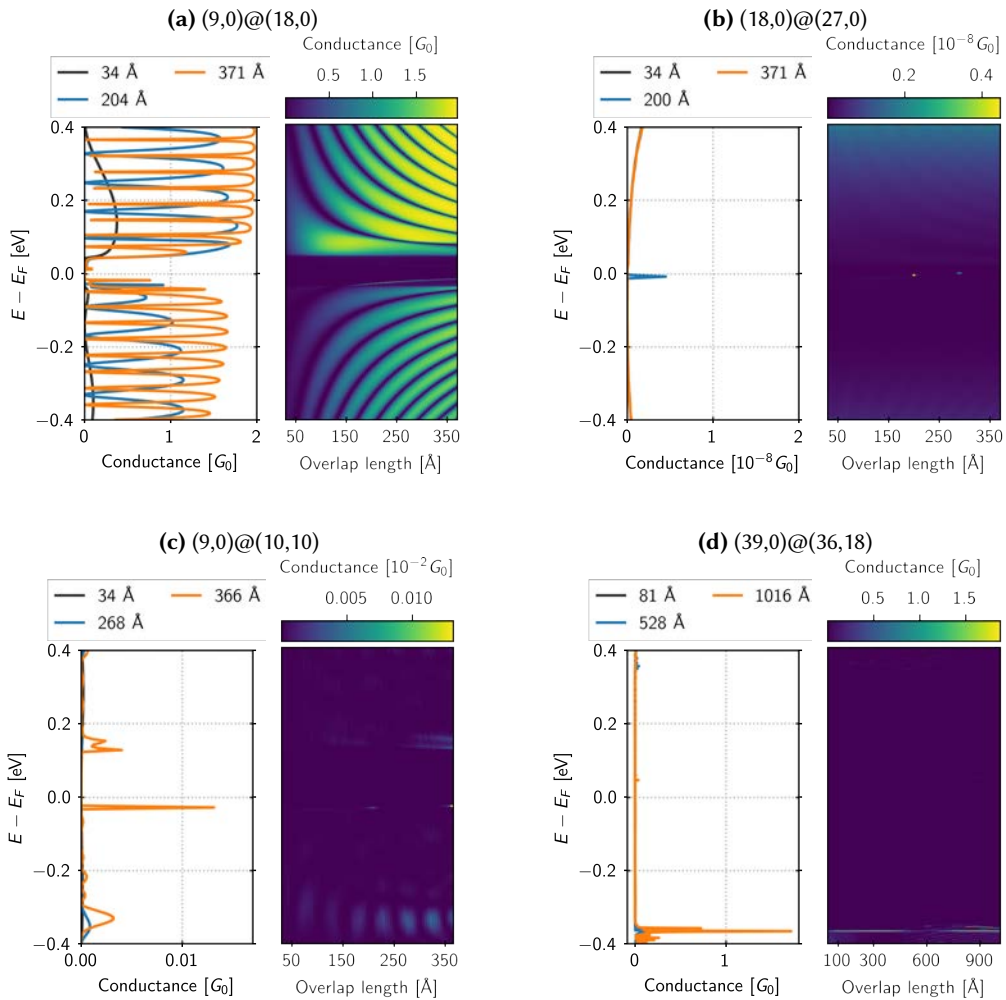


Figure 9.18: Density of states and electron transmission of two telescopic DWNTs in the *weak coupling* regime for different overlap lengths L . **(a)** The transmission from (9,0) into (18,0) is not suppressed due to 3-fold rotational symmetry and oscillates as a function of L . **(b)** The transmission from (18,0) into (27,0) is suppressed due to weak inter-layer coupling. **(c)** The transmission from (9,0) into (10,10) is suppressed due to weak inter-layer coupling. **(d)** The transmission from (39,0) into (36,18) is suppressed due to weak inter-layer coupling.

9.5 Conclusion

In conclusion, we show that telescopic DWNTs exhibit the same coupling regimes predicted for infinite double-wall carbon nanotubes, despite the finite length of the DWNT segments. Even when the DWNT segments are short, all three regimes should be identifiable in experimental setups. In strong coupling metallic nanotubes, the interlayer transmission is significant and tunable. Controlling the overlap length makes it possible to change between the periodically occurring insulating and metallic behavior. These oscillations of the conductance can be described using the picture of wave interference in one dimension. Based on this simplistic picture, we derived an expression for the transmission that can predict the periodicity of the oscillation with excellent accuracy. Strong-coupling metallic nanotubes armchair@armchair exhibit multiple dips in the transmission function. We show that these dips correspond to standing wave formation in the overlap region, which has quantized wave vectors and quantized energies. Standing waves do not form in chiral nanotubes as a result of broken rotational symmetries. In (10,10)@(15,15), rotational symmetries prohibit transmission through one of the electrode channels and thus reduce the maximum transmission. This specific characteristic of armchair@armchair nanotubes with three-fold rotation symmetries shed light on a long unexplained measurement of $1G_0$ conductance plateaus in some carbon nanotube bundles [Fra+98].

In weak-coupling metallic tDWNTs, the interlayer transmission is negligible in almost all cases. Metallic zigzag@zigzag tDWNTs are the only type of weak-coupling nanotube that can exhibit significant interlayer transmission, as seen for (9,0)@(18,0). Again, rotational symmetries play a crucial role in achiral tDWNTs. While the interlayer transmission of (9,0)@(18,0) is significant, it is negligible in (18,0)@(27,0). In other weak-coupling tDWNTs, where at least one tube is chiral or the two tubes are incommensurate, the interlayer transmission is negligible. In the localized insulating regime, the interlayer transmission is also heavily suppressed near the Fermi level. In this regime, the emergence of flat bands causes oscillations in the DOS. In particular, the flat bands already appear in segments significantly shorter than the predicted spatial periodicity of the underlying effective potential ($\approx 1200 \text{ \AA}$ for tubes discussed above). The number of localized states is directly related to the overlap length.

The coupling regime, in addition to the metallicity of the layers, plays an important role in predicting the conductivity of a tDWNT. As a result of the low interlayer conductance for weak coupling and localized insulating tDWNT, metallic layers in multiwall CNTs are contributing less to the overall conductance than previously expected. This explains, for example, the low interlayer conductivity reported in [UA05].

In addition, our results highlight that applications such as nanoelectronic switches based

on tDWNTs are very sensitive to their structure. Chiral tDWNTs are the most promising candidates for such applications. These tubes preserve the oscillating behavior found in all strongly coupled tDWNTs, while the absence of rotational symmetries prevents backscattering at localized states.

Bismuthene (monolayer bismuth) hosts nontrivial topological phases in some of its metastable polymorphs. However, it is yet unknown whether these polymorphs can bind to a substrate, whether their topological characteristics are maintained, and how to design the best substrate to strengthen their topological phase. In this chapter, we show, by means of first-principles methods, that bismuthene polymorphs can bind to silicon carbide (SiC), silicon (Si), and silicon dioxide (SiO₂), and that proximity interaction in these heterostructures, even in the presence of weak bonding, significantly affects the electronic structure of the monolayer. For the non-covalently bound heterostructure, we demonstrate that the main mechanisms affecting the electronic structure are van der Waals interactions and symmetry breaking. Our research demonstrates that the topological characteristics of bismuthene polymorphs can be strengthened by substrate interaction, allowing them to be used for experimental analysis and practical use.

The content of this chapter has been published in January 2022 in Carbon [WOZ22].

10.1 Introduction

Although the topology of bulk bismuth is disputed, atomically thin layers of Bi(111) (buckled hexagonal or b-hex bismuthene) are unanimously predicted to be topological [Kor+08; Liu+11; Ma+15; Sin+19; Zho+15] and a prime example of a Haldane-type topological material. However, two main issues limit the applicability of b-hex bismuthene: it is only metastable, and its band gap (0.08 eV) [Sin+19] is too small for room-temperature applications. Finding a substrate that can increase the gap while maintaining the topological features is one potential answer to these issues. Additionally, topologically trivial monolayers can become topological through interaction with substrates. For example, flat hexagonal (f-hex) bismuthene becomes topological when grown on SiC(0001) [Rei+17] or partially passivated Si (111) [Zho+15]. In addition to b-hex and f-hex bismuthene, other two-dimensional polymorphs of bismuthene exist or have recently been predicted. The energetically most favored phase is the puckered monoclinic bismuthene (Bi(110)), which is topologically trivial. In the order of formation energy, Bi(110) is followed by the b-hex, α , β , γ and f-hex [Sin+19]. In free-standing form, only the b-hex and γ phases are topologically nontrivial.

In this chapter, we focus only on the b-hex and f-hex phases, which can be Haldane-type TIs because of their hexagonal in-plane symmetry. We address the most important questions about the robustness of their topological phases:

1. Are the topological properties preserved on a substrate?
2. Can we design an optimal substrate to make the topological properties more robust?
3. Can a metastable polymorph become stable through interaction with a substrate?

To answer these questions, we performed a complete first-principles study of the interactions between topological states in bismuthene monolayers and silicon-based substrates. We show that interaction with the substrate can stabilize bismuthene polymorphs and strengthen their topological properties, making them accessible for experimental investigation and technological applications. In particular, we show that the Bi-monolayer phases can be stabilized on silicon carbide (SiC), silicon (Si), and silicon dioxide (SiO₂). We demonstrate that the proximity interaction has a significant effect on the electronic structure of the monolayer even when no bonding occurs. We further identify van der Waals interactions and the breaking of the sublattice symmetry of the monolayer as the main factors driving changes in the electronic structure. We also show that the structure of the surface greatly affects the interaction between b-hex and SiO₂: a hydroxylated SiO₂ surface can increase the topological band gap, whereas a surface with cleaved silicon ends can considerably decrease the band gap.

10.2 Methods

We perform fully relativistic DFT calculations using SIESTA [CC12; Cua+21; Gar+20; Sol+02] and employ optimized norm-conserving Vanderbilt pseudopotentials [Ham13] in the PSML format [Gar+18] from the PseudoDojo database [van+18] generated with PBE [PBE96] exchange-correlation functional. We expand the Kohn-Sham states using a standard double- ζ polarized basis set [Art+99].

We solve the Kohn-Sham equations using an electronic temperature of 5 meV and a $15 \times 15 \times 1$ Monkhorst-Pack grid for a single bismuthene unit cell. For larger cells, the k-point sampling is scaled accordingly. All structures are relaxed with a force threshold of 0.01 eV/Å and a maximum stress tolerance of 0.006 eV/Å³. We employ a real space grid with a mesh cut-off of 600 Ry.

For heterostructures, we use the van der Waals density functional of Dion et al. [Dio+04] (vdW-DRSSL), fix the substrate lattice vectors, and strain the bismuthene monolayer. This approach recreates the experimental conditions under which the monolayer will adjust to the

more rigid substrate. To determine the binding energies, we apply a counterpoise correction for the basis set superposition error [BB70]. Because GGA functionals, such as PBE, routinely underestimate binding energies for vdW materials [Laz+10], the adoption of a vdW functional is essential for heterostructures. Except for f-hex@SiC, the GGA functional predicts that none of the heterostructures is binding. For the free-standing bismuthene phases, we compare the effects of PBE and vdW-DRSSL functionals on the electronic structure. For the relaxation of the isolated substrate slabs, we use the PBE functional [PBE96].

To ensure that the slabs are thick enough to consider the upper and lower slab surfaces as decoupled, we increase the slab thickness layer by layer until the change in surface energy for any extra layer is smaller than 1 meV. We reach the following slab thicknesses:

1. **Si(111)**: 4 layers (2 Si per layer)
2. **SiC(0001)**: 4 layers (1 Si and 1 C per layer)
3. **Hydroxylated SiO₂(0001)**: 7 layers (1 Si and 2 O per layer) + 1 Si + 4 OH groups displayed in Figure 10.6 (a,b) with 3 layers.
4. **Reconstructed SiO₂(0001)**: 5 layers (1 Si and 2 O per layer) + 1 Si + 2 surface layers (2 Si and 5 O); displayed in Figure 10.6 (c,d) with 1 layer.
5. **Silicon-terminated SiO₂(0001)**: 5 layers (1 Si and 2 O per layer) + 1 Si displayed in Figure 10.6 (e,f) with 3 layers.

To avoid overestimation of the dipole moments of the heterostructures, we use a dipole correction, which removes the interaction between periodic images along the vacuum direction.

In general, the substrate and the free-standing monolayer lattices are incommensurate. To find realistic representations of the possible heterostructures, we take into account all possible combinations of supercells of the two materials and select the combination with a lattice mismatch of less than 5% and the least number of atoms possible. In this process, we also include supercells of $(\sqrt{3} \times \sqrt{3})R30^\circ$ cells of either material, which are obtained by rotating the unit cell lattice vectors by 30° and enlarging them by a factor of $\sqrt{3}$.

We apply a counterpoise correction for the basis set superposition error (BSSE) [BB70] to evaluate the binding energies (E_B) between the monolayer and the substrate. The BSSE refers to the overestimation of binding energy when comparing the total energy of a combined system and its components obtained from simulations with localized basis sets. This overestimation is a consequence of additional orbitals at the interface, which can be shared between the two components to lower their individual energy. To correct this error we calculate the total energy

of the components using ghost orbital, i.e., basis set functions without associated electrons. The corrected binding energy is given

$$E_{Binding} = E(\text{bismuthene} + \text{subs.}) - E(\text{bismuthene} + \text{ghost subs.}) \quad (10.1)$$

$$- E(\text{ghost bismuthene} + \text{subs.}) \quad (10.2)$$

Our new interface for Z2Pack [Gre+17] is used here to determine the topological invariant \mathbb{Z}_2 .

10.3 Results and Discussion

10.3.1 Free-Standing Bismuthene

Before studying the effect of substrates on bismuthene monolayer phases, it is essential to establish the structure, topological and electronic properties of the free-standing monolayers as a reference point.

The two hexagonal phases of bismuthene (f-hex and b-hex) have a similar crystal structure. In both phases, the bismuth atoms are arranged in a honeycomb lattice. In flat hexagonal bismuthene, the two sublattices lie in a common plane (Figure 10.1 (d,e)) whereas in buckled hexagonal bismuthene, they form two distinct parallel planes (Figure 10.1 (a,b)). The structural relaxation of flat hexagonal bismuthene yields a lattice constant of 5.35 Å, which corresponds to a distance of 3.09 Å between neighboring bismuth atoms. The bond lengths (3.04 Å) in buckled hexagonal bismuthene and its lattice constant (4.28 Å) are slightly shorter. The formation energy of the free-standing buckled hexagonal bismuthene is higher compared to that of f-hex

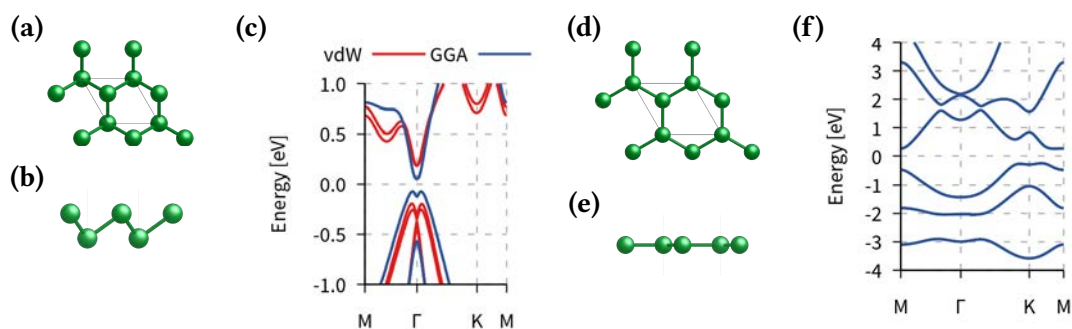


Figure 10.1: Crystal structure of free-standing buckled hexagonal bismuthene (top view (a); side view (b)) and flat hexagonal bismuthene (top view (d); side view (e)); (c) and (f) corresponding DFT electronic band structure.

($\Delta E = 0.4 \text{ eV}$). The buckling height, that is, the distance between the two planes of bismuth atoms, is approximately 1.78 \AA .

Both bismuthene phases are semiconductors with an indirect band gap. The band gap of flat hexagonal bismuthene (0.5 eV) is larger than that of buckled hexagonal bismuthene (0.13 eV ; PBE). We calculate the invariant \mathbb{Z}_2 for both phases and find that the f-hex phase is topologically trivial ($\mathbb{Z}_2 = 0$), while the b-hex phase is topologically nontrivial ($\mathbb{Z}_2 = 1$). These results are consistent with the literature, for example, the work of Singh et al. [Sin+19]. Compared to Singh et al., we observe a slightly larger band gap for b-hex. However, this level of deviation with respect to the literature is reasonable, taking into account the use of different DFT codes, pseudopotentials, and basis sets (plane waves vs. localized basis sets).

While the results for the flat hexagonal phase do not depend on whether the calculations are performed with the PBE or vdW-DRSSL functions, we find that the band gap of buckled hexagonal bismuthene is sensitive to the choice of the exchange-correlation functional. Including the vdW interaction leads to an increase in the band gap to 0.38 eV with the functional vdW-DRSSL. The difference in sensitivity to the choice of functional can be attributed to the crystal structure. In the buckled hexagonal phase, the vdW interactions lead to an attraction of the two sublattice planes and decrease the buckling height to approximately 1.65 \AA . However, in the flat hexagonal phase, the vdW interactions do not result in an effective attraction because it is flat. In addition to a reduction of the buckling height, the vdW interaction induces small magnetic moments ($0.01 \mu_B$), which break the time-reversal symmetry and cause the Kramer pairs to split (Figure 10.1 (f) and Figure 10.1 (c)). The \mathbb{Z}_2 invariant remains unchanged and indicates that the topological phase of buckled hexagonal bismuthene is robust enough to persist despite the small spontaneous magnetization.

10.3.2 SiC(0001)

The first substrate we consider is silicon carbide, a wide-bandgap semiconductor with hexagonal symmetry. We demonstrate that the f-hex and b-hex bismuthene phases bind to (partially) hydrogen-passivated SiC(0001) substrates and the resulting heterostructures are topological.

The most stable crystal structure for SiC is the Moissanite-6H crystal structure. Other closely related metastable polymorphs, such as SiC-4H or SiC-3C, also occur naturally and have similar electronic properties. When cut along the (0001) direction, these SiC polymorphs possess a hexagonal in-plane symmetry, similar to that of our two monolayer phases. The in-plane lattice constant of SiC(0001), about 3.1 \AA , is considerably shorter compared to f-hex and b-hex bismuthene. Nevertheless, f-hex bismuthene can be grown on silicon-terminated SiC(0001) and becomes topological, as recently demonstrated by Reis et al. [Rei+17]. In this case, the

two crystal structures are rotated by 30° with respect to each other, forming a superlattice of one $(\sqrt{3}\times\sqrt{3})R30^\circ$ supercell of SiC(0001) and one f-hex unit cell (Figure 10.2 (a) and (b)). The Bi atoms of the monolayer bind to the Si atoms at the surface. Below the center of each Bi hexagon lies one unpaired Si atom, which is expected to be hydrogen-passivated.

To simulate this structure, we place a 1% strained unit cell of f-hex bismuthene on the rotated unit cell $(\sqrt{3}\times\sqrt{3})R30^\circ$ of Si(0001). We passivate the unpaired Si atom at the center of the Bi hexagons and those at the opposite side with hydrogen atoms to avoid metallic states in the substrate. After structural relaxation, we find the monolayer remains flat and binds strongly to the surface. The distance between the monolayer and the silicon surface layer is approximately 2.76 Å and the binding energy is 1.5 eV per bismuth atom. The Bi- p_z orbitals play a dominant role in the formation of Bi-Si bonds (Figure 10.3). As a result, the Bi- p_z orbitals are shifted away from the Fermi level, which drives the phase transition from trivial to topological [Rei+17; Zho+15].

Our simulations accurately reproduce the electronic structure and structural characteristics described by Reis et al. [Rei+17]. We confirm the existence of a topological phase and an indirect band gap with the valence band maximum at K and the conduction band minimum at Γ . We find very little variation in the electronic structure calculated with the GGA-PBE and vdW-DRSSL functionals. This can be attributed in part to the covalent nature of the bonding and, in part, to the insensitivity of the isolated monolayer to the choice of function. We calculate a band

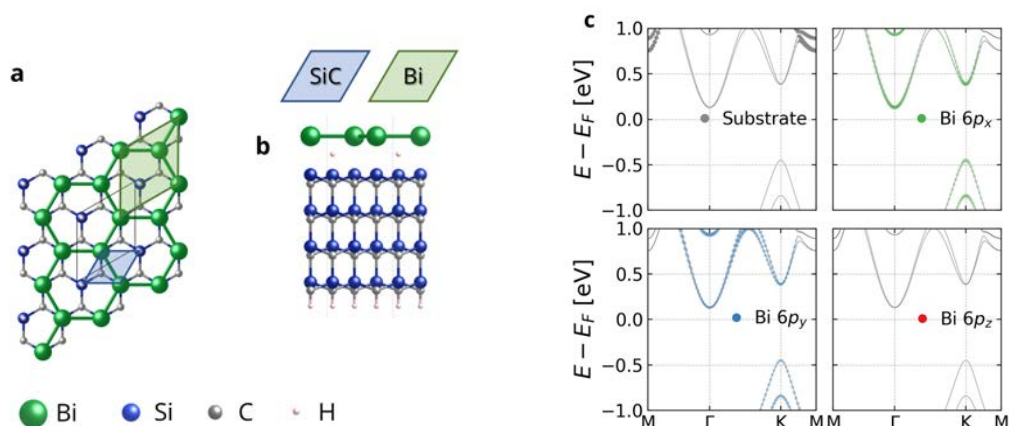


Figure 10.2: Crystal structure of **flat hexagonal bismuthene@SiC(0001)** (top view **a**; side view **b**). Color code and schematic of the individual unit cells are displayed in the inset. Orbital projected DFT electronic band structure (**c**): in each panel, the contribution of different orbitals is proportional to the line width.

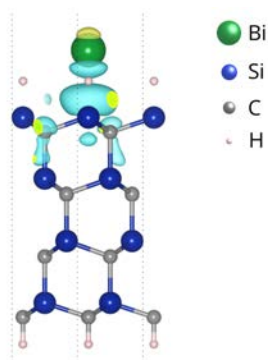


Figure 10.3: Flat hexagonal bismuthene@SiC(0001): Change in charge density due to interaction between monolayer and substrate. The shape of the isosurface reveals, that bonds between Bi and Si are primarily formed by p_z orbitals. The teal and yellow colors indicate a decrease and increase in the charge density respectively.

gap of 0.6 eV for both functionals, which is only marginally higher than that reported by Reis et al. [Rei+17], namely 0.5 eV.

The lattice mismatch between b-hex bismuthene and SiC(0001) is larger than that of f-hex bismuthene, and an unrealistic amount of strain would be required to realize a one-to-one correspondence between Bi atoms and surface Si as for f-hex@SiC. Attempting to place b-hex bismuthene directly on silicon-terminated SiC(0001) would create a structure with several undercoordinated Si atoms resulting in a metallic heterostructure. Instead, we consider a fully hydrogen-passivated slab of SiC(0001) as a substrate for b-hex bismuthene. The interactions between a fully passivated surface and the monolayer can be expected to be dominated by van der Waals interactions, which should favor the more stable buckled hexagonal phase or

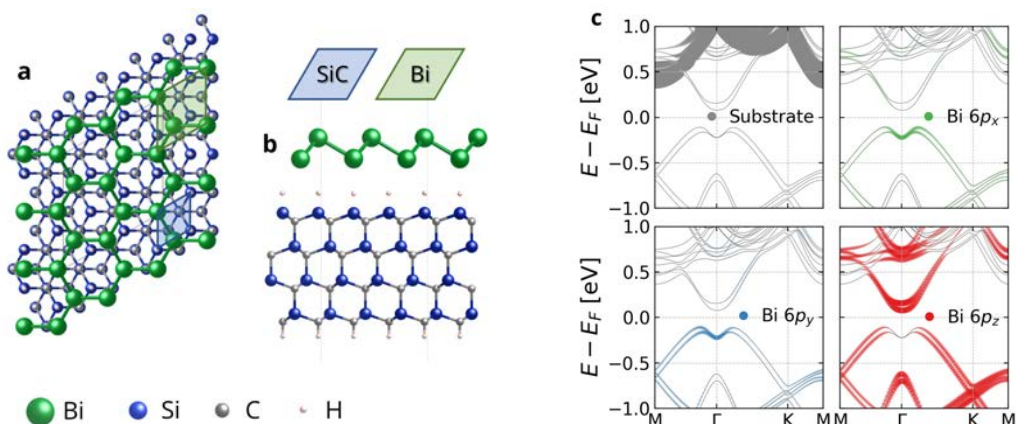


Figure 10.4: Crystal structure of **buckled hexagonal bismuthene@SiC(0001)** (top view **a**; side view **b**). Color code and schematic of the individual unit cells are displayed in the inset. Orbital projected DFT electronic band structure (**c**): in each panel, the contribution of different orbitals is proportional to the line width.

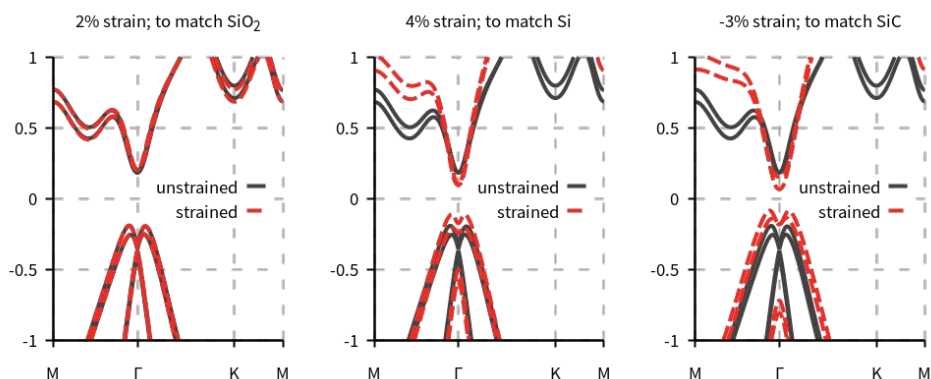


Figure 10.5: Effect of the strain on the band structure of free-standing b-hex bismuthene. The topological features are resilient to strain.

puckered monoclinic phase over the flat hexagonal phase. Furthermore, the vdW interactions can be expected to perturb the electronic structure of the monolayer only weakly and preserve the topological phase.

Our **b-hex@H-SiC(0001)** heterostructure consists of a 4×4 supercell of hydrogen-passivated SiC(0001) and a -3% strained 3×3 supercell of b-hex bismuthene (Figure 10.4 (a) and (b)). Again, we passivate the silicon atoms on the bottom side of the slab with hydrogen atoms to avoid metallic substrate states. As predicted, the binding energy per Bi atom in the heterostructure ($E_B = 0.08$ eV) is much lower than in f-hex@SiC and results in a van der Waals heterostructure. Despite the low binding energy, the first SiC layer is slightly deformed as a result of the proximity interaction. However, we find that the \mathbb{Z}_2 invariant of the monolayer remains unchanged ($\mathbb{Z}_2=1$). The band gap of the heterostructure (0.18 eV) is reduced with respect to the free-standing monolayer. This effect can be largely attributed to the imposed strain (Figure 10.5). However, the proximity interaction also has a significant effect. It produces a more pronounced Mexican-hat profile and causes stronger splitting of the Kramer pairs. Because of the robust topological phase, hydrogen-passivated SiC is a reasonable substrate candidate for b-hex bismuthene, irrespective of the slightly reduced band gap.

10.3.3 SiO₂(0001) α -Quartz

Commonly used silicon dioxide substrates are amorphous (a-SiO₂), and cannot be modeled directly with DFT methods that rely on periodic boundary conditions. Rather than using large supercells that aim to model a-SiO₂, we chose different surface terminations of crystalline SiO₂ α -quartz(0001) and compared the effect of these crystalline substrates on the bismuthene

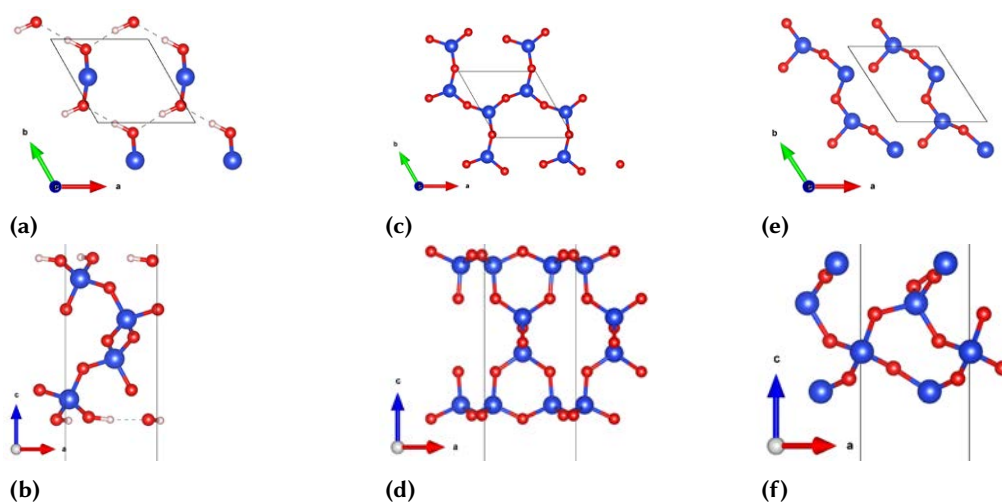


Figure 10.6: Crystal structure of SiO_2 slabs with different surfaces (side view (a,c,e) and top view (b,d,f)): hydroxylated (OHT) (a,b), reconstructed oxygen terminated (ROT) (c,d), and silicon terminated (SiT) (e,f).

monolayers. The approximation of a- SiO_2 through crystalline surfaces is possible because (a) the atomic structure of a- SiO_2 is locally very similar to α -quartz, (b) the roughness of a- SiO_2 substrates can be very small $\sigma = 2 \text{ \AA}$, and (c) monolayer can closely follow the surface roughness [Que+14]. We consider a silicon-terminated cleaved surface (SiT), a reconstructed oxygen-terminated surface (ROT), and a hydroxylated silicon-terminated surface (OHT) (Figure 10.6). We ignored a non-reconstructed oxygen-terminated surface because of its structural instability.

As in the case of SiC substrates, b-hex bismuthene binds to SiO_2 weakly due to van der Waals interactions and could potentially be experimentally synthesized⁷. Although the binding is dominated by van der Waals interactions on all three surfaces, the electronic structure is highly sensitive to the surface configuration. In particular, the hydroxylated surface enhances the band gap and a silicon-terminated, cleaved surface significantly reduces the band gap.

The b-hex@ SiO_2 heterostructures consist of a $(\sqrt{3} \times \sqrt{3})R30^\circ$ supercell of SiO_2 , and a 2% strained 2×2 supercell of b-hex bismuthene (Figure 10.7). On all three surfaces, b-hex bismuthene binds weakly with binding energies between 0.06 eV and 0.11 eV per bismuth atom (Table 10.1). Among the three heterostructures, **b-hex@OHT- SiO_2** is the most promising candidate for the realization of room-temperature quantum spin Hall (QSH) states because it possesses the

⁷ Positive binding energy does not imply thermodynamic stability of these heterostructures, nor do these energies allow comparison of the stability of the different heterostructures. As such, it is possible that it *could* be synthesized but this is not guaranteed.

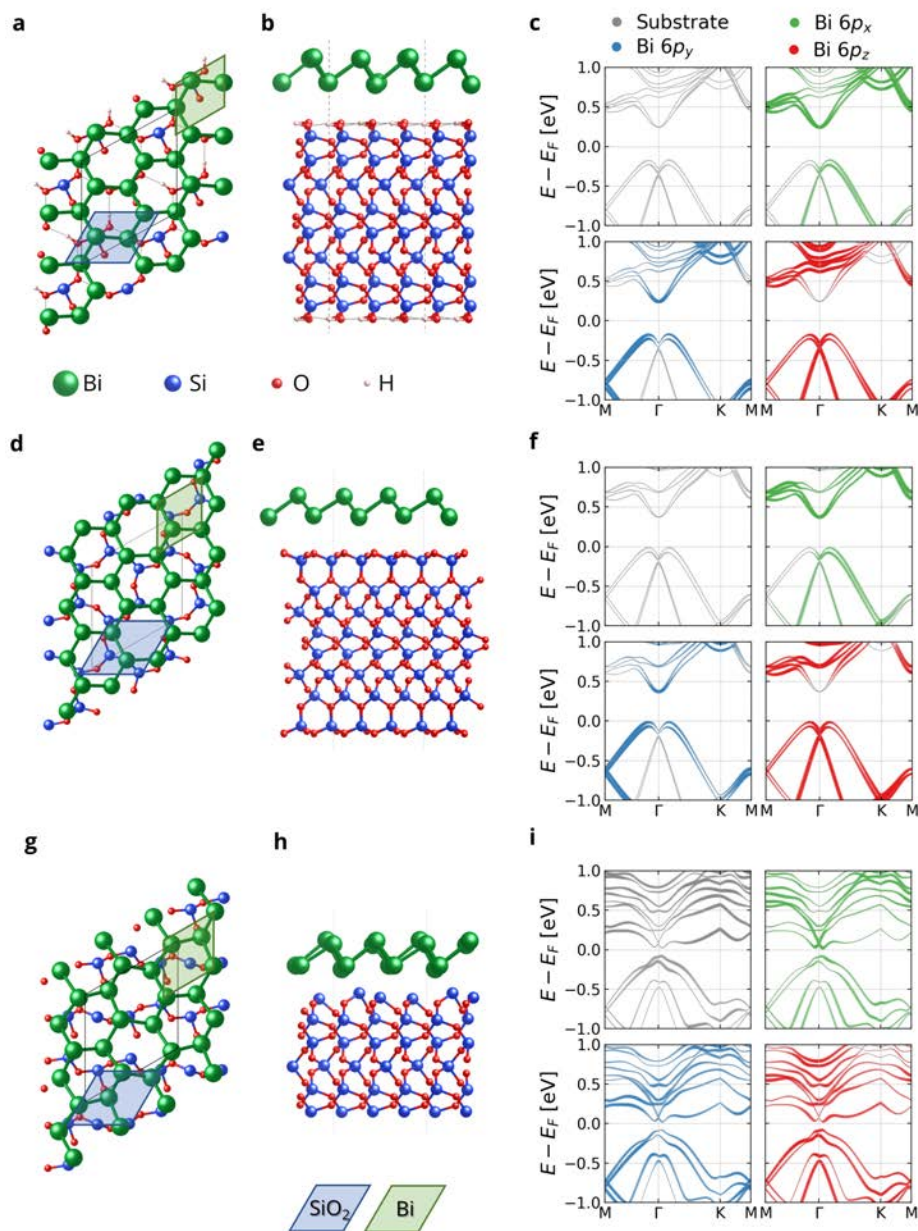


Figure 10.7: Crystal structure of buckled hexagonal bismuthene on SiO_2 (top view and side view) and orbital projected DFT electronic band structure for three different surface terminations: hydroxylated (a-c), reconstructed (d-f), and Si terminated (g-i). In each panel, the contribution of different orbitals is proportional to the line width. On the hydroxylated and reconstructed surfaces, the signature of a band inversion is visible in the projection of Bi $6p_y$ orbitals. Bi $6s$ orbitals do not contribute to the bands near the Fermi level.

largest band gap (0.40 eV, Figure 10.7 (c)) and remains topologically nontrivial ($\mathbb{Z}_2 = 1$). With respect to the free-standing monolayer, the band gap is slightly increased, and the orbital character of the states near the Fermi level changes. In the free-standing monolayer, all three Bi- p orbitals have equal contributions to the valence and conduction bands. In contrast, in the heterostructure, Bi- p_x orbitals contribute primarily to the conduction bands and Bi- p_y orbitals to the valence band. The p_x - p_y symmetry is lifted due to the breaking of D3d symmetry of the free-standing b-hex monolayer in the heterostructure⁸. As a result, the position of the valence bands near M and K is lowered (Figure 10.7 (c)), and the valence band minimum at Γ increases, thus increasing the direct band gap at Γ slightly. Analysis of the orbital contributions of the bands also illustrates the signature of a band inversion at Γ . These two characteristics indicate a very robust topological phase of b-hex@OHT-SiO₂.

We observe very similar characteristics in the **b-hex@ROT-SiO₂** heterostructure. The nontrivial topology of the monolayer is preserved, and the broken in-plane symmetry changes the orbital character of the valence and conduction bands. Again, the signature of a band inversion can be observed Γ (Figure 10.7 (f)). We find that the band gap of the free-standing monolayer is preserved (0.38 eV) on the ROT surface, which makes ROT-SiO₂ a good substrate if b-hex bismuthene.

In contrast, the **b-hex@SiT-SiO₂** heterostructure shows very different behavior. In this heterostructure, the interaction between the surface and the monolayer is significantly enhanced due to a decrease in the spacing between the two materials compared to b-hex@OHT-SiO₂ or b-hex@ROT-SiO₂ (Table 10.1). The stronger interaction in this heterostructure also causes the Bi-hexagons to become skewed and the buckling height to be non-uniform (Figure 10.7 (g)). Furthermore, the Bi- $6p$ orbitals hybridize with the Si- $3p$ of the substrate. As a result, the band gap is significantly smaller and the splitting of the Kramer pairs increased (Figure 10.7 (i)). Despite these strong perturbations of the electronic structure, the calculated \mathbb{Z}_2 -invariant remains 1, demonstrating the robustness of the topological phase of b-hex bismuthene. The reduction of the band gap in b-hex@SiT-SiO₂ prevents its application in quantum spin Hall devices. We predict that an optimal experimental realization of the topological b-hex requires a hydroxylated SiO₂ surface.

F-hex bismuthene also binds to the SiO₂ surfaces with varying binding energies per Bi atom: 0.09 eV (ROT-SiO₂), 0.11 eV (OHT-SiO₂), and 0.19 eV (SiT-SiO₂) (Figure 10.8). The f-hex@SiO₂ heterostructures consist of a -4% strained f-hex unit cell and a substrate unit cell. On all three surfaces, we observe that the crystal structure of the flat monolayer is perturbed, causing it to buckle slightly. This effect is caused in part by the imposed strain and is further enhanced

8 the point group of bismuthene@OHT-SiO₂ heterostructure is P1

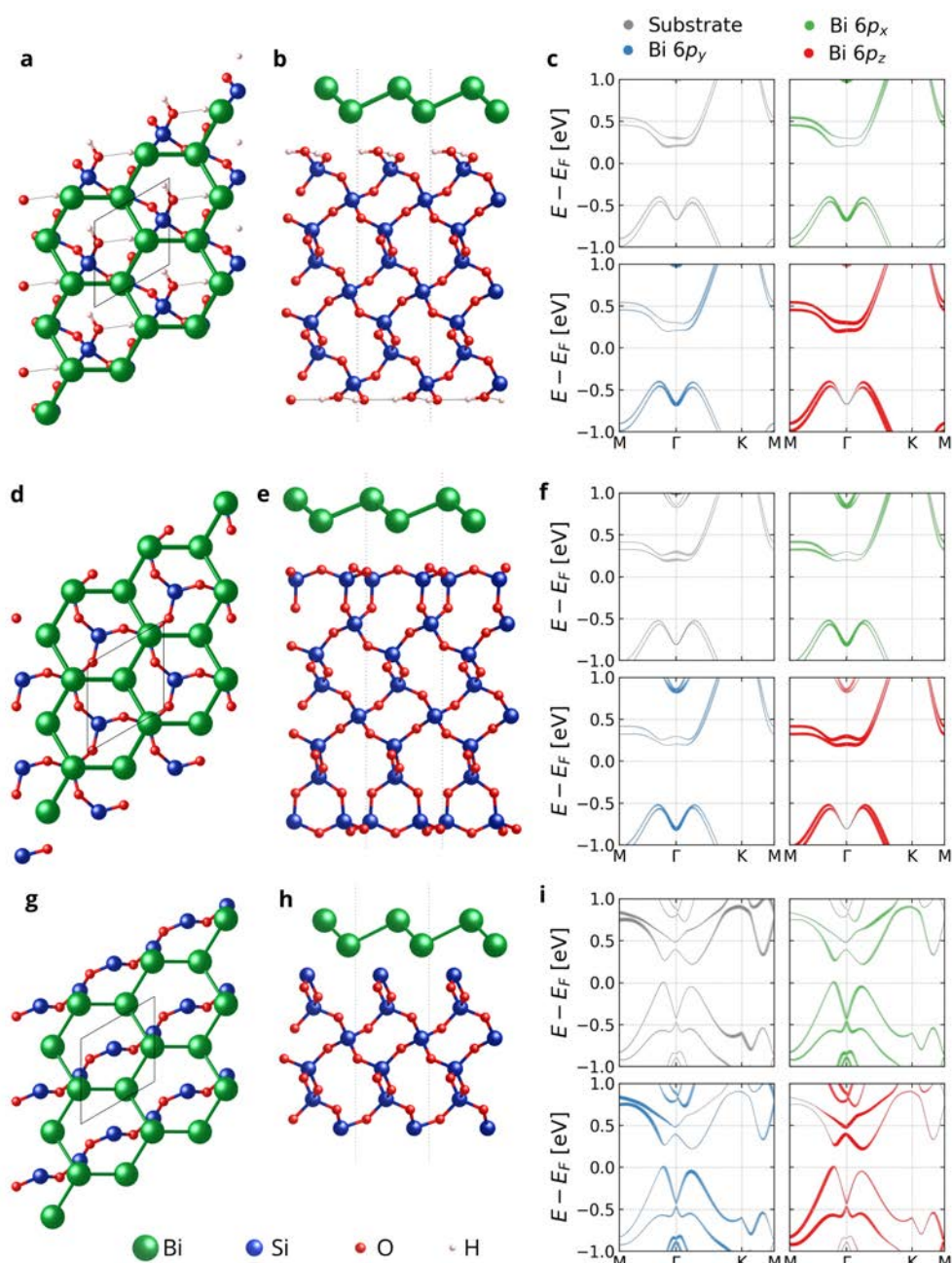


Figure 10.8: Crystal structure of flat hexagonal bismuthene on SiO_2 (top view and side view) and orbital projected DFT electronic band structure for three different surface terminations: hydroxylated (a-c), reconstructed (d-f), and Si terminated (g-i). In each panel, the contribution of different orbitals is proportional to the line width. Bi $6s$ orbitals do not contribute to the bands near the Fermi level.

by the surface geometry. The buckling is particularly strong on the SiT surface, where the atoms of one Bi-sublattice sit in the middle of the cleavages in the surface, while the second set of atoms sits on top of the ridges. We observe a Mexican hat profile in the topmost valence bands, similar to the case of the b-hex bismuthene. Despite these similarities, the f-hex@SiO₂ heterostructures are topologically trivial ($\mathbb{Z}_2=0$). However, by comparing the band structures, we can see that the band gap closes with increasing buckling height. This could indicate that the monolayer on the SiT-SiO₂ surface is close to a topological phase transition. Using the inverse piezoelectric effect to modulate the strain and thus the buckling height could make it possible to tune between a topologically trivial and nontrivial phase of hexagonal bismuthene on SiO₂.

10.3.4 Si(111)

Buckled hexagonal bismuthene binds to Si(111) and remains topologically nontrivial. However, Si(111) is a poor choice for bismuthene-based topological insulator devices because the band gap is significantly reduced.

The **b-hex@Si(111)** heterostructure is composed of a 2×2 Si(111) supercell and a 4% strained ($\sqrt{3}\times\sqrt{3}$)R30°b-hex supercell (Figure 10.9 (a) and (b)). The monolayer binds weakly to the substrate with a binding energy of 0.07 eV per Bi atom. Similarly to b-hex@SiC, the lattice mismatch requires passivation of the Si(111) substrate to prevent the heterostructure from being metallic and results in a van der Waals heterostructure. In this heterostructure, the

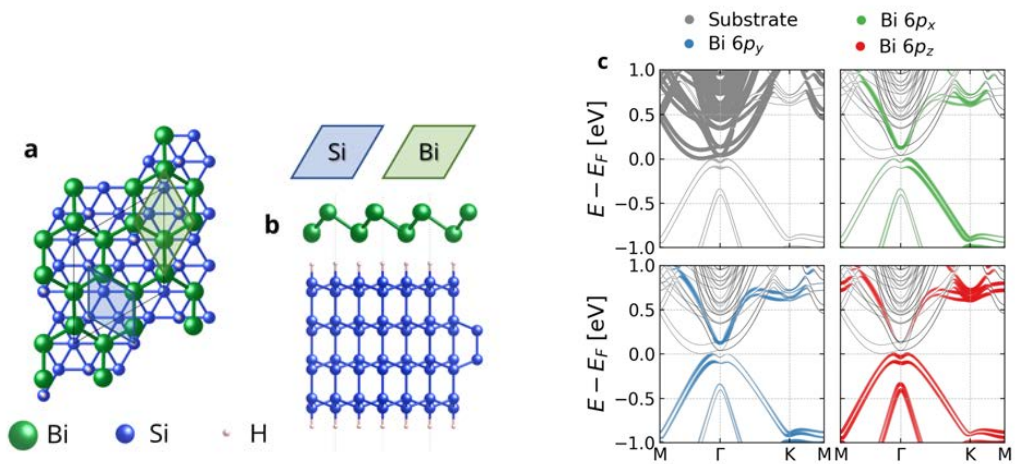


Figure 10.9: Crystal structure of **buckled hexagonal bismuthene@passivated Si(111)** (top view **a**; side view **b**). DFT electronic band structure (**c**) in each panel the contribution of different orbitals is proportional to the line width.

contributions of the Bi- p_x and Bi- p_y orbitals to the bands are not symmetric due to the broken in-plane symmetry of the monolayer. Analysis of the orbital contributions to the eigenstates reveals that the electronic structures of the two materials are largely independent. For all the heterostructures discussed above, the Fermi level falls within the band gap of the substrate and the monolayer. Here, however, the electronic structures of the two materials are aligned so that the Fermi level lies slightly above the top edge of the substrate band gap and slightly below the bottom edge of the monolayer band gap. This creates very small electron and hole pockets and makes this heterostructure semimetallic. Even if the substrate states are excited at finite temperatures, these states should not interfere with the monolayer states since both materials are effectively decoupled. Therefore, the topological band gap should here be defined as the gap between the valence and conduction bands of the monolayer: 0.12 eV (Figure 10.9 (c)). Compared to the free-standing phase, this gap is significantly reduced due to the strain (Figure 10.5) and the interaction with the substrate. Overall, Si is a poor substrate choice for b-hex bismuthene.

To create an f-hex@Si heterostructure with less than 5% monolayer strains, large supercells are required, for example, a $4 \times 4 (\sqrt{3} \times \sqrt{3}) R30^\circ$ supercell of Bi and a 5×5 unit cell of Si with more than 500 atoms in total. Preliminary screening of the topological properties of the initial unrelaxed structure, a partially relaxed structure, and a fully relaxed smaller heterostructure with larger strain revealed a topologically trivial character of this heterostructure. For this reason, we exclude f-hex@Si from our study.

10.4 Conclusion

In this work, we have studied the proximity interaction between hexagonal Bi monolayer phases and silicon-based substrates to identify potential substrates for room-temperature TI applications based on Bi monolayers. We showed that these heterostructures have positive binding energies (Table 10.1) and therefore buckled hexagonal and flat hexagonal bismuthene could be stabilized on H-SiC(0001), H-Si(111), and α -quartz SiO₂(0001). As such, our work can help guide experimental studies in the choice of potential substrates.

Except for f-hex@SiC(0001), which covalently binds, all other monolayer substrate combinations considered here form vdW heterostructures. The interaction with the substrate has no effect on the topology of the hexagonal Bi monolayers (f-hex: trivial, b-hex: nontrivial), except for f-hex@SiC(0001). We expect that this topological character is also preserved, when geometrical edges are created in monolayers, to ultimately observe the quantum spin Hall effect. Technically, these edges introduce a new perturbation of the electronic structure. However, Bieniek et al. [BWP17], Reis et al. [Rei+17], and Wu et al. [Wu+16] have shown that the creation

Bi phase	Substrate	Surface	Z_2	Lattice Constant [Å]	Lattice Mismatch	E_B per Bi [eV]	Interlayer Distance [Å]	E_g [eV]
b-hex	<i>free-standing</i>		1	4.28	-	-	-	0.38
	SiC(0001)	Si term. & H passivated	1	3.12	3%	0.08	2.73	0.18
	Si(111)	H passivated	1	3.88	4%	0.07	2.66	0.12
	SiO ₂ (0001)	hydroxylated	1	5.03	-2%	0.06	2.90	0.40
	SiO ₂ (0001)	reconstructed	1	5.03	-2%	0.07	2.96	0.38
	SiO ₂ (0001)	Si terminated	1	5.03	-2%	0.11	2.34	0.08
f-hex	<i>free-standing</i>		0	5.35	-	-	-	0.51
	SiC(0001)	Si terminated	1	3.12	1%	1.49	2.76	0.62
	SiO ₂ (0001)	hydroxylated	0	5.03	-2%	0.11	3.22	0.19
	SiO ₂ (0001)	reconstructed	0	5.03	-2%	0.09	2.76	0.80
	SiO ₂ (0001)	Si terminated	0	5.03	-2%	0.19	-	-

Table 10.1: Summary of basic properties of buckled hexagonal and flat hexagonal Bi monolayer phases in free-standing form and supported by different substrates. The positive binding energies indicate that the heterostructures can bind to the substrate. The topological properties of the b-hex phase are preserved independently of the strain and the details of the interaction with the substrate. Similarly, the f-hex phase remains trivial, except on top of SiC, where it covalently binds to the surface.

of such edges does not affect the topology in the covalently bound heterostructure. Therefore, the topology in the vdW heterostructure discussed here should remain unchanged as well.

We demonstrate that even in the absence of bonding, proximity interactions in the heterostructure have a considerable impact on the electronic structure of the monolayer. The main causes of the change in the electronic structure are the structural realignment and the breaking of the sublattice symmetry of the hexagonal monolayers. The substrate material and its surface influence the precise nature of this proximity interaction. In particular, the magnitude of the topological gap of b-hex bismuthene changes greatly depending on the substrate selected. Due to an increase in the topological gap, hydroxylated SiO₂ appears as an exceptionally promising substrate option for b-hex bismuthene and may allow for room-temperature use.

In this chapter, we use our newly developed methods in the TRANSIESTA code to study the effect of SOC and non-collinear spin configuration on transport properties of 1D, 2D and 3D nanomaterials. First, we determine the anisotropic magnetoresistance (AMR) in an infinite monatomic iron chain and study the domain wall resistance in the constraint domain wall between two semi-infinite ferromagnetic chain segments. Next, we test whether our new implementation can correctly predict the tunneling magnetoresistance (TMR) in Fe/MgO/Fe junctions and whether these junction exhibit tunnel anisotropic magnetoresistance (TAMR). As a third test case, we simulate a lateral MoS₂/WS₂ heterojunction, which exhibits strong intrinsic SOC. Lastly, we determine the effects of spin-orbit coupling and electron correlation on the transport properties of carbon nanotubes decorated with antiferromagnetic molecules.

11.1 Monatomic Iron Chain (1D)

In an infinite monatomic iron chain, the Hamiltonian of the scattering region is independent of k . With this system, we test the part of our implementation without k -point sampling. We check whether the magnetic moments in the scattering region relax when the initial guess does not match the spin orientation of the electrodes. Furthermore, we calculate the transport properties of monatomic iron chains with different magnetic configurations: infinite periodic chains with collinear spin moments (Figure 11.1 (a) and (b)) and constraint domain walls (Figure 11.1 (c), (d), and (e)). We compare the contribution of different spin channels between the scalar relativistic (SR; collinear spin approximation and no SOC) and fully relativistic (FR; with SOC) simulations using the previously induced concept of spin-channel projected transmission. Before discussing these properties obtained with the NEGF formalism, it is important to study the electronic structure of the infinite periodic iron chain (Figure 11.1 (a) and (b)).

The magnetic anisotropy energy (MAE) describes how the free energy of magnetic materials depends on the relative orientation of magnetic moments with respect to the crystal structure. MAE emerges as the result of Coulomb repulsion, SOC, and the broken rotational symmetry in the crystal. The anisotropic magnetoresistance (AMR) is the transport counterpart of MAE and describes the dependence of the resistance on the relative orientation between magnetization and current flow. While AMR is known to have a small effect in bulk materials (<5% in 3d

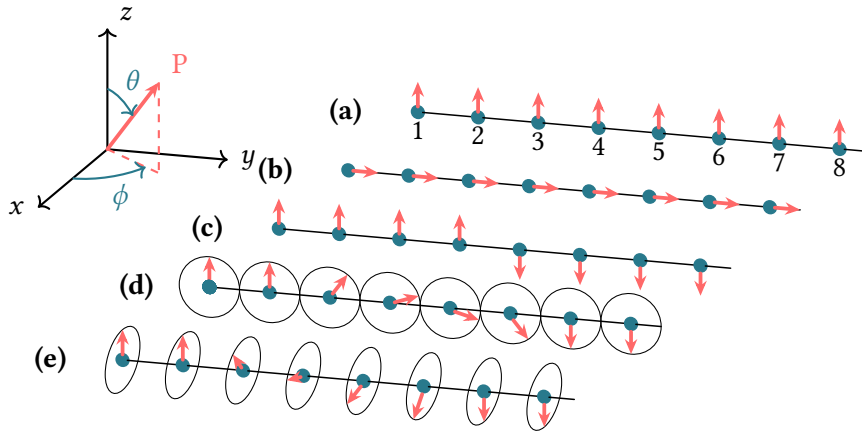


Figure 11.1: Schematic of five different spin alignments in monoatomic chains: **(a)** parallel spins perpendicular to the chain axis ($\theta_i = 0$), **(b)** parallel spin along the chain axis ($\theta_i = \pi/2, \phi_i = \pi/2$), **(c)** abrupt domain wall between two domains with $\theta_i = 0$ and $\theta_i = \pi$, **(d)** Néel type domain wall ($\theta_i \in [0, \pi], \phi_i = \pi/2$) **(e)** Bloch-type domain wall ($\theta_i \in [0, \pi], \phi_i = 0$).

alloys [MP75]), a variety of low-dimensional systems have a large AMR (20-50% in 3d transition metal nanojunction [BPM04], >100,000% in (Ga, Mn)As/GaAs/(Ga, Mn) stacks [Rüs+05]). Here, we will use our new implementation to determine the AMR of ferromagnetic monoatomic iron chains and constraint domain walls.

11.1.1 Magnetic Anisotropy in the Ideal Iron Chain

The ground state of an iron chain is characterized by an interatomic spacing of 2.26 Å and ferromagnetic alignment of spin magnetic moments with $3.35\mu_B$ per iron atom. We observe small differences in the total energy depending on the alignment of the spin moments relative to the chain axis. This MAE favors an alignment of the spin moments parallel to the chain axis ($E(\theta = \pi/2) - E(\theta = 0) \approx 1$ meV per Fe). Similarly, the band structure of the iron chain is anisotropic with respect to the direction of the spin magnetic moments. Like MAE, the anisotropy of bands arises because of the SOC in Fe. When the spin moments are parallel to the chain axis ($\theta = \pi/2$), SOC acts like an effective magnetic field and splits some of the bands, which are doubly degenerate in the scalar relativistic case (Figure 11.2 (a)). Not all bands split, nor is the splitting uniform for all bands that are split. Jacob et al. [JFP08] show that the same effect can be observed in nickel chains. Furthermore, they showed that the size of this splitting is proportional to the size of the orbital magnetic moment (m_{\parallel}) and spin (σ_{\parallel}) parallel to the chain axis. Effectively, the SOC introduces an orbital Zeeman effect along the spin-polarization

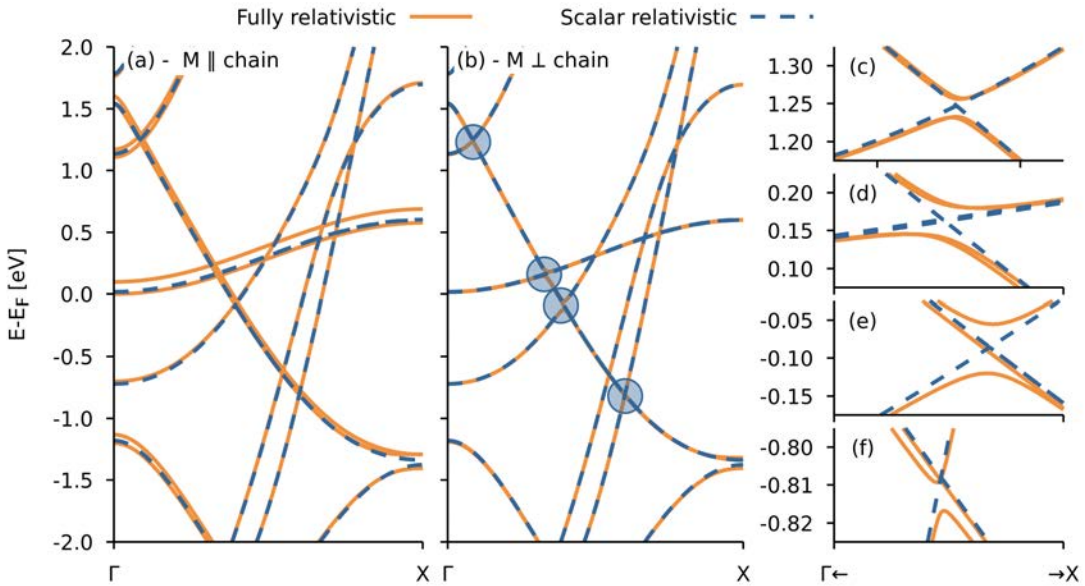


Figure 11.2: Comparison of scalar relativistic (SR) and fully relativistic (FR) spin band structure of a monatomic iron chain with spin moment parallel to the chain axis (**a**) and perpendicular to the chain axis (**b - f**). For spins aligned with the chain axis SOC acts as an effective magnetic field, shifting bands proportionally to their orbital magnetic moment (**a**). For spins perpendicular to the chain axis (**b**), the two band structures are almost identical, except for SOC induced avoided band crossings, which are highlighted with blue circles. Zoomed-in views of each avoided band crossing in the energy range from -2 eV to 2 eV are displayed in panels (**c - f**).

axis. This same effect is responsible for band splitting in the iron chain with spin moments parallel to the chain axis [TG07].

In contrast, the band structure of an iron chain with perpendicular moments features no shifted bands. It reproduces the scalar-relativistic case almost exactly. However, closer inspection of the intersection points of all bands reveals avoided band crossings for some bands (Figure 11.2 (b to f)). These avoided band crossings are absent when the spin moments are parallel to the chain axis or without SOC. Whether SOC repels two bands is determined by their respective spin σ and orbital magnetic quantum numbers m projected along the magnetic axis of the chain: crossings of bands with (σ, m) and $(\pm\sigma, \mp m)$ are lifted [JFP08]. The results we obtain for the electronic and magnetic structure of infinite monatomic iron chains match previously published studies [DP98; EKF03; TG07]. Only the magnetic anisotropy energy we obtain is a factor of 2 lower compared to other studies [OYC+09; Wij86]. Given that all other properties are reproduced well and our focus is on the transport properties, we can proceed safely with our simulation parameters.

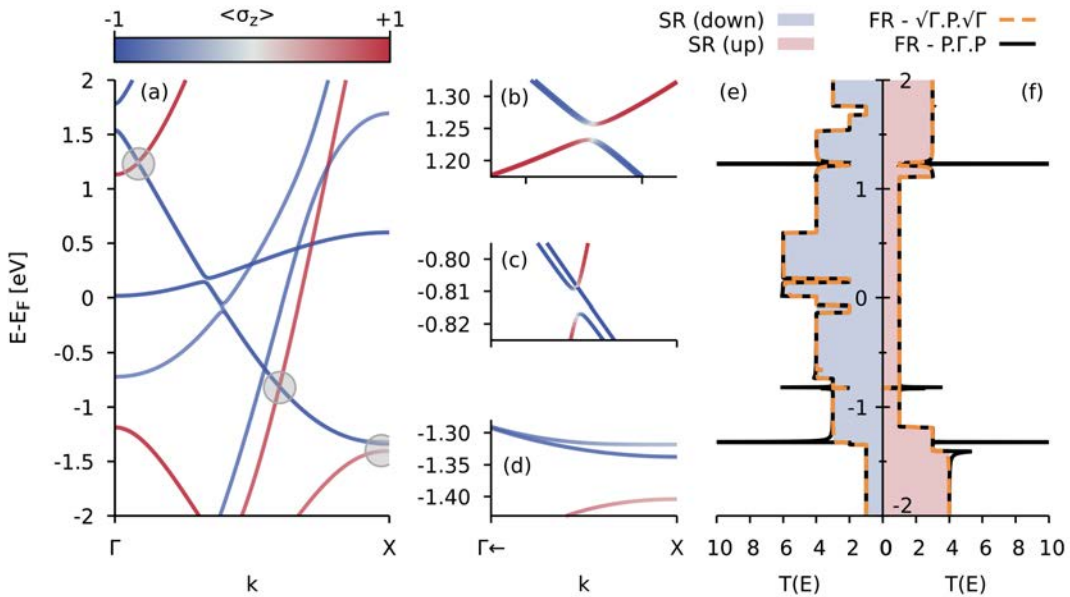


Figure 11.3: Spin texture (a - d) and spin-channel projected transmission ((e, f)) of an iron chain with spin magnetic moments perpendicular to the chain axis ($\theta = 0$). The spin texture is collinear to the magnetic axis in the -2 eV to 2 eV energy window except for three points (grey circles in (a) and zoomed-in graphs (b - d)). The spin channel projected transmission calculated with Equation (6.19) ($\sqrt{\Gamma}P\sqrt{\Gamma}$) reproduces the scalar relativistic spin channel transmission except for the energy corresponding to avoided crossings (-0.81 eV, -0.10 eV, 0.15 eV, and 1.25 eV) where it is reduced according to the number of split bands. The spin channel projected transmission calculated with Equation (6.23) ($P\Gamma P$) also reproduces the scalar relativistic case closely but diverges at those energies where the spin texture is not collinear to the projection axis.

Regardless of the alignment of the spin relative to the chain axis, the bands of the iron chain are almost perfectly spin-polarized along the magnetic axis of the system (Figure 11.3 (a) and Figure 11.4 (b)). In the case of spins perpendicular to the chain axis ($\theta = 0$) the spin texture becomes non-collinear at the two avoided band crossings where bands with opposite spin magnetic moment are repelled (Figure 11.3 (b) and (c)), and near the band edges of the two parabolic bands with opposite spin moments at X (Figure 11.3 (d)). The fully relativistic spin channel projected transmission calculated using Equation (6.19) (orange dashed line in Figure 11.3) reproduces the scalar relativistic spin channel transmissions. It corresponds to the number of spin-up (spin-down) bands at any given energy (Landauer formula) and deviates from the scalar-relativistic calculation at the avoided band crossing. Depending on the number of bands that repel due to the SOC, the transmission is reduced by the same number, either by 2 or 4. The spin-channel-projected transmission calculated using Equation (6.23) performs equally well for most energies but diverges at those points where the spin texture becomes

non-collinear. This showcases that the two methods work as expected: where the spin texture is collinear, the projector commutes with the broadening matrix, and the two methods become equivalent. At the points where the spin texture is non-collinear to the projection axis, the equivalence breaks down, and the approximation in Equation (6.23) is not good enough to describe the transmission properly. From this point on, we only use Equation (6.19) to calculate the spin-channel projected transmission. In the case of spins parallel to the chain axis ($\theta = \pi/2$), the difference between the scalar relativistic and fully relativistic transmissions is slightly larger.

Due to band splitting, new plateaus arise in the transmission function. This is particularly evident near the Fermi level, where the size of the band splitting is the largest. Overall, the transmission function still closely resembles the scalar relativistic case. The total transmission at the Fermi level is reduced by 1 (14%) even for small angles (Figure 11.4 (d)). This magnetic anisotropy of the transmission at the Fermi level is the signature of anisotropic magnetoresistance. Therefore, our work demonstrates that the anisotropic magnetoresistance

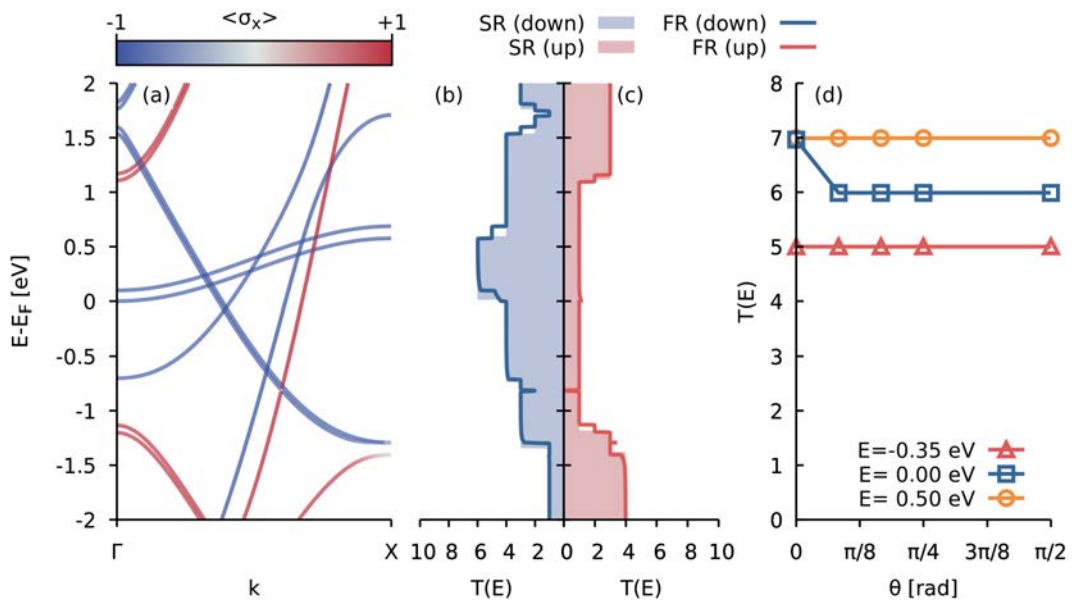


Figure 11.4: Spin texture (a) and spin-channel projected transmission (b, c) of an iron chain with spin magnetic moments parallel to the chain axis ($\theta = \pi/2$) and magnetic anisotropy of the transmission. The spin texture is collinear to the magnetic axis (x). The fully and scalar relativistic transmission function match closely. Near the band edges of the bands shifted by SOC, the fully relativistic transmission function exhibits additional plateaus corresponding in width to the band splitting. In both cases, the transmission corresponds to the number of bands at any given energy. (d) Transmission as a function of the angle between the spins and the chain axis for three energies. The transmission at the Fermi level changes between 7 and 6, implying that iron chains exhibit anisotropic magnetoresistance at sufficiently low temperatures.

predicted for nanowires [Hu+15; OYC+09] can also be observed in the one-dimensional limit (the monatomic chain). Further away from the Fermi level, the transmission is constant and no magnetoresistance is observed. Therefore the magnetoresistance can only be observed at low temperatures.

11.1.2 Domain Wall Conductivity

To model a constrained domain wall, we set up a transport system with two electrodes (orange atoms in Fig. 11.5) with non-parallel spin moments. We then relax the direction and amplitude of the spin moments of the atoms between the electrodes (blue atoms in Fig. 11.5). The NEGF approach serves two purposes in these calculations: it provides a natural way of fixing the spin direction in parts of the system, and it allows us to simulate a domain wall without interactions between periodic images.

The magnitude of the spin moments in the domain wall is constant at $3.35 \mu_B$, irrespective of the angular offset between the spin moments in the two electrodes (θ) (Figure 11.6). Depending on the initialization of the density matrix, the spin moments form different types of domain walls. If the density matrix is initialized with all spin moments in the yz -plane, i.e., in a plane containing the chain axis, then the final magnetic moments form a Néel-type domain wall (Figure 11.1 (d)). Similarly, if all initial spin moments lie in the xz -plane, i.e., all perpendicular to the chain axis, then we obtain a Bloch-type domain wall (Figure 11.1 (e)). We can produce these different types of domain walls because the initial guess determines the symmetry of the Hamiltonian, and there are no external fields that break the symmetry of the initial magnetic structure. There is one other notable high-symmetry case for electrodes with antiparallel spin

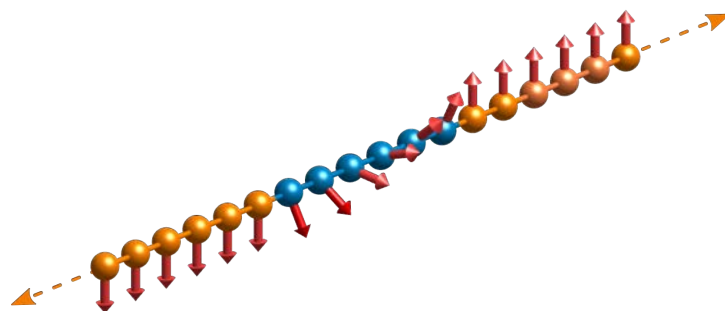


Figure 11.5: Infinite iron chain with a 6-atom wide domain wall (blue atoms) between two semi-infinite sections with opposite magnetic moments (orange atoms).

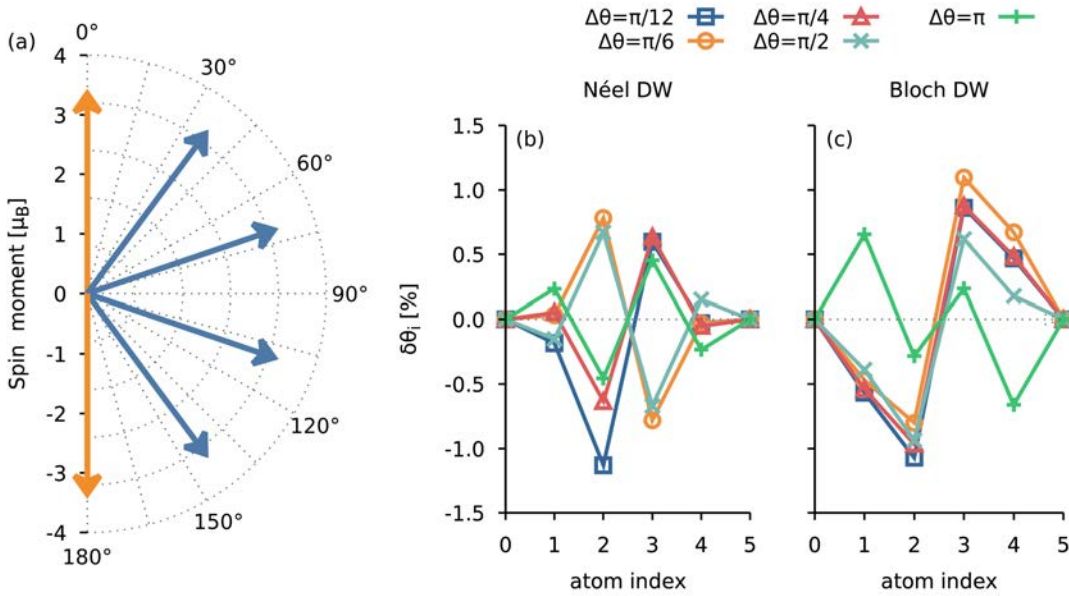


Figure 11.6: Direction and size of spin moments in a 4-atom wide, constraint domain wall with $\Delta\theta = \pi$ (a). Orange atoms indicate the fixed spin moments in the electrode and blue arrows the spin moments of the device atoms. Relative deviation from ideal positions $\delta\theta_i = \theta_i - i\Delta\theta/(N + 1)$ for 4-atom wide domain walls with $\Delta\theta \in \{\pi/12, \pi/6, \pi/4, \pi/2, \pi\}$ for Néel (b) and Bloch domain walls (c).

moments: when the initial magnetic moments in the device are all collinear to the electrodes, we obtain an abrupt domain wall (Figure 11.1 (c)). In principle, we could choose random initial spin moments to find the most stable domain wall. However, because of the small size of the MAE in the iron chain, this becomes a very challenging task. Even high-symmetry structures require up to a thousand SCF steps to converge. Instead, we focus on the three high-symmetry cases: abrupt, Néel, and Bloch domain walls.

In Néel and Bloch domain walls, we observe an equal change in the angle from one atom to the next (Figure 11.6). The change in angle between two neighboring atoms in the domain wall is equal to $\Delta\theta/(N + 1)$, where N is the number of atoms in the domain wall and $\Delta\theta$ is the difference in the polar angle (θ) that describes the spin direction in the left and right electrodes. The magnetic coupling between the atoms in the unit cell should be the same, considering that all species, coordination, and bond lengths in the device region are equal. Therefore, the constraint domain wall should be symmetric with equal change in angle. In Néel-type domain walls, the magnetic anisotropy could lead to a deviation from this uniformity. However, the Fe-Fe magnetic exchange constant (≈ 10 meV [Ant+10; Bez+13]) is approximately one order of magnitude larger than the MAE [OYC+09; Wij86], and would thus push the system to a

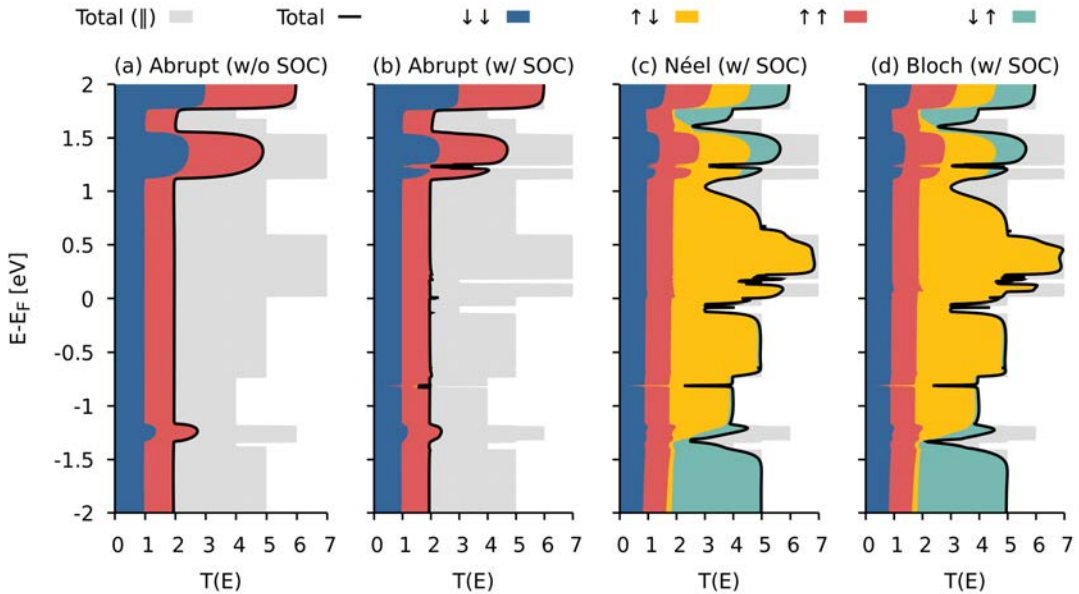


Figure 11.7: Zero-bias transmission of 180° domain walls calculated with scalar relativistic formalism with collinear spin (a), fully relativistic formalism (b-d). Filled curves are stacked on top of each other to visualize the decomposition of the total transmission (black line) in terms of different spin channels and spin flips. The shaded grey area in the background displays the transmission of an iron chain without a domain wall ($T_{||}$) as a point of reference. For the abrupt domain wall (a) and (b), the total and spin channel projected transmission (blue (down) and red (up)) are significantly reduced compared to the iron chain without a domain wall. SOC has no significant effect on the transmission through the abrupt domain wall. For 4-atom wide Néel (c) and Bloch (d) domain walls, the transmission is much higher. The gradual change in the magnetic moment along the domain wall allows for significant spin flip transmission (yellow and green filled curves). The contributions of the pure spin-up and spin-down transmissions are comparable to the abrupt domain wall.

more uniform domain wall like the one we observe. We conclude that the relaxation of spin moments in our code is consistent with expectations based on the symmetry of the system and the comparison of MAE and magnetic exchange constant.

The non-periodic structure of the domain wall gives rise to electron scattering. The resulting transmission is not a step function as in the periodic parallel case (Figure 11.7). We find that the resistance of an abrupt domain wall is significantly higher than that of the Néel or Bloch domain walls. SOC in Fe is not strong enough to allow for spin-flips in an abrupt domain wall. As a result, the scalar and fully relativistic transmissions are almost identical and reduced by a factor of 3 compared to the parallel case near the Fermi level. In Néel or Bloch domain walls, a width of 4 atoms, spin-flip transmissions are significant. The pure spin-up and spin-down transmissions remain equally suppressed as in the abrupt domain-wall case. The reduction of

these contributions in all four cases can be immediately understood from the band structure of the iron chain. In the left electrode with magnetic moments pointing along z , only one band with spin $\sigma_z = 1$ exists. Therefore, the spin-up transmission can not exceed one. The same is true for the spin-down channel in the right electrode. Thus both pure spin-channel transmissions are limited to 1. In Néel and Bloch domain wall, the change in spin moments is gradual and allows for spin-flip, i.e., scattering between different spin channels. The contribution of the two spin-flip transmissions (down into up (yellow) and up into down (green)) are not equal. This allows spin-down states in the left electrodes to scatter into spin-up states in the right electrode (down-up spin-flip transmission; depicted as a yellow curve in [Figure 11.7](#)). Below 1 eV the availability of spin-down and spin-up channels in the left and right electrodes is reversed, and up-down spin-flip transmission becomes dominant. We also performed calculations with 5 and 6-atom-wide domain walls, which show qualitatively the same results. The low TAMR in domain walls with more than two atoms matches predictions by Autès et al. [[Aut+08](#)] and Velev and Butler [[VB04](#)].

11.1.3 Computational Details

Our transport setup consists of an infinite chain with Fe atoms. The simulation cell contains 12 atoms: 4 atoms on each side correspond to one principal electrode layer, and the 4 atoms in the center represent the scattering device. In the electrode calculations, we sample the reciprocal space along the chain axis with 101 k points. We used a double-zeta-polarized basis set for the Fe atoms (energy shift 0.2 eV, split norm 0.15), a real space grid with a cut-off of 700 Ry, an electronic temperature of 8 meV, and the PBE exchange-correlation functional [[PBE96](#)]. The lattice constant is optimized up to a stress tolerance of 0.1 meV/Å. Calculations were carried out within the fully relativistic pseudo-potential formalism [[CC12](#)], i.e., including spin-orbit interactions, and the scalar relativistic collinear spin formalism. We used pseudo-potentials from the PseudoDojo database [[van+18](#)].

The density matrix in the scattering region is initialized from a periodic SIESTA calculation. For the initial guess of the density matrix in the domain walls, we extend the scattering region by three extra iron atoms on each side and terminate the chain with hydrogen atoms. We then initialize the moments along the domain wall in one of the high symmetry configurations discussed above and perform a few SCF steps in SIESTA. It is important to terminate the initial SIESTA early enough for the spin moment to remain non-collinear but late enough for the charge density to converge reasonably well. If the convergence criteria for this initial calculation are chosen too tight all magnetic moments will become parallel. On the other hand, if the convergence criteria are chosen too loosely the DFT+NEGF SCF loop diverges in the first few

steps. We find that a good initial guess can be obtained with a convergence threshold of 10^{-3} for the density matrix and 10^{-2} eV for the Hamiltonian works. For the subsequent DFT+NEGF SCF loop, we choose much more stringent convergence thresholds: 10^{-6} for the density matrix and 10^{-4} eV for the Hamiltonian. We perform the complex contour integral with a circle contour starting at $(-20+0.1i)$ eV which transitions into a line contour at $(0.08+1.6085i)$ eV. The contour encircles 32 poles of the Fermi function. The transmission function is calculated with `TBTRANS` using a contour along the real axis with a spacing of 0.2 meV.

The band structure and spin texture of the iron chains with different magnetic moments are calculated in the primitive unit cell. To resolve the SOC-induced band gaps, we calculate the band structure and spin texture on 4800 points along the Γ -X direction.

11.2 Fe-MgO-Fe Hetero Structure (3D)

In addition to AMR, magnetic transport devices may also exhibit tunneling magnetoresistance (TMR), which refers to changes in the resistance of a magnetic tunneling junction depending on the relative magnetic alignment of its magnetic components. Magnesium oxide (MgO) based tunneling junctions, such as Fe / MgO / Fe, have been predicted to yield TMR ratios between a few hundred and a few thousand percent [But+01; MU01]. We test whether our new implementation could previously reproduce TMR in Fe / MgO / Fe and whether these junctions exhibit tunnel anisotropic magnetoresistance (TAMR).

Fe / MgO / Fe junctions are periodic in the two directions parallel to the interface and therefore require sampling at k points in these directions. With this system, we check whether our code also works for more realistic cases with three-dimensional electrodes and non-homogenous geometries in the scattering device. We will first characterize the transport properties of the electrode (bulk iron) and then move on to tunneling junctions. Previous works on Fe/MgO/Fe tunneling junctions (with scalar-relativistic DFT) [BVT05; Hei+08; Wal+06] and studies of magnetic anisotropy in bulk iron [KHB08; Zwi+08] will serve as a reference point for our calculations.

11.2.1 Magneto Resistance of Bulk Iron

Similarly to iron chains, bulk iron (bcc) exhibits magnetic anisotropy in its band structure. Without SOC, the Brillouin zone of iron contains six equivalent H points. However, with SOC these six equivalent points split into two or three inequivalent groups depending on the alignment of the spin magnetic moments with respect to the crystal structure. For magnetic moments aligned along one of the high-symmetry axes [001] or [100], there are two inequivalent

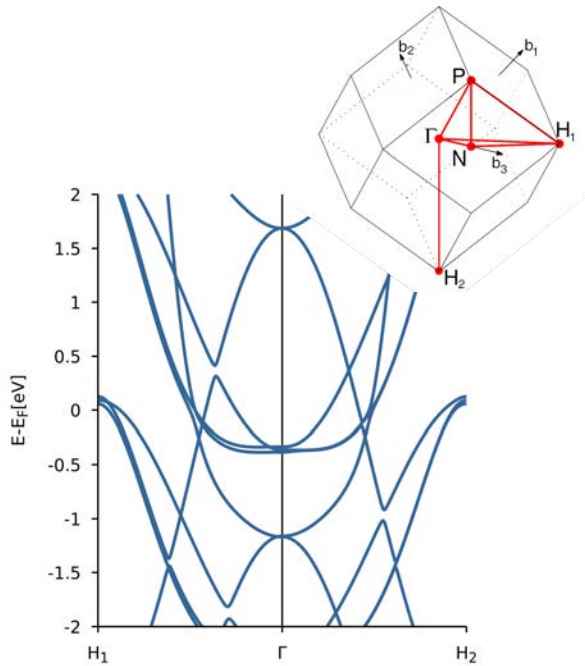


Figure 11.8: Band structure of bulk iron magnetized along the [001] direction. The band structure is calculated along a line parallel to the magnetization axis (H_1 - Γ) and a line perpendicular to the magnetization axis Γ - H_2 . Along parallel direction, the degeneracy of the parabolic band crossing the Fermi level at H_1 is lifted due to SOC. Along the Γ - H_2 the degeneracy is not lifted. Instead, multiple band crossings are opened up. The inequivalence of the structure along these two lines demonstrates a magnetic anisotropy electronic structure of the bulk iron.

H points (H_1 and H_2). Analogous to the iron chain, SOC causes band splitting or avoided crossing depending on the relative alignment of the spin magnetic and orbital magnetic moments of the bands (Figure 11.8). The effects are different along the Γ - H_1 (parallel to the magnetic axis) and Γ - H_2 (perpendicular to the magnetic axis) directions. As a result, the transmission function for transport along the [001] direction also changes depending on the orientation of the magnetic moments. This effect is particularly strong at $E = -0.97$ eV, where a large gap opens in the direction perpendicular to the magnetic moment. This gap opening can also be observed in the zero-bias transmission function for bulk iron when the magnetic moment is perpendicular to the transport direction. In this case, the transmission function at $E = -0.97$ eV features a circular plateau at the center of the Brillouin zone (Figure 11.9 (d)). For magnetic moments parallel to the transport direction, this plateau is absent (Figure 11.9 (b)). Instead, a small ring appears at the center of the Brillouin zone, which likely corresponds to a mini gap opening at the same energy at another point in the Brillouin zone perpendicular to the transport direction. To calculate the AMR of iron, we need to calculate the average of the transmission function of the whole BZ. For magnetic moments parallel and perpendicular to the transport direction, we obtain a total transmittance of 4.311 and 4.257, respectively. This corresponds to an AMR of only 1%. At the Fermi level (Figure 11.10), this effect is even further reduced to less than 0.1%. Although AMR is small in bulk iron, we can understand from the transmission function of bulk iron why nano-constriction in iron can lead to a large AMR. The constriction acts as

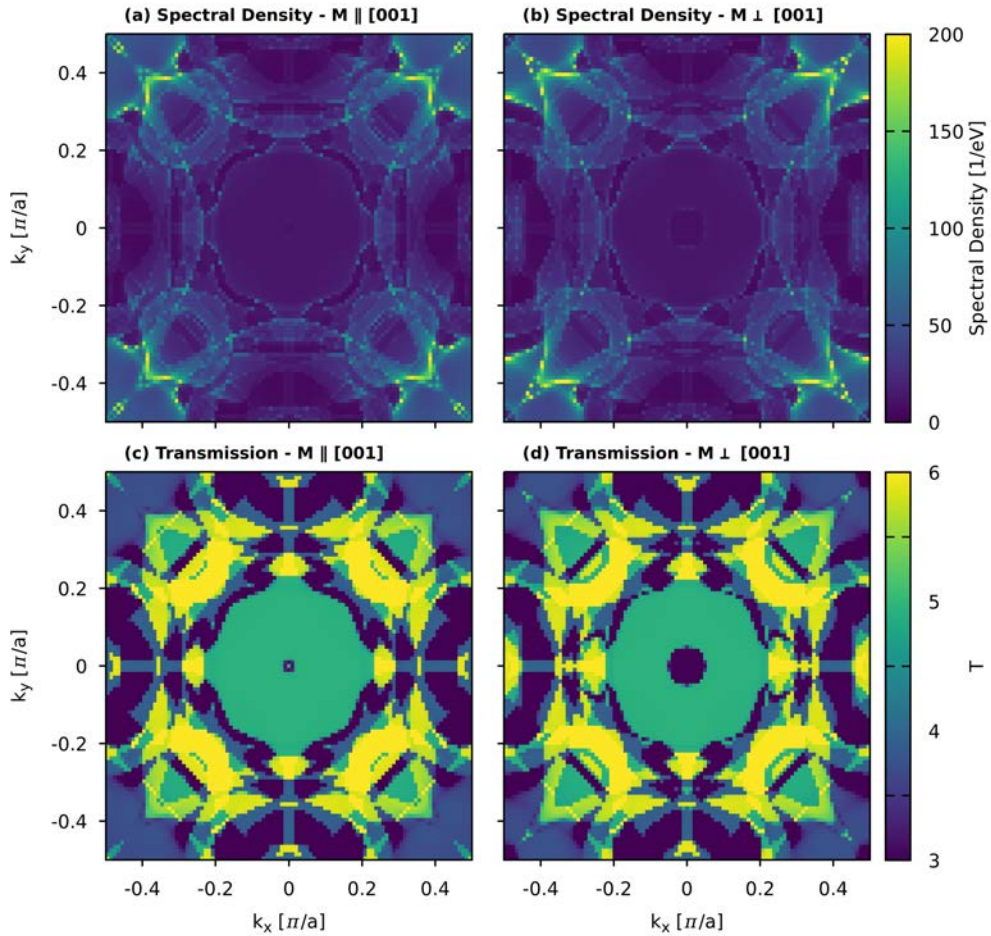


Figure 11.9: Spectral function and zero-bias transmission of bulk iron magnetization (\mathbf{M}) parallel and perpendicular to the transport direction ($[001]$) at $E = -0.97$ eV. For $\mathbf{M} \parallel [001]$, the transmission function has an extended plateau ($T=5$) around Γ . For $\mathbf{M} \perp [001]$, an additional circular plateau ($T=3$) emerges at the center of the Brillouin zone. The spectral density exhibits the same symmetry as the transmission function.

a phase space filter and restricts transmission to channels with vanishing lattice momentum perpendicular to the transport direction ($k_x = k_y = 0$). Thus, the reduction of AMR due to k -space averaging is avoided and AMR can be orders of magnitude larger than in bulk iron. Our results for bulk iron are consistent with previous studies of magnetic anisotropy and AMR in iron [KHB08; Zwi+08].

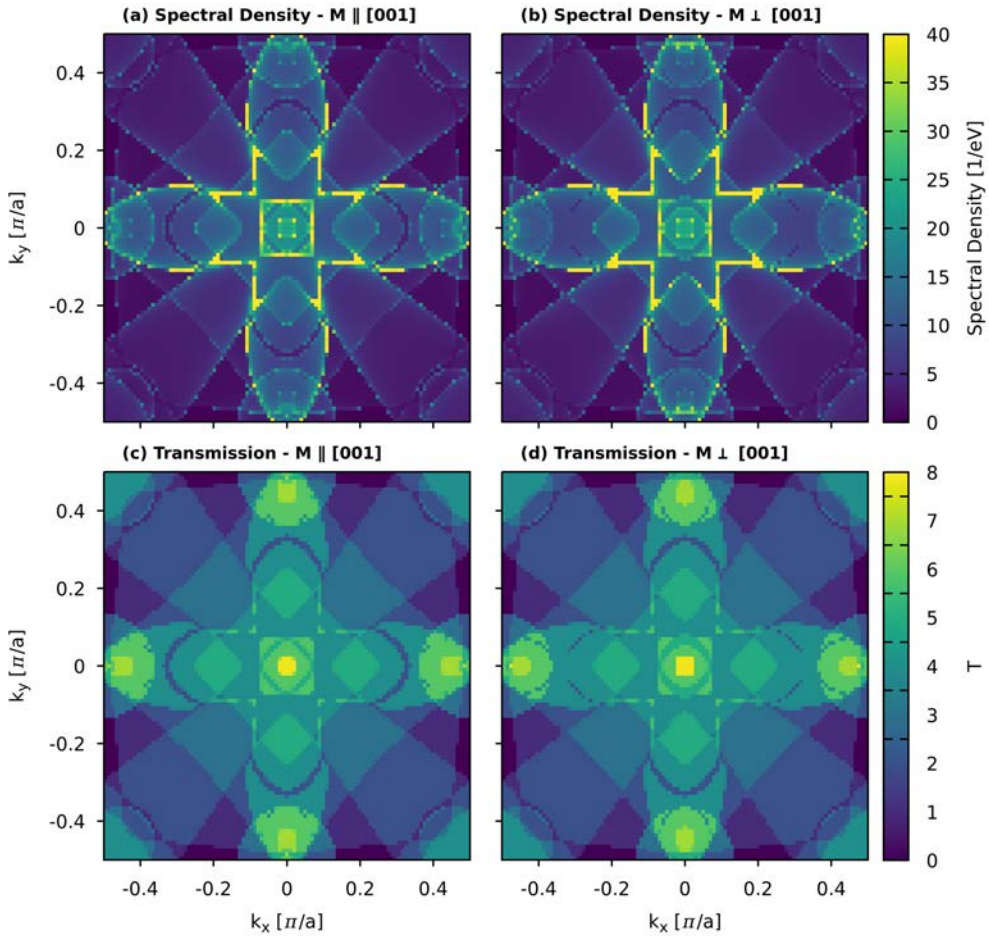


Figure 11.10: Spectral function and zero-bias transmission of bulk iron for magnetization (M) parallel and perpendicular to the transport direction $[001]$ at the Fermi level. The effect of the magnetic direction is much weaker at the Fermi level compared to $E=-0.97$ eV. The central plateau of the transmission function is circular for $M||[001]$ to the transport direction and square otherwise. The spectral density exhibits the same symmetry as the transmission function.

11.2.2 Magneto Resistance in Fe/MgO/Fe Tunneling Junctions

Fe/MgO/Fe tunneling junction consists of a few layers of MgO sandwiched between multiple layers of iron (Figure 11.11). The MgO $[110]$ plane is parallel to the Fe $[100]$, creating a clean interface between the two materials. The iron atoms of the contact layer sit on top of the oxygen sites in MgO. The transmission of the junction decays exponentially with the number of MgO layers between the iron electrodes [Hei+08]. Here we choose 4 MgO layers, for which we

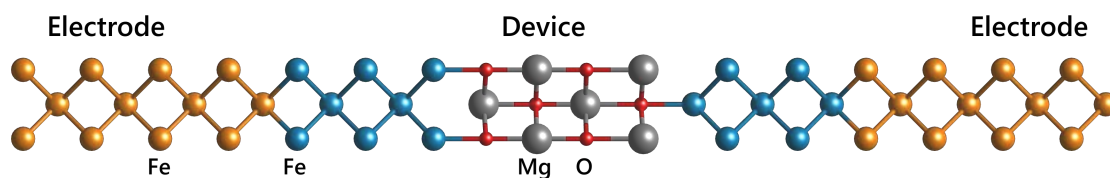


Figure 11.11: Ball and stick model of a Fe/MgO/Fe junction.

expect to observe a significant TMR effect and a transmittance that does not require excessive computational accuracy.

Figure 11.12 depicts the transmission function of this tunneling junction for electrodes with parallel magnetization at the Fermi level. The MgO tunneling barrier acts as a phase filter, and the transmission function becomes strongly localized at the center of the Brillouin zone. The average transmission is reduced by a factor of 650 to 0.0044. Both aspects are consistent with the prediction of previous DFT studies for Fe/MgO/Fe junctions with 4 MgO layers. We go beyond previous studies [BVT05; Hei+08; Wal+06] and include spin-orbit coupling. As a result, we observe two additional features in the zero-bias transmission: a) a small ring at which the transmission is reduced, which corresponds to the ring of reduced transmission in the bulk electrode, and b) if the magnetization is perpendicular to the transport direction the cubic symmetry of the transmission function is broken and additional sharp features emerge in the transmission spectrum. The decomposition of the total transmission into spin-up and spin-down components reveals that the primary contributions to the transmission stem from the spin channel parallel to the magnetization axis (spin-up) (Figure 11.13). The average transmission of the spin-down channel is one order of magnitude smaller and features sharp peaks along the reciprocal lattice directions.

11.2.3 Computation Details

All calculations were carried out within the fully relativistic pseudo-potential formalism, [CC12] and the PBE functional [PBE96]. We used a double-zeta-polarized basis set for the Fe atoms (energy shift 0.27 eV, split norm 0.15), a real space grid with a cut-off of 800 Ry, and an electronic temperature of 10 meV.

For bulk iron, our transport setup consists of 4 MgO layers sandwiched between 13 layers of iron on each side. In the electrode calculations, we sample the reciprocal space using a Monkhorst Pack grid with 100 points along the semi-infinite direction and 16 points along the transversal direction. We use the same number of transversal k points in the DFT+NEGF

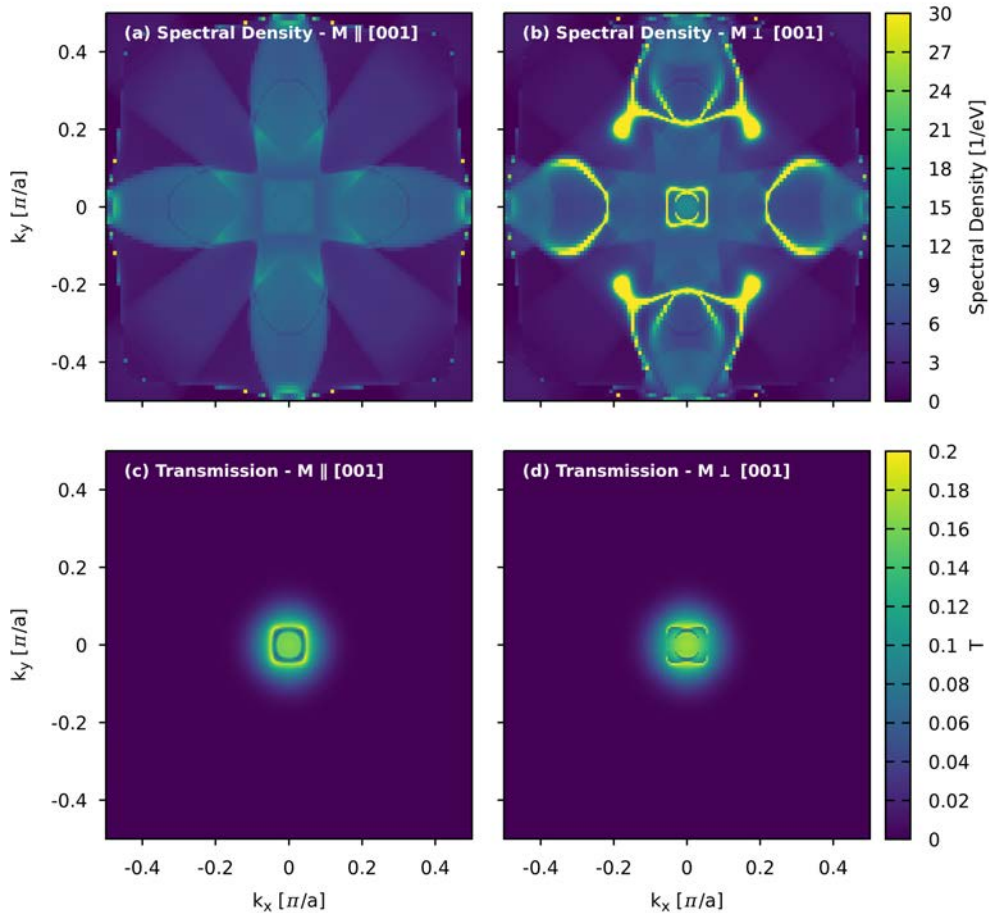


Figure 11.12: Spectral function and zero-bias transmission of a Fe/MgO/Fe tunneling junction with 4 MgO layers. For magnetization in the iron layers parallel to the transport direction, the spectral density is smooth throughout the Brillouin zone and resembles the spectral density of bulk iron closely. For magnetization perpendicular to the transport direction, sharp features emerge in the density, and new sharp features emerge in the density. For both orientations of the magnetization, the transmission function is zero in most of the Brillouin zone. Only around the center of the Brillouin zone do we observe significant transmission. For magnetization perpendicular to the transport direction, this feature in the transmission has cubic symmetry. For magnetization perpendicular to the transport direction, the cubic symmetry is broken, and an additional structure in the transmission function emerges. A feature of the same shape can be observed in the density of spectral density.

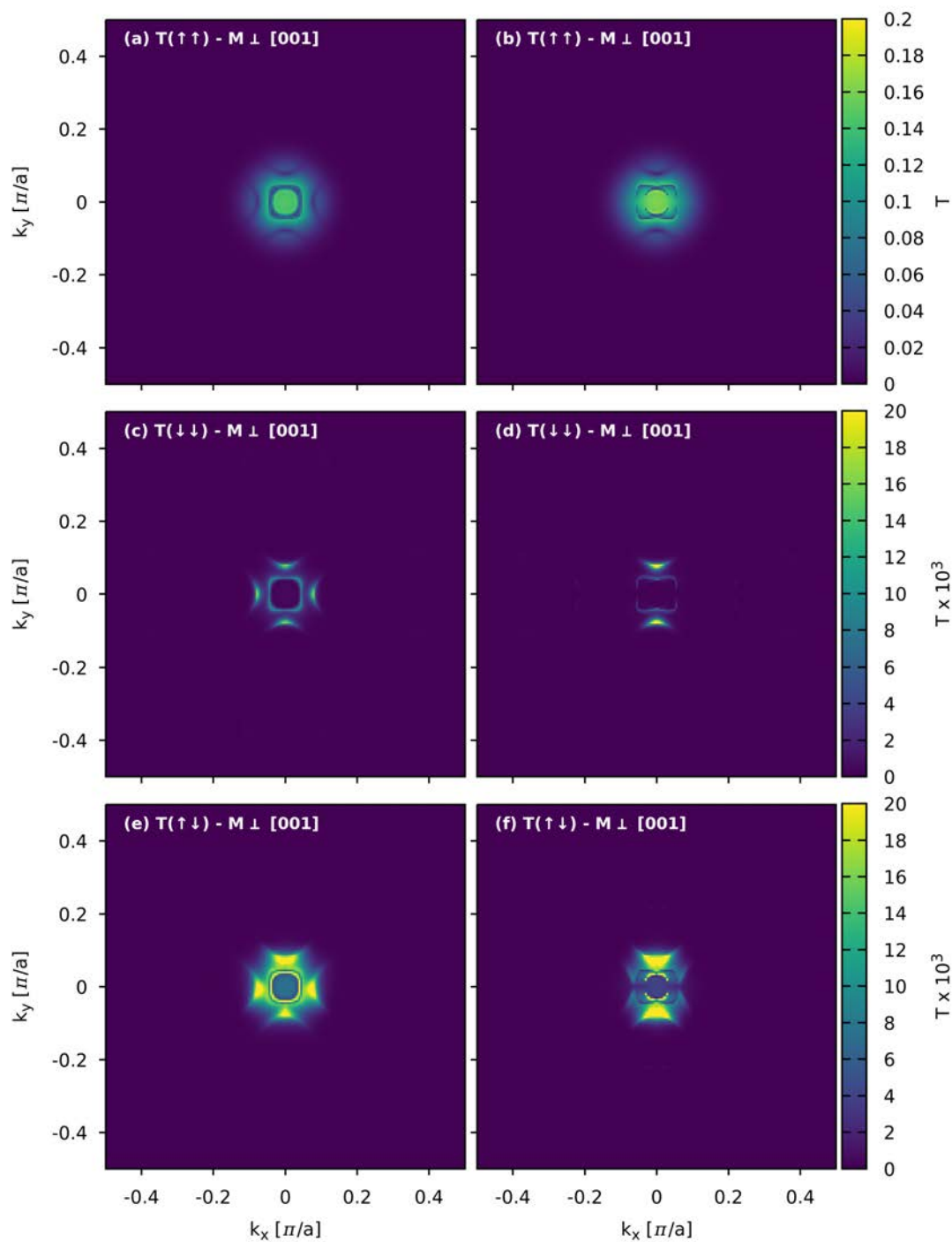


Figure 11.13: Spin channel projected zero-bias transmission of a Fe/MgO/Fe tunneling junction with 4 MgO layers.

calculation. The lattice constant of bulk iron is optimized up to a stress tolerance of $0.1 \text{ meV}/\text{\AA}$. We relax the atoms in the central part of the transport device until the forces acting on them are smaller than $10 \text{ meV}/\text{\AA}$ and stress along the direction perpendicular to the interface is smaller than $0.1 \text{ meV}/\text{\AA}$. During the relaxation, we keep the electrode regions (8 atoms per principal layer) and the lattice vectors in the transversal direction fixed. Comparison of the transmission function for Fe/MgO/Fe tunneling junctions with a different number of additionally fixed layers shows that relaxing all atoms between the two electrodes introduces additional scattering (Figure 11.14). Keeping one or two extra layers fixed removes this contact scattering. Here we keep a single layer fixed. Similarly, we find that including less than 5 iron layers between the electrodes and the MgO layer introduces additional scattering.

For the parallel magnetic configurations, we initialize the density matrix from a normal SIESTA calculation with the same geometry and magnetic structure. For the antiparallel magnetic configuration, we initialize the density matrix from a SIESTA calculation of $1 \times 1 \times 2$ supercells with matching magnetic moments at the periodic boundary [13 layers Fe(\uparrow), 4 layers MgO, 26 layers Fe(\downarrow), 4 layers MgO, 13 layer Fe(\uparrow), repeat...]. In the TRANSIESTA calculation, the second half of this cell is discarded.

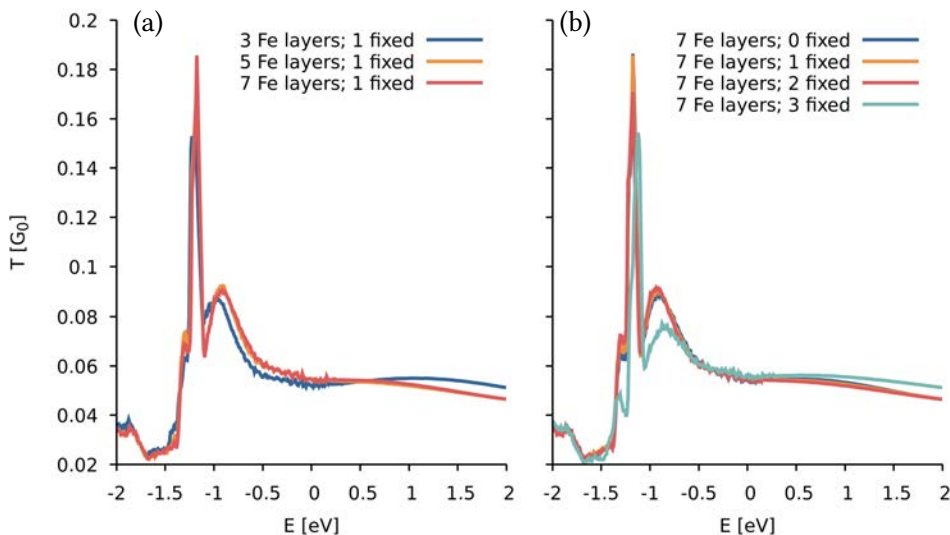


Figure 11.14: Convergence of the transmission function in a Fe/MgO/Fe junction with number of iron layers between the MgO layers and the electrodes (a) and with number of fixed layers (b).

11.3 Transition Metal Dichalcogenides (2D)

As a third test case, we simulate a lateral MoS₂/WS₂ heterojunction, which has been shown to function as monolayer p-n junctions, [Gon+14]. Transition metal dichalcogenides (TMDs) are semiconductors of the type MX₂, where M is a transition metal atom (such as Mo or W), and X is a chalcogen atom (such as S, Se, or Te). TMDs are promising materials for a wide range of possible applications, including energy conversion [Wi+14] and storage [Din+12] and hydrogen evolution reaction [Li+11], due to their unique combination of the direct band gap, strong spin-orbit coupling, and favorable electronic and mechanical properties. In addition, TMDs are great materials for spintronics applications because of the SOC-induced splitting of the valence and conduction bands into different spin states. This splitting makes manipulations of the electron spin possible through optical excitation [Wan+18].

In the example of iron chains, we have seen that our code works well for non-collinear spin systems. However, SOC in Fe is relatively weak. To ensure the correct treatment of systems with significant spin-orbit interactions, we simulate two infinite transition metal dichalcogenide TMD monolayers (MoS₂, WS₂), and study the transport properties of a lateral heterojunction of the two materials. We will use reference calculations performed by Mads Brandbyge with QUNATUMATK as a reference point for our TRANSIESTA calculations. Like our new implementation, QUNATUMATK can simulate quantum transport with spin-orbit coupling. It also employs the NEGF formalism and can use localized basis sets making it a good point of reference.

11.3.1 Monolayer MoS₂ and WS₂

MoS₂ and WS₂ monolayers exhibit a direct band gap at K and K' . In MoS₂ this band gap is 1.79 eV wide and 1.48 eV in WS₂. Around the valence band maximum (VBM), the bands of MoS₂ and WS₂ are split by 0.15 eV and 0.45 eV, respectively (Figure 11.15). SOC acts as a magnetic field perpendicular to the monolayer on the top valence bands near K and K' and causes this band splitting. The direction of this interaction is opposite for K and K' , i.e., the spin moment of the upper split band is ± 1 for K and K' , respectively. These properties of the electronic ground state of MoS₂ and WS₂ and the overall band dispersion are comparable to our reference calculations with QuantumATK and other DFT studies [Zah+13; Zen+13].

In the pristine monolayers, the transport gap is equal to the electronic band gap, and the electron conductance increases linearly at the edges of the band gap. The TRANSIESTA and QUNATUMATK simulations agree well within a few electronvolts around the Fermi level. Thus, we demonstrate that it is possible to correctly calculate the transmission of materials with strong spin-orbit coupling. The most noticeable deviation occurs for MoS₂ at approximately

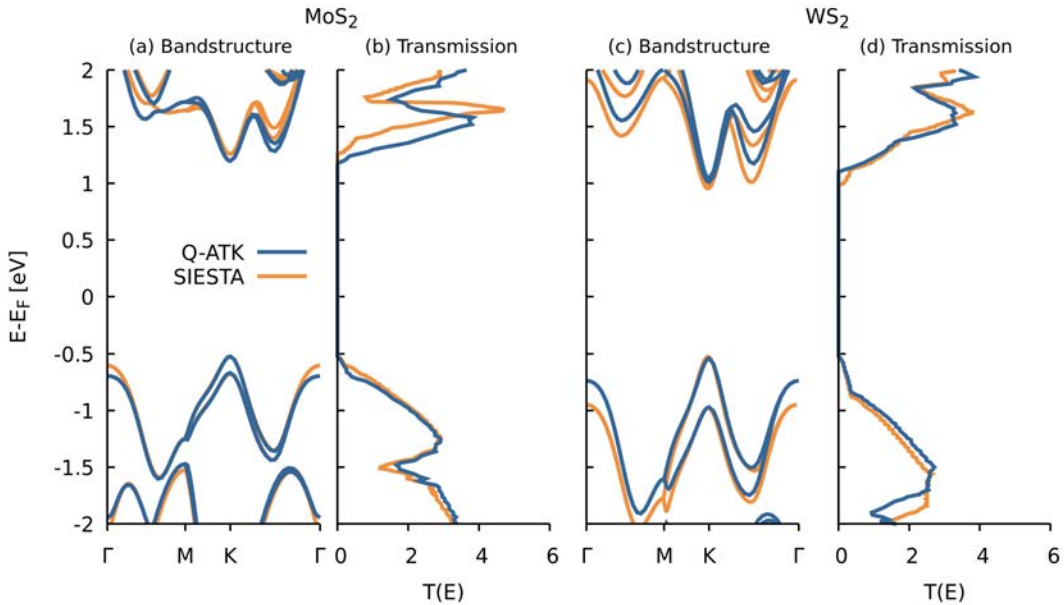


Figure 11.15: Band structure and zero-bias transmission function of MoS₂ (a, b) and WS₂ (c, d) monolayer. Orange lines show band structure and transmission function calculated with (TRAN)SIESTA, and blue dashed lines those calculated with QUANTUMATK. The simulation results agree well within a few eV around the Fermi level. Along the $M - K$ and $K - \Gamma$ directions, the band dispersion of MoS₂ obtained with the two codes is slightly different, resulting in a shift of the first peak of the transmission function above the transport gap.

1.6 eV, where the bands calculated with SIESTA are flatter than the QUANTUMATK bands and the two maxima along the $M - K$ and $K - \Gamma$ directions align. As a result, the maximum of the TransSIESTA transmission function is slightly higher compared to QUANTUMATK, and its position is shifted upward. These deviations are already present at the ground state DFT level and likely arises due to the use of different pseudopotential and basis set.

11.3.2 Lateral MoS₂-WS₂ Heterojunction

Simulations of bulk semiconductors within the NEGF formalism are unproblematic. However, when two different semiconductors come into contact, problems arise because it is unclear how to match the electrostatic potentials of the two materials. Furthermore, the low carrier density in semiconductors gives rise to very long electrostatic screening lengths, which would require extremely large device regions, to ensure proper screening of the electrode regions. Measurements of the built-in potential along WS₂-MoS₂ lateral junction show a step between the two potentials of about 0.1 eV, which is more than 2 μm wide [Che+15; Wan+22]. To avoid these issues, we uniformly gate the WS₂ and MoS₂ monolayers and the junction by

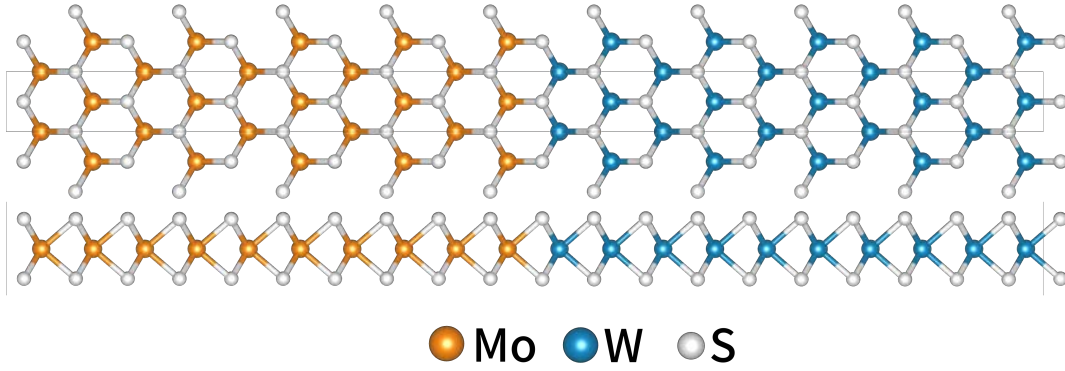


Figure 11.16: Crystal structure of a lateral MoS₂-WS₂ heterojunction top view (**top**) and side view (**bottom**).

adding a plane with constant charge density ($5.76 \cdot 10^{-3} \text{ e}/\text{\AA}^2$) 30 Å below the monolayers. This plane of charge induces a countercharge of the same magnitude but of the opposite sign in the monolayer. Therefore, the valence bands of the two materials are partially depopulated, making them metallic. The transmission function of both materials is similar near the Fermi level ($T(E_F) \approx 0.4$). In comparison to the ungated monolayer, the transmission functions are rigidly shifted, which indicates that this amount of doping has no significant effect on the electronic structure other than shifting the chemical potential.

To evaluate whether this level of doping is sufficient to screen electrodes from the potential step at the interface, we calculate the planar and macroscopic average [BBR88] of the electrostatic potential (V_H):

$$\text{Planar average: } \bar{V}_H(z) = \frac{1}{S} \iint_S dx dy V_H(x, y, z) \quad (11.1)$$

$$\text{Macroscopic average: } \bar{\bar{V}}_H(z) = \iint dx dy \frac{1}{a} \theta\left(\frac{a}{2} - |z|\right) \bar{V}_H(z) \quad (11.2)$$

where x is the position along the vacuum direction, y is the position along the periodic direction, z is the position along the transport direction, a is the strained lattice constant and Θ is the Heaviside step function. The convolution with a step function filters out the components of the planar average with a period of a . In Figure 11.17 the planar and macroscopic averages of the electrostatic potential and the charge density are displayed. The planar average is represented as orange and light grey lines in Figure 11.17 (c and d) for the scattering region and the electrodes, respectively. The planar average oscillates throughout the system: close to the nuclei, the potential is the lowest, and the charge density is the highest, and vice versa in

between the nuclei. These periodic oscillations are absent in the macroscopic average. Due to uniform doping, the macroscopic average of the charge density is equal in the two electrodes and close to constant in the scattering region. Immediately at the interface layer, we observe a small depletion region with electron exchange from WS_2 to MoS_2 and a step in the electrostatic potential of approximately 0.1 eV, which is consistent with the built-in potential observed experimentally [Che+15; Wan+22]. At contact with the electrode, the potential is smooth, which indicates that the electrode regions are appropriately screened from the interface.

Near the Fermi level, the transmission function of the heterojunction follows the minimum of the transmission functions of the two electrodes. This indicates that the interface introduces very little scattering and that the limiting factor for transmission through this system is the availability of transport channels in the electrodes. At -1 eV backscattering is much more significant, and the transmission function of the junction almost drops to zero. Since this effect occurs well below the Fermi level, it should not affect the transport for reasonable hole doping levels. This behavior and the overall shape and amplitude are consistent between our SIESTA and QUANTUMATK simulations.

After doping, the edge of the valence band in WS_2 (0.30 eV) is approximately 0.25 eV higher

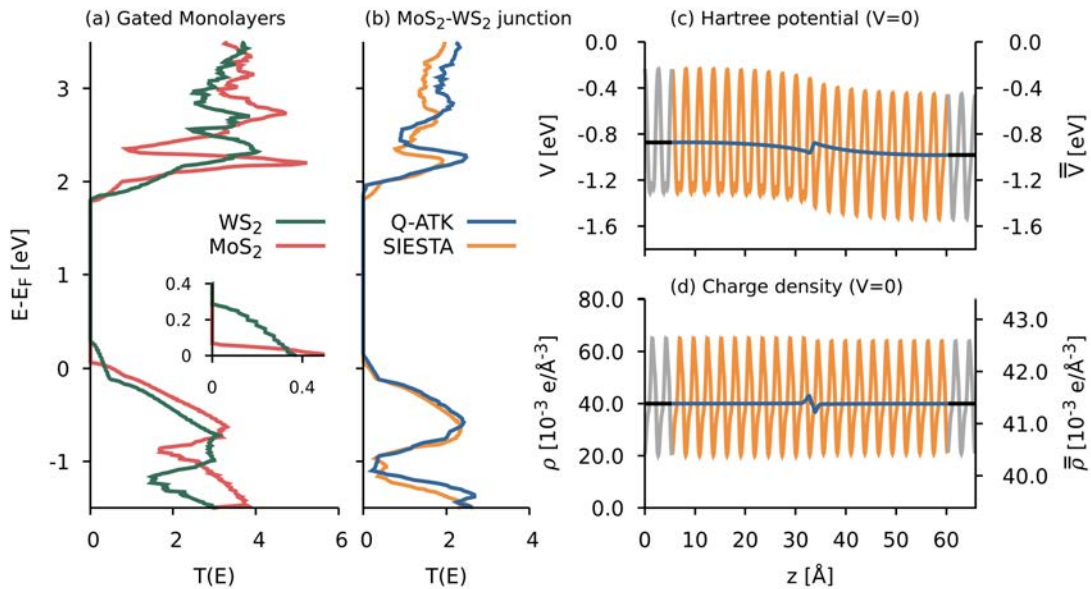


Figure 11.17: (a) Zero-bias transmission of hole-doped ($5.76 \cdot 10^{-3} e/\text{Å}^2$) MoS_2 (red line), WS_2 (dark green line) monolayers and (b) a lateral MoS_2 - WS_2 heterojunction with same doping concentration; (c) planar and macroscopic averaged electrostatic potential and (d) charge density of the same heterojunction. A comparison of the transmission function of the heterojunction in (b) calculated with TRANSIESTA and QuantumATK shows very good agreement.

than that of MoS₂ (0.05 eV), which should lead to a band bending effect near the interface. To visualize this effect and test this aspect of our implementation, we calculate the local density of states $\rho(E, \mathbf{r})$

$$\rho^{\sigma\sigma'}(E, \mathbf{r}) = \sum_{\mu\nu} \phi_{\mu}(\mathbf{r})\phi_{\nu}(\mathbf{r}) \frac{1}{2}(\mathbf{G} - \mathbf{G}^{\dagger})_{\mu\nu}^{\sigma\sigma'} \quad (11.3)$$

$$\rho(E, \mathbf{r}) = \text{Re}\{\rho^{\uparrow\uparrow}(E, \mathbf{r}) + \rho^{\downarrow\downarrow}(E, \mathbf{r})\} \quad (11.4)$$

and integrate over the x and y directions. This density is visualized in Figure 11.18 as a function of energy and position along the transport direction. The magnitude of the local density is indicated by the dark-blue-to-yellow color scale. The edge of the highest valence band of MoS₂ appears as a sharp feature 0.05 eV above the Fermi level (Figure 11.18 (e)). In contrast, the edge of the band of WS₂ is visible only as a faint halo. In WS₂ the valence band maximum lies 0.4 eV above the band maximum at Γ and 0.45 eV above the next maximum at K . This results in a low density of states between 0.25 eV and -0.1 eV. The larger contrast on the MoS₂ side is a reflection of a comparatively sharp increase in the number of states at this energy. This effect is also visible in the transmission function of bulk MoS₂ which increases rapidly at the edge of the

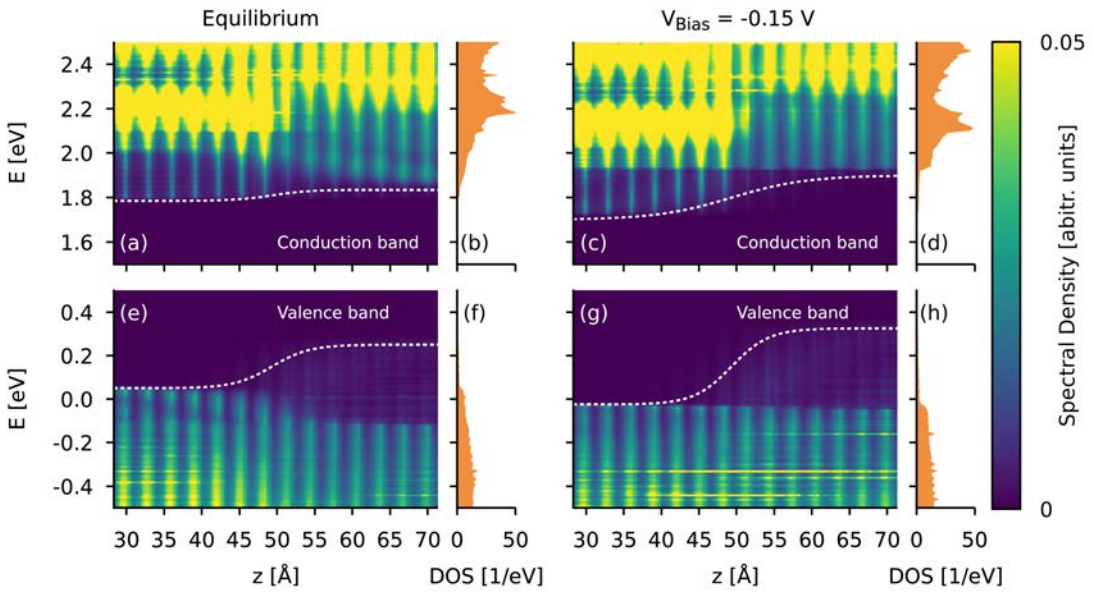


Figure 11.18: Local and total density of states of a lateral MoS₂-WS₂ heterojunction without applied bias (a-d) and with -0.15 V bias (e-h). To highlight the band bending in the heterojunction the color scale is cut off. In the bright yellow regions in conduction bands the local density of states exceeds the maximum value of the color range and is, therefore, not accurately represented.

band (Figure 11.17 (inset)). In the conduction bands, the total density of states is significantly higher (Figure 11.18 (b) and (f)), and the band edges are much clearer (Figure 11.18 (a)). Upon application of a bias (Figure 11.18 (c,h)), the bands are shifted by $\pm V_{\text{Bias}}/2$ away from the Fermi level. These trends are consistent with the expected behavior of a junction with misaligned band edges. Furthermore, the intensity of the local density of states is consistent with the total density of states in the heterojunction.

Figure 11.19 (b) depicts the change in the planar averaged potential for different values of applied bias. The bias-induced potential is continuous and has an inflection point at the interface. Toward the electrodes the potential change becomes constant, demonstrating that even under applied bias the electrode regions are sufficiently screened. For perfect three-dimensional metals, the screening length is vanishingly small, and the potential should drop off sharply right at the interface. However, in our simulations, the electrodes are neither three-dimensional nor are they perfect metals. Therefore the screening length becomes finite and we observe this as a smoothed potential dropoff. In Figure 11.19 (c), we show the IV characteristic of the heterojunction for bias voltages for which the chemical potential in the electrodes remains within the valence bands (-0.1 eV to 0.25 eV). Depending on the direction of the applied bias,

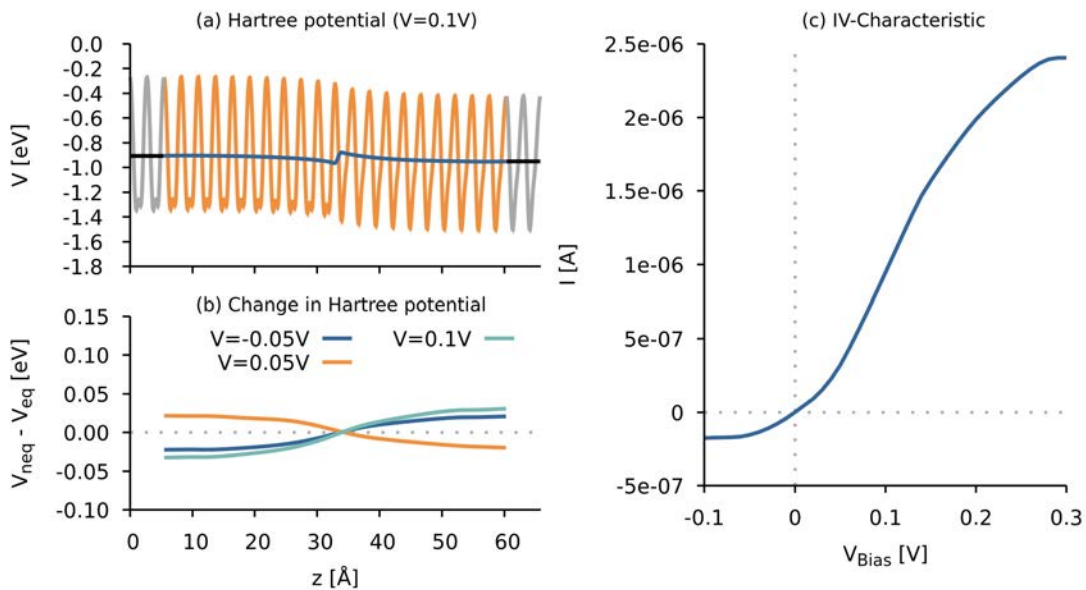


Figure 11.19: (a) Zero-bias transmission of hole-doped ($5.76 \cdot 10^{-3} \text{ e}/\text{\AA}^2$) MoS₂ (blue line), WS₂ (orange line) and (b) a lateral MoS₂-WS₂ heterojunction with same doping concentration ; (c) planar and macro averaged electrostatic potential and (d) charge density xof of the same heterojunction. The band gap in WS₂ is approximately 0.02 eV large than in MoS₂

the valence bands of the two materials are either further misaligned (negative bias) or become more aligned (positive bias). As a result, the IV characteristic of the MoS₂-WS₂ heterojunction is asymmetric. For a small bias (between -10 meV and 10 meV), the current is proportional to the applied bias, as expected. For a larger positive bias, the conductivity increases until the band edges are aligned around $V_{\text{Bias}} = 0.15$ eV at which point the conductivity decreases slightly. For negative bias, the conductivity decreases until the edge of the valence band of MoS₂ falls below the Fermi level at $V_{\text{Bias}} = -0.1$ eV and the electrode becomes semiconducting. This behavior corresponds to the diode-like behavior expected in this type of semiconductor junction. The relatively large leakage current for negative biases can be attributed to the high doping concentration in our calculations.

11.3.3 Computational Details

QUANTUMATK only supports electrodes with rectangular unit cells. We, therefore, choose the conventional unit cell of the TMDs for the bulk calculations with QUANTUMATK. In TRANSIESTA, we calculate the transmission using the primitive unit cell. The width of the transversal dimension of the conventional unit cell is twice as large as in the primitive cell. The corresponding transmission function is also twice as large. To correct for this geometric factor, we divide the QUANTUMATK transmission function by a factor of 2. As a fail-safe, we also verified that using the same conventional unit cell in TRANSIESTA yields a 2-times higher transmission function consistent with QUANTUMATK.

For the heterojunction, we perform the NEGF calculations with device region consisting of 9 conventional unicells of Mo₂ and WS₂ each. The in-plane lattice constants of the two monolayers are strained by 0.4% to match the two materials ($a_{\text{Lat}} = 3.165$ Å). The distance between the Mo and S layers is slightly different on the two sides and amounts to 1.574 Å on the MoS₂ side and 1.607 Å on the WS₂ side. Monolayers are separated by 70 Å of vacuum in the perpendicular direction. We calculate the transport properties in the direction of the first lattice vector. We performed electrode calculations in the conventional unit cell on a 111×15×1 grid in reciprocal space, and the transmission function is sampled on 1×51×1 grid. The real space integrals are performed on a grid with a mesh cut-off of 800 Ry. The Kohn-Sham orbitals are extended using a standard double- ζ polarized basis set. Doping of the structures is achieved by including a plane with constant charge density ($5.76 \cdot 10^{-3}$ e/Å²) 30 Å below the monolayer. This charge gate shifts the Fermi level into the valence band by removing 1.8 electrons from the device region (0.1 electrons per conventional unit cell of MoS₂/WS₂).

11.4 CNT with Magnetic Molecule (1D)

The results presented in this section have, in part, been published in [Bes+21].

In this section, we study carbon nanotubes functionalized with tetranuclear clusters $\{M_4\} = [M_4(H_2L)_2(OAc)_4]$ (Figure 11.20). These tetranuclear clusters consist of 4 magnetic atoms linked by two different ligands H_2L (2,6-bis-(1-(2-hydroxyphenyl)iminoethyl)pyridine) and acetate $C_2H_3O_2^-$. The core of the cluster is formed by the four magnetic ($M=Mn,Co$) and four oxygen atoms which are arranged in nearly cubic structures. In the magnetic ground state of the cluster, the magnetic atoms with an acetate bridge are antiferromagnetically aligned, and the pairs without the acetate bridge are aligned ferromagnetically [Ach+22; Kam+09]. Thus, the whole cluster is a molecular antiferromagnet and could be used in antiferromagnetic spintronic devices such as magnetic random access memories or THz information technologies. To make such applications possible, multiple of clusters need to be electrically contacted and linked together, for example, using metallic carbon nanotubes. Our collaborators have synthesized and characterized such $\{M_4\}$ CNT devices with manganese (Mn) and cobalt (Co) as magnetic centers. Statistical analysis of the random telegraph signal in current passing through these devices indicates that $\{Mn_4\}$ clusters exhibit long-lived coherent states, and $\{Co_4\}$ do not. These excitation states correspond to excitation of non-degenerate $S_{total} = 0$ eigenstates of the cluster and do not involve spin flips. These excited states can not be modeled with our first-principles methods. However, we can study the interaction between the cluster and

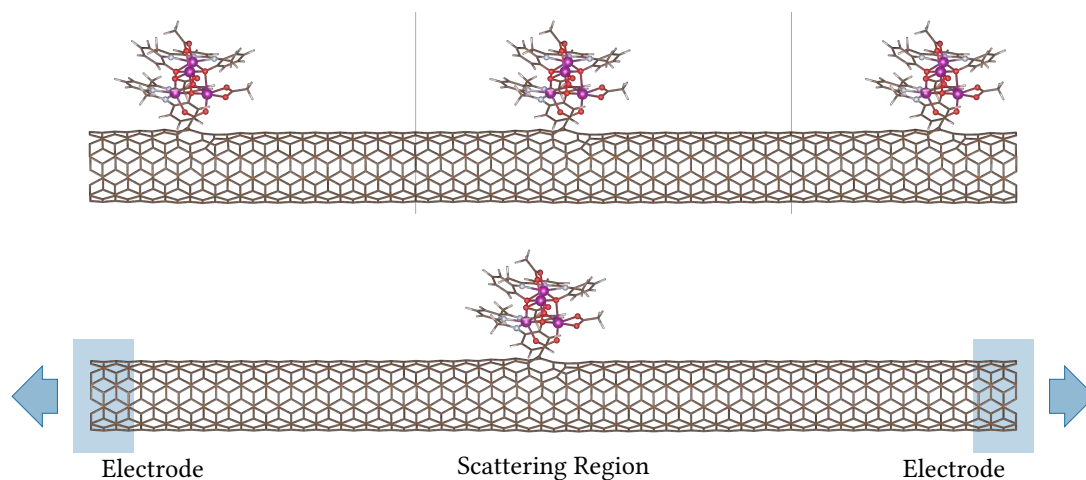


Figure 11.20: Periodic boundary conditions (**top**) and open system (**bottom**) set-up for first-principles simulations of $\{M_4\}$ -CNT hybrid systems.

Cluster	Cell size (#CNT Rings)	S - PBC [μ_B]	S Open System [μ_B]
Mn ₄	15	0.231	–
Mn ₄	23	0.173	0.028
Mn ₄	27	0.083	0.028
Mn ₄	31	0.057	0.030
Co ₄	15	0.176	–
Co ₄	23	0.258	0.150
Co ₄	27	0.447	0.147
Co ₄	31	0.333	0.139

Table 11.1: Magnetic moments of carbon nanotubes functionalized with tetranuclear clusters ($\{Mn_4\}$ and $\{Co_4\}$) computed in the LDA+U approximation with periodic boundary conditions (PBC) and with Green's function techniques (Open System) for different cell sizes. The units of the magnetic moment are Bohr magnetons (μ_B).

nanotube to understand the difference in the coupling of the two clusters to the nanotube. For this purpose, we have performed DFT simulations of carbon nanotubes functionalized with a single $\{Mn_4\}$ and $\{Co_4\}$ clusters.

We consider two simulation set-ups: a supercell with periodic boundary conditions (PBC), and an open system (OPEN) in which a single molecule is attached to an infinite tube (Figure 11.20). The latter allows us to ascertain the nature of the interaction between the molecule and the CNT by avoiding spurious interaction between the periodic replicas of the molecule, mediated by the electronic states of the metallic CNT [CKF05; Kir+08; ZC10]. In our simulations, the $\{M_4\}$ clusters are bound to the dangling carbon atom of a mono-vacancy in a metallic (5,5) carbon nanotube. The bond between the cluster and the nanotubes is formed by a $-CO_2^-$ group obtained by removing the CH_3 group from one of the acetate groups in the cluster. Previous studies have demonstrated that the mono-vacancy site is especially favorable for the functionalization of CNTs with molecules [ZC09] or magnetic nanoparticles [ZC12].

We compare the magnetic moments obtained in the open system setup with the values calculated for the periodic system by increasing the PBC cell size. We verified that the magnetic moment of $\{Mn_4\}$ -CNT tends to the open system solution (0.03 μ_B) while this is not the case for $\{Co_4\}$ -CNT, where the PBC magnetic moment is not converged even for a simulation cell containing 35 unit cells of the nanotube (Table 11.1 and Figure 11.21). This happens due to the long-range character of the indirect exchange coupling between magnetic clusters mediated by the conduction electrons of metallic carbon nanotubes [CKF05]. Therefore, we base our analysis on the spin and orbital moment in the OPEN system setup. From the latter, we find that the total magnetic moment of the $\{Co_4\}$ -CNT system is 0.14 μ_B , an order of magnitude larger than

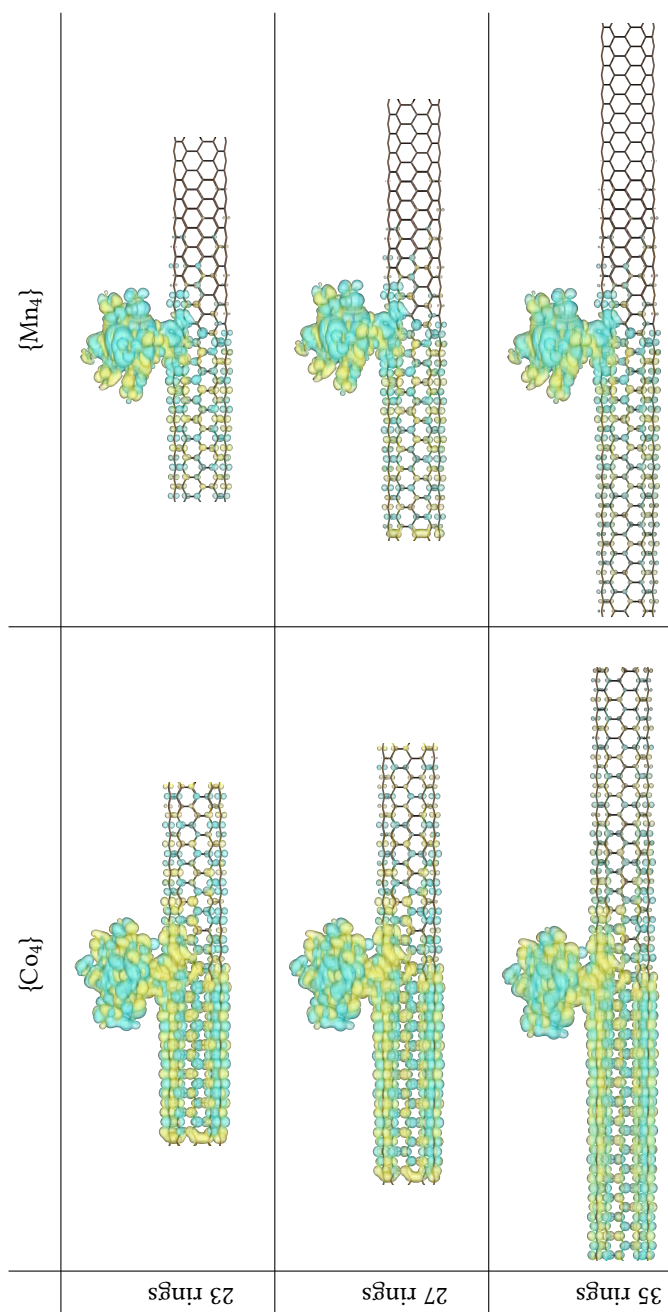


Figure 11.21: Spin density of $\{\text{Co}_4\}$ -CNT (left) and $\{\text{Mn}_4\}$ -CNT (right) calculated with periodic boundary conditions; (top) LDA+U and collinear spin, (middle) LDA and collinear spin, and (bottom) LDA and spin-orbit coupling. Iso surface at $0.001 \mu\text{B}/\text{\AA}^3$

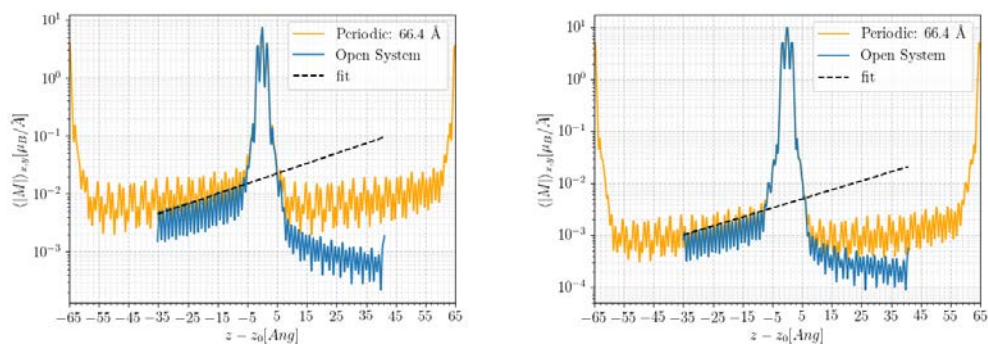


Figure 11.22: (Open System) Absolute value of spin density integrated over x and y ($z = 0$ located at the molecule) for the $\{\text{Co}_4\}$ -CNT (left) and $\{\text{Mn}_4\}$ -CNT (right). The decay of the spin density in the open system is exponential: $\{\text{Co}_4\}$: $e^{(0.04z-4)}$ / $\{\text{Mn}_4\}$: $e^{(0.04z-5.5)}$. The asymmetry in the blue curve arises due to the asymmetry of the molecule-CNT link. This effect is not visible in PBC due to the periodic repetition of the grafted molecules.

in the $\{\text{Mn}_4\}$ -CNT case. The net magnetization of the cluster is almost one order of magnitude smaller than the total magnetization of the hybrid systems. The remaining magnetization is located on the linking carbon atom and nanotube. The spin moment induced in the tube decay exponentially from the vacancy site (Figure 11.22). The larger net magnetization of the $\{\text{Co}_4\}$ -CNT indicates that the nature of the interaction between $\{\text{Co}_4\}$ molecules is longer range than $\{\text{Mn}_4\}$, which is reflected in the interaction between the periodic replicas. On the other hand, the decay of the magnetic perturbation in the two systems is similar (Figure 11.22), as it is determined by the conduction electrons of the nanotube.

The transmission function of the functionalized nanotube (Figure 11.23) closely resembles that of (5,5) carbon nanotubes with a tilted divacancy [ZC10]. Around the Fermi level, the transmission is reduced by a factor of two compared to that of the pristine. Near the edge of the step, transmission increases and is slightly lower in the central part of the step. The transmission function is distinct from that of a (5,5) CNT with a monovacancy. The shape of the transmission function is largely insensitive to the type of cluster attached to it. Both systems also exhibit a series of dips and spikes in the transmission function. These dips are not predicted for the transmission function of (5,5) nanotubes with a divacancy, and their number and position depend on the type of cluster attached to the nanotube. This provides evidence of coupling between molecular states on the cluster and carbon nanotube.

In Figure 11.23, we compare the transmission function of the two clusters calculated with and without SOC and Hubbard-like correction (Hubbard U). Using the Hubbard U correction in these systems is essential to account for the strong Coulomb interaction of the localized

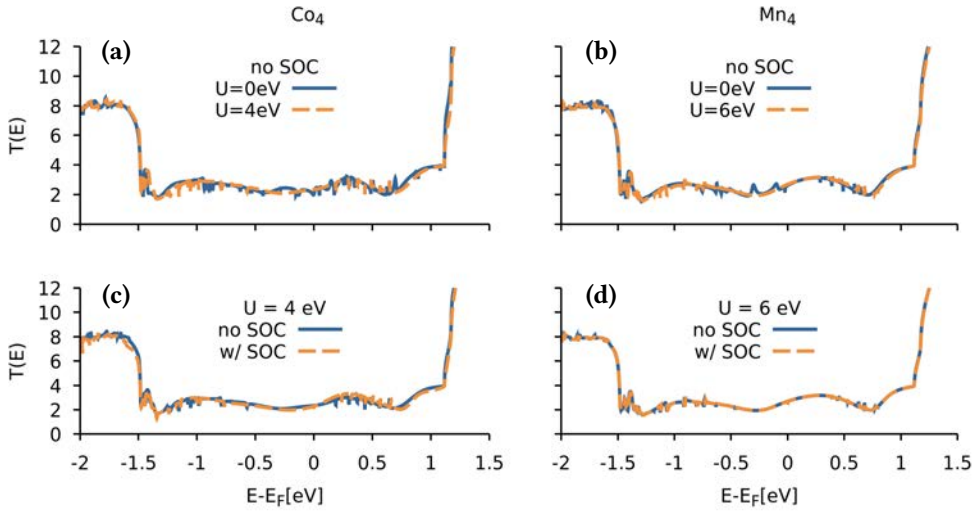


Figure 11.23: Transmission function of $\{\text{Co}_4\}$ -CNT (a, c) and $\{\text{Mn}_4\}$ -CNT (b, d); (a, b) comparison of the effect of Hubbard-like correction on the transmission function (without SOC); (c, d) comparison of the effect of SOC (without Hubbard U).

d-electrons in Mn and Co which affects the magnetic properties of the molecule [Ach+22; Kam+09; Rit+14]. Due to recent developments in the SIESTA code, it is now possible to perform calculations with spin-orbit coupling and Hubbard U. Here we combine the two features with the NEGF formalism for the first time. For both systems, the inclusion of the Hubbard U term affects the transmission function slightly near the Fermi level. The changes are limited to the position of the dips and spikes. Since the Hubbard U is only included for the magnetic atoms in the cluster, this implies that states on the cluster are at least partially coupled to the electronic structure of the carbon nanotube. However, the electron correlation in the magnetic atoms is insignificant for electronic transport at large. Similarly, the effect of SOC on the transmission function is insignificant for both systems. In the $\{\text{Mn}_4\}$ -CNT system, the effect of SOC is unnoticeable. In the $\{\text{Co}_4\}$ -CNT the effect is slightly larger, and small differences in the transmission curve are observable. This is consistent with the expectation of a larger orbital angular momentum in Co [Ach+22].

In order, to Each of these features corresponds to a bound state in the cluster. We can identify bound states in the hybrid system by calculating the density of states from the Green's function in the scattering region ($\rho^G(E) = \text{Tr}\{GS\}$) and the spectral functions for the two electrodes ($\rho_e^{\mathcal{A}}(E) = \text{Tr}\{\mathcal{A}_e S\}$). The density of states calculated from the spectral functions only includes states that couple to the electrode. The density of states calculated from the Green's function

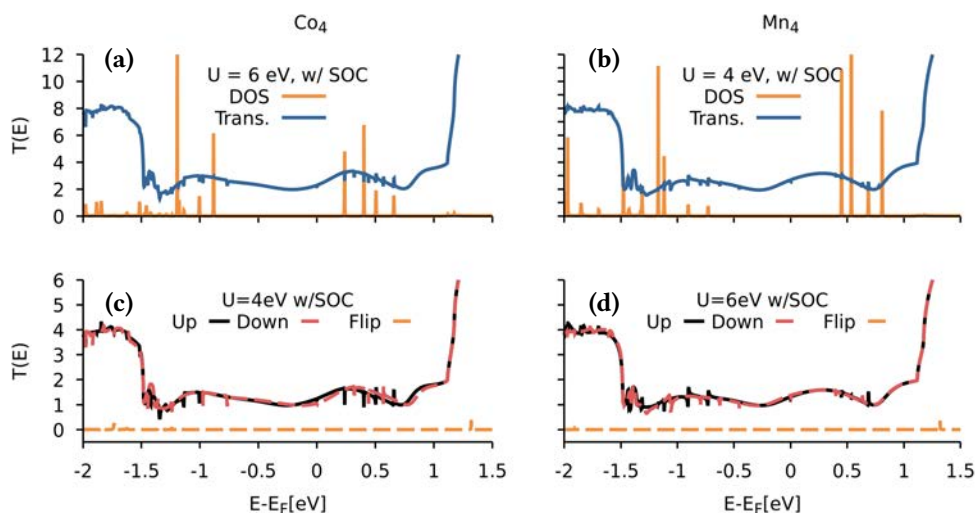


Figure 11.24: Bound density of states and spin-channel-projected transmission of $\{\text{Co}_4\}$ -CNT (a,c) and $\{\text{Mn}_4\}$ -CNT (b,d) calculated with SOC and with Hubbard U ; (a) and (b) comparison of the bound density of states and the zero-bias transmission function; (c) and (d) spin-channel-projected transmission functions.

includes all states in the scattering region. As such, we can identify the bound density of states from the difference of densities ($\rho^{\text{bound}} = \rho^{\text{G}}(E) - \sum_e \rho_e^{\mathcal{A}}(E)$). In Figure 11.24, we can see that some of the bound states line up with the dips in the transmission function. This suggests that the dips in the transmissions occur due to the coupling of the conduction channels in the nanotube and the electronic states of the molecule.

Finally, we analyze the spin-dependent properties of the functionalized nanotubes. The transmission function of $\{\text{Mn}_4\}$ -CNT is the same for the spin-up and down channels. On the contrary, the transmission function for the spin-down channels is noticeably lower in $\{\text{Co}_4\}$ -CNT compared to the spin-up channel. Above the Fermi level, the transmission function for the spin-down channel is shifted to higher energies. This difference in the transmission of the up and down channels arises due to the net magnetization of the system. The $\{\text{Mn}_4\}$ -CNT does not exhibit this effect because its net magnetization is significantly lower. In both systems, the position of the dips in the transmission is distinct for the two spin channels. This indicates that electric manipulations of the magnetic states of the molecule could be possible. Scattering between the spin channels (spin-flip transmission) is negligible in both systems.

11.4.1 Computational Details

To account for the strong correlation of the 3d electrons and avoid the excessive delocalization of the d-states predicted in the Local Density Approximation, Hubbard-like corrections with $U=6$ eV and $U=4$ eV were used for Mn and Co, respectively. The same value was used by Kampert et al. [Kam+09] in their calculations on $\{Mn_4\}$. A standard double-zeta polarized (DZP) basis set was used for carbon, nitrogen, and hydrogen, and an optimized double-zeta (DZ) for Mn, Co, and O. Calculations were spin-polarized and performed assuming collinear spins. Convergence of electronic structure and magnetic properties was achieved for a real-space grid cut-off of 400 Ry, and a Fermi-Dirac smearing of 100 K in the LDA+U calculation, while with SOC, a cut-off of 650 Ry and electronic temperature of 1 K was adopted. The atomic positions were relaxed in standard periodic boundary conditions simulations, with a $1 \times 1 \times 12$ k-points sampling of the Brillouin zone for 15 cells of M_4 -CNT (shifted grid), and the conjugate gradient algorithm. The maximum force on atoms was smaller than 0.04 eV/Å for the CNT+M4 system.

Periodic boundary conditions simulations were performed for 15, 23, 27, and 35 supercells of the (5, 5) CNT to analyze the long-range decay of the induced spin polarization in the system. The supercells correspond to a distance between the graft points of 36.9, 56.6, 66.5, 86.2 Å, and a separation between the molecules of 23.5, 43.0, 53.0, 73.0 Å, as the lateral size of the molecule is about 13.5 Å. We used a sampling of the Brillouin zone equivalent to $1 \times 1 \times 12$ k points for 15 cells of $\{M_4\}$ -CNT (shifted grid).

11.5 Conclusion

We have presented the non-equilibrium Green's function approach to quantum transport and its implementation at the DFT+NEGF level for systems with non-collinear spins and spin-orbit coupling. This makes TranSIESTA the first open-source DFT+NEGF code capable of performing non-equilibrium, multi-terminal transport in the presence of non-collinear spin configuration and general spin-orbit phenomena. This new implementation can utilize all highly scaleable and effective algorithms that were recently added to the code [Pap+17] and is suitable for large-scale transport simulations. As such, this implementation represents a significant step forward for simulations of quantum materials and spintronics devices at large.

We apply our new implementation to a series of systems to demonstrate possible applications and show the code's validity. In particular, we calculate the anisotropic magnetoresistance in one-dimensional iron chains and a Fe/MgO/Fe tunneling junction. Furthermore, we study quantum transport in TMD nanodevices, which are characterized by strong spin-orbit coupling.

Lastly, we determine the importance of spin-orbit coupling and electron correlation (DFT+U) in carbon nanotubes functionalized with antiferromagnetic molecules.

In this thesis, we have presented the development of first-principles computational methods for quantum materials. We have applied these methods to gain new insights into the electronic, topological, superconducting, and transport properties of different materials and devices. In particular, we have implemented the DFT+NEGF approach for systems with noncollinear spins and spin-orbit coupling (Chapter 6) and the BdG+DFT method for modeling superconductors in SIESTA (Chapter 7). Furthermore, we have developed post-processing tools to extract the \mathbb{Z}_2 topological invariant and spin textures from SIESTA outputs (Chapter 8).

We studied double-wall carbon nanotubes as examples of ideal one-dimensional moiré crystals (Chapter 9), characterized by two parameters (the angle between chiral vectors, the difference in diameters) that can be used to control their electronic properties. Experimental realizations of 1D moirés impose finite-length constraints, and electron transport is generally assumed to be exclusively ruled by the external shell. We performed Landauer-Büttiker transport simulations on top of a new tight-binding model. We showed that the inter-layer coupling between nanotube walls plays a crucial role in the electron transport of the multi-wall systems and leads to non-conventional transport properties. We showed that different coupling regimes feature markedly distinguishable characteristics already in finite tube segments within experimental reach. We proposed a predictive transmission model based on wave interference in a quantum box yielding an impressive agreement with tight-binding calculations. We explained that previously reported dips in inter-layer transmission between armchair nanotubes result from the finite-length constraint and originate from back-scattering at localized states. A possible application of this effect is nano switches based on carbon nanotubes.

Furthermore, we performed a complete first-principle study of the interactions between topological states in bismuthene monolayers and silicon-based substrates (Chapter 10). In particular, we showed that the Bi-monolayer phases bind to silicon carbide (SiC), silicon (Si), and silicon dioxide (SiO₂) and that the proximity interaction in the heterostructures has a significant effect on the electronic structure of the monolayer, even when no bonding occurs. We further demonstrated that van der Waals interactions and the breaking of the sublattice symmetry of the monolayer are the main factors driving changes in the electronic structure. Our work illustrates that the growth of buckled-hexagonal bismuthene on a silicon-based

substrate is possible and retains the topological properties of the freestanding phase, in contrast to flat-hexagonal bismuthene, which only becomes topological on SiC.

We applied our new DFT+NEGF implementation to a series of systems to demonstrate possible applications and show the code's validity (Chapter 6). In particular, we calculated the anisotropic magnetoresistance in one-dimensional iron chains and a Fe/MgO/Fe tunneling junction. Furthermore, we studied quantum transport in TMD nanodevices, characterized by strong spin-orbit coupling, and the importance of spin-orbit coupling and electron correlation (DFT+U) in carbon nanotubes functionalized with antiferromagnetic molecules. In the future, our spinor version of the DFT+NEGF method could be used to simulate charge and spin transport in realistic nanodevices based on quantum materials. Important examples of such nanodevices are topological insulator/ferromagnetic metal heterostructures. Introducing ferromagnetism at the surface of a topological insulator (TI) can produce spin-to-charge conversion with extremely high efficiency and strong spin-orbit torque. This opens many opportunities for spintronics applications.

Our implementation of the BdG+DFT method can consider all details of the band structure, including SOC, in the description of the superconducting states. This way, complex superconductors with interactions between multiple Fermi surfaces can be accurately described. This is essential for the modeling of superconductors like MgB₂, and NbSe₂. By employing the *fixed- λ* method, the symmetry of the superconducting gap does not have to be assumed. Instead, it emerges due to the symmetry of the states involved in the pairing near the Fermi level. Our implementation of the BdG+DFT method in SIESTA is particularly well-suited to study heterostructure and other device configurations due to SIESTA's inherent scalability. Of particular interest are heterostructure consisting of a superconductor and an insulator with strong spin-orbit coupling because they are expected to host Majorana zero modes. These modes are very promising components for topological quantum computers due to their non-Abelian nature. Other possible applications are the surfaces of superconductors and the interface between superconductors. Furthermore, our implementation can model superconductivity beyond the spin-singlet pairing and could be used to study the *p*-wave spin-triplet superconductors such as Sr₂RuO₄. Finally, the BdG+DFT and DFT+NEGF approaches could be combined to create a method for simulating the transport properties of superconductor junctions and topological superconductor devices.

To conclude, the novel methods and insights presented in this thesis address some of the significant problems in the field of first-principles modeling of quantum materials and create many opportunities for future exploration of quantum materials.

Bibliography

- [AAU16] Abdulrhman M. Alsharari, Mahmoud M. Asmar, and Sergio E. Ulloa. **Mass Inversion in Graphene by Proximity to Dichalcogenide Monolayer**. *Physical Review B* 94:24 (Dec. 2016), 241106. ISSN: 2469-9950, 2469-9969. DOI: [10.1103/PhysRevB.94.241106](https://doi.org/10.1103/PhysRevB.94.241106) (see pages 3, 76).
- [AAU18] Abdulrhman M. Alsharari, Mahmoud M. Asmar, and Sergio E. Ulloa. **Topological Phases and Twisting of Graphene on a Dichalcogenide Monolayer**. *Physical Review B* 98:19 (Nov. 2018), 195129. ISSN: 2469-9950, 2469-9969. DOI: [10.1103/PhysRevB.98.195129](https://doi.org/10.1103/PhysRevB.98.195129). (Visited on 03/21/2023) (see page 76).
- [Ach+22] Simona Achilli, Claire Besson, Xu He, Pablo Ordejón, Carola Meyer, and Zeila Zanolli. **Magnetic Properties of Coordination Clusters with $\{Mn_4\}$ and $\{Co_4\}$ Antiferromagnetic Cores**. *Physical Chemistry Chemical Physics* 24:6 (2022), 3780–3787. ISSN: 1463-9076, 1463-9084. DOI: [10.1039/D1CP03904K](https://doi.org/10.1039/D1CP03904K) (see pages 147, 151).
- [AE73] F. W. Averill and D. E. Ellis. **An Efficient Numerical Multicenter Basis Set for Molecular Orbital Calculations: Application to $FeCl_4$** . *The Journal of Chemical Physics* 59:12 (Dec. 1973), 6412–6418. ISSN: 0021-9606, 1089-7690. DOI: [10.1063/1.1680020](https://doi.org/10.1063/1.1680020) (see page 22).
- [AFG10] N. P. Armitage, P. Fournier, and R. L. Greene. **Progress and Perspectives on Electron-Doped Cuprates**. *Reviews of Modern Physics* 82:3 (Sept. 2010), 2421–2487. ISSN: 0034-6861, 1539-0756. DOI: [10.1103/RevModPhys.82.2421](https://doi.org/10.1103/RevModPhys.82.2421) (see page 43).
- [All79a] Roland E. Allen. **Green’s Function and Generalized Phase Shift for Surface and Interface Problems**. *Physical Review B* 19:2 (Jan. 1979), 917–924. ISSN: 0163-1829. DOI: [10.1103/PhysRevB.19.917](https://doi.org/10.1103/PhysRevB.19.917) (see page 32).
- [All79b] Roland E. Allen. **Green’s Functions for Surface Physics**. *Physical Review B* 20:4 (Aug. 1979), 1454–1472. ISSN: 0163-1829. DOI: [10.1103/PhysRevB.20.1454](https://doi.org/10.1103/PhysRevB.20.1454) (see page 32).
- [Ame+01] Patrick R. Amestoy, Iain S. Duff, Jean-Yves L’Excellent, and Jacko Koster. **A Fully Asynchronous Multifrontal Solver Using Distributed Dynamic Scheduling**. *SIAM Journal on Matrix Analysis and Applications* 23:1 (Jan. 2001), 15–41. ISSN: 0895-4798, 1095-7162. DOI: [10.1137/S0895479899358194](https://doi.org/10.1137/S0895479899358194) (see page 55).
- [Ame+19] Patrick R. Amestoy, Alfredo Buttari, Jean-Yves L’Excellent, and Theo Mary. **Performance and Scalability of the Block Low-Rank Multifrontal Factorization on Multicore Architectures**. *ACM Transactions on Mathematical Software* 45:1 (Mar. 2019), 1–26. ISSN: 0098-3500, 1557-7295. DOI: [10.1145/3242094](https://doi.org/10.1145/3242094) (see page 55).

- [And+99] E. Anderson, Z. Bai, C. Bischof, S. Blackford, J. Demmel, J. Dongarra, J. Du Croz, A. Greenbaum, S. Hammarling, A. McKenney, and D. Sorensen. **LAPACK Users' Guide**. Third. Philadelphia, PA: Society for Industrial and Applied Mathematics, 1999. ISBN: 0-89871-447-8 (paperback) (see page 55).
- [Ang+02] Eduardo Anglada, José M. Soler, Javier Junquera, and Emilio Artacho. **Systematic Generation of Finite-Range Atomic Basis Sets for Linear-Scaling Calculations**. *Physical Review B* 66:20 (Nov. 2002), 205101. ISSN: 0163-1829, 1095-3795. DOI: [10.1103/PhysRevB.66.205101](https://doi.org/10.1103/PhysRevB.66.205101) (see page 24).
- [Ant+10] C. Antoniak, J. Lindner, K. Fauth, J.-U. Thiele, J. Minár, S. Mankovsky, H. Ebert, H. Wende, and M. Farle. **Composition Dependence of Exchange Stiffness in Fe x Pt 1 - x Alloys**. *Physical Review B* 82:6 (Aug. 2010), 064403. ISSN: 1098-0121, 1550-235X. DOI: [10.1103/PhysRevB.82.064403](https://doi.org/10.1103/PhysRevB.82.064403) (see page 129).
- [Art+99] E. Artacho, D. Sánchez-Portal, P. Ordejón, A. García, and J. M. Soler. **Linear-Scaling Ab-Initio Calculations for Large and Complex Systems**. *physica status solidi (b)* 215:1 (1999), 809–817. ISSN: 1521-3951. DOI: [10.1002/\(SICI\)1521-3951\(199909\)215:1<809::AID-PSSB809>3.0.CO;2-0](https://doi.org/10.1002/(SICI)1521-3951(199909)215:1<809::AID-PSSB809>3.0.CO;2-0) (see pages 24, 108).
- [Aut+08] Gabriel Autès, Cyrille Barreteau, Daniel Spanjaard, and Marie-Catherine Desjonquères. **Electronic Transport in Iron Atomic Contacts: From the Infinite Wire to Realistic Geometries**. *Physical Review B* 77:15 (Apr. 2008), 155437. ISSN: 1098-0121, 1550-235X. DOI: [10.1103/PhysRevB.77.155437](https://doi.org/10.1103/PhysRevB.77.155437) (see page 131).
- [Avs+14] A. Avsar, J. Y. Tan, T. Taychatanapat, J. Balakrishnan, G.K.W. Koon, Y. Yeo, J. Lahiri, A. Carvalho, A. S. Rodin, E.C.T. O'Farrell, G. Eda, A. H. Castro Neto, and B. Özyilmaz. **Spin–Orbit Proximity Effect in Graphene**. *Nature Communications* 5:1 (Sept. 2014), 4875. ISSN: 2041-1723. DOI: [10.1038/ncomms5875](https://doi.org/10.1038/ncomms5875). (Visited on 03/21/2023) (see page 76).
- [Bae+15] S-H. Baek, D. V. Efremov, J. M. Ok, J. S. Kim, Jeroen van den Brink, and B. Büchner. **Orbital-Driven Nematicity in FeSe**. *Nature Materials* 14:2 (Feb. 2015), 210–214. ISSN: 1476-1122, 1476-4660. DOI: [10.1038/nmat4138](https://doi.org/10.1038/nmat4138). (Visited on 03/17/2023) (see page 70).
- [BB70] S.F. Boys and F. Bernardi. **The Calculation of Small Molecular Interactions by the Differences of Separate Total Energies. Some Procedures with Reduced Errors**. *Molecular Physics* 19:4 (Oct. 1970), 553–566. ISSN: 0026-8976, 1362-3028. DOI: [10.1080/00268977000101561](https://doi.org/10.1080/00268977000101561) (see page 109).
- [BBR88] Alfonso Baldereschi, Stefano Baroni, and Raffaele Resta. **Band Offsets in Lattice-Matched Heterojunctions: A Model and First-Principles Calculations for GaAs / AlAs**. *Physical Review Letters* 61:6 (Aug. 1988), 734–737. ISSN: 0031-9007. DOI: [10.1103/PhysRevLett.61.734](https://doi.org/10.1103/PhysRevLett.61.734) (see page 142).
- [BCS57] J. Bardeen, L. N. Cooper, and J. R. Schrieffer. **Theory of Superconductivity**. *Physical Review* 108:5 (Dec. 1957), 1175–1204. ISSN: 0031-899X. DOI: [10.1103/PhysRev.108.1175](https://doi.org/10.1103/PhysRev.108.1175) (see page 43).

- [Bec93] Axel D. Becke. **A New Mixing of Hartree–Fock and Local Density–functional Theories**. *The Journal of Chemical Physics* 98:2 (Jan. 1993), 1372–1377. ISSN: 0021-9606. DOI: [10.1063/1.464304](https://doi.org/10.1063/1.464304) (see page 16).
- [Bec96] Axel D. Becke. **Density-functional Thermochemistry. IV. A New Dynamical Correlation Functional and Implications for Exact-exchange Mixing**. *The Journal of Chemical Physics* 104:3 (Jan. 1996), 1040–1046. ISSN: 0021-9606. DOI: [10.1063/1.470829](https://doi.org/10.1063/1.470829) (see page 16).
- [Bee97] C. W. J. Beenakker. **Random-Matrix Theory of Quantum Transport**. *Reviews of Modern Physics* 69:3 (July 1997), 731–808. ISSN: 0034-6861, 1539-0756. DOI: [10.1103/RevModPhys.69.731](https://doi.org/10.1103/RevModPhys.69.731) (see page 44).
- [Ber96] L. Berger. **Emission of Spin Waves by a Magnetic Multilayer Traversed by a Current**. *Physical Review B* 54:13 (Oct. 1996), 9353–9358. ISSN: 0163-1829, 1095-3795. DOI: [10.1103/PhysRevB.54.9353](https://doi.org/10.1103/PhysRevB.54.9353) (see page 1).
- [Bes+21] Claire Besson, Philipp Stegmann, Michael Schnee, Zeila Zanolli, Simona Achilli, Nils Witte-meier, Asmus Vierck, Robert Frielinghaus, Paul Kögerler, Janina Maultzsch, Pablo Ordejón, Claus M. Schneider, Alfred Hucht, Jürgen König, and Carola Meyer. **Independent and Coherent Transitions between Antiferromagnetic States of Few-Molecule Systems** (2021). DOI: [10.48550/ARXIV.2107.07723](https://doi.org/10.48550/ARXIV.2107.07723) (see page 147).
- [Bez+13] Manoel M. Bezerra-Neto, Marcelo S. Ribeiro, Biplab Sanyal, Anders Bergman, Roberto B. Muniz, Olle Eriksson, and Angela B. Klautau. **Complex Magnetic Structure of Clusters and Chains of Ni and Fe on Pt(111)**. *Scientific Reports* 3:1 (Oct. 2013), 3054. ISSN: 2045-2322. DOI: [10.1038/srep03054](https://doi.org/10.1038/srep03054) (see page 129).
- [BH72] U von Barth and L Hedin. **A Local Exchange–Correlation Potential for the Spin Polarized Case. i**. *Journal of Physics C: Solid State Physics* 5:13 (July 1972), 1629–1642. ISSN: 0022-3719. DOI: [10.1088/0022-3719/5/13/012](https://doi.org/10.1088/0022-3719/5/13/012) (see page 17).
- [BHS33] R. Becker, G. Heller, and F. Sauter. **Über die Stromverteilung in einer supraleitenden Kugel**. *Zeitschrift für Physik* 85:11-12 (Nov. 1933), 772–787. ISSN: 1434-6001, 1434-601X. DOI: [10.1007/BF01330324](https://doi.org/10.1007/BF01330324) (see page 42).
- [BHZ06] B. A. Bernevig, T. L. Hughes, and S.-C. Zhang. **Quantum Spin Hall Effect and Topological Phase Transition in HgTe Quantum Wells**. *Science* 314:5806 (Dec. 2006), 1757–1761. ISSN: 0036-8075, 1095-9203. DOI: [10.1126/science.1133734](https://doi.org/10.1126/science.1133734) (see page 3).
- [Bla+97] L. S. Blackford, J. Choi, A. Cleary, E. D’Azevedo, J. Demmel, I. Dhillon, J. Dongarra, S. Hammarling, G. Henry, A. Petitet, K. Stanley, D. Walker, and R. C. Whaley. **ScaLAPACK Users’ Guide**. Philadelphia, PA: Society for Industrial and Applied Mathematics, 1997. ISBN: 0-89871-397-8 (paperback) (see page 55).
- [Blo29] Felix Bloch. **Über die Quantenmechanik der Elektronen in Kristallgittern**. *Zeitschrift für Physik* 52:7-8 (July 1929), 555–600. ISSN: 1434-6001, 1434-601X. DOI: [10.1007/BF01339455](https://doi.org/10.1007/BF01339455) (see page 18).

- [BM11] Rafi Bistritzer and Allan H. MacDonald. **Moiré Bands in Twisted Double-Layer Graphene**. *Proceedings of the National Academy of Sciences* 108:30 (July 2011), 12233–12237. ISSN: 0027-8424, 1091-6490. DOI: [10.1073/pnas.1108174108](https://doi.org/10.1073/pnas.1108174108) (see page 3).
- [BM69] B. L. Blackford and R. H. March. **Tunneling Investigation of Energy-Gap Anisotropy in Superconducting Bulk Pb**. *Physical Review* 186:2 (Oct. 1969), 397–399. ISSN: 0031-899X. DOI: [10.1103/PhysRev.186.397](https://doi.org/10.1103/PhysRev.186.397). (Visited on 03/17/2023) (see page 69).
- [BO27] M. Born and R. Oppenheimer. **Zur Quantentheorie der Molekeln**. *Annalen der Physik* 389:20 (1927), 457–484. ISSN: 00033804, 15213889. DOI: [10.1002/andp.19273892002](https://doi.org/10.1002/andp.19273892002) (see page 10).
- [Bog58] N. N. Bogoljubov. **On a New Method in the Theory of Superconductivity**. *Il Nuovo Cimento* 7:6 (Mar. 1958), 794–805. ISSN: 0029-6341, 1827-6121. DOI: [10.1007/BF02745585](https://doi.org/10.1007/BF02745585) (see page 42).
- [Bon+16] Roméo Bonnet, Aurélien Lherbier, Clément Barraud, Maria Luisa Della Rocca, Philippe Lafarge, and Jean-Christophe Charlier. **Charge Transport through One-Dimensional Moiré Crystals**. *Scientific Reports* 6:1 (Apr. 2016), 19701. ISSN: 2045-2322. DOI: [10.1038/srep19701](https://doi.org/10.1038/srep19701) (see pages 83, 87).
- [Bon48] Bonnet. **La Théoria Générale Des Surfaces**. *Journal de l'Ecole polytechnique*: 19 (1848), 1–146 (see page 37).
- [Boy50] Samuel Francis Boys. **Electronic Wave Functions - I. A General Method of Calculation for the Stationary States of Any Molecular System**. *Proceedings of the Royal Society of London. Series A. Mathematical and Physical Sciences* 200:1063 (Feb. 1950), 542–554. ISSN: 0080-4630, 2053-9169. DOI: [10.1098/rspa.1950.0036](https://doi.org/10.1098/rspa.1950.0036) (see page 22).
- [BPM04] A. Bagrets, N. Papanikolaou, and I. Mertig. **Magnetoresistance of Atomic-Sized Contacts: An Ab Initio Study**. *Physical Review B* 70:6 (Aug. 2004), 064410. ISSN: 1098-0121, 1550-235X. DOI: [10.1103/PhysRevB.70.064410](https://doi.org/10.1103/PhysRevB.70.064410) (see page 124).
- [Bra+02] Mads Brandbyge, José-Luis Mozos, Pablo Ordejón, Jeremy Taylor, and Kurt Stokbro. **Density-Functional Method for Nonequilibrium Electron Transport**. *Physical Review B* 65:16 (Mar. 2002), 165401. DOI: [10.1103/PhysRevB.65.165401](https://doi.org/10.1103/PhysRevB.65.165401) (see pages 29, 34, 35, 57, 86).
- [Bru12] Fabien Bruneval. **Range-Separated Approach to the RPA Correlation Applied to the van Der Waals Bond and to Diffusion of Defects**. *Physical Review Letters* 108:25 (June 2012), 256403. ISSN: 0031-9007, 1079-7114. DOI: [10.1103/PhysRevLett.108.256403](https://doi.org/10.1103/PhysRevLett.108.256403) (see page 17).
- [BS17] Yunkyu Bang and G R Stewart. **Superconducting Properties of the s^{\pm} -Wave State: Fe-based Superconductors**. *Journal of Physics: Condensed Matter* 29:12 (Mar. 2017), 123003. ISSN: 0953-8984, 1361-648X. DOI: [10.1088/1361-648X/aa564b](https://doi.org/10.1088/1361-648X/aa564b) (see page 42).

- [BTŠ58] N. N. Bogoljubov, V. V. Tolmachov, and D. V. Širkov. **A New Method in the Theory of Superconductivity**. *Fortschritte der Physik* 6:11-12 (1958), 605–682. ISSN: 00158208, 15213979. DOI: [10.1002/prop.19580061102](https://doi.org/10.1002/prop.19580061102) (see page 42).
- [But+01] W. H. Butler, X.-G. Zhang, T. C. Schulthess, and J. M. MacLaren. **Spin-Dependent Tunneling Conductance of Fe | MgO | Fe Sandwiches**. *Physical Review B* 63:5 (Jan. 2001), 054416. ISSN: 0163-1829, 1095-3795. DOI: [10.1103/PhysRevB.63.054416](https://doi.org/10.1103/PhysRevB.63.054416) (see page 132).
- [Büt+85] M. Büttiker, Y. Imry, R. Landauer, and S. Pinhas. **Generalized Many-Channel Conductance Formula with Application to Small Rings**. *Physical Review B* 31:10 (May 1985), 6207–6215. ISSN: 0163-1829. DOI: [10.1103/PhysRevB.31.6207](https://doi.org/10.1103/PhysRevB.31.6207) (see page 29).
- [BVT05] K. D. Belashchenko, J. Velez, and E. Y. Tsymbal. **Effect of Interface States on Spin-Dependent Tunneling in Fe / Mg O / Fe Tunnel Junctions**. *Physical Review B* 72:14 (Oct. 2005), 140404. ISSN: 1098-0121, 1550-235X. DOI: [10.1103/PhysRevB.72.140404](https://doi.org/10.1103/PhysRevB.72.140404) (see pages 132, 136).
- [BWP17] Maciej Bieniek, Tomasz Woźniak, and Paweł Potasz. **Stability of Topological Properties of Bismuth (1 1 1) Bilayer**. *Journal of Physics: Condensed Matter* 29:15 (Apr. 2017), 155501. ISSN: 0953-8984, 1361-648X. DOI: [10.1088/1361-648X/aa5e79](https://doi.org/10.1088/1361-648X/aa5e79) (see page 120).
- [Cao+18a] Yuan Cao, Valla Fatemi, Ahmet Demir, Shiang Fang, Spencer L. Tomarken, Jason Y. Luo, Javier D. Sanchez-Yamagishi, Kenji Watanabe, Takashi Taniguchi, Efthimios Kaxiras, Ray C. Ashoori, and Pablo Jarillo-Herrero. **Correlated Insulator Behaviour at Half-Filling in Magic-Angle Graphene Superlattices**. *Nature* 556:7699 (Apr. 2018), 80–84. ISSN: 0028-0836, 1476-4687. DOI: [10.1038/nature26154](https://doi.org/10.1038/nature26154) (see page 3).
- [Cao+18b] Yuan Cao, Valla Fatemi, Shiang Fang, Kenji Watanabe, Takashi Taniguchi, Efthimios Kaxiras, and Pablo Jarillo-Herrero. **Unconventional Superconductivity in Magic-Angle Graphene Superlattices**. *Nature* 556:7699 (Apr. 2018), 43–50. ISSN: 0028-0836, 1476-4687. DOI: [10.1038/nature26160](https://doi.org/10.1038/nature26160) (see page 3).
- [Cao+20] Yuan Cao, Debanjan Chowdhury, Daniel Rodan-Legrain, Oriol Rubies-Bigorda, Kenji Watanabe, Takashi Taniguchi, T. Senthil, and Pablo Jarillo-Herrero. **Strange Metal in Magic-Angle Graphene with near Planckian Dissipation**. *Physical Review Letters* 124:7 (Feb. 2020), 076801. ISSN: 0031-9007, 1079-7114. DOI: [10.1103/PhysRevLett.124.076801](https://doi.org/10.1103/PhysRevLett.124.076801) (see page 3).
- [Car+72] C Caroli, R Combescot, P Nozieres, and D Saint-James. **A Direct Calculation of the Tunnelling Current: IV. Electron-phonon Interaction Effects**. *Journal of Physics C: Solid State Physics* 5:1 (Jan. 1972), 21–42. ISSN: 0022-3719. DOI: [10.1088/0022-3719/5/1/006](https://doi.org/10.1088/0022-3719/5/1/006) (see page 34).
- [CBR07] Jean-Christophe Charlier, Xavier Blase, and Stephan Roche. **Electronic and Transport Properties of Nanotubes**. *Reviews of Modern Physics* 79:2 (May 2007), 677–732. ISSN: 0034-6861, 1539-0756. DOI: [10.1103/RevModPhys.79.677](https://doi.org/10.1103/RevModPhys.79.677) (see page 93).

- [CC12] R Cuadrado and J I Cerdá. **Fully Relativistic Pseudopotential Formalism under an Atomic Orbital Basis: Spin–Orbit Splittings and Magnetic Anisotropies.** *Journal of Physics: Condensed Matter* 24:8 (Feb. 2012), 086005. ISSN: 0953-8984, 1361-648X. DOI: 10.1088/0953-8984/24/8/086005 (see pages 24, 25, 108, 131, 136).
- [CCS99] S. Corbel, J. Cerdá, and P. Sautet. **Ab Initio Calculations of Scanning Tunneling Microscopy Images within a Scattering Formalism.** *Physical Review B* 60:3 (July 1999), 1989–1999. ISSN: 0163-1829, 1095-3795. DOI: 10.1103/PhysRevB.60.1989 (see page 35).
- [CFR18] Tarik P. Cysne, Aires Ferreira, and Tatiana G. Rappoport. **Crystal-Field Effects in Graphene with Interface-Induced Spin-Orbit Coupling.** *Physical Review B* 98:4 (July 2018), 045407. ISSN: 2469-9950, 2469-9969. DOI: 10.1103/PhysRevB.98.045407 (see pages 3, 76).
- [Che+09] Y. L. Chen, J. G. Analytis, J.-H. Chu, Z. K. Liu, S.-K. Mo, X. L. Qi, H. J. Zhang, D. H. Lu, X. Dai, Z. Fang, S. C. Zhang, I. R. Fisher, Z. Hussain, and Z.-X. Shen. **Experimental Realization of a Three-Dimensional Topological Insulator, Bi₂Te₃.** *Science* 325:5937 (July 2009), 178–181. ISSN: 0036-8075, 1095-9203. DOI: 10.1126/science.1173034 (see pages 74, 75).
- [Che+15] Kun Chen, Xi Wan, Weiguang Xie, Jinxiu Wen, Zhiwen Kang, Xiaoliang Zeng, Huanjun Chen, and Jianbin Xu. **Lateral Built-In Potential of Monolayer MoS₂-WS₂ In-Plane Heterostructures by a Shortcut Growth Strategy.** *Advanced Materials* 27:41 (Nov. 2015), 6431–6437. ISSN: 09359648. DOI: 10.1002/adma.201502375 (see pages 141, 143).
- [Číž66] Jiří Čížek. **On the Correlation Problem in Atomic and Molecular Systems. Calculation of Wavefunction Components in Ursell-Type Expansion Using Quantum-Field Theoretical Methods.** *The Journal of Chemical Physics* 45:11 (Dec. 1966), 4256–4266. ISSN: 0021-9606, 1089-7690. DOI: 10.1063/1.1727484 (see page 12).
- [CK60] F. Coester and H. Kümmel. **Short-Range Correlations in Nuclear Wave Functions.** *Nuclear Physics* 17 (June 1960), 477–485. ISSN: 00295582. DOI: 10.1016/0029-5582(60)90140-1 (see page 12).
- [CKF05] A. T. Costa, D. F. Kirwan, and M. S. Ferreira. **Indirect Exchange Coupling between Magnetic Adatoms in Carbon Nanotubes.** *Physical Review B* 72:8 (Aug. 2005), 085402. ISSN: 1098-0121, 1550-235X. DOI: 10.1103/PhysRevB.72.085402 (see page 148).
- [Coe58] F. Coester. **Bound States of a Many-Particle System.** *Nuclear Physics* 7 (June 1958), 421–424. ISSN: 00295582. DOI: 10.1016/0029-5582(58)90280-3 (see page 12).
- [CS82] Yia-Chung Chang and J. N. Schulman. **Complex Band Structures of Crystalline Solids: An Eigenvalue Method.** *Physical Review B* 25:6 (Mar. 1982), 3975–3986. ISSN: 0163-1829. DOI: 10.1103/PhysRevB.25.3975 (see page 32).

- [Csi+18] Gábor Csire, András Deák, Bendegúz Nyári, Hubert Ebert, James F. Annett, and Balázs Újfalussy. **Relativistic Spin-Polarized KKR Theory for Superconducting Heterostructures: Oscillating Order Parameter in the Au Layer of Nb/Au/Fe Trilayers**. *Physical Review B* 97:2 (Jan. 2018), 024514. ISSN: 2469-9950, 2469-9969. DOI: [10.1103/PhysRevB.97.024514](https://doi.org/10.1103/PhysRevB.97.024514) (see pages 4, 64).
- [Csi17] Gábor Csire. **Quasiparticle Spectrum of Superconducting Heterostructures**. PhD thesis. Budapest: Eötvös Loránd University, 2017 (see page 64).
- [CTJ12] Jingzhe Chen, Kristian S. Thygesen, and Karsten W. Jacobsen. **Ab Initio Nonequilibrium Quantum Transport and Forces with the Real-Space Projector Augmented Wave Method**. *Physical Review B* 85:15 (Apr. 2012), 155140. ISSN: 1098-0121, 1550-235X. DOI: [10.1103/PhysRevB.85.155140](https://doi.org/10.1103/PhysRevB.85.155140) (see page 35).
- [Cua+21] R. Cuadrado, R. Robles, A. García, M. Pruneda, P. Ordejón, J. Ferrer, and Jorge I. Cerdá. **Validity of the On-Site Spin-Orbit Coupling Approximation**. *Physical Review B* 104:19 (Nov. 2021), 195104. DOI: [10.1103/PhysRevB.104.195104](https://doi.org/10.1103/PhysRevB.104.195104) (see page 108).
- [Dat95] Supriyo Datta. **Electronic Transport in Mesoscopic Systems**. First. Cambridge University Press, Sept. 1995. ISBN: 978-0-511-80577-6. DOI: [10.1017/CBO9780511805776](https://doi.org/10.1017/CBO9780511805776) (see pages 27, 29, 32, 34).
- [Dav+19] Alessandro David, Péter Rakyta, Andor Kormányos, and Guido Burkard. **Induced Spin-Orbit Coupling in Twisted Graphene–Transition Metal Dichalcogenide Heterobilayers: Twistrionics Meets Spintronics**. *Physical Review B* 100:8 (Aug. 2019), 085412. ISSN: 2469-9950, 2469-9969. DOI: [10.1103/PhysRevB.100.085412](https://doi.org/10.1103/PhysRevB.100.085412). (Visited on 03/21/2023) (see page 76).
- [De 18] P. G. De Gennes. **Superconductivity of Metals and Alloys**. First. CRC Press, Mar. 2018. ISBN: 978-0-429-49703-2. DOI: [10.1201/9780429497032](https://doi.org/10.1201/9780429497032) (see page 42).
- [DG07] Y. Dagan and R. L. Greene. **Hole Superconductivity in the Electron-Doped Superconductor $\text{Pr}_{2-x}\text{Ce}_x\text{CuO}_4$** . *Physical Review B* 76:2 (July 2007), 024506. ISSN: 1098-0121, 1550-235X. DOI: [10.1103/PhysRevB.76.024506](https://doi.org/10.1103/PhysRevB.76.024506) (see page 43).
- [Din+12] Shujiang Ding, Dongyang Zhang, Jun Song Chen, and Xiong Wen (David) Lou. **Facile Synthesis of Hierarchical MoS_2 Microspheres Composed of Few-Layered Nanosheets and Their Lithium Storage Properties**. *Nanoscale* 4:1 (2012), 95–98. ISSN: 2040-3364, 2040-3372. DOI: [10.1039/C1NR11552A](https://doi.org/10.1039/C1NR11552A) (see page 140).
- [Dio+04] M. Dion, H. Rydberg, E. Schröder, D. C. Langreth, and B. I. Lundqvist. **Van Der Waals Density Functional for General Geometries**. *Physical Review Letters* 92:24 (June 2004), 246401. ISSN: 0031-9007, 1079-7114. DOI: [10.1103/PhysRevLett.92.246401](https://doi.org/10.1103/PhysRevLett.92.246401) (see page 108).
- [Dir30] P. A. M. Dirac. **Note on Exchange Phenomena in the Thomas Atom**. *Mathematical Proceedings of the Cambridge Philosophical Society* 26:3 (July 1930), 376–385. ISSN: 0305-0041, 1469-8064. DOI: [10.1017/S0305004100016108](https://doi.org/10.1017/S0305004100016108) (see page 12).

- [DP98] J. Dorantes-Dávila and G. M. Pastor. **Magnetic Anisotropy of One-Dimensional Nanostructures of Transition Metals**. *Physical Review Letters* 81:1 (July 1998), 208–211. ISSN: 0031-9007, 1079-7114. DOI: [10.1103/PhysRevLett.81.208](https://doi.org/10.1103/PhysRevLett.81.208) (see page 125).
- [DS99] C. David Sherrill and Henry F. Schaefer. “The Configuration Interaction Method: Advances in Highly Correlated Approaches.” In: *Advances in Quantum Chemistry*. Vol. 34. Elsevier, 1999, 143–269. ISBN: 978-0-12-034834-3. DOI: [10.1016/S0065-3276\(08\)60532-8](https://doi.org/10.1016/S0065-3276(08)60532-8) (see page 12).
- [Dub+09] S. M.-M. Dubois, Z. Zanolli, X. Declerck, and J.-C. Charlier. **Electronic Properties and Quantum Transport in Graphene-based Nanostructures**. *The European Physical Journal B* 72:1 (Nov. 2009), 1–24. ISSN: 1434-6028, 1434-6036. DOI: [10.1140/epjb/e2009-00327-8](https://doi.org/10.1140/epjb/e2009-00327-8) (see page 93).
- [DWS79] K. S. Dy, Shi-Yu Wu, and T. Spratlin. **Exact Solution for the Resolvent Matrix of a Generalized Tridiagonal Hamiltonian**. *Physical Review B* 20:10 (Nov. 1979), 4237–4243. ISSN: 0163-1829. DOI: [10.1103/PhysRevB.20.4237](https://doi.org/10.1103/PhysRevB.20.4237) (see page 32).
- [ED11] Eberhard Engel and Reiner M. Dreizler. **Density Functional Theory: An Advanced Course**. Theoretical and Mathematical Physics. Heidelberg [Germany] ; New York: Springer, 2011. ISBN: 978-3-642-14089-1 (see page 10).
- [EKF03] Claude Ederer, Matej Komelj, and Manfred Fähnle. **Magnetism in Systems with Various Dimensionalities: A Comparison between Fe and Co**. *Physical Review B* 68:5 (Aug. 2003), 052402. ISSN: 0163-1829, 1095-3795. DOI: [10.1103/PhysRevB.68.052402](https://doi.org/10.1103/PhysRevB.68.052402) (see page 125).
- [Eps26] Paul S. Epstein. **The Stark Effect from the Point of View of Schrodinger’s Quantum Theory**. *Physical Review* 28:4 (Oct. 1926), 695–710. ISSN: 0031-899X. DOI: [10.1103/PhysRev.28.695](https://doi.org/10.1103/PhysRev.28.695) (see page 12).
- [Fer+14] J Ferrer, C J Lambert, V M García-Suárez, D Zs Manrique, D Visontai, L Oroszlany, R Rodríguez-Ferradás, I Grace, S W D Bailey, K Gillemot, Hatef Sadeghi, and L A Algharagholy. **GOLLUM: A next-Generation Simulation Tool for Electron, Thermal and Spin Transport**. *New Journal of Physics* 16:9 (Sept. 2014), 093029. ISSN: 1367-2630. DOI: [10.1088/1367-2630/16/9/093029](https://doi.org/10.1088/1367-2630/16/9/093029) (see pages 4, 35).
- [Fer+15] Andrea C. Ferrari, Francesco Bonaccorso, Vladimir Fal’ko, Konstantin S. Novoselov, Stephan Roche, Peter Bøggild, Stefano Borini, Frank H. L. Koppens, Vincenzo Palermo, Nicola Pugno, José A. Garrido, Roman Sordan, Alberto Bianco, Laura Ballerini, Maurizio Prato, Elefterios Lidorikis, Jani Kivioja, Claudio Marinelli, Tapani Ryhänen, Alberto Morpurgo, Jonathan N. Coleman, Valeria Nicolosi, Luigi Colombo, Albert Fert, Mar Garcia-Hernandez, Adrian Bachtold, Grégory F. Schneider, Francisco Guinea, Cees Dekker, Matteo Barbone, Zhipei Sun, Costas Galiotis, Alexander N. Grigorenko, Gerasimos Konstantatos, Andras Kis, Mikhail Katsnelson, Lieven Vandersypen, Annick Loiseau, Vittorio Morandi, Daniel Neumaier, Emanuele Treossi, Vittorio Pellegrini, Marco Polini, Alessandro Tredicucci, Gareth M. Williams, Byung Hee Hong, Jong-Hyun Ahn, Jong Min Kim, Herbert Zirath, Bart J. van Wees, Herre van der Zant, Luigi Occhipinti, Andrea

- Di Matteo, Ian A. Kinloch, Thomas Seyller, Etienne Quesnel, Xinliang Feng, Ken Teo, Nalin Rupesinghe, Pertti Hakonen, Simon R. T. Neil, Quentin Tannock, Tomas Löfwander, and Jari Kinaret. **Science and Technology Roadmap for Graphene, Related Two-Dimensional Crystals, and Hybrid Systems**. *Nanoscale* 7:11 (2015), 4598–4810. ISSN: 2040-3364, 2040-3372. DOI: [10.1039/C4NR01600A](https://doi.org/10.1039/C4NR01600A). (Visited on 03/21/2023) (see page 76).
- [Fer08] Albert Fert. **Nobel Lecture: Origin, Development, and Future of Spintronics**. *Reviews of Modern Physics* 80:4 (Dec. 2008), 1517–1530. ISSN: 0034-6861, 1539-0756. DOI: [10.1103/RevModPhys.80.1517](https://doi.org/10.1103/RevModPhys.80.1517) (see page 1).
- [Fer27] Enrico Fermi. **Un Metodo Statistico per La Determinazione Di Alcune Proprietà Dell'atome**. 6:602-607 (1927), 32 (see page 12).
- [Fer28] E. Fermi. **Eine statistische Methode zur Bestimmung einiger Eigenschaften des Atoms und ihre Anwendung auf die Theorie des periodischen Systems der Elemente**. *Zeitschrift für Physik* 48:1-2 (Jan. 1928), 73–79. ISSN: 1434-6001, 1434-601X. DOI: [10.1007/BF01351576](https://doi.org/10.1007/BF01351576) (see page 12).
- [FL81] Daniel S. Fisher and Patrick A. Lee. **Relation between Conductivity and Transmission Matrix**. *Physical Review B* 23:12 (June 1981), 6851–6854. ISSN: 0163-1829. DOI: [10.1103/PhysRevB.23.6851](https://doi.org/10.1103/PhysRevB.23.6851) (see page 32).
- [FNM03] C. Fiolhais, F. Nogueira, and Miguel A. L. Marques, eds. **A Primer in Density Functional Theory**. Lecture Notes in Physics 620. Berlin ; New York: Springer, 2003. ISBN: 978-3-540-03083-6 (see page 10).
- [Foc30] V. Fock. **Näherungsmethode zur Lösung des quantenmechanischen Mehrkörperproblems**. *Zeitschrift für Physik* 61:1-2 (Jan. 1930), 126–148. ISSN: 1434-6001, 1434-601X. DOI: [10.1007/BF01340294](https://doi.org/10.1007/BF01340294) (see page 11).
- [Fra+98] Stefan Frank, Philippe Poncharal, Z. L. Wang, and Walt A. de Heer. **Carbon Nanotube Quantum Resistors**. *Science* 280:5370 (June 1998), 1744–1746. ISSN: 0036-8075, 1095-9203. DOI: [10.1126/science.280.5370.1744](https://doi.org/10.1126/science.280.5370.1744) (see page 104).
- [FRC20] Luis E. F. Foa Torres, Stephan Roche, and Jean-Christophe Charlier. **Introduction to Graphene-Based Nanomaterials: From Electronic Structure to Quantum Transport**. Second. Cambridge University Press, Jan. 2020. ISBN: 978-1-108-66446-2. DOI: [10.1017/9781108664462](https://doi.org/10.1017/9781108664462) (see page 31).
- [Frö50] H. Fröhlich. **Theory of the Superconducting State. I. The Ground State at the Absolute Zero of Temperature**. *Physical Review* 79:5 (Sept. 1950), 845–856. ISSN: 0031-899X. DOI: [10.1103/PhysRev.79.845](https://doi.org/10.1103/PhysRev.79.845) (see page 43).
- [Gaj+12] M. Gajek, J. J. Nowak, J. Z. Sun, P. L. Trouilloud, E. J. O'Sullivan, D. W. Abraham, M. C. Gaidis, G. Hu, S. Brown, Y. Zhu, R. P. Robertazzi, W. J. Gallagher, and D. C. Worledge. **Spin Torque Switching of 20 Nm Magnetic Tunnel Junctions with Perpendicular Anisotropy**. *Applied Physics Letters* 100:13 (Mar. 2012), 132408. ISSN: 0003-6951, 1077-3118. DOI: [10.1063/1.3694270](https://doi.org/10.1063/1.3694270) (see page 1).

- [Gar+09] Sandra García-Gil, Alberto García, Nicolás Lorente, and Pablo Ordejón. **Optimal Strictly Localized Basis Sets for Noble Metal Surfaces**. *Physical Review B* 79:7 (Feb. 2009), 075441. DOI: [10.1103/PhysRevB.79.075441](https://doi.org/10.1103/PhysRevB.79.075441) (see pages 23, 87).
- [Gar+18] Alberto García, Matthieu J. Verstraete, Yann Pouillon, and Javier Junquera. **The Psml Format and Library for Norm-Conserving Pseudopotential Data Curation and Interoperability**. *Computer Physics Communications* 227 (June 2018), 51–71. ISSN: 00104655. DOI: [10.1016/j.cpc.2018.02.011](https://doi.org/10.1016/j.cpc.2018.02.011) (see page 108).
- [Gar+20] Alberto García, Nick Papior, Arsalan Akhtar, Emilio Artacho, Volker Blum, Emanuele Bosoni, Pedro Brandimarte, Mads Brandbyge, J. I. Cerdá, Fabiano Corsetti, Ramón Cuadrado, Vladimir Dikan, Jaime Ferrer, Julian Gale, Pablo García-Fernández, V. M. García-Suárez, Sandra García, Georg Huhs, Sergio Illera, Richard Korytár, Peter Koval, Irina Lebedeva, Lin Lin, Pablo López-Tarifa, Sara G. Mayo, Stephan Mohr, Pablo Ordejón, Andrei Postnikov, Yann Pouillon, Miguel Pruneda, Roberto Robles, Daniel Sánchez-Portal, Jose M. Soler, Rafi Ullah, Victor Wen-zhe Yu, and Javier Junquera. **Siesta: Recent Developments and Applications**. *The Journal of Chemical Physics* 152:20 (May 2020), 204108. ISSN: 0021-9606, 1089-7690. DOI: [10.1063/5.0005077](https://doi.org/10.1063/5.0005077) (see pages 23, 86, 108).
- [GBL04] I. M. Grace, S. W. Bailey, and C. J. Lambert. **Electron Transport in Carbon Nanotube Shuttles and Telescopes**. *Physical Review B* 70:15 (Oct. 2004), 153405. ISSN: 1098-0121, 1550-235X. DOI: [10.1103/PhysRevB.70.153405](https://doi.org/10.1103/PhysRevB.70.153405) (see page 83).
- [Giu+20] Feliciano Giustino, Jin Hong Lee, Felix Trier, Manuel Bibes, Stephen M Winter, Roser Valentí, Young-Woo Son, Louis Taillefer, Christoph Heil, Adriana I Figueroa, Bernard Plaçais, QuanSheng Wu, Oleg V Yazyev, Erik P A M Bakkers, Jesper Nygård, Pol Forn-Díaz, Silvano De Franceschi, J W McIver, L E F Foa Torres, Tony Low, Anshuman Kumar, Regina Galceran, Sergio O Valenzuela, Marius V Costache, Aurélien Manchon, Eun-Ah Kim, Gabriel R Schleder, Adalberto Fazzio, and Stephan Roche. **The 2021 Quantum Materials Roadmap**. *Journal of Physics: Materials* 3:4 (Oct. 2020), 042006. ISSN: 2515-7639. DOI: [10.1088/2515-7639/abb74e](https://doi.org/10.1088/2515-7639/abb74e) (see pages 1, 3).
- [GJL79] O. Gunnarsson, M. Jonson, and B. I. Lundqvist. **Descriptions of Exchange and Correlation Effects in Inhomogeneous Electron Systems**. *Physical Review B* 20:8 (Oct. 1979), 3136–3164. ISSN: 0163-1829. DOI: [10.1103/PhysRevB.20.3136](https://doi.org/10.1103/PhysRevB.20.3136) (see page 15).
- [GL50] VL Ginzburg and LD Landau. **Phenomenological Theory**. 20:1064 (1950), 17 (see page 43).
- [Gmi+16] Martin Gmitra, Denis Kochan, Petra Högl, and Jaroslav Fabian. **Trivial and Inverted Dirac Bands and the Emergence of Quantum Spin Hall States in Graphene on Transition-Metal Dichalcogenides**. *Physical Review B* 93:15 (Apr. 2016), 155104. ISSN: 2469-9950, 2469-9969. DOI: [10.1103/PhysRevB.93.155104](https://doi.org/10.1103/PhysRevB.93.155104) (see pages 3, 76).

- [GN07] A. K. Geim and K. S. Novoselov. **The Rise of Graphene**. *Nature Materials* 6:3 (Mar. 2007), 183–191. ISSN: 1476-1122, 1476-4660. DOI: [10.1038/nmat1849](https://doi.org/10.1038/nmat1849). (Visited on 03/21/2023) (see page 76).
- [Góm21] María Camrasa Gómez. **Ab Initio Electronic Transport in Single-Molecule Junctions: Quantum Interference Effects and Spin-Orbit Torque**. PhD thesis. Regensburg: University of Regensburg, Sept. 2021 (see pages 4, 35).
- [Gon+14] Yongji Gong, Junhao Lin, Xingli Wang, Gang Shi, Sidong Lei, Zhong Lin, Xiaolong Zou, Gonglan Ye, Robert Vajtai, Boris I. Yakobson, Humberto Terrones, Mauricio Terrones, Beng Kang Tay, Jun Lou, Sokrates T. Pantelides, Zheng Liu, Wu Zhou, and Pulickel M. Ajayan. **Vertical and In-Plane Heterostructures from WS₂/MoS₂ Monolayers**. *Nature Materials* 13:12 (Dec. 2014), 1135–1142. ISSN: 1476-1122, 1476-4660. DOI: [10.1038/nmat4091](https://doi.org/10.1038/nmat4091) (see page 140).
- [Gor59] Lev Petrovich Gor’kov. **Microscopic Derivation of the Ginzburg-Landau Equations in the Theory of Superconductivity**. *Soviet Physics–JETP [translation of Zhurnal Eksperimentalnoi i Teoreticheskoi Fiziki]* 9:6 (1959), 1364–1367 (see page 43).
- [Gre+17] Dominik Gresch, Gabriel Autès, Oleg V. Yazyev, Matthias Troyer, David Vanderbilt, B. Andrei Bernevig, and Alexey A. Soluyanov. **Z2Pack: Numerical Implementation of Hybrid Wannier Centers for Identifying Topological Materials**. *Physical Review B* 95:7 (Feb. 2017), 075146. ISSN: 2469-9950, 2469-9969. DOI: [10.1103/PhysRevB.95.075146](https://doi.org/10.1103/PhysRevB.95.075146) (see pages 77, 110).
- [Gri+10] Stefan Grimme, Jens Antony, Stephan Ehrlich, and Helge Krieg. **A Consistent and Accurate Ab Initio Parametrization of Density Functional Dispersion Correction (DFT-D) for the 94 Elements H-Pu**. *The Journal of Chemical Physics* 132:15 (Apr. 2010), 154104. ISSN: 0021-9606. DOI: [10.1063/1.3382344](https://doi.org/10.1063/1.3382344) (see page 16).
- [Gri06] Stefan Grimme. **Semiempirical GGA-type density functional constructed with a long-range dispersion correction**. *Journal of Computational Chemistry* 27:15 (2006), 1787–1799. ISSN: 1096-987X. DOI: [10.1002/jcc.20495](https://doi.org/10.1002/jcc.20495) (see page 16).
- [GSA70] Carl Friedrich Gauss, Ernst Christian Julius Schering, and Göttingen Akademie der Wissenschaften. **Werke. Hrsg. von der Gesellschaft der Wissenschaften zu Göttingen**. [Göttingen K. Gesellschaft der Wissenschaften zu Göttingen], 1870 (see page 37).
- [GTN02] Michael Galperin, Sivan Toledo, and Abraham Nitzan. **Numerical Computation of Tunneling Fluxes**. *The Journal of Chemical Physics* 117:23 (Dec. 2002), 10817–10826. ISSN: 0021-9606, 1089-7690. DOI: [10.1063/1.1522404](https://doi.org/10.1063/1.1522404) (see page 32).
- [Gyo+98] B. L. Gyorffy, Z. Szotek, W. M. Temmerman, O. K. Andersen, and O. Jepsen. **Quasiparticle Spectra of High-Temperature Superconductors**. *Physical Review B* 58:2 (July 1998), 1025–1042. ISSN: 0163-1829, 1095-3795. DOI: [10.1103/PhysRevB.58.1025](https://doi.org/10.1103/PhysRevB.58.1025) (see page 44).

- [Hal19] Ali Hallal. **Graphene-Based Spinmechatronic Valve**. *2D Materials* 7:1 (Oct. 2019), 015005. ISSN: 2053-1583. DOI: [10.1088/2053-1583/ab48d2](https://doi.org/10.1088/2053-1583/ab48d2). (Visited on 03/21/2023) (see page 76).
- [Hal82] B. I. Halperin. **Quantized Hall Conductance, Current-Carrying Edge States, and the Existence of Extended States in a Two-Dimensional Disordered Potential**. *Physical Review B* 25:4 (Feb. 1982), 2185–2190. ISSN: 0163-1829. DOI: [10.1103/PhysRevB.25.2185](https://doi.org/10.1103/PhysRevB.25.2185) (see page 38).
- [Ham13] D. R. Hamann. **Optimized Norm-Conserving Vanderbilt Pseudopotentials**. *Physical Review B* 88:8 (Aug. 2013), 085117. ISSN: 1098-0121, 1550-235X. DOI: [10.1103/PhysRevB.88.085117](https://doi.org/10.1103/PhysRevB.88.085117) (see pages 86, 108).
- [Hao+13] Pan Hao, Jianwei Sun, Bing Xiao, Adrienn Ruzsinszky, Gábor I. Csonka, Jianmin Tao, Stephen Glindmeyer, and John P. Perdew. **Performance of Meta-GGA Functionals on General Main Group Thermochemistry, Kinetics, and Noncovalent Interactions**. *Journal of Chemical Theory and Computation* 9:1 (Jan. 2013), 355–363. ISSN: 1549-9618. DOI: [10.1021/ct300868x](https://doi.org/10.1021/ct300868x) (see page 16).
- [Har28] D. R. Hartree. **The Wave Mechanics of an Atom with a Non-Coulomb Central Field. Part I. Theory and Methods**. *Mathematical Proceedings of the Cambridge Philosophical Society* 24:1 (Jan. 1928), 89–110. ISSN: 0305-0041, 1469-8064. DOI: [10.1017/S0305004100011919](https://doi.org/10.1017/S0305004100011919) (see page 11).
- [He+22] Qing Lin He, Taylor L. Hughes, N. Peter Armitage, Yoshinori Tokura, and Kang L. Wang. **Topological Spintronics and Magnetoelectronics**. *Nature Materials* 21:1 (Jan. 2022), 15–23. ISSN: 1476-1122, 1476-4660. DOI: [10.1038/s41563-021-01138-5](https://doi.org/10.1038/s41563-021-01138-5) (see page 1).
- [Hed65] Lars Hedin. **New Method for Calculating the One-Particle Green's Function with Application to the Electron-Gas Problem**. *Physical Review* 139:3A (Aug. 1965), A796–A823. ISSN: 0031-899X. DOI: [10.1103/PhysRev.139.A796](https://doi.org/10.1103/PhysRev.139.A796) (see page 16).
- [Hei+08] Christian Heiliger, Peter Zahn, Bogdan Yu. Yavorsky, and Ingrid Mertig. **Thickness Dependence of the Tunneling Current in the Coherent Limit of Transport**. *Physical Review B* 77:22 (June 2008), 224407. ISSN: 1098-0121, 1550-235X. DOI: [10.1103/PhysRevB.77.224407](https://doi.org/10.1103/PhysRevB.77.224407) (see pages 132, 135, 136).
- [Hei+10] R. Heid, K.-P. Bohnen, I. Yu Sklyadneva, and E. V. Chulkov. **Effect of Spin-Orbit Coupling on the Electron-Phonon Interaction of the Superconductors Pb and Tl**. *Physical Review B* 81:17 (May 2010), 174527. ISSN: 1098-0121, 1550-235X. DOI: [10.1103/PhysRevB.81.174527](https://doi.org/10.1103/PhysRevB.81.174527). (Visited on 03/17/2023) (see page 69).
- [Hil64] Alvin F. Hildebrandt. **Magnetic Field of a Rotating Superconductor**. *Physical Review Letters* 12:8 (Feb. 1964), 190–191. ISSN: 0031-9007. DOI: [10.1103/PhysRevLett.12.190](https://doi.org/10.1103/PhysRevLett.12.190) (see page 42).

- [Hir+20] Atsufumi Hirohata, Keisuke Yamada, Yoshinobu Nakatani, Ioan-Lucian Prejbeanu, Bernard Diény, Philipp Pirro, and Burkard Hillebrands. **Review on Spintronics: Principles and Device Applications**. *Journal of Magnetism and Magnetic Materials* 509 (Sept. 2020), 166711. ISSN: 0304-8853. DOI: [10.1016/j.jmmm.2020.166711](https://doi.org/10.1016/j.jmmm.2020.166711) (see page 1).
- [Hir08] J. E. Hirsch. **Spin Meissner Effect in Superconductors and the Origin of the Meissner Effect**. *EPL (Europhysics Letters)* 81:6 (Mar. 2008), 67003. ISSN: 0295-5075, 1286-4854. DOI: [10.1209/0295-5075/81/67003](https://doi.org/10.1209/0295-5075/81/67003) (see page 43).
- [Hir16] Peter J. Hirschfeld. **Using Gap Symmetry and Structure to Reveal the Pairing Mechanism in Fe-based Superconductors**. *Comptes Rendus Physique* 17:1-2 (Jan. 2016), 197–231. ISSN: 16310705. DOI: [10.1016/j.crhy.2015.10.002](https://doi.org/10.1016/j.crhy.2015.10.002) (see page 42).
- [HJ78] J. Harris and R. O. Jones. **Pseudopotentials in Density-Functional Theory**. *Physical Review Letters* 41:3 (July 1978), 191–194. DOI: [10.1103/PhysRevLett.41.191](https://doi.org/10.1103/PhysRevLett.41.191) (see page 21).
- [HJ96] Hartmut Haug and Antti-Pekka Jauho. **Quantum Kinetics in Transport and Optics of Semiconductors**. 1.ed. Springer Series in Solid-State Sciences 123. Berlin: Springer Berlin Heidelberg, 1996. ISBN: 978-3-540-61602-3 (see page 34).
- [HK10] M. Z. Hasan and C. L. Kane. **Colloquium: Topological Insulators**. *Reviews of Modern Physics* 82:4 (Nov. 2010), 3045–3067. ISSN: 0034-6861, 1539-0756. DOI: [10.1103/RevModPhys.82.3045](https://doi.org/10.1103/RevModPhys.82.3045) (see page 1).
- [HK64] P. Hohenberg and W. Kohn. **Inhomogeneous Electron Gas**. *Physical Review* 136:3B (Nov. 1964), B864–B871. ISSN: 0031-899X. DOI: [10.1103/PhysRev.136.B864](https://doi.org/10.1103/PhysRev.136.B864) (see pages 12, 13).
- [HM89] J.E. Hirsch and F. Marsiglio. **Hole Superconductivity: Review and Some New Results**. *Physica C: Superconductivity and its Applications* 162–164 (Dec. 1989), 591–598. ISSN: 09214534. DOI: [10.1016/0921-4534\(89\)91165-9](https://doi.org/10.1016/0921-4534(89)91165-9) (see page 43).
- [HSC79] D. R. Hamann, M. Schlüter, and C. Chiang. **Norm-Conserving Pseudopotentials**. *Physical Review Letters* 43:20 (Nov. 1979), 1494–1497. ISSN: 0031-9007. DOI: [10.1103/PhysRevLett.43.1494](https://doi.org/10.1103/PhysRevLett.43.1494) (see page 20).
- [Hu+15] Chen Hu, Jiao Teng, Guanghua Yu, Wengang Lu, and Wei Ji. **Conditions for Quantized Anisotropic Magnetoresistance**. *Physical Review B* 91:4 (Jan. 2015), 045438. ISSN: 1098-0121, 1550-235X. DOI: [10.1103/PhysRevB.91.045438](https://doi.org/10.1103/PhysRevB.91.045438) (see page 128).
- [Iij91] Sumio Iijima. **Helical Microtubules of Graphitic Carbon**. *Nature* 354:6348 (Nov. 1991), 56–58. ISSN: 0028-0836, 1476-4687. DOI: [10.1038/354056a0](https://doi.org/10.1038/354056a0) (see page 85).
- [JE07] Hong Jiang and Eberhard Engel. **Random-Phase-Approximation-Based Correlation Energy Functionals: Benchmark Results for Atoms**. *The Journal of Chemical Physics* 127:18 (Nov. 2007), 184108. ISSN: 0021-9606. DOI: [10.1063/1.2795707](https://doi.org/10.1063/1.2795707) (see page 16).

- [Jér+80] D. Jérôme, A. Mazaud, M. Ribault, and K. Bechgaard. **Superconductivity in a Synthetic Organic Conductor (TMTSF)2PF 6**. *Journal de Physique Lettres* 41:4 (1980), 95–98. ISSN: 0302-072X. DOI: [10.1051/jphyslet:0198000410409500](https://doi.org/10.1051/jphyslet:0198000410409500) (see page 43).
- [Jev05] Tatjana Jevremovic. **Nuclear Principles in Engineering**. New York: Springer, 2005. ISBN: 978-0-387-23284-3 (see page 9).
- [JFP08] D. Jacob, J. Fernández-Rossier, and J. J. Palacios. **Anisotropic Magnetoresistance in Nanocontacts**. *Physical Review B* 77:16 (Apr. 2008), 165412. ISSN: 1098-0121, 1550-235X. DOI: [10.1103/PhysRevB.77.165412](https://doi.org/10.1103/PhysRevB.77.165412) (see pages 124, 125).
- [JI99] Hyoung Joon Choi and Jisoon Ihm. **Ab Initio Pseudopotential Method for the Calculation of Conductance in Quantum Wires**. *Physical Review B* 59:3 (Jan. 1999), 2267–2275. ISSN: 0163-1829, 1095-3795. DOI: [10.1103/PhysRevB.59.2267](https://doi.org/10.1103/PhysRevB.59.2267) (see page 35).
- [Joh+96] M T Johnson, P J H Bloemen, F J A den Broeder, and J J de Vries. **Magnetic Anisotropy in Metallic Multilayers**. *Reports on Progress in Physics* 59:11 (Nov. 1996), 1409–1458. ISSN: 0034-4885, 1361-6633. DOI: [10.1088/0034-4885/59/11/002](https://doi.org/10.1088/0034-4885/59/11/002) (see page 3).
- [Jon18] Nicola Jones. **How to Stop Data Centres from Gobbling up the World’s Electricity**. *Nature* 561:7722 (Sept. 2018), 163–166. ISSN: 0028-0836, 1476-4687. DOI: [10.1038/d41586-018-06610-y](https://doi.org/10.1038/d41586-018-06610-y) (see page 1).
- [Jos62] B. D. Josephson. **Possible New Effects in Superconductive Tunnelling**. *Physics Letters* 1:7 (July 1962), 251–253. ISSN: 0031-9163. DOI: [10.1016/0031-9163\(62\)91369-0](https://doi.org/10.1016/0031-9163(62)91369-0) (see page 42).
- [Jos74] B. D. Josephson. **The Discovery of Tunnelling Supercurrents**. *Reviews of Modern Physics* 46:2 (Apr. 1974), 251–254. ISSN: 0034-6861. DOI: [10.1103/RevModPhys.46.251](https://doi.org/10.1103/RevModPhys.46.251) (see page 42).
- [Jun+01] Javier Junquera, Óscar Paz, Daniel Sánchez-Portal, and Emilio Artacho. **Numerical Atomic Orbitals for Linear-Scaling Calculations**. *Physical Review B* 64:23 (Nov. 2001), 235111. ISSN: 0163-1829, 1095-3795. DOI: [10.1103/PhysRevB.64.235111](https://doi.org/10.1103/PhysRevB.64.235111) (see page 24).
- [Kam+09] Erik Kampert, Femke F. B. J. Janssen, Danil W. Boukhvalov, Jaap C. Russcher, Jan M. M. Smits, René de Gelder, Bas de Bruin, Peter C. M. Christianen, Uli Zeitler, Mikhail I. Katsnelson, Jan C. Maan, and Alan E. Rowan. **Ligand-Controlled Magnetic Interactions in Mn₄ Clusters**. *Inorganic Chemistry* 48:24 (Dec. 2009), 11903–11908. ISSN: 0020-1669, 1520-510X. DOI: [10.1021/ic901930w](https://doi.org/10.1021/ic901930w) (see pages 147, 151, 153).
- [Kan13] C.L. Kane. “Topological Band Theory and the \mathbb{Z}_2 Invariant.” In: *Contemporary Concepts of Condensed Matter Science*. Vol. 6. Elsevier, 2013, 3–34. ISBN: 978-0-444-63314-9. DOI: [10.1016/B978-0-444-63314-9.00001-9](https://doi.org/10.1016/B978-0-444-63314-9.00001-9) (see pages 1, 37–39).

- [Kas+14] Shigeru Kasahara, Tatsuya Watashige, Tetsuo Hanaguri, Yuhki Kohsaka, Takuya Yamashita, Yusuke Shimoyama, Yuta Mizukami, Ryota Endo, Hiroaki Ikeda, Kazushi Aoyama, Taichi Terashima, Shinya Uji, Thomas Wolf, Hilbert von Löhneysen, Takasada Shibauchi, and Yuji Matsuda. **Field-Induced Superconducting Phase of FeSe in the BCS-BEC Cross-Over**. *Proceedings of the National Academy of Sciences* 111:46 (Nov. 2014), 16309–16313. ISSN: 0027-8424, 1091-6490. DOI: [10.1073/pnas.1413477111](https://doi.org/10.1073/pnas.1413477111). (Visited on 03/17/2023) (see pages 69, 70).
- [Kat+00] J. A. Katine, F. J. Albert, R. A. Buhrman, E. B. Myers, and D. C. Ralph. **Current-Driven Magnetization Reversal and Spin-Wave Excitations in Co / Cu / Co Pillars**. *Physical Review Letters* 84:14 (Apr. 2000), 3149–3152. ISSN: 0031-9007, 1079-7114. DOI: [10.1103/PhysRevLett.84.3149](https://doi.org/10.1103/PhysRevLett.84.3149) (see page 1).
- [Kaw+12] T. Kawahara, K. Ito, R. Takemura, and H. Ohno. **Spin-Transfer Torque RAM Technology: Review and Prospect**. *Microelectronics Reliability* 52:4 (Apr. 2012), 613–627. ISSN: 00262714. DOI: [10.1016/j.microrel.2011.09.028](https://doi.org/10.1016/j.microrel.2011.09.028) (see page 1).
- [KB62] Leo P. Kadanoff and Gordon Baym. **Quantum Statistical Mechanics: Green's Function Methods in Equilibrium and Nonequilibrium Problems**. First. CRC Press, 1962 (see page 34).
- [KC02] D.-H. Kim and K. J. Chang. **Electron Transport in Telescoping Carbon Nanotubes**. *Physical Review B* 66:15 (Oct. 2002), 155402. ISSN: 0163-1829, 1095-3795. DOI: [10.1103/PhysRevB.66.155402](https://doi.org/10.1103/PhysRevB.66.155402) (see pages 83, 97, 102).
- [KE01] Alex Kleiner and Sebastian Eggert. **Band Gaps of Primary Metallic Carbon Nanotubes**. *Physical Review B* 63:7 (Jan. 2001), 073408. ISSN: 0163-1829, 1095-3795. DOI: [10.1103/PhysRevB.63.073408](https://doi.org/10.1103/PhysRevB.63.073408) (see page 102).
- [Kel65] Leonid Veniaminovich Keldysh. **Diagram Technique for Nonequilibrium Processes**. *Soviet Physics–JETP [translation of Zhurnal Eksperimentalnoi i Teoreticheskoi Fiziki]* 20:4 (1965), 1018–1026 (see page 34).
- [KGO89] W. Kohn, E.K.U. Gross, and L.N. Oliveira. **Orbital Magnetism in the Density Functional Theory of Superconductors**. *Journal de Physique* 50:18 (1989), 2601–2612. ISSN: 0302-0738. DOI: [10.1051/jphys:0198900500180260100](https://doi.org/10.1051/jphys:0198900500180260100) (see page 49).
- [KHB08] M N Khan, J Henk, and P Bruno. **Anisotropic Magnetoresistance in Fe/MgO/Fe Tunnel Junctions**. *Journal of Physics: Condensed Matter* 20:15 (Apr. 2008), 155208. ISSN: 0953-8984, 1361-648X. DOI: [10.1088/0953-8984/20/15/155208](https://doi.org/10.1088/0953-8984/20/15/155208) (see pages 132, 134).
- [Khv+13] A V Khvalkovskiy, D Apalkov, S Watts, R Chepulskaa, R S Beach, A Ong, X Tang, A Driskill-Smith, W H Butler, P B Visscher, D Lottis, E Chen, V Nikitin, and M Krounbi. **Basic Principles of STT-MRAM Cell Operation in Memory Arrays**. *Journal of Physics D: Applied Physics* 46:7 (Feb. 2013), 074001. ISSN: 0022-3727, 1361-6463. DOI: [10.1088/0022-3727/46/7/074001](https://doi.org/10.1088/0022-3727/46/7/074001) (see page 1).

- [KIF17] Denis Kochan, Susanne Irmer, and Jaroslav Fabian. **Model Spin-Orbit Coupling Hamiltonians for Graphene Systems**. *Physical Review B* 95:16 (Apr. 2017), 165415. ISSN: 2469-9950, 2469-9969. DOI: [10.1103/PhysRevB.95.165415](https://doi.org/10.1103/PhysRevB.95.165415) (see page 76).
- [Kir+08] D. F. Kirwan, C. G. Rocha, A. T. Costa, and M. S. Ferreira. **Sudden Decay of Indirect Exchange Coupling between Magnetic Atoms on Carbon Nanotubes**. *Physical Review B* 77:8 (Feb. 2008), 085432. ISSN: 1098-0121, 1550-235X. DOI: [10.1103/PhysRevB.77.085432](https://doi.org/10.1103/PhysRevB.77.085432) (see page 148).
- [KM05] C. L. Kane and E. J. Mele. **Quantum Spin Hall Effect in Graphene**. *Physical Review Letters* 95:22 (Nov. 2005), 226801. ISSN: 0031-9007, 1079-7114. DOI: [10.1103/PhysRevLett.95.226801](https://doi.org/10.1103/PhysRevLett.95.226801) (see pages 1, 3).
- [KMS15] Mikito Koshino, Pilkyung Moon, and Young-Woo Son. **Incommensurate Double-Walled Carbon Nanotubes as One-Dimensional Moiré Crystals**. *Physical Review B* 91:3 (Jan. 2015), 035405. ISSN: 1098-0121, 1550-235X. DOI: [10.1103/PhysRevB.91.035405](https://doi.org/10.1103/PhysRevB.91.035405) (see pages 83, 99, 100).
- [Kor+08] Yu. M Koroteev, G. Bihlmayer, E. V. Chulkov, and S. Blügel. **First-Principles Investigation of Structural and Electronic Properties of Ultrathin Bi Films**. *Physical Review B* 77:4 (Jan. 2008), 045428. ISSN: 1098-0121, 1550-235X. DOI: [10.1103/PhysRevB.77.045428](https://doi.org/10.1103/PhysRevB.77.045428) (see page 107).
- [Kra30] Hendrik Antoon Kramers. **Théorie Générale de La Rotation Paramagnétique Dans Les Cristaux**. 33:6 (1930) (see page 39).
- [KS65] W. Kohn and L. J. Sham. **Self-Consistent Equations Including Exchange and Correlation Effects**. *Physical Review* 140:4A (Nov. 1965), A1133–A1138. ISSN: 0031-899X. DOI: [10.1103/PhysRev.140.A1133](https://doi.org/10.1103/PhysRev.140.A1133) (see page 13).
- [KW15] Andrew D. Kent and Daniel C. Worledge. **A New Spin on Magnetic Memories**. *Nature Nanotechnology* 10:3 (Mar. 2015), 187–191. ISSN: 1748-3387, 1748-3395. DOI: [10.1038/nnano.2015.24](https://doi.org/10.1038/nnano.2015.24) (see page 1).
- [Lan57] R. Landauer. **Spatial Variation of Currents and Fields Due to Localized Scatterers in Metallic Conduction**. *IBM Journal of Research and Development* 1:3 (July 1957), 223–231. ISSN: 0018-8646, 0018-8646. DOI: [10.1147/rd.13.0223](https://doi.org/10.1147/rd.13.0223) (see page 29).
- [Lan70] Rolf Landauer. **Electrical Resistance of Disordered One-Dimensional Lattices**. *Philosophical Magazine* 21:172 (Apr. 1970), 863–867. ISSN: 0031-8086. DOI: [10.1080/14786437008238472](https://doi.org/10.1080/14786437008238472) (see page 29).
- [Laz+10] Predrag Lazić, Nicolae Atodiresei, Mojtaba Alaei, Vasile Caciuc, Stefan Blügel, and Radovan Brako. **JuNoLo – Jülich Nonlocal Code for Parallel Post-Processing Evaluation of vdW-DF Correlation Energy**. *Computer Physics Communications* 181:2 (Feb. 2010), 371–379. ISSN: 0010-4655. DOI: [10.1016/j.cpc.2009.09.016](https://doi.org/10.1016/j.cpc.2009.09.016) (see page 109).

- [LC05] Vincent L. Lignères and Emily A. Carter. “An Introduction to Orbital-Free Density Functional Theory.” In: *Handbook of Materials Modeling*. Ed. by Sidney Yip. Dordrecht: Springer Netherlands, 2005, 137–148. ISBN: 978-1-4020-3286-8. DOI: [10.1007/978-1-4020-3286-8_9](https://doi.org/10.1007/978-1-4020-3286-8_9) (see page 15).
- [Lev79] Mel Levy. **Universal Variational Functionals of Electron Densities, First-Order Density Matrices, and Natural Spin-Orbitals and Solution of the v -Representability Problem.** *Proceedings of the National Academy of Sciences* 76:12 (Dec. 1979), 6062–6065. ISSN: 0027-8424, 1091-6490. DOI: [10.1073/pnas.76.12.6062](https://doi.org/10.1073/pnas.76.12.6062) (see page 13).
- [Li+11] Yanguang Li, Hailiang Wang, Liming Xie, Yongye Liang, Guosong Hong, and Hongjie Dai. **MoS₂ Nanoparticles Grown on Graphene: An Advanced Catalyst for the Hydrogen Evolution Reaction.** *Journal of the American Chemical Society* 133:19 (May 2011), 7296–7299. ISSN: 0002-7863, 1520-5126. DOI: [10.1021/ja201269b](https://doi.org/10.1021/ja201269b) (see page 140).
- [Li+19] Yangmu Li, W. Tabis, Y. Tang, G. Yu, J. Jaroszynski, N. Barišić, and M. Greven. **Hole Pocket-Driven Superconductivity and Its Universal Features in the Electron-Doped Cuprates.** *Science Advances* 5:2 (Feb. 2019), eaap7349. ISSN: 2375-2548. DOI: [10.1126/sciadv.aap7349](https://doi.org/10.1126/sciadv.aap7349) (see page 43).
- [Liu+11] Zheng Liu, Chao-Xing Liu, Yong-Shi Wu, Wen-Hui Duan, Feng Liu, and Jian Wu. **Stable Nontrivial Z₂ Topology in Ultrathin Bi (111) Films: A First-Principles Study.** *Physical Review Letters* 107:13 (Sept. 2011), 136805. ISSN: 0031-9007, 1079-7114. DOI: [10.1103/PhysRevLett.107.136805](https://doi.org/10.1103/PhysRevLett.107.136805) (see page 107).
- [LJ81] D. H. Lee and J. D. Joannopoulos. **Simple Scheme for Surface-Band Calculations. II. The Green’s Function.** *Physical Review B* 23:10 (May 1981), 4997–5004. ISSN: 0163-1829. DOI: [10.1103/PhysRevB.23.4997](https://doi.org/10.1103/PhysRevB.23.4997) (see page 32).
- [LK19] Yang Li and Mikito Koshino. **Twist-Angle Dependence of the Proximity Spin-Orbit Coupling in Graphene on Transition-Metal Dichalcogenides.** *Physical Review B* 99:7 (Feb. 2019), 075438. ISSN: 2469-9950, 2469-9969. DOI: [10.1103/PhysRevB.99.075438](https://doi.org/10.1103/PhysRevB.99.075438). (Visited on 03/21/2023) (see page 76).
- [LK71] N. D. Lang and W. Kohn. **Theory of Metal Surfaces: Work Function.** *Physical Review B* 3:4 (Feb. 1971), 1215–1223. DOI: [10.1103/PhysRevB.3.1215](https://doi.org/10.1103/PhysRevB.3.1215) (see page 15).
- [LL35] Fritz London and Heinz London. **The Electromagnetic Equations of the Superconductor.** *Proceedings of the Royal Society of London. Series A - Mathematical and Physical Sciences* 149:866 (Mar. 1935), 71–88. ISSN: 0080-4630, 2053-9169. DOI: [10.1098/rspa.1935.0048](https://doi.org/10.1098/rspa.1935.0048) (see page 42).
- [LM83] David C. Langreth and M. J. Mehl. **Beyond the Local-Density Approximation in Calculations of Ground-State Electronic Properties.** *Physical Review B* 28:4 (Aug. 1983), 1809–1834. ISSN: 0163-1829. DOI: [10.1103/PhysRevB.28.1809](https://doi.org/10.1103/PhysRevB.28.1809) (see page 16).
- [Lon50] Fritz London. **Superfluids: Macroscopic Theory of Superconductivity.** Vol. 1. Structure of Matter Series. New York: Wiley, 1950 (see page 42).

- [LS50] B. A. Lippmann and Julian Schwinger. **Variational Principles for Scattering Processes. I.** *Physical Review* 79:3 (Aug. 1950), 469–480. ISSN: 0031-899X. DOI: [10.1103/PhysRev.79.469](https://doi.org/10.1103/PhysRev.79.469) (see page 32).
- [Lüd+05] M. Lüdgers, M. A. L. Marques, N. N. Lathiotakis, A. Floris, G. Profeta, L. Fast, A. Continenza, S. Massidda, and E. K. U. Gross. **Ab Initio Theory of Superconductivity. I. Density Functional Formalism and Approximate Functionals.** *Physical Review B* 72:2 (July 2005), 024545. ISSN: 1098-0121, 1550-235X. DOI: [10.1103/PhysRevB.72.024545](https://doi.org/10.1103/PhysRevB.72.024545) (see pages 4, 44, 49).
- [Lyk+71] G. I. Lykken, A. L. Geiger, K. S. Dy, and E. N. Mitchell. **Measurement of the Superconducting Energy Gap and Fermi Velocity in Single-Crystal Lead Films by Electron Tunneling.** *Physical Review B* 4:5 (Sept. 1971), 1523–1530. ISSN: 0556-2805. DOI: [10.1103/PhysRevB.4.1523](https://doi.org/10.1103/PhysRevB.4.1523). (Visited on 03/17/2023) (see pages 69, 70).
- [Ma+15] Yandong Ma, Xiao Li, Liangzhi Kou, Binghai Yan, Chengwang Niu, Ying Dai, and Thomas Heine. **Two-Dimensional Inversion-Asymmetric Topological Insulators in Functionalized III-Bi Bilayers.** *Physical Review B* 91:23 (June 2015), 235306. ISSN: 1098-0121, 1550-235X. DOI: [10.1103/PhysRevB.91.235306](https://doi.org/10.1103/PhysRevB.91.235306) (see page 107).
- [Mar+05] M. A. L. Marques, M. Lüdgers, N. N. Lathiotakis, G. Profeta, A. Floris, L. Fast, A. Continenza, E. K. U. Gross, and S. Massidda. **Ab Initio Theory of Superconductivity. II. Application to Elemental Metals.** *Physical Review B* 72:2 (July 2005), 024546. ISSN: 1098-0121, 1550-235X. DOI: [10.1103/PhysRevB.72.024546](https://doi.org/10.1103/PhysRevB.72.024546) (see pages 4, 44, 49).
- [Mar04] Richard M. Martin. **Electronic Structure: Basic Theory and Practical Methods.** Cambridge, UK ; New York: Cambridge University Press, 2004. ISBN: 978-0-521-78285-2 (see page 10).
- [Mas+16] Pierre Massat, Donato Farina, Indranil Paul, Sandra Karlsson, Pierre Strobel, Pierre Toulemonde, Marie-Aude Méasson, Maximilien Cazayous, Alain Sacuto, Shigeru Kasahara, Takasada Shibauchi, Yuji Matsuda, and Yann Gallais. **Charge-Induced Nematicity in FeSe.** *Proceedings of the National Academy of Sciences* 113:33 (Aug. 2016), 9177–9181. ISSN: 0027-8424, 1091-6490. DOI: [10.1073/pnas.1606562113](https://doi.org/10.1073/pnas.1606562113). (Visited on 03/17/2023) (see page 70).
- [MO33] W. Meissner and R. Ochsenfeld. **Ein neuer Effekt bei Eintritt der Supraleitfähigkeit.** *Die Naturwissenschaften* 21:44 (Nov. 1933), 787–788. ISSN: 0028-1042, 1432-1904. DOI: [10.1007/BF01504252](https://doi.org/10.1007/BF01504252) (see page 41).
- [MP34] Chr Møller and M. S. Plesset. **Note on an Approximation Treatment for Many-Electron Systems.** *Physical Review* 46:7 (Oct. 1934), 618–622. ISSN: 0031-899X. DOI: [10.1103/PhysRev.46.618](https://doi.org/10.1103/PhysRev.46.618) (see page 12).
- [MP75] T. McGuire and R. Potter. **Anisotropic Magnetoresistance in Ferromagnetic 3d Alloys.** *IEEE Transactions on Magnetism* 11:4 (July 1975), 1018–1038. ISSN: 1941-0069. DOI: [10.1109/TMAG.1975.1058782](https://doi.org/10.1109/TMAG.1975.1058782) (see pages 3, 124).

- [MR03] Douglas L. Mills and Sergio M. Rezende. “Spin Damping in Ultrathin Magnetic Films.” In: *Spin Dynamics in Confined Magnetic Structures II*. Ed. by Burkard Hillebrands and Kamel Ounadjela. Topics in Applied Physics. Berlin, Heidelberg: Springer, 2003, 27–59. ISBN: 978-3-540-46097-8. DOI: [10.1007/3-540-46097-7_2](https://doi.org/10.1007/3-540-46097-7_2) (see page 3).
- [MU01] J. Mathon and A. Umerski. **Theory of Tunneling Magnetoresistance of an Epitaxial Fe/MgO/Fe(001) Junction**. *Physical Review B* 63:22 (May 2001), 220403. ISSN: 0163-1829, 1095-3795. DOI: [10.1103/PhysRevB.63.220403](https://doi.org/10.1103/PhysRevB.63.220403) (see page 132).
- [Nag+10] Naoto Nagaosa, Jairo Sinova, Shigeki Onoda, A. H. MacDonald, and N. P. Ong. **Anomalous Hall Effect**. *Reviews of Modern Physics* 82:2 (May 2010), 1539–1592. ISSN: 0034-6861, 1539-0756. DOI: [10.1103/RevModPhys.82.1539](https://doi.org/10.1103/RevModPhys.82.1539) (see page 3).
- [Nak+20] Dekel Nakar, Georgy Gordeev, Leonardo D. Machado, Ronit Popovitz-Biro, Katya Rechav, Eliezer F. Oliveira, Patryk Kusch, Ado Jorio, Douglas S. Galvão, Stephanie Reich, and Ernesto Joselevich. **Few-Wall Carbon Nanotube Coils**. *Nano Letters* 20:2 (Feb. 2020), 953–962. ISSN: 1530-6984, 1530-6992. DOI: [10.1021/acs.nanolett.9b03977](https://doi.org/10.1021/acs.nanolett.9b03977) (see page 84).
- [Nes55] R. K. Nesbet. **Configuration Interaction in Orbital Theories**. *Proceedings of the Royal Society of London. Series A. Mathematical and Physical Sciences* 230:1182 (June 1955), 312–321. ISSN: 0080-4630, 2053-9169. DOI: [10.1098/rspa.1955.0134](https://doi.org/10.1098/rspa.1955.0134) (see page 12).
- [NG04] Y. M. Niquet and X. Gonze. **Band-Gap Energy in the Random-Phase Approximation to Density-Functional Theory**. *Physical Review B* 70:24 (Dec. 2004), 245115. ISSN: 1098-0121, 1550-235X. DOI: [10.1103/PhysRevB.70.245115](https://doi.org/10.1103/PhysRevB.70.245115) (see page 16).
- [NIST18] **Fundamental Physical Constants from NIST** (). URL: <https://physics.nist.gov/cuu/Constants/index.html> (see page xv).
- [Nov04] K. S. Novoselov. **Electric Field Effect in Atomically Thin Carbon Films**. *Science* 306:5696 (Oct. 2004), 666–669. ISSN: 0036-8075, 1095-9203. DOI: [10.1126/science.1102896](https://doi.org/10.1126/science.1102896) (see page 85).
- [OGK88] L. N. Oliveira, E. K. U. Gross, and W. Kohn. **Density-Functional Theory for Superconductors**. *Physical Review Letters* 60:23 (June 1988), 2430–2433. ISSN: 0031-9007. DOI: [10.1103/PhysRevLett.60.2430](https://doi.org/10.1103/PhysRevLett.60.2430) (see pages 4, 49).
- [ONK10] Taisuke Ozaki, Kengo Nishio, and Hiori Kino. **Efficient Implementation of the Nonequilibrium Green Function Method for Electronic Transport Calculations**. *Physical Review B* 81:3 (Jan. 2010), 035116. ISSN: 1098-0121, 1550-235X. DOI: [10.1103/PhysRevB.81.035116](https://doi.org/10.1103/PhysRevB.81.035116) (see page 35).
- [Onn11] Heike Kamerlingh Onnes. **The Resistance of Pure Mercury at Helium Temperatures**. *Commun. Phys. Lab. Univ. Leiden, b* 120 (1911) (see page 41).
- [OYC+09] MN Ou, TJ Yang, YY Chen, et al. **Anisotropic Magnetism and Magnetoresistance in Iron Nanowire Arrays**. *Chinese Journal of Physics* 47:6 (2009), 847–852 (see pages 125, 128, 129).

- [Pal+02] J. J. Palacios, A. J. Pérez-Jiménez, E. Louis, E. SanFabián, and J. A. Vergés. **First-Principles Approach to Electrical Transport in Atomic-Scale Nanostructures**. *Physical Review B* 66:3 (July 2002), 035322. ISSN: 0163-1829, 1095-3795. DOI: [10.1103/PhysRevB.66.035322](https://doi.org/10.1103/PhysRevB.66.035322) (see page 35).
- [Pap+17] Nick Papior, Nicolás Lorente, Thomas Frederiksen, Alberto García, and Mads Brandbyge. **Improvements on Non-Equilibrium and Transport Green Function Techniques: The next-Generation Transiesta**. *Computer Physics Communications* 212 (Mar. 2017), 8–24. ISSN: 00104655. DOI: [10.1016/j.cpc.2016.09.022](https://doi.org/10.1016/j.cpc.2016.09.022) (see pages 29, 35, 55, 59, 86, 153).
- [Pav+17] Eva Pavarini, Erik Koch, Richard Scalettar, Richard Martin, Institute for Advanced Simulation, and German Research School for Simulation Sciences, eds. **The Physics of Correlated Insulators, Metals, and Superconductors: Lecture Notes of the Autumn School on Correlated Electrons 2017: At Forschungszentrum Jülich, 25-29 September 2017**. Schriften Des Forschungszentrums Jülich. Reihe Modeling and Simulation Band 7. Jülich: Forschungszentrum, Zentralbibliothek, 2017. ISBN: 978-3-95806-224-5 (see page 44).
- [PB07] Magnus Paulsson and Mads Brandbyge. **Transmission Eigenchannels from Nonequilibrium Green's Functions**. *Physical Review B* 76:11 (Sept. 2007), 115117. ISSN: 1098-0121, 1550-235X. DOI: [10.1103/PhysRevB.76.115117](https://doi.org/10.1103/PhysRevB.76.115117) (see page 59).
- [PBE96] John P. Perdew, Kieron Burke, and Matthias Ernzerhof. **Generalized Gradient Approximation Made Simple**. *Physical Review Letters* 77:18 (Oct. 1996), 3865–3868. ISSN: 0031-9007, 1079-7114. DOI: [10.1103/PhysRevLett.77.3865](https://doi.org/10.1103/PhysRevLett.77.3865) (see pages 71, 86, 108, 109, 131, 136).
- [Pec+08] A Pecchia, G Penazzi, L Salvucci, and A Di Carlo. **Non-Equilibrium Green's Functions in Density Functional Tight Binding: Method and Applications**. *New Journal of Physics* 10:6 (June 2008), 065022. ISSN: 1367-2630. DOI: [10.1088/1367-2630/10/6/065022](https://doi.org/10.1088/1367-2630/10/6/065022) (see page 35).
- [Pez+21] Armando Pezo, Zeila Zanolli, Nils Wittemeier, Pablo Ordejon, Adalberto Fazzio, Stephan Roche, and José Hugo Garcia. **Manipulation of Spin Transport in Graphene/Transition Metal Dichalcogenide Heterobilayers upon Twisting**. *2D Materials* (Oct. 2021). ISSN: 2053-1583. DOI: [10.1088/2053-1583/ac3378](https://doi.org/10.1088/2053-1583/ac3378) (see pages 3, 76).
- [PG10] Johnpierre Paglione and Richard L. Greene. **High-Temperature Superconductivity in Iron-Based Materials**. *Nature Physics* 6:9 (Sept. 2010), 645–658. ISSN: 1745-2473, 1745-2481. DOI: [10.1038/nphys1759](https://doi.org/10.1038/nphys1759). (Visited on 03/17/2023) (see page 70).
- [Po+18] Hoi Chun Po, LiuJun Zou, Ashvin Vishwanath, and T. Senthil. **Origin of Mott Insulating Behavior and Superconductivity in Twisted Bilayer Graphene**. *Physical Review X* 8:3 (Sept. 2018), 031089. ISSN: 2160-3308. DOI: [10.1103/PhysRevX.8.031089](https://doi.org/10.1103/PhysRevX.8.031089) (see page 3).

- [Pow08] James R. Powell. **The Quantum Limit to Moore’s Law**. *Proceedings of the IEEE* 96:8 (Aug. 2008), 1247–1248. ISSN: 0018-9219, 1558-2256. DOI: [10.1109/JPROC.2008.925411](https://doi.org/10.1109/JPROC.2008.925411) (see page 27).
- [PR72] M.M. Pant and A.K. Rajagopal. **Theory of Inhomogeneous Magnetic Electron Gas**. *Solid State Communications* 10:12 (June 1972), 1157–1160. ISSN: 00381098. DOI: [10.1016/0038-1098\(72\)90934-9](https://doi.org/10.1016/0038-1098(72)90934-9) (see page 17).
- [Pue+20] Jorge Puebla, Junyeon Kim, Kouta Kondou, and Yoshichika Otani. **Spintronic Devices for Energy-Efficient Data Storage and Energy Harvesting**. *Communications Materials* 1:1 (May 2020), 1–9. ISSN: 2662-4443. DOI: [10.1038/s43246-020-0022-5](https://doi.org/10.1038/s43246-020-0022-5) (see page 1).
- [Que+14] J. Quereda, A. Castellanos-Gomez, N. Agrait, and G. Rubio-Bollinger. **Single-Layer MoS₂ Roughness and Sliding Friction Quenching by Interaction with Atomically Flat Substrates**. *Applied Physics Letters* 105:5 (Aug. 2014), 053111. ISSN: 0003-6951, 1077-3118. DOI: [10.1063/1.4892650](https://doi.org/10.1063/1.4892650) (see page 115).
- [QZ11] Xiao-Liang Qi and Shou-Cheng Zhang. **Topological Insulators and Superconductors**. *Reviews of Modern Physics* 83:4 (Oct. 2011), 1057–1110. ISSN: 0034-6861, 1539-0756. DOI: [10.1103/RevModPhys.83.1057](https://doi.org/10.1103/RevModPhys.83.1057) (see page 3).
- [RB22a] Philipp Rüßmann and Stefan Blügel. **Density Functional Bogoliubov-de Gennes Analysis of Superconducting Nb and Nb(110) Surfaces**. *Physical Review B* 105:12 (Mar. 2022), 125143. ISSN: 2469-9950, 2469-9969. DOI: [10.1103/PhysRevB.105.125143](https://doi.org/10.1103/PhysRevB.105.125143) (see pages 4, 64).
- [RB22b] Philipp Rüßmann and Stefan Blügel. **Proximity Induced Superconductivity in a Topological Insulator** (2022). DOI: [10.48550/ARXIV.2208.14289](https://doi.org/10.48550/ARXIV.2208.14289) (see page 64).
- [Rei+02] S. Reich, J. Maultzsch, C. Thomsen, and P. Ordejón. **Tight-Binding Description of Graphene**. *Physical Review B* 66:3 (July 2002), 035412. ISSN: 0163-1829, 1095-3795. DOI: [10.1103/PhysRevB.66.035412](https://doi.org/10.1103/PhysRevB.66.035412) (see page 87).
- [Rei+17] F. Reis, G. Li, L. Dudy, M. Bauernfeind, S. Glass, W. Hanke, R. Thomale, J. Schäfer, and R. Claessen. **Bismuthene on a SiC Substrate: A Candidate for a High-Temperature Quantum Spin Hall Material**. *Science* 357:6348 (July 2017), 287–290. ISSN: 0036-8075, 1095-9203. DOI: [10.1126/science.aai8142](https://doi.org/10.1126/science.aai8142) (see pages 107, 111–113, 120).
- [Rit+14] Andrew M. Ritzmann, Michele Pavone, Ana B. Muñoz-García, John A. Keith, and Emily A. Carter. **Ab Initio DFT+U Analysis of Oxygen Transport in LaCoO₃: The Effect of Co³⁺ Magnetic States**. *J. Mater. Chem. A* 2:21 (2014), 8060–8074. ISSN: 2050-7488, 2050-7496. DOI: [10.1039/C4TA00801D](https://doi.org/10.1039/C4TA00801D). (Visited on 03/26/2023) (see page 151).
- [RK11] Zohar Ringel and Yaacov E. Kraus. **Determining Topological Order from a Local Ground-State Correlation Function**. *Physical Review B* 83:24 (June 2011), 245115. ISSN: 1098-0121, 1550-235X. DOI: [10.1103/PhysRevB.83.245115](https://doi.org/10.1103/PhysRevB.83.245115) (see page 79).

- [RLO05] R. Rurali, N. Lorente, and P. Ordejón. **Comment on “Molecular Distortions and Chemical Bonding of a Large π -Conjugated Molecule on a Metal Surface”**. *Physical Review Letters* 95:20 (Nov. 2005), 209601. DOI: [10.1103/PhysRevLett.95.209601](https://doi.org/10.1103/PhysRevLett.95.209601) (see page 87).
- [Roc+05] Alexandre R. Rocha, Víctor M. García-suárez, Steve W. Bailey, Colin J. Lambert, Jaime Ferrer, and Stefano Sanvito. **Towards Molecular Spintronics**. *Nature Materials* 4:4 (Apr. 2005), 335–339. ISSN: 1476-1122, 1476-4660. DOI: [10.1038/nmat1349](https://doi.org/10.1038/nmat1349) (see page 35).
- [Roc+15] Stephan Roche, Johan Åkerman, Bernd Beschoten, Jean-Christophe Charlier, Mairbek Chshiev, Saroj Prasad Dash, Bruno Dlubak, Jaroslav Fabian, Albert Fert, Marcos Guimarães, Francisco Guinea, Irina Grigorieva, Christian Schönemberger, Pierre Seneor, Christoph Stampfer, Sergio O Valenzuela, Xavier Waintal, and Bart van Wees. **Graphene Spintronics: The European Flagship Perspective**. *2D Materials* 2:3 (July 2015), 030202. ISSN: 2053-1583. DOI: [10.1088/2053-1583/2/3/030202](https://doi.org/10.1088/2053-1583/2/3/030202). (Visited on 03/21/2023) (see page 76).
- [Roc07] Alexandre Reily Rocha. **Theoretical and Computational Aspects of Electronic Transport at the Nanoscale**. PhD thesis. Trinity College Dublin, 2007 (see pages 34, 35).
- [Roo07] Björn O. Roos. “The Complete Active Space Self-Consistent Field Method and Its Applications in Electronic Structure Calculations.” In: *Advances in Chemical Physics*. Ed. by K. P. Lawley. Hoboken, NJ, USA: John Wiley & Sons, Inc., Mar. 2007, 399–445. ISBN: 978-0-470-14294-3 978-0-471-90901-9. DOI: [10.1002/9780470142943.ch7](https://doi.org/10.1002/9780470142943.ch7) (see page 12).
- [RS09] Guillermo Román-Pérez and José M. Soler. **Efficient Implementation of a van Der Waals Density Functional: Application to Double-Wall Carbon Nanotubes**. *Physical Review Letters* 103:9 (Aug. 2009), 096102. ISSN: 0031-9007, 1079-7114. DOI: [10.1103/PhysRevLett.103.096102](https://doi.org/10.1103/PhysRevLett.103.096102) (see page 86).
- [RSA99] Alain Rochefort, Dennis R. Salahub, and Phaedon Avouris. **Effects of Finite Length on the Electronic Structure of Carbon Nanotubes**. *The Journal of Physical Chemistry B* 103:4 (Jan. 1999), 641–646. ISSN: 1520-6106, 1520-5207. DOI: [10.1021/jp983725m](https://doi.org/10.1021/jp983725m) (see pages 84, 90).
- [Rub+99] Angel Rubio, Daniel Sánchez-Portal, Emilio Artacho, Pablo Ordejón, and José M. Soler. **Electronic States in a Finite Carbon Nanotube: A One-Dimensional Quantum Box**. *Physical Review Letters* 82:17 (Apr. 1999), 3520–3523. ISSN: 0031-9007, 1079-7114. DOI: [10.1103/PhysRevLett.82.3520](https://doi.org/10.1103/PhysRevLett.82.3520) (see pages 84, 90).
- [Rüs+05] C. Rüster, C. Gould, T. Jungwirth, J. Sinova, G. M. Schott, R. Giraud, K. Brunner, G. Schmidt, and L. W. Molenkamp. **Very Large Tunneling Anisotropic Magnetoresistance of a (Ga,Mn)As/GaAs/(Ga,Mn)As Stack**. *Physical Review Letters* 94:2 (Jan. 2005), 027203. ISSN: 0031-9007, 1079-7114. DOI: [10.1103/PhysRevLett.94.027203](https://doi.org/10.1103/PhysRevLett.94.027203) (see page 124).
- [SA19] Pier Luigi Silvestrelli and Alberto Ambrosetti. **Van Der Waals Interactions in DFT Using Wannier Functions without Empirical Parameters**. *The Journal of Chemical Physics* 150:16 (Apr. 2019), 164109. ISSN: 0021-9606. DOI: [10.1063/1.5093125](https://doi.org/10.1063/1.5093125) (see page 16).

- [Sai+20] Yu Saito, Jingyuan Ge, Kenji Watanabe, Takashi Taniguchi, and Andrea F. Young. **Independent Superconductors and Correlated Insulators in Twisted Bilayer Graphene**. *Nature Physics* 16:9 (Sept. 2020), 926–930. ISSN: 1745-2473, 1745-2481. DOI: [10.1038/s41567-020-0928-3](https://doi.org/10.1038/s41567-020-0928-3) (see page 3).
- [San+18] Antonio Sanna, José A. Flores-Livas, Arkadiy Davydov, Gianni Profeta, Kay Dewhurst, Sangeeta Sharma, and E. K. U. Gross. **Ab Initio Eliashberg Theory: Making Genuine Predictions of Superconducting Features**. *Journal of the Physical Society of Japan* 87:4 (Apr. 2018), 041012. ISSN: 0031-9015, 1347-4073. DOI: [10.7566/JPSJ.87.041012](https://doi.org/10.7566/JPSJ.87.041012) (see pages 44, 49).
- [Sau+20] Tom G. Saunderson, Zsolt Györgypál, James F. Annett, Gábor Csire, Balázs Újfalussy, and Martin Gradhand. **Real-Space Multiple Scattering Theory for Superconductors with Impurities**. *Physical Review B* 102:24 (Dec. 2020), 245106. ISSN: 2469-9950, 2469-9969. DOI: [10.1103/PhysRevB.102.245106](https://doi.org/10.1103/PhysRevB.102.245106) (see page 4).
- [Sch10] Jörg Schmalian. **Failed Theories Of Superconductivity**. *Modern Physics Letters B* 24:27 (Oct. 2010), 2679–2691. ISSN: 0217-9849, 1793-6640. DOI: [10.1142/S0217984910025280](https://doi.org/10.1142/S0217984910025280) (see page 42).
- [Sch26a] E. Schrödinger. **Quantisierung als Eigenwertproblem (erste Mitteilung)**. *Annalen der Physik* 384:4 (1926), 361–376. ISSN: 00033804, 15213889. DOI: [10.1002/andp.19263840404](https://doi.org/10.1002/andp.19263840404) (see page 9).
- [Sch26b] E. Schrödinger. **Quantisierung als Eigenwertproblem (vierte Mitteilung)**. *Annalen der Physik* 386:18 (1926), 109–139. ISSN: 00033804, 15213889. DOI: [10.1002/andp.19263861802](https://doi.org/10.1002/andp.19263861802) (see page 9).
- [Sch26c] E. Schrödinger. **Quantisierung als Eigenwertproblem (zweite Mitteilung)**. *Annalen der Physik* 384:6 (1926), 489–527. ISSN: 00033804, 15213889. DOI: [10.1002/andp.19263840602](https://doi.org/10.1002/andp.19263840602) (see page 9).
- [SG92] M.B. Suvasini and B.L. Gyorffy. **A Multiple Scattering Method for Solving Bogoliubov-de Gennes Equations of Superconductivity**. *Physica C: Superconductivity* 195:1-2 (May 1992), 109–126. ISSN: 09214534. DOI: [10.1016/0921-4534\(92\)90081-M](https://doi.org/10.1016/0921-4534(92)90081-M) (see page 49).
- [Sha+19] Aaron L. Sharpe, Eli J. Fox, Arthur W. Barnard, Joe Finney, Kenji Watanabe, Takashi Taniguchi, M. A. Kastner, and David Goldhaber-Gordon. **Emergent Ferromagnetism near Three-Quarters Filling in Twisted Bilayer Graphene**. *Science* 365:6453 (Aug. 2019), 605–608. ISSN: 0036-8075, 1095-9203. DOI: [10.1126/science.aaw3780](https://doi.org/10.1126/science.aaw3780) (see page 3).
- [Sha21] R.G. Sharma. **Superconductivity: Basics and Applications to Magnets**. Vol. 214. Springer Series in Materials Science. Cham: Springer International Publishing, 2021. ISBN: 978-3-030-75672-7. DOI: [10.1007/978-3-030-75672-7](https://doi.org/10.1007/978-3-030-75672-7) (see pages 42, 43).

- [Sie+21] Juan F. Sierra, Jaroslav Fabian, Roland K. Kawakami, Stephan Roche, and Sergio O. Valenzuela. **Van Der Waals Heterostructures for Spintronics and Opto-Spintronics**. *Nature Nanotechnology* 16:8 (Aug. 2021), 856–868. ISSN: 1748-3387, 1748-3395. DOI: [10.1038/s41565-021-00936-x](https://doi.org/10.1038/s41565-021-00936-x). (Visited on 03/21/2023) (see page 76).
- [Sin+19] Sobhit Singh, Zeila Zanolli, Maximilian Amsler, Brahim Belhadji, Jorge O. Sofo, Matthieu J. Verstraete, and Aldo H. Romero. **Low-Energy Phases of Bi Monolayer Predicted by Structure Search in Two Dimensions**. *The Journal of Physical Chemistry Letters* 10:23 (Dec. 2019), 7324–7332. ISSN: 1948-7185, 1948-7185. DOI: [10.1021/acs.jpcclett.9b03043](https://doi.org/10.1021/acs.jpcclett.9b03043) (see pages 3, 107, 111).
- [Sir+16] Anshu Sirohi, Preetha Saha, Sirshendu Gayen, Avtar Singh, and Goutam Sheet. **Transport Spectroscopy on Trapped Superconducting Nano-Islands of Pb: Signature of Unconventional Pairing**. *Nanotechnology* 27:28 (July 2016), 285701. ISSN: 0957-4484, 1361-6528. DOI: [10.1088/0957-4484/27/28/285701](https://doi.org/10.1088/0957-4484/27/28/285701). (Visited on 03/17/2023) (see page 69).
- [Skl+12] I. Yu Sklyadneva, R. Heid, P. M. Echenique, K.-B. Bohnen, and E. V. Chulkov. **Electron-Phonon Interaction in Bulk Pb: Beyond the Fermi Surface**. *Physical Review B* 85:15 (Apr. 2012), 155115. ISSN: 1098-0121, 1550-235X. DOI: [10.1103/PhysRevB.85.155115](https://doi.org/10.1103/PhysRevB.85.155115). (Visited on 03/17/2023) (see page 69).
- [Sla28] J. C. Slater. **The Self Consistent Field and the Structure of Atoms**. *Physical Review* 32:3 (Sept. 1928), 339–348. ISSN: 0031-899X. DOI: [10.1103/PhysRev.32.339](https://doi.org/10.1103/PhysRev.32.339) (see page 11).
- [Sla30a] J. C. Slater. **Atomic Shielding Constants**. *Physical Review* 36:1 (July 1930), 57–64. ISSN: 0031-899X. DOI: [10.1103/PhysRev.36.57](https://doi.org/10.1103/PhysRev.36.57) (see page 22).
- [Sla30b] J. C. Slater. **Note on Hartree's Method**. *Physical Review* 35:2 (Jan. 1930), 210–211. ISSN: 0031-899X. DOI: [10.1103/PhysRev.35.210.2](https://doi.org/10.1103/PhysRev.35.210.2) (see page 11).
- [Sla51] J. C. Slater. **A Simplification of the Hartree-Fock Method**. *Physical Review* 81:3 (Feb. 1951), 385–390. ISSN: 0031-899X. DOI: [10.1103/PhysRev.81.385](https://doi.org/10.1103/PhysRev.81.385) (see page 11).
- [Sla64] J. C. Slater. **Atomic Radii in Crystals**. *The Journal of Chemical Physics* 41:10 (Nov. 1964), 3199–3204. ISSN: 0021-9606, 1089-7690. DOI: [10.1063/1.1725697](https://doi.org/10.1063/1.1725697) (see page 9).
- [Slo96] J.C. Slonczewski. **Current-Driven Excitation of Magnetic Multilayers**. *Journal of Magnetism and Magnetic Materials* 159:1-2 (June 1996), L1–L7. ISSN: 03048853. DOI: [10.1016/0304-8853\(96\)00062-5](https://doi.org/10.1016/0304-8853(96)00062-5) (see page 1).
- [Smi+20] Søren Smidstrup, Troels Markussen, Pieter Vancaeyveld, Jess Wellendorff, Julian Schneider, Tue Gunst, Brecht Verstichel, Daniele Stradi, Petr A Khomyakov, Ulrik G Vej-Hansen, Maeng-Eun Lee, Samuel T Chill, Filip Rasmussen, Gabriele Penazzi, Fabiano Corsetti, Ari Ojanperä, Kristian Jensen, Mattias L N Palsgaard, Umberto Martinez, Anders Blom, Mads Brandbyge, and Kurt Stokbro. **QuantumATK: An Integrated Platform of Electronic and Atomic-Scale Modelling Tools**. *Journal of Physics: Condensed Matter* 32:1 (Jan. 2020), 015901. ISSN: 0953-8984, 1361-648X. DOI: [10.1088/1361-648X/ab4007](https://doi.org/10.1088/1361-648X/ab4007) (see page 4).

- [SN02] Elisabeth Sjöstedt and Lars Nordström. **Noncollinear Full-Potential Studies of γ - Fe**. *Physical Review B* 66:1 (July 2002), 014447. ISSN: 0163-1829, 1095-3795. DOI: [10.1103/PhysRevB.66.014447](https://doi.org/10.1103/PhysRevB.66.014447) (see page 25).
- [SN21] J. J. Sakurai and Jim Napolitano. **Modern Quantum Mechanics**. Third edition. Cambridge: Cambridge University Press, 2021. ISBN: 978-1-108-47322-4 (see page 29).
- [SN89] Otto F. Sankey and David J. Niklewski. **Ab Initio Multicenter Tight-Binding Model for Molecular-Dynamics Simulations and Other Applications in Covalent Systems**. *Physical Review B* 40:6 (Aug. 1989), 3979–3995. ISSN: 0163-1829. DOI: [10.1103/PhysRevB.40.3979](https://doi.org/10.1103/PhysRevB.40.3979) (see page 24).
- [SO96] Attila Szabo and Neil S. Ostlund. **Modern Quantum Chemistry: Introduction to Advanced Electronic Structure Theory**. Mineola, N.Y: Dover Publications, 1996. ISBN: 978-0-486-69186-2 (see page 12).
- [SOA21] Fabian Schrodi, Peter M. Oppeneer, and Alex Aperis. **Unconventional Superconductivity Mediated Solely by Isotropic Electron-Phonon Interaction**. *Physical Review B* 104:14 (Oct. 2021), L140506. ISSN: 2469-9950, 2469-9969. DOI: [10.1103/PhysRevB.104.L140506](https://doi.org/10.1103/PhysRevB.104.L140506) (see page 43).
- [Sol+02] José M Soler, Emilio Artacho, Julian D Gale, Alberto García, Javier Junquera, Pablo Ordejón, and Daniel Sánchez-Portal. **The SIESTA Method for Ab Initio Order- N Materials Simulation**. *Journal of Physics: Condensed Matter* 14:11 (Mar. 2002), 2745–2779. ISSN: 0953-8984, 1361-648X. DOI: [10.1088/0953-8984/14/11/302](https://doi.org/10.1088/0953-8984/14/11/302) (see pages 23, 86, 108).
- [Sol+10] Gemma C. Solomon, Carmen Herrmann, Thorsten Hansen, Vladimiro Mujica, and Mark A. Ratner. **Exploring Local Currents in Molecular Junctions**. *Nature Chemistry* 2:3 (Mar. 2010), 223–228. ISSN: 1755-4330, 1755-4349. DOI: [10.1038/nchem.546](https://doi.org/10.1038/nchem.546) (see page 59).
- [SSR85] M. P. Lopez Sancho, J. M. Lopez Sancho, and J. Rubio. **Highly Convergent Schemes for the Calculation of Bulk and Surface Green Functions**. *Journal of Physics F: Metal Physics* 15:4 (Apr. 1985), 851–858. ISSN: 0305-4608. DOI: [10.1088/0305-4608/15/4/009](https://doi.org/10.1088/0305-4608/15/4/009) (see pages 32, 55).
- [Stä+99] M. Städele, M. Moukara, J. A. Majewski, P. Vogl, and A. Görling. **Exact Exchange Kohn-Sham Formalism Applied to Semiconductors**. *Physical Review B* 59:15 (Apr. 1999), 10031–10043. ISSN: 0163-1829, 1095-3795. DOI: [10.1103/PhysRevB.59.10031](https://doi.org/10.1103/PhysRevB.59.10031) (see page 16).
- [Ste+20] Petr Stepanov, Ipsita Das, Xiaobo Lu, Ali Fahimniya, Kenji Watanabe, Takashi Taniguchi, Frank H. L. Koppens, Johannes Lischner, Leonid Levitov, and Dmitri K. Efetov. **Untying the Insulating and Superconducting Orders in Magic-Angle Graphene**. *Nature* 583:7816 (July 2020), 375–378. ISSN: 0028-0836, 1476-4687. DOI: [10.1038/s41586-020-2459-6](https://doi.org/10.1038/s41586-020-2459-6) (see page 3).

- [Ste+79] F. Steglich, J. Aarts, C. D. Bredl, W. Lieke, D. Meschede, W. Franz, and H. Schäfer. **Superconductivity in the Presence of Strong Pauli Paramagnetism: Ce Cu₂ Si₂**. *Physical Review Letters* 43:25 (Dec. 1979), 1892–1896. ISSN: 0031-9007. DOI: [10.1103/PhysRevLett.43.1892](https://doi.org/10.1103/PhysRevLett.43.1892) (see page 43).
- [Ste17] G. R. Stewart. **Unconventional Superconductivity**. *Advances in Physics* 66:2 (Apr. 2017), 75–196. ISSN: 0001-8732, 1460-6976. DOI: [10.1080/00018732.2017.1331615](https://doi.org/10.1080/00018732.2017.1331615) (see page 43).
- [STG93] M. B. Suvasini, W. M. Temmerman, and B. L. Gyorffy. **Computational Aspects of Density-Functional Theories of Superconductors**. *Physical Review B* 48:2 (July 1993), 1202–1210. ISSN: 0163-1829, 1095-3795. DOI: [10.1103/PhysRevB.48.1202](https://doi.org/10.1103/PhysRevB.48.1202) (see pages 50, 64).
- [SV11] Alexey A. Soluyanov and David Vanderbilt. **Computing Topological Invariants without Inversion Symmetry**. *Physical Review B* 83:23 (June 2011), 235401. ISSN: 1098-0121, 1550-235X. DOI: [10.1103/PhysRevB.83.235401](https://doi.org/10.1103/PhysRevB.83.235401) (see page 79).
- [Tao+03] Jianmin Tao, John P. Perdew, Viktor N. Staroverov, and Gustavo E. Scuseria. **Climbing the Density Functional Ladder: Nonempirical Meta-Generalized Gradient Approximation Designed for Molecules and Solids**. *Physical Review Letters* 91:14 (Sept. 2003), 146401. DOI: [10.1103/PhysRevLett.91.146401](https://doi.org/10.1103/PhysRevLett.91.146401) (see page 16).
- [TC06] M. A. Tunney and N. R. Cooper. **Effects of Disorder and Momentum Relaxation on the Intertube Transport of Incommensurate Carbon Nanotube Ropes and Multiwall Nanotubes**. *Physical Review B* 74:7 (Aug. 2006), 075406. ISSN: 1098-0121, 1550-235X. DOI: [10.1103/PhysRevB.74.075406](https://doi.org/10.1103/PhysRevB.74.075406) (see page 83).
- [Tem+96] W. M. Temmerman, Z. Szotek, B. L. Gyorffy, O. K. Andersen, and O. Jepsen. **Gap Anisotropy in the Layered High Temperature Superconductors**. *Physical Review Letters* 76:2 (Jan. 1996), 307–310. ISSN: 0031-9007, 1079-7114. DOI: [10.1103/PhysRevLett.76.307](https://doi.org/10.1103/PhysRevLett.76.307) (see page 44).
- [TG07] J. C. Tung and G. Y. Guo. **Systematic *Ab Initio* Study of the Magnetic and Electronic Properties of All 3 d Transition Metal Linear and Zigzag Nanowires**. *Physical Review B* 76:9 (Sept. 2007), 094413. ISSN: 1098-0121, 1550-235X. DOI: [10.1103/PhysRevB.76.094413](https://doi.org/10.1103/PhysRevB.76.094413) (see page 125).
- [TGW01a] Jeremy Taylor, Hong Guo, and Jian Wang. ***Ab Initio* Modeling of Open Systems: Charge Transfer, Electron Conduction, and Molecular Switching of a C₆₀ Device**. *Physical Review B* 63:12 (Mar. 2001), 121104. ISSN: 0163-1829, 1095-3795. DOI: [10.1103/PhysRevB.63.121104](https://doi.org/10.1103/PhysRevB.63.121104) (see page 35).
- [TGW01b] Jeremy Taylor, Hong Guo, and Jian Wang. ***Ab Initio* Modeling of Quantum Transport Properties of Molecular Electronic Devices**. *Physical Review B* 63:24 (June 2001), 245407. ISSN: 0163-1829, 1095-3795. DOI: [10.1103/PhysRevB.63.245407](https://doi.org/10.1103/PhysRevB.63.245407) (see page 35).
- [Tho+82] D. J. Thouless, M. Kohmoto, M. P. Nightingale, and M. den Nijs. **Quantized Hall Conductance in a Two-Dimensional Periodic Potential**. *Physical Review Letters* 49:6 (Aug. 1982), 405–408. ISSN: 0031-9007. DOI: [10.1103/PhysRevLett.49.405](https://doi.org/10.1103/PhysRevLett.49.405) (see page 38).

- [Tho27] L. H. Thomas. **The Calculation of Atomic Fields**. *Mathematical Proceedings of the Cambridge Philosophical Society* 23:5 (Jan. 1927), 542–548. ISSN: 0305-0041, 1469-8064. DOI: [10.1017/S0305004100011683](https://doi.org/10.1017/S0305004100011683) (see page 12).
- [TKV19] Jacob Townsend, Justin K. Kirkland, and Konstantinos D. Vogiatzis. “Post-Hartree-Fock Methods: Configuration Interaction, Many-Body Perturbation Theory, Coupled-Cluster Theory.” In: *Mathematical Physics in Theoretical Chemistry*. Elsevier, 2019, 63–117. ISBN: 978-0-12-813651-5. DOI: [10.1016/B978-0-12-813651-5.00003-6](https://doi.org/10.1016/B978-0-12-813651-5.00003-6) (see page 12).
- [TMM10] G. Trambly de Laissardière, D. Mayou, and L. Magaud. **Localization of Dirac Electrons in Rotated Graphene Bilayers**. *Nano Letters* 10:3 (Mar. 2010), 804–808. ISSN: 1530-6984, 1530-6992. DOI: [10.1021/nl902948m](https://doi.org/10.1021/nl902948m) (see page 87).
- [Tod02] Tchavdar N Todorov. **Tight-Binding Simulation of Current-Carrying Nanostructures**. *Journal of Physics: Condensed Matter* 14:11 (Mar. 2002), 3049–3084. ISSN: 0953-8984, 1361-648X. DOI: [10.1088/0953-8984/14/11/314](https://doi.org/10.1088/0953-8984/14/11/314) (see page 60).
- [Tra16] Morgan Trassin. **Low Energy Consumption Spintronics Using Multiferroic Heterostructures**. *Journal of Physics: Condensed Matter* 28:3 (Jan. 2016), 033001. ISSN: 0953-8984, 1361-648X. DOI: [10.1088/0953-8984/28/3/033001](https://doi.org/10.1088/0953-8984/28/3/033001) (see page 1).
- [TS02] John K. Tomfohr and Otto F. Sankey. **Complex Band Structure, Decay Lengths, and Fermi Level Alignment in Simple Molecular Electronic Systems**. *Physical Review B* 65:24 (May 2002), 245105. ISSN: 0163-1829, 1095-3795. DOI: [10.1103/PhysRevB.65.245105](https://doi.org/10.1103/PhysRevB.65.245105) (see page 32).
- [TS66] B. Y. Tong and L. J. Sham. **Application of a Self-Consistent Scheme Including Exchange and Correlation Effects to Atoms**. *Physical Review* 144:1 (Apr. 1966), 1–4. DOI: [10.1103/PhysRev.144.1](https://doi.org/10.1103/PhysRev.144.1) (see page 15).
- [TSH05] Ryo Tamura, Yoko Sawai, and Junji Haruyama. **Suppression of the Pseudoantisymmetry Channel in the Conductance of Telescoped Double-Wall Nanotubes**. *Physical Review B* 72:4 (July 2005), 045413. ISSN: 1098-0121, 1550-235X. DOI: [10.1103/PhysRevB.72.045413](https://doi.org/10.1103/PhysRevB.72.045413) (see pages 83, 96).
- [UA05] Seiji Uryu and Tsuneya Ando. **Electronic Intertube Transfer in Double-Wall Carbon Nanotubes**. *Physical Review B* 72:24 (Dec. 2005), 245403. ISSN: 1098-0121, 1550-235X. DOI: [10.1103/PhysRevB.72.245403](https://doi.org/10.1103/PhysRevB.72.245403) (see pages 83, 104).
- [Ume97] A. Umerski. **Closed-Form Solutions to Surface Green’s Functions**. *Physical Review B* 55:8 (Feb. 1997), 5266–5275. ISSN: 0163-1829, 1095-3795. DOI: [10.1103/PhysRevB.55.5266](https://doi.org/10.1103/PhysRevB.55.5266) (see page 32).
- [van+18] M.J. van Setten, M. Giantomassi, E. Bousquet, M.J. Verstraete, D.R. Hamann, X. Gonze, and G.-M. Rignanese. **The PseudoDojo: Training and Grading a 85 Element Optimized Norm-Conserving Pseudopotential Table**. *Computer Physics Communications* 226 (May 2018), 39–54. ISSN: 00104655. DOI: [10.1016/j.cpc.2018.01.012](https://doi.org/10.1016/j.cpc.2018.01.012) (see pages 71, 86, 108, 131).

- [Van18] David Vanderbilt. **Berry Phases in Electronic Structure Theory: Electric Polarization, Orbital Magnetization and Topological Insulators**. First. Cambridge University Press, Oct. 2018. ISBN: 978-1-316-66220-5 978-1-107-15765-1. DOI: [10.1017/9781316662205](https://doi.org/10.1017/9781316662205) (see pages 37, 38, 78).
- [VB04] Julian Velez and William H. Butler. **Domain-Wall Resistance in Metal Nanocontacts**. *Physical Review B* 69:9 (Mar. 2004), 094425. ISSN: 1098-0121, 1550-235X. DOI: [10.1103/PhysRevB.69.094425](https://doi.org/10.1103/PhysRevB.69.094425) (see page 131).
- [Wak+18] T. Wakamura, F. Reale, P. Palczynski, S. Guéron, C. Mattevi, and H. Bouchiat. **Strong Anisotropic Spin-Orbit Interaction Induced in Graphene by Monolayer WS₂**. *Physical Review Letters* 120:10 (Mar. 2018), 106802. ISSN: 0031-9007, 1079-7114. DOI: [10.1103/PhysRevLett.120.106802](https://doi.org/10.1103/PhysRevLett.120.106802). (Visited on 03/21/2023) (see page 76).
- [Wak+19] T. Wakamura, F. Reale, P. Palczynski, M. Q. Zhao, A. T. C. Johnson, S. Guéron, C. Mattevi, A. Ouerghi, and H. Bouchiat. **Spin-Orbit Interaction Induced in Graphene by Transition Metal Dichalcogenides**. *Physical Review B* 99:24 (June 2019), 245402. ISSN: 2469-9950, 2469-9969. DOI: [10.1103/PhysRevB.99.245402](https://doi.org/10.1103/PhysRevB.99.245402). (Visited on 03/21/2023) (see page 76).
- [Wal+06] Derek Waldron, Vladimir Timoshevskii, Yibin Hu, Ke Xia, and Hong Guo. **First Principles Modeling of Tunnel Magnetoresistance of Fe / MgO / Fe Trilayers**. *Physical Review Letters* 97:22 (Nov. 2006), 226802. ISSN: 0031-9007, 1079-7114. DOI: [10.1103/PhysRevLett.97.226802](https://doi.org/10.1103/PhysRevLett.97.226802) (see pages 132, 136).
- [Wan+15] Zhiyong Wang, Chi Tang, Raymond Sachs, Yafis Barlas, and Jing Shi. **Proximity-Induced Ferromagnetism in Graphene Revealed by the Anomalous Hall Effect**. *Physical Review Letters* 114:1 (Jan. 2015), 016603. ISSN: 0031-9007, 1079-7114. DOI: [10.1103/PhysRevLett.114.016603](https://doi.org/10.1103/PhysRevLett.114.016603). (Visited on 03/21/2023) (see page 76).
- [Wan+16] Qisi Wang, Yao Shen, Bingying Pan, Xiaowen Zhang, K. Ikeuchi, K. Iida, A. D. Christianson, H. C. Walker, D. T. Adroja, M. Abdel-Hafiez, Xiaojia Chen, D. A. Chareev, A. N. Vasiliev, and Jun Zhao. **Magnetic Ground State of FeSe**. *Nature Communications* 7:1 (July 2016), 12182. ISSN: 2041-1723. DOI: [10.1038/ncomms12182](https://doi.org/10.1038/ncomms12182). (Visited on 08/18/2022) (see page 71).
- [Wan+18] Gang Wang, Alexey Chernikov, Mikhail M. Glazov, Tony F. Heinz, Xavier Marie, Thierry Amand, and Bernhard Urbaszek. **Colloquium: Excitons in Atomically Thin Transition Metal Dichalcogenides**. *Reviews of Modern Physics* 90:2 (Apr. 2018), 021001. DOI: [10.1103/RevModPhys.90.021001](https://doi.org/10.1103/RevModPhys.90.021001) (see page 140).
- [Wan+21] Yizhen Wang, Yajing Li, Jun Chen, Igor Ying Zhang, and Xin Xu. **Doubly Hybrid Functionals Close to Chemical Accuracy for Both Finite and Extended Systems: Implementation and Test of XYG3 and XYGJ-OS**. *JACS Au* 1:5 (May 2021), 543–549. ISSN: 2691-3704. DOI: [10.1021/jacsau.1c00011](https://doi.org/10.1021/jacsau.1c00011) (see page 16).

- [Wan+22] Shuang Wang, Yan Chen, Tianhao Tan, Yanping Sui, Chuang Tian, Ziqiang Kong, Haomin Wang, Sunwen Zhao, Runhan Xiao, Zhiying Chen, Yanhui Zhang, Dong Wang, Jianlu Wang, and Guanghui Yu. **One-Step Synthesis of a Bilayer MoS₂/WS₂ Lateral Heterojunction for Photoelectric Detection**. *ACS Applied Nano Materials* 5:11 (Nov. 2022), 17203–17211. ISSN: 2574-0970, 2574-0970. DOI: [10.1021/acsanm.2c04189](https://doi.org/10.1021/acsanm.2c04189) (see pages 141, 143).
- [WCJ94] S. Y. Wu, J. Cocks, and C. S. Jayanthi. **General Recursive Relation for the Calculation of the Local Green's Function in the Resolvent-Matrix Approach**. *Physical Review B* 49:12 (Mar. 1994), 7957–7963. ISSN: 0163-1829, 1095-3795. DOI: [10.1103/PhysRevB.49.7957](https://doi.org/10.1103/PhysRevB.49.7957) (see page 32).
- [Wi+14] Sungjin Wi, Hyunsoo Kim, Mikai Chen, Hongsuk Nam, L. Jay Guo, Edgar Meyhofer, and Xiaogan Liang. **Enhancement of Photovoltaic Response in Multilayer MoS₂ Induced by Plasma Doping**. *ACS Nano* 8:5 (May 2014), 5270–5281. ISSN: 1936-0851, 1936-086X. DOI: [10.1021/nn5013429](https://doi.org/10.1021/nn5013429) (see page 140).
- [WIB02] D. Wortmann, H. Ishida, and S. Blügel. **Ab Initio Green-function Formulation of the Transfer Matrix: Application to Complex Band Structures**. *Physical Review B* 65:16 (Mar. 2002), 165103. ISSN: 0163-1829, 1095-3795. DOI: [10.1103/PhysRevB.65.165103](https://doi.org/10.1103/PhysRevB.65.165103) (see page 35).
- [Wij86] H.P.J. Wijn, ed. **3d, 4d and 5d Elements, Alloys and Compounds**. Vol. 19a. Landolt-Börnstein - Group III Condensed Matter. Berlin/Heidelberg: Springer-Verlag, 1986. ISBN: 978-3-540-15904-9. DOI: [10.1007/b29710](https://doi.org/10.1007/b29710) (see pages 125, 129).
- [Wil+13] Thomas Williams, Colin Kelley, Russell Lang, Dave Kotz, John Campbell, and Elber Gershon. *Gnuplot: An Interactive Plotting Program*. Apr. 2013 (see page 73).
- [Wit+22] Nils Wittemeier, Matthieu J. Verstraete, Pablo Ordejón, and Zeila Zanolli. **Interference Effects in One-Dimensional Moiré Crystals**. *Carbon* 186 (Jan. 2022), 416–422. ISSN: 00086223. DOI: [10.1016/j.carbon.2021.10.028](https://doi.org/10.1016/j.carbon.2021.10.028) (see page 83).
- [WJW10] M W Wu, J H Jiang, and M Q Weng. **Spin Dynamics in Semiconductors**. *Physics Reports* (2010), 176 (see page 3).
- [WK78] Jun-ichi Wakabayashi and Shinji Kawaji. **Hall Effect in Silicon MOS Inversion Layers under Strong Magnetic Fields**. *Journal of the Physical Society of Japan* 44:6 (June 1978), 1839–1849. ISSN: 0031-9015, 1347-4073. DOI: [10.1143/JPSJ.44.1839](https://doi.org/10.1143/JPSJ.44.1839) (see page 38).
- [Woh+07] S. Wohlthat, F. Pauly, J. K. Viljas, J. C. Cuevas, and Gerd Schön. **Ab Initio Study of Charge Transport through Single Oxygen Molecules in Atomic Aluminum Contacts**. *Physical Review B* 76:7 (Aug. 2007), 075413. ISSN: 1098-0121, 1550-235X. DOI: [10.1103/PhysRevB.76.075413](https://doi.org/10.1103/PhysRevB.76.075413) (see page 35).

- [Wol+10] Stuart A. Wolf, Jiwei Lu, Mircea R. Stan, Eugene Chen, and Daryl M. Treger. **The Promise of Nanomagnetism and Spintronics for Future Logic and Universal Memory**. *Proceedings of the IEEE* 98:12 (Dec. 2010), 2155–2168. ISSN: 1558-2256. DOI: [10.1109/JPROC.2010.2064150](https://doi.org/10.1109/JPROC.2010.2064150) (see page 1).
- [Won+20] Dillon Wong, Kevin P. Nuckolls, Myungchul Oh, Biao Lian, Yonglong Xie, Sangjun Jeon, Kenji Watanabe, Takashi Taniguchi, B. Andrei Bernevig, and Ali Yazdani. **Cascade of Electronic Transitions in Magic-Angle Twisted Bilayer Graphene**. *Nature* 582:7811 (June 2020), 198–202. ISSN: 0028-0836, 1476-4687. DOI: [10.1038/s41586-020-2339-0](https://doi.org/10.1038/s41586-020-2339-0) (see page 3).
- [Woo92] Gordon Kemble Woodgate. **Elementary Atomic Structure**. 2. ed., reprinted. Oxford: Clarendon Press, 1992. ISBN: 978-0-19-851156-4 (see page 3).
- [WOZ22] Nils Wittemeier, Pablo Ordejón, and Zeila Zanolli. **Tuning the Topological Band Gap of Bismuthene with Silicon-Based Substrates**. *Journal of Physics: Materials* 5:3 (July 2022), 035002. ISSN: 2515-7639. DOI: [10.1088/2515-7639/ac84ad](https://doi.org/10.1088/2515-7639/ac84ad) (see pages 80, 107).
- [Wu+16] R. Wu, J.-Z. Ma, S.-M. Nie, L.-X. Zhao, X. Huang, J.-X. Yin, B.-B. Fu, P. Richard, G.-F. Chen, Z. Fang, X. Dai, H.-M. Weng, T. Qian, H. Ding, and S. H. Pan. **Evidence for Topological Edge States in a Large Energy Gap near the Step Edges on the Surface of ZrTe₅**. *Physical Review X* 6:2 (May 2016), 021017. ISSN: 2160-3308. DOI: [10.1103/PhysRevX.6.021017](https://doi.org/10.1103/PhysRevX.6.021017) (see page 120).
- [WW13] Tomasz A. Wesolowski and Yan Alexander Wang, eds. **Recent Progress in Orbital-Free Density Functional Theory**. Recent Advances in Computational Chemistry vol. 6. [Hackensack,] New Jersey: World Scientific, 2013. ISBN: 978-981-4436-72-4 (see page 15).
- [Yam+00] S. Yamanaka, D. Yamaki, Y. Shigeta, H. Nagao, Y. Yoshioka, N. Suzuki, and K. Yamaguchi. **Generalized Spin Density Functional Theory for Noncollinear Molecular Magnetism**. *International Journal of Quantum Chemistry* 80:4-5 (2000), 664–671. ISSN: 1097-461X. DOI: [10.1002/1097-461X\(2000\)80:4/5<664::AID-QUA15>3.0.CO;2-C](https://doi.org/10.1002/1097-461X(2000)80:4/5<664::AID-QUA15>3.0.CO;2-C) (see page 25).
- [Yam+01] S. Yamanaka, D. Yamaki, Y. Shigeta, H. Nagao, and K. Yamaguchi. **Noncollinear Spin Density Functional Theory for Spin-Frustrated and Spin-Degenerate Systems**. *International Journal of Quantum Chemistry* 84:6 (2001), 670–676. ISSN: 1097-461X. DOI: [10.1002/qua.1422](https://doi.org/10.1002/qua.1422) (see page 25).
- [Yan+06] Qimin Yan, Gang Zhou, Shaogang Hao, Jian Wu, and Wenhui Duan. **Mechanism of Nanoelectronic Switch Based on Telescoping Carbon Nanotubes**. *Applied Physics Letters* 88:17 (Apr. 2006), 173107. ISSN: 0003-6951, 1077-3118. DOI: [10.1063/1.2198481](https://doi.org/10.1063/1.2198481) (see page 83).

- [Yan+19] Matthew Yankowitz, Shaowen Chen, Hryhoriy Polshyn, Yuxuan Zhang, K. Watanabe, T. Taniguchi, David Graf, Andrea F. Young, and Cory R. Dean. **Tuning Superconductivity in Twisted Bilayer Graphene**. *Science* 363:6431 (Mar. 2019), 1059–1064. ISSN: 0036-8075, 1095-9203. DOI: [10.1126/science.aav1910](https://doi.org/10.1126/science.aav1910) (see page 3).
- [Zah+13] Ferdows Zahid, Lei Liu, Yu Zhu, Jian Wang, and Hong Guo. **A Generic Tight-Binding Model for Monolayer, Bilayer and Bulk MoS₂**. *AIP Advances* 3:5 (May 2013), 052111. ISSN: 2158-3226. DOI: [10.1063/1.4804936](https://doi.org/10.1063/1.4804936) (see page 140).
- [Zan+07] Z. Zanolli, F. Fuchs, J. Furthmüller, U. von Barth, and F. Bechstedt. **Model GW Band Structure of InAs and GaAs in the Wurtzite Phase**. *Physical Review B* 75:24 (June 2007), 245121. ISSN: 1098-0121, 1550-235X. DOI: [10.1103/PhysRevB.75.245121](https://doi.org/10.1103/PhysRevB.75.245121) (see page 20).
- [Zan+11] Zeila Zanolli, Radouane Leghrib, Alexandre Felten, Jean-Jacques Pireaux, Eduard Llobet, and Jean-Christophe Charlier. **Gas Sensing with Au-Decorated Carbon Nanotubes**. *ACS Nano* 5:6 (June 2011), 4592–4599. ISSN: 1936-0851, 1936-086X. DOI: [10.1021/nn200294h](https://doi.org/10.1021/nn200294h) (see page 92).
- [Zan+18] Z. Zanolli, C. Niu, G. Bihlmayer, Y. Mokrousov, P. Mavropoulos, M. J. Verstraete, and S. Blügel. **Hybrid Quantum Anomalous Hall Effect at Graphene-Oxide Interfaces**. *Physical Review B* 98:15 (Oct. 2018), 155404. ISSN: 2469-9950, 2469-9969. DOI: [10.1103/PhysRevB.98.155404](https://doi.org/10.1103/PhysRevB.98.155404) (see page 3).
- [ZC09] Zeila Zanolli and J.-C. Charlier. **Defective Carbon Nanotubes for Single-Molecule Sensing**. *Physical Review B* 80:15 (Oct. 2009), 155447. ISSN: 1098-0121, 1550-235X. DOI: [10.1103/PhysRevB.80.155447](https://doi.org/10.1103/PhysRevB.80.155447) (see pages 92, 148).
- [ZC10] Zeila Zanolli and J.-C. Charlier. **Spin Transport in Carbon Nanotubes with Magnetic Vacancy-Defects**. *Physical Review B* 81:16 (Apr. 2010), 165406. ISSN: 1098-0121, 1550-235X. DOI: [10.1103/PhysRevB.81.165406](https://doi.org/10.1103/PhysRevB.81.165406) (see pages 92, 148, 150).
- [ZC12] Zeila Zanolli and J.-C. Charlier. **Single-Molecule Sensing Using Carbon Nanotubes Decorated with Magnetic Clusters**. *ACS Nano* 6:12 (Dec. 2012), 10786–10791. ISSN: 1936-0851, 1936-086X. DOI: [10.1021/nn304111a](https://doi.org/10.1021/nn304111a) (see pages 92, 148).
- [Zen+13] Hualing Zeng, Gui-Bin Liu, Junfeng Dai, Yajun Yan, Bairen Zhu, Ruicong He, Lu Xie, Shijie Xu, Xianhui Chen, Wang Yao, and Xiaodong Cui. **Optical Signature of Symmetry Variations and Spin-Valley Coupling in Atomically Thin Tungsten Dichalcogenides**. *Scientific Reports* 3:1 (Dec. 2013), 1608. ISSN: 2045-2322. DOI: [10.1038/srep01608](https://doi.org/10.1038/srep01608) (see page 140).
- [ŽFD04] Igor Žutić, Jaroslav Fabian, and S. Das Sarma. **Spintronics: Fundamentals and Applications**. *Reviews of Modern Physics* 76:2 (Apr. 2004), 323–410. ISSN: 0034-6861, 1539-0756. DOI: [10.1103/RevModPhys.76.323](https://doi.org/10.1103/RevModPhys.76.323) (see page 1).

- [Zha+15] P. Zhang, T. Qian, P. Richard, X. P. Wang, H. Miao, B. Q. Lv, B. B. Fu, T. Wolf, C. Meingast, X. X. Wu, Z. Q. Wang, J. P. Hu, and H. Ding. **Observation of Two Distinct $d_x z / d_y z$ Band Splittings in FeSe**. *Physical Review B* 91:21 (June 2015), 214503. ISSN: 1098-0121, 1550-235X. DOI: [10.1103/PhysRevB.91.214503](https://doi.org/10.1103/PhysRevB.91.214503). (Visited on 03/17/2023) (see pages 70, 71).
- [Zha+20] Sihan Zhao, Pilkyung Moon, Yuhei Miyauchi, Taishi Nishihara, Kazunari Matsuda, Mikito Koshino, and Ryo Kitaura. **Observation of Drastic Electronic-Structure Change in a One-Dimensional Moiré Superlattice**. *Physical Review Letters* 124:10 (Mar. 2020), 106101. ISSN: 0031-9007, 1079-7114. DOI: [10.1103/PhysRevLett.124.106101](https://doi.org/10.1103/PhysRevLett.124.106101) (see pages 83, 84).
- [Zho+15] Miao Zhou, Wenmei Ming, Zheng Liu, Zhengfei Wang, Yugui Yao, and Feng Liu. **Formation of Quantum Spin Hall State on Si Surface and Energy Gap Scaling with Strength of Spin Orbit Coupling**. *Scientific Reports* 4:1 (May 2015), 7102. ISSN: 2045-2322. DOI: [10.1038/srep07102](https://doi.org/10.1038/srep07102) (see pages 107, 112).
- [Zhu16] Jian-Xin Zhu. **Bogoliubov-de Gennes Method and Its Applications**. Vol. 924. Lecture Notes in Physics. Cham: Springer International Publishing, 2016. ISBN: 978-3-319-31314-6. DOI: [10.1007/978-3-319-31314-6](https://doi.org/10.1007/978-3-319-31314-6) (see pages 44, 46).
- [ZKN17] Yi Zhou, Kazushi Kanoda, and Tai-Kai Ng. **Quantum Spin Liquid States**. *Reviews of Modern Physics* 89:2 (Apr. 2017), 025003. ISSN: 0034-6861, 1539-0756. DOI: [10.1103/RevModPhys.89.025003](https://doi.org/10.1103/RevModPhys.89.025003) (see page 25).
- [Zon+20] U. Zondiner, A. Rozen, D. Rodan-Legrain, Y. Cao, R. Queiroz, T. Taniguchi, K. Watanabe, Y. Oreg, F. von Oppen, Ady Stern, E. Berg, P. Jarillo-Herrero, and S. Ilani. **Cascade of Phase Transitions and Dirac Revivals in Magic-Angle Graphene**. *Nature* 582:7811 (June 2020), 203–208. ISSN: 0028-0836, 1476-4687. DOI: [10.1038/s41586-020-2373-y](https://doi.org/10.1038/s41586-020-2373-y) (see page 3).
- [ZT06] Yan Zhao and Donald G. Truhlar. **A New Local Density Functional for Main-Group Thermochemistry, Transition Metal Bonding, Thermochemical Kinetics, and Noncovalent Interactions**. *The Journal of Chemical Physics* 125:19 (Nov. 2006), 194101. ISSN: 0021-9606. DOI: [10.1063/1.2370993](https://doi.org/10.1063/1.2370993) (see page 16).
- [Zwi+08] M. Zwierzycki, P. A. Khomyakov, A. A. Starikov, K. Xia, M. Talanana, P. X. Xu, V. M. Karpan, I. Marushchenko, I. Turek, G. E. W. Bauer, G. Brocks, and P. J. Kelly. **Calculating Scattering Matrices by Wave Function Matching**. *physica status solidi (b)* 245:4 (Apr. 2008), 623–640. ISSN: 03701972, 15213951. DOI: [10.1002/pssb.200743359](https://doi.org/10.1002/pssb.200743359) (see pages 132, 134).

Appendices

List of Publications

Articles in Peer-Reviewed Journals as Main Author

- [1] Nils Wittemeier, Matthieu J. Verstraete, Pablo Ordejón, and Zeila Zanolli. **Interference Effects in One-Dimensional Moiré Crystals**. en. *Carbon* 186 (Jan. 2022), 416–422. ISSN: 00086223. DOI: [10.1016/j.carbon.2021.10.028](https://doi.org/10.1016/j.carbon.2021.10.028).
- [2] Nils Wittemeier, Pablo Ordejon, and Zeila Zanolli. **Tuning the Topological Band Gap of Bismuthene with Silicon-based Substrates**. *Journal of Physics: Materials* (July 2022). ISSN: 2515-7639. DOI: [10.1088/2515-7639/ac84ad](https://doi.org/10.1088/2515-7639/ac84ad).

Articles in Peer-Reviewed Journals as Collaborating Author

- [1] Claire Besson, Philipp Stegmann, Michael Schnee, Zeila Zanolli, Simona Achilli, Nils Wittemeier, Asmus Vierck, Robert Frielinghaus, Paul Kögerler, Janina Maultzsch, Pablo Ordejón, Claus M. Schneider, Alfred Hucht, Jürgen König, and Carola Meyer. **Independent and Coherent Transitions between Antiferromagnetic States of Few-Molecule Systems** (2021). DOI: [10.48550/ARXIV.2107.07723](https://doi.org/10.48550/ARXIV.2107.07723).
- [2] Armando Pezo, Zeila Zanolli, Nils Wittemeier, Pablo Ordejón, Adalberto Fazzio, Stephan Roche, and Jose H Garcia. **Manipulation of Spin Transport in Graphene/-Transition Metal Dichalcogenide Heterobilayers upon Twisting**. *2D Materials* 9:1 (Jan. 2022), 015008. ISSN: 2053-1583. DOI: [10.1088/2053-1583/ac3378](https://doi.org/10.1088/2053-1583/ac3378).

Articles in Preparation

- [1] Nils Wittemeier, Nick Papior, Mads Brandbyge, Zeila Zanolli, and Pablo Ordejon. **Quantum Transport with Spin Orbit Coupling: New Developments in Transiesta** (2023).
- [2] Nils Wittemeier, Riccardo Reho, Arnold Kole, Gabor Csire, Pablo Ordejón, and Zeila Zanolli. **Density Functional Bogoliubov-de Gennes Method: Theory and Implementation in the SIESTA code** (2023).

Invited Talks

- [1] **Interference Effects in One-Dimensional Moiré Crystals**. ETSF Webinar Series. online, April 29th, 2022. URL: <https://www.etsf.eu/webinars>.

Contributed Talks

- [1] **Interference Effects in One-Dimensional Moiré Crystals**. DPG Meeting of the Condensed Matter Section (SKM). Regensburg, Germany, September 4th-9th, 2022. URL: <https://regensburg22.dpg-tagungen.de/>.
- [2] **Quantum Transport with Spin Orbit Coupling**. Psi-k Conference. Lausanne, Switzerland, August 22nd-25th, 2022. URL: <https://www.psi2022.net/>.
- [3] **Tuning the Topological Band Gap of Bismuthene with Silicon-based Substrates**. Graphene 2022. Aachen, Germany, July 5th – 8th, 2022. URL: <https://www.grapheneconf.com/2022/>.

Poster Presentations

- [1] **Electronic and Transport Properties of Single and Double Wall Carbon Nanotubes**. Workshop in TBtrans + TranSiesta + sisl. Lyngby, Denmark, November 20th – 23rd, 2018.
- [2] **Electronic and Transport Properties of Single and Double Wall Carbon Nanotubes**. 23rd ETSF workshop on electronic excitations. Milan, Italy, September 10th - 14th, 2018. URL: <http://ws23.pcpm.ucl.ac.be/>.
- [3] **Electronic and Transport Properties of Single and Double Wall Carbon Nanotubes**. Modelling nanostructures symposium. Namur, Belgium, January 31st and February 1st, 2019. URL: <https://www.unamur.be/en/sci/physics/modelling-nanostructures>.
- [4] **Quantum Transport with Spin Orbit Coupling**. 20th International Workshop on Computational Physics and Materials Science: Total Energy and Force Methods. online, February 25th, 2021. URL: <https://indico.ictp.it/event/9510/>.

List of Figures

3.1	Schematic of the quantum mechanical transport problem in 1D	28
3.2	Sketch of a 3-electrode transport setup.	31
3.3	Flow chart of the self-consistent DFT+NEGF method	35
3.4	Closed complex contours for NEGF method.	36
6.1	Performance characterization of TRANSIESTA	59
7.1	Density of states of lead and iron selenide calculated with the BdG+DFT method.	69
7.2	Density of states of iron selenide for different orbital dependent pairing potentials calculated with the BdG+DFT method.	70
8.1	Spin texture of a Bi(111) monolayer	74
8.2	In-plane spin texture of 3-quintuple-layer Bi ₂ Se ₃ on two constant energy paths	75
8.3	Electronic band structure and spin texture of graphene/MoTe ₂ twisted by 15°	76
8.4	Sketch of the three different trajectories of an HWCC as a function of k_y on a rolled (top) and unrolled (bottom) cylinder.	78
8.5	Sketch of possible evolutions of HWCCs for a system with two occupied bands and time-reversal symmetry.	79
9.1	Schematic of three different types of DWNT geometries	84
9.2	Schematic of three chiral vectors and corresponding carbon nanotube axes.	85
9.3	Schematic of p orbitals in a double-wall carbon nanotube, each perpendicular to the tube surface.	87
9.4	Fit of tight-binding band structure	88
9.5	Transport set-up consists of two overlapping nanotubes	90
9.6	TB electron transmission through infinite (10,10)@(15,15) tDWNT and energy levels of the same tDWNT	92
9.7	Projected TB band structure of an ideal (10,10)@(15,15) DWNT	93
9.8	DFT wave functions of a telescopic (10,10)@(15,15) DWNT	94
9.9	TB electron transmission from a (10,10) SWNT into a (15,15) SWNT through a finite overlap region at different overlap lengths	95

9.10	Schematic of one-dimensional scattering waves in the quantum box of the overlap region between two semi-infinite nanotubes.	96
9.11	TB electron transmission from (18,15) into (23,20)	98
9.12	Projected band structure of a periodic approximation of the incommensurate (18,15)@(23,20)	99
9.13	DFT wave function of a chiral (18,15) nanotube	99
9.14	Band structure and density of states of a periodic equivalent of the incommensurate (27, 3)@(35,3)	100
9.15	Density of states and electron transmission of a telescopic (27,3)@(35,3) DWNT	100
9.16	Density of states and electron transmission of a telescopic (27,3)@(36,3) DWNT	101
9.17	Density of states and electron transmission of a telescopic (45,18)@(54,18) DWNT	102
9.18	Density of states and electron transmission of two telescopic DWTNs in the <i>weak coupling</i> regime for different overlap lengths L	103
10.1	Crystal structure of free-standing buckled and flat hexagonal bismuthene . . .	110
10.2	Crystal structure and orbital projected DFT electronic band structure of flat hexagonal bismuthene@SiC(0001).	112
10.3	Change in charge density due to interaction between monolayer and substrate in flat hexagonal bismuthene@SiC(0001)	113
10.4	Crystal structure and orbital projected DFT electronic band structure of buckled hexagonal bismuthene@SiC(0001)	113
10.5	Effect of strain on the band structure of free-standing bismuthene	114
10.6	Crystal structure of SiO ₂ slabs	115
10.7	Crystal structure and orbital projected DFT electronic band structure of buckled hexagonal bismuthene on different SiO ₂ surfaces	116
10.8	Crystal structure and orbital-projected band structure of flat hexagonal bismuthene on SiO ₂	118
10.9	Crystal structure and orbital projected DFT electronic band structure of buckled hexagonal bismuthene@passivated Si(111)	119
11.1	Schematic of five different spin alignments in monoatomic chains	124
11.2	Comparison of scalar relativistic and fully relativistic spin band structure of a monatomic iron chain with spin moment parallel and perpendicular to the chain axis	125
11.3	Spin texture and spin-channel projected transmission of an iron chain with spin magnetic moments perpendicular to the chain axis	126

11.4 Spin texture and spin-channel projected transmission of an iron chain with spin magnetic moments parallel to the chain axis	127
11.5 Infinite iron chain with a 6-atom wide domain wall between two semi-infinite sections with opposite magnetic moments	128
11.6 Direction and size of spin moments in a 4-atom wide, constraint domain walls	129
11.7 Zero-bias transmission of 180° domain walls	130
11.8 Band structure of bulk iron magnetized along the [001] direction.	133
11.9 Spectral function and zero-bias transmission of bulk iron for magnetization (M) parallel and perpendicular to the transport direction ([001]) at $E = -0.97$ eV .	134
11.10 Spectral function and zero-bias transmission of bulk iron for magnetization parallel and perpendicular to the transport direction ([001]) at the Fermi level	135
11.11 Ball and stick model of a Fe/MgO/Fe junction.	136
11.12 Spectral function and zero-bias transmission of a Fe/MgO/Fe tunneling junction with 4 MgO layers at $E = E_F$	137
11.13 Spin channel projected zero-bias transmission of a Fe/MgO/Fe tunneling junction with 4 MgO layers.	138
11.14 Convergence of the transmission function in a Fe/MgO/Fe junction with number of iron layers between the MgO layers and the electrodes (a) and with number of fixed layers (b).	139
11.15 Band structure and zero-bias transmission function of MoS ₂ and WS ₂ monolayers	141
11.16 Crystal structure of a lateral MoS ₂ -WS ₂ heterojunction top view and side view	142
11.17 Zero-bias transmission of hole-doped MoS ₂ and WS ₂ monolayers and a lateral MoS ₂ -WS ₂ heterojunction	143
11.18 Local and total density of states of a lateral MoS ₂ -WS ₂ heterjunction	144
11.20 Simulations set up for carbon nanotubes functionalized with antiferromagnetic tetranuclear clusters	147
11.21 Spin density of {Co ₄ }-CNT and {Mn ₄ }-CNT calculated with periodic boundary conditions	149
11.22 Decay of magnetic density carbon nanotubes functionalized with antiferromagnetic tetranuclear clusters	150
11.23 Transmission function of {Co ₄ }-CNT and {Mn ₄ }-CNT	151
11.24 Bound density of states and spin-channel-projected transmission of {Co ₄ }-CNT and {Mn ₄ }-CNT	152

List of Tables

6.1	Sparse matrix format for the Hamiltonian and density matrix in SIESTA. . . .	56
9.1	Optimized tight-binding parameters.	89
9.2	Summary of key characteristics of DWNTs covering all possible combinations of coupling regimes, chirality, and commensurability	91
9.3	Oscillation periods in density-of-states of telescopic (27,3)@(36,3) DWNT for different overlap lengths	101
10.1	Summary of the basic properties of buckled hexagonal and flat hexagonal Bi monolayer phases in free-standing form and supported by different substrates.	121
11.1	Comparison of magnetic moments of carbon nanotubes functionalized with tetranuclear clusters calculated in differently sized cells	148